7-25-2022 1:30 PM

The Role of Nonideal Magnetohydrodynamic Effects, Gravitational Instability, and Episodic Accretion in Star-Formation

Indrani Das, *The University of Western Ontario*

Supervisor: Basu, Shantanu, *The University of Western Ontario*

A thesis submitted in partial fulfillment of the requirements for the Doctor of Philosophy degree in Physics

Abstract

My dissertation focuses on the effect of magnetic fields on disk and core evolution during star-formation. We investigate the fragmentation scales of gravitational instability of a rotationally-supported self-gravitating protostellar disk using linear perturbation analysis in the presence of two nonideal magnetohydrodynamic (MHD) effects: Ohmic dissipation and ambipolar diffusion. Our results show that molecular clouds exhibit a preferred lengthscale for collapse that depends on mass-to-flux ratio, magnetic diffusivities, and the Toomre-Q parameter. In addition, the influence of the magnetic field on the preferred mass for collapse leads to a modified threshold for the fragmentation mass, as opposed to a Jeans mass, that might lead to giant planet formation in the early embedded phase. Furthermore, we apply the nonideal MHD threshold for fragmentation scales to fit the data of prestellar core lifetimes and as well as the number of enclosed cores formed in a clump, as found with the observations of *Herschel* and *Submillimeter Array* (SMA), respectively. Our results show that the trend found in the observed lifetime and fragmentation mass cannot be explained in a purely hydrodynamic scenario. Our best-fit model exhibits $B \propto n^{0.43}$, which signifies a means to indirectly infer the effect of the ambipolar diffusion on mildly supercritical dense regions of molecular clouds. We also develop a semi-analytic formalism of episodic mass accretion (therefore episodic luminosity) from a disk to star, which provides a good match to the observed luminosity distribution of protostars. In contrast, neither a constant nor a time-dependent but smoothly varying mass accretion rate is able to do so. Our analytic work provides insight into global MHD simulations of protoplanetary disks that we carry out using the FEOSAD numerical code. Our numerical results demonstrate the long-term evolution of disks, including the formation and evolution of clumps, and especially the episodic nature of accretion, which might explain the origin of observed knots in the molecular jet outflows.

Keywords: ISM: clouds - magnetic fields - magnetohydrodynamics (MHD) - stars: formation, gravitational collapse, disk evolution: episodic accretion, young stellar objects (YSOs)

Summary for lay audience

Stars are the essential links between galaxies and planetary systems. The present-day solar system is thought to be created about 4.5 billion years ago from the solar nebula- a giant cloud of dust and gas in interstellar space (i.e., the space between the stars in a galaxy). During the transformation from a gaseous nebula into a star-disk system there are many fundamental physical mechanisms such as gravity, thermal pressure, and the magnetic fields that have to come into action together. Their role in star formation is a matter of ongoing study. To form a star, enough matter has to pile up to the center of a gas cloud such that no other force can prevent the gravitational collapse. In recent times, cutting-edge observations have revealed new horizons to studying star formation at high resolution and even beyond the confines of our Galaxy. In this thesis, different evolutionary epochs of star formation have been studied, starting from the collapse of a gas cloud to the birth of a star-disk system where the planets may also form. Our results show that the gravitational fragmentation scales include the effects beyond that set by thermal pressure alone. These findings signify the indirect imprints of the magnetic fields on the star-forming clouds that are consistent with observations. Furthermore, we develop a model that explains the basic mechanisms of how the matter falls onto the central star through a series of luminous eruptive outbursts. Finally, we show that magnetic field can further drive the rapid accumulation of matter from the inner disk onto the center, thereby expediting star formation.

Co-Authorship Statement

This thesis is comprised of the four projects as presented in Chapter 2-5 and and all of them co-authored with various collaborators. Three of chapters are published in peer reviewed journals and the fourth one is in preparation.

For the paper as presented in Chapter 2, I am the first author, and Prof. Shantanu Basu is the second author. The idea of the paper was proposed by Prof. Shantanu Basu. I built the numerical code for this extensive work, and produced the results. Prof. Shantanu Basu helped me to analyze and interpret the results. Both of us wrote the paper after I wrote a first draft. This work is published in Astrophysical Journal, 910, 163 on April 1, 2021.

For the paper as presented in Chapter 3, I am the principal author. This is an extension of the project in Chapter 2 and the idea was proposed by Prof. Shantanu Basu, who is a co-author. Our collaborator Prof. Philippe Andre is also a co-author of this paper. I wrote the numerical code for this work. Prof. Basu and Prof. Andre helped me in the interpretation of the results and to write the manuscript after I wrote a first draft. This work is published in Astronomy & Astrophysics, 649, L13 on May 13, 2021.

For the paper as presented in Chapter 4, I am the first author, and Prof. Shantanu Basu is the second author. The idea was originated by Prof. Shantanu Basu. The working numerical code is written by me. Prof. Basu helped me to analyze and comprehend the results. Both of us wrote the paper after I wrote the first draft. This work is published in Monthly Notices of Royal Astronomical Society, 514, 5659 on June 20, 2022.

For the project as presented in Chapter 5, the numerical magnetohydrodynamic (MHD) code FEOSAD is used that has been developed by Prof. Eduard Vorobyov. This idea of this project was proposed by Prof. Shantanu Basu and Prof. Eduard Vorobyov. With this simulation code, my task was modifying the numerical code, running simulations, and analyzing and interpreting the resulting data. This chapter is written by me. Prof. Basu helped me to write the chapter by giving valuable inputs.

Permissions

The figures in Chapter 1 and Chapter 5 of this thesis which are reproductions from the published works are accompanied by their original citations. Additional permissions and licensing are listed here:

Figure 1.1 has been obtained with permission from the author of the original paper: Larson R. B., 1969, MNRAS, 145, 271 (DOI: 10.1093/mnras/145.3.271).

Figure 1.2 has been obtained from a review note by Tassis et al. 2018 (arXiv ID: 1810.05652) available in the public domain arXiv.

Figure 1.3 has been obtained with permission from the author of the original paper: Crutcher R. M., 2012, ARA&A, 50, 29 (DOI: 10.1146/annurev-astro-081811-125514).

Figure 5.1 has been obtained with permission from the author of the original paper: Vorobyov E. I., Basu S., 2010, ApJ, 719, 1896 (DOI: 10.1088/0004-637X/719/2/1896).

Figure 5.4 has been obtained with permission from the author of the original paper: Vorobyov E. I., Basu S., 2006, ApJ, 650, 956 (DOI: 10.1086/507320).

Figure 5.9 has been taken from the public domain NASA images.

Figure 5.10 has been obtained with permission from the author of the original paper: Lee C.-F., Ho P. T. P., Li Z.-Y., Hirano N., Zhang Q., Shang H., 2017, Nature Astronomy, 1, 0152 (DOI: 10.1038/s41550-017-0152).

Dedicated to my mother Tamasa Das and my father Susanta Das...

"Science doesn't always go forwards. It's a bit like doing a Rubik's cube. You sometimes have to make more of a mess with a Rubik's cube before you can get it to go right."

_____ *Jocelyn Bell Burnell*

Acknowledgements

It is my genuine pleasure to acknowledge all the people who have made this thesis possible. First and foremost, I am immensely grateful to my advisor, Prof. Shantanu Basu, for his advice and encouragement at every step of the way during the past four years. His deep physical insight and curiosity for scientific excellence greatly motivated my interest in research on star formation. I will always cherish all the scientific discussions with Prof. Basu and how he explains the complicated concepts starting from the fundamental ideas without going into rigorous derivations. I learned so much from you and will continue to learn. It is my pleasure to pursue my Ph.D. under your supervision. My sincere thanks to you for your constant support and guidance and for helping me make research career prospects.

Next, I would like to thank my collaborators for working together on several exciting projects. I want to thank Prof. Philippe Andre for the interesting scientific discussions during our collaborative project. I also want to express my special gratitude to Prof. Eduard Vorobyov for providing me with his MHD simulation code for my research, which he has been developing for several years. During my Ph.D. tenure at Western, I participated in some projects outside my thesis. I owe immense gratitude to Prof. Christopher Essex for his continuous support throughout my Ph.D. I want to express my sincere thanks to Prof. Essex for involving me in his project, which gave me a chance to explore outside the research line of my thesis. I am immensely thankful to Prof. Christopher Essex, Prof. Matthew Kunz, and Prof. Philippe Andre for guiding me toward my future research career developments along with my advisor. I also want to thank all of my group members for giving me a chance to collaborate with them on some exciting projects. I especially want to thank Kundan, Aris, and Franco for the helpful scientific discussions.

This acknowledgment section would have been incomplete without thanking all my incredible teachers who taught me the ABCs of the fundamental physics that I could not forget. I am indebted to Prof. Shantanu Basu and Prof. Somnath Bharadwaj for teaching me everything I know about Astrophysics and Cosmology. Rather than mentioning everyone here, I sincerely thank Prof. Sayan Kar, Prof. Somnath Bharadwaj, Prof. Tapas Kumar Das, Prof. Ajita Sengupta, Prof. Shatadal Bhattacharya, and Prof. Partha Ghosh for being the most influential persons in my life who inspired me to pursue a research career.

On top of everything, I am eternally grateful to my beloved parents, the best role models in my life. I do not have words to express my gratitude to my parents for their never-ending care, enormous support, and sacrifices in bringing me up to be a better individual. Staying abroad for four years at a stretch and without being able to come home due to the pandemic has been very difficult for me, sometimes unbearable. I can not thank you enough for boosting me up towards life, which helped me to overcome my struggles throughout this period. In addition, my heartfelt thanks to my boyfriend Sahel for always being there for me. Thank you for putting up with me, cheering me up when needed, and, most importantly, trusting me all along. I immensely enjoyed and will continue to enjoy all the scientific conversations with you, from the pesky numerical bugs to theoretical astrophysics. I express a heartfelt appreciation to my loving parents and Sahel for always having my back, even from 12,600 km across the oceans during this big adventure that has always been my dream. I could not have done this without you all.

I feel blessed to have so much affection and good wishes from my relatives and friends back in India. I also want to thank my friends and colleagues in Physics & Astronomy department at Western University for all the good times and chat I had with them. I express my special gratitude to Sheran ma'am for all her love, kindness, and hospitality that she has given me since the day one of my stay in Canada. From the bottom of my heart, a special thank you to Amrapali di, my closest friend in London, for everything you did for me throughout the time. Thanks for being so caring to me and making me surprised with the delicious Bengali dishes that I can never imagine having in Canada.

Finally, I thank my beautiful motherland, India. I am fortunate enough to complete my Bachelor's and Master's degree education in India with the support of INSPIRE Scholarship. I will always try to carry my liability to my nation.

Contents

Abstract ii

Summary for Lay audience iii

Co-Authorship Statement iv

Permissions v

Acknowledgements viii

List of Figures xiv

List of Tables xvii

1 Introduction 1

1.1 Preliminaries and Overview . . . 1

1.2 Zooming in on star-forming regions . . . 2

1.2.1 From molecular clouds to the birth of star-forming cores . . . 2

1.2.2 Tracers of the Molecular cloud . . . 5

1.3 Microphysics of star formation . . . 7

1.3.1 Gravitational collapse to star-forming cores . . . 7

1.3.2 Magnetic fields . . . 9

1.3.2.1 Nonideal magnetohydrodynamic effects . . . 11

1.3.2.2 Measurements of magnetic fields . . . 16

1.3.2.3 Density scaling of magnetic fields . . . 18

1.3.3 Effects of turbulence . . . 21

1.4 Collapse to a star-disk system . . . 23

1.4.1 Origin of episodic bursts in the early stages of star-formation . . . 25

1.4.2 Disk Physics: mechanism of transport . . . 28

1.4.2.1 Transport in self-gravitating disk . . . 29

1.4.2.2 Magnetic field as a source of transport . . . 31

1.5 Chapter review . . . 33
Bibliography . . . 34

2 Linear Stability Analysis of a Magnetic Rotating Disk with Ohmic Dissipation and Ambipolar Diffusion 40
2.1 Introduction . . . 40
2.2 Analytic Considerations . . . 44
2.2.1 Physical Formulation . . . 44
2.2.2 Fundamental Equations . . . 48
2.2.3 Stability of the model: Linearization and Analysis . . . 51
2.2.4 Dispersion Relation . . . 53
2.2.5 Normalization . . . 55
2.2.6 Generalized Toomre Criterion . . . 58
2.2.7 Stationary Magnetic Field Limit . . . 63
2.3 Numerical Results . . . 65
2.3.1 Flux-frozen Model . . . 65
2.3.2 Theoretical Models with Nonideal MHD . . . 66
2.3.3 Results for a Protostellar Disk . . . 71
2.3.4 $\tau'_{g,m}$ and $\lambda'_{g,m}$ as Functions of the Diffusion Parameters . . . 75
2.3.5 Critical Limit of the Generalized Toomre Criterion . . . 78
2.4 Discussion . . . 80
2.5 Summary . . . 83
2.6 Appendices . . . 85
2.6.1 Units of Defined Parameters . . . 85
2.6.2 Collision timescales . . . 86
2.6.3 Characteristic diffusion length scales for OD and AD . . . 86
2.6.4 Effective Sound Speed . . . 87
2.6.5 Notes on Generalized Toomre Criterion . . . 88
2.6.6 Notes on Stationary field limit . . . 90
2.6.7 Additional figures of normalized growth timescale vs. length scale . . . 91
2.6.8 Monochromatic Perturbation . . . 92
2.6.9 Calculation of W_* . . . 98
Bibliography . . . 100

3 Variation of the core lifetime and fragmentation scale in molecular clouds as an indication of ambipolar diffusion 103
3.1 Introduction . . . 103

3.2 Analytic model . . . 105
3.3 Observational correspondence to prestellar cores . . . 108
3.3.1 Lifetime of prestellar cores . . . 108
3.3.2 Number of enclosed cores . . . 111
3.3.3 Estimation of magnetic field . . . 113
3.4 Conclusions . . . 115
3.5 Appendices . . . 116
3.5.1 System of equations . . . 116
3.5.2 Tables . . . 122
Bibliography . . . 123

4 A semi-analytic model for the temporal evolution of the episodic disc-to-star accretion rate during star formation 125
4.1 Introduction . . . 125
4.2 Methodology . . . 128
4.2.1 Prestellar density profile . . . 128
4.2.2 Spherical envelope accretion . . . 129
4.2.2.1 Mass accretion rate from collapse of the cloud . . . 129
4.2.2.2 Evolution of mass accretion rate for different density models . 131
4.2.3 Disc accretion . . . 132
4.2.4 Episodic accretion bursts . . . 134
4.3 Results . . . 136
4.3.1 Envelope accretion . . . 137
4.3.1.1 Spatial profiles of mass and angular momentum . . . 139
4.3.2 Formalism of stellar accretion . . . 143
4.3.3 Temporal evolution of the mass accretion rate . . . 146
4.3.4 Mass estimation . . . 150
4.3.5 Estimating luminosity and comparing with observations . . . 152
4.4 Discussion . . . 156
4.5 Summary . . . 160
4.6 Appendix . . . 161
4.6.1 Analytic solutions for mass and specific angular momentum profile . . . 161
Bibliography . . . 163

5 Numerical simulations of mass accretion bursts in magnetized gas-dust protoplanetary disks 166
5.1 Introduction . . . 166

5.2 Methods . . . 168
5.2.1 Initial Conditions . . . 168
5.2.2 Numerical Equations for gaseous component . . . 170
5.2.3 Dust Physics . . . 172
5.2.4 Adaptive viscosity and ionization fraction . . . 174
5.2.5 Boundary Conditions . . . 178
5.3 Results . . . 179
5.4 Conclusions and Discussions . . . 192
Bibliography . . . 193

6 Summary **196**
Bibliography . . . 200

Curriculum Vitae **201**

List of Figures

1.1 The variation of the density distribution in the collapsing cloud with radial distance at different times . . . 7

1.2 Polarization of dust emission . . . 18

1.3 Zeeman measurements of the magnitude of the line-of-sight (LOS) magnetic field component plotted against number density from the set of diffuse cloud and molecular cloud . . . 19

2.1 Schematic diagram of the thin-disk model. . . . 44

2.2 Normalized generalized rotation parameter ($Q_{\rm eff}$) as a function of μ_0 for different values of Toomre-Q parameter . . . 59

2.3 Modified critical rotation parameter $Q_{\rm crit,m}$ as a function of μ_0 . . . 60

2.4 Normalized maximum and minimum wavelength for rotationally modulated instability as a function of μ_0. . . . 62

2.5 Normalized growth time of the gravitationally unstable mode as a function of normalized wavelength for flux-frozen models with and without the effect of rotation . . . 65

2.6 Normalized growth time of the gravitationally unstable mode as a function of normalized wavelength for the cases with different normalized Ohmic diffusivities and normalized neutral-ion collision times . . . 66

2.7 Normalized growth time of gravitationally unstable mode as a function of the normalized wavelength for models with different normalized Ohmic diffusivities and different normalized mass-to-flux-ratios . . . 67

2.8 Normalized shortest growth timescale and preferred length scale of the gravitationally unstable mode as a function of the normalized mass-to-flux ratio for the case with only ohmic dissipation and only ambipolar diffusion . . . 69

2.9 Normalized shortest growth timescale and preferred length scale of the most unstable mode as a function of normalized mass-to-flux ratio for models with different normalized rotations and a fixed normalized Ohmic diffusivity . . . 72

2.10 Normalized shortest growth timescale, preferred length scale, and preferred fragmentation mass of the most unstable mode as a function of normalized mass-to-flux ratio for a fixed normalized Ohmic diffusivity and normalized neutral-ion collision time . . . 73
2.11 Normalized shortest growth time of gravitationally unstable mode and normalized preferred length scale of most unstable mode as a function of normalized Ohmic diffusivity ($\tilde{\eta}_{\rm OD,0}$) for a fixed normalized rotation . . . 75
2.12 Normalized shortest growth time of gravitationally unstable mode and normalized preferred length scale of most unstable mode as a function of normalized neutral-ion collision time . . . 76
2.13 Normalized growth time of gravitationally unstable mode as a function of normalized wavelength (i) for the flux-frozen models with different rotation parameter and with a fixed mass-to-flux ratio; (ii) also for the models with different ohmic diffusivities and neutral–ion collision times . . . 78
2.14 Normalized local effective sound speed and normalized effective local vertical half-thickness as functions of the normalized external pressure . . . 88
2.15 Normalized growth time of gravitationally unstable mode as a function of the normalized wavelength for models with a fixed normalized Ohmic diffusivity and neutral-ion collision time, for different normalized mass-to-flux-ratio . . . 91
2.16 Normalized amplitudes of perturbed eigenfunctions as a function of spacial lengthscale . . . 93
2.17 Normalized maximum amplitude of perturbed velocity field and perturbed magnetic field as a function of normalized mass-to-flux-ratio . . . 97

3.1 Growth timescale (in the units of dynamical or free-fall time) and the preferred fragmentation mass (in the units of preferred thermal fragmentation mass) of the most unstable mode as a function of the normalized mass-to-flux ratio for the model with ambipolar diffusion . . . 107
3.2 Estimated lifetime as a function of number density . . . 109
3.3 Number of enclosed cores as a function of Jeans number of clumps . . . 111
3.4 Magnetic field vs. number density . . . 114
3.5 Normalized shortest growth time and preferred length scale of gravitationally unstable mode as a function of normalized mass-to-flux ratio for the model only with ambipolar diffusion . . . 121

4.1 2D representations of mass accretion rate as a function of space and time for the isothermal density profile. . . . 137

4.2 2D representations of mass accretion rate as a function of space and time for the modified density profile with different outer radius (a) $R_{\rm out} = 3.2r_c$, (b) $R_{\rm out} = 4r_c$, (c) $R_{\rm out} = 5r_c$. 138
4.3 1D representation of the temporal evolution of mass accretion rate for models with $R_{\rm out} = 3.2r_c$ (red line), $R_{\rm out} = 4r_c$ (green line), $R_{\rm out} = 5r_c$ (blue line) calculated at a fixed radial distance $r = 2r_c$. 139
4.4 Radial profiles of density and mass accretion rate; Column density and specific angular momentum as a function of radial offset 140
4.5 Schematic illustration of a cut through a spherical cloud of radius R 141
4.6 Flowchart of our formalism for the episodic accretion model. 144
4.7 Temporal evolution of the mass accretion rate for MODEL1 147
4.8 Temporal evolution of the mass accretion rate for MODEL2 148
4.9 Temporal evolution of the mass accretion rate for MODEL3 149
4.10 Histograms of luminosities from our episodic model and observations 153
4.11 Column density $\Sigma(x)/\Sigma_c$ (green), the specific angular momentum $j(x)$ (blue) as a function of radial offset x/r_c at $t = 0$ (analytic solution). 161

5.1 Schematic picture of star-disk system 169
5.2 Layered structure of a protoplanetary accretion disk 175
5.3 Long-term evolution of mass accretion rate, total luminosity, and mass distribution 180
5.4 Gas density distribution within the protostellar disk immediately before and after a burst 181
5.5 Zoomed-in a single luminosity burst and compare with observed FUOri 183
5.6 Time evolution of several characteristics of a burst as it developes and decays . 184
5.7 Spatial distribution of gas temperature, ionization fraction, and $\alpha_{\rm eff}-$parameter before and after the burst 186
5.8 Time evolution of several characteristics of a series of bursts 187
5.9 Herbig-Haro 30 (HH 30), a prototypical young stellar object surrounded by a disk and jet 188
5.10 ALMA SiO and continuum observations of the rotating outflow from the Class 0 protostar HH 212 189
5.11 Radial profile of surface density and temperature as the developes and decays . 190

List of Tables

2.1 Feasible Range of Q in Different Regimes. 79

3.1 Fitting data for calculating the lifetime of prestellar cores 122
3.2 Fitting data for calculating the number of enclosed cores 122

4.1 Model parameters: temperature T, the central number density n_c, the central flat region of the core r_c, outer radius of the core $R_{\rm out}$, mass of core $M_{\rm core}$, and final stellar mass M_* at the end of the desired evolution. 136

5.1 Parameters of the simulation model 179

Chapter 1

Introduction

1.1 Preliminaries and Overview

Stars are the fundamental building blocks of our observable universe. Therefore, the study of star formation is at the center of galactic and planetary astrophysics. The overall evolutionary cycle of the galaxies and structure formation within these galaxies is driven by star formation, which in turn, determines the luminosity of galaxies. In addition to that, star formation is also inextricably tied up with the formation and early evolution of planetary systems. Stellar outflows/winds may also directly impact on the evolution of galaxies, the interstellar medium (ISM), and the intergalactic medium (IGM). The interstellar medium (ISM) is composed of all forms of matter and radiation in space between stars in a galaxy, which includes gas (in atomic, molecular and ionized form) and dust, as well as magnetic fields and cosmic rays. Whereas the intergalactic medium (IGM) permeating between galaxies, is comprised of the hot ionized X-ray emitting gas. In the simplest terms, stars form when the densest regions of the ISM (which are the so-called molecular clouds) get fragmented into locally collapsing objects. The fragmentation of molecular clouds is a complex phenomenon driven by the interplay of several forces e.g., gravity, magnetic fields, thermal pressure, and turbulence. Stars are formed when the force primarily due to gravity exceeds all other opposing forces. In this context, the key question is how and at what circumstances gravity wins over the other forces? The key astrophysical problem of star formation has been addressed in many literatures from various perspectives (Mouschovias & Spitzer, 1976; Larson, 1981; Shu et al., 1987). Despite significant progress over the past decades, complete theoretical and observational understanding of

star formation remains elusive.

In this thesis, we investigate the physical processes which are responsible for the star formation in molecular clouds. We provide a comprehensive study of the fragmentation of large-scale molecular clouds into cores, which eventually collapse under their self-gravity to form stars and the protostellar (or protoplanetary or circumstellar) disks. The formation of a protostellar disk is a natural outcome because of the conservation (or near conservation) of angular momentum during the star formation process. We use theoretical semi-analytic models, magnetohydrodynamic (MHD) simulations, and observational data to bridge some of the existing gaps in our current understanding of the role of the gravitational instability (GI), nonideal MHD, and episodic accretion in the formation of a star-disk system. We find indirect signatures of the magnetic fields on the observable structures, for example, the density scaling of magnetic field strength, fragmentation mass and lengthscales, and timescales of the collapsing prestellar (starless) cores. Finally, we explore the role of episodic accretion on the mass growth of pre-main sequence star (protostar) and their observed luminosity. We also study the role of the magnetorotational instability (MRI) in the formation and long-term global evolution of a protostellar disk including the onset of giant-planet formation.

1.2 Zooming in on star-forming regions

1.2.1 From molecular clouds to the birth of star-forming cores

Molecular clouds (the densest phase of the ISM) are the cradles of star formation. Molecular clouds consist primarily of molecular hydrogen (H_2), having significant self-gravity with mean densities $10^2 - 10^4\,\mathrm{cm}^{-3}$ and temperature $T \simeq 10 - 50\,\mathrm{K}$. The chemistry and physical conditions of the interior of a molecular cloud are quite different from those of the surrounding low-density interstellar medium (for example, warm and cold neutral medium). A large fraction of matter in the ISM resides in the Giant Molecular Clouds (GMCs), which are the largest scales of molecular clouds, having masses up to a few million $M_\odot$ ($1\,M_\odot$ = 1 solar mass = 1.99×10^{33} g). GMCs are opaque clumps consisting of cold gas and dust. However, dust constitutes a very tiny fraction of the total mass of the ISM, with an approximate dust-to-gas mass ratio of 0.01 (Goldsmith et al., 1997). Star formation begins when the denser colder parts of molecular cloud start to collapse under its own gravity. If gravity alone was

responsible in the process of accumulating all the matter (gas and dust) present in our Galaxy ($\sim$ few billion $M_\odot$) and converting these into stars, then the expected galactic star formation rate ($\sim M_{\rm gas}/t_{\rm ff}$) would be $\sim 200\,M_\odot\,{\rm yr}^{-1}$, given that the free-fall time (also known as dynamical time), $t_{\rm ff} \propto 1/\sqrt{G\rho}$ (Jeans, 1929) associated with such an unrestrained gravitational collapse of a region with a typical number density of $10^4\,{\rm cm}^{-3}$ would be $\sim 0.2\,{\rm Myr}$. However, the observed star formation rate (SFR) in our Galaxy is only $\sim 1-3\,M_\odot\,{\rm yr}^{-1}$ (McKee & Williams, 1997; Robitaille & Whitney, 2010; Chomiuk & Povich, 2011). Why is there such discrepancy between the observed and theoretically predicted SFR? It signifies that only a few percent of total gas actually form stars (Myers et al., 1986; Evans et al., 2009; Lada et al., 2010). So, what are the additional forces that can counter the pull of gravity? The observed spectral linewidths as measured in ISM and GMCs (Zuckerman & Palmer, 1974) captures the supersonic motions (due to turbulence) that provides additional support (beyond thermal pressure) against gravity. Another possible explanation is the magnetic field, which provides a non-thermal support against gravity. Thus, the magnetic field can inhibit the gravitational collapse and rapid star formation except in the densest regions of the cloud (known as "core") undergoes a runaway collapse due to dissipation of magnetic fields (see discussions in in Section 1.3.2.1).

Over the decades, theory (Mestel & Spitzer, 1956; Mestel, 1965) and observations (Planck Collaboration et al., 2015, 2016) suggest that the magnetic field plays a pivotal role in star formation. Observations (Planck Collaboration et al., 2015, 2016) indicate that magnetic fields are ubiquitous in the interstellar medium. This naturally raises the question: what generates the magnetic fields in the ISM? Some large scale dynamo process (the process through which a rotating electrically conducting fluid can maintain a magnetic field and can be described by the induction equation of Maxwell's theory) is necessary to generate the large scale magnetic field B of astrophysical plasma. However, whatever the mechanism, a small drift in velocity between electrons (v_e) and positively charged ions (v_i) has to be maintained. This small differential velocity drift gives rise to conduction current density $J = n_e e|v_e - v_i|$. We can use Ampere's law $\boldsymbol{J} = c\boldsymbol{\nabla} \times \boldsymbol{B}/(4\pi)$ along with definition of electric current density and replace gradient with $1/L$ to get the relation $B = |v_e - v_i|4\pi e n_e L/c$, where n_e, L, e, and c are the electron number density, length scale of the cloud, electron charge, and speed of light, respectively. For a typical molecular cloud of size 10 pc ($\sim 10^{19}$ cm, since $1\,{\rm pc} = 3.09 \times 10^{18}\,{\rm cm}$), and average

electron number density n_e of $\sim 10^{-2}\,\mathrm{cm}^{-3}$, a tiny velocity drift of $\sim 10^{-3}\,\mathrm{cm\,s}^{-1}$ is sufficient to produce the typically observed magnetic field strength of $\approx 3\mu$G. Due to the high electrical conductivity of the ISM (as it contains plasma i.e., positively/negatively charged fluid), the magnetic field is effectively frozen in (coupled to) the matter and can prevent gravitational collapse. The clouds have nested structures ranging from larger filaments and clumps to dense cores and disks, which are often created by the process of hierarchical fragmentation as seen in the recent observational and simulation studies (see Dobbs et al., 2014; Heyer & Dame, 2015; Pokhrel et al., 2018). Depending on the spatial environments, as the cloud (typical size of $\gtrsim 10\,\mathrm{pc}$) collapses, they fragment into clumps of typical size of $\sim$1 pc (Ridge et al., 2006; Sadavoy et al., 2014). The clumps are usually defined as the largest scale of fragmentation of a molecular cloud. Clumps may or may not be gravitationally bound, however star formation requires to start with a gravitationally bound clump. Inside the clumps, there are elongated gaseous filament ($\sim$ 0.1pc) like structures (Arzoumanian et al., 2011), where $0.05-0.1$ pc wide dense cores (di Francesco et al., 2007) are observed that are the sites of star-formation. Deep down in the cores, there are further dense concentrations of envelopes ($\sim 3000\,\mathrm{AU}$), within which there are protostellar disks ($\sim 10-500\,\mathrm{AU}$) surrounding a central young protostar (of size few $R_\odot$). A protostar is defined as an object that is undergoing its main mass accumulation phase. Residual mass accretion through the surrounding accretion disk continues into the so-called pre-main-sequence phase. To understand the whole star-formation process starting from the cloud scale down to protostar scale, theoretical study on the hierarchical structure formation in a self-consistent manner is required to be carried out along with the observations.

The ISM is mathematically modeled with the theory of magnetohydrodynamics (MHD). MHD is 'fluid-approximation' theory, which means that the ISM is treated as a continuum. For a cloud of typical size $L \sim 10\,\mathrm{pc}$ (or $\sim$0.1 pc for cores), elastic scattering cross section $\sigma \sim 10^{-15}\,\mathrm{cm}^{-2}$, and typical density $n \sim 10^4\,\mathrm{cm}^{-3}$ (or $\sim 10^6\,\mathrm{cm}^{-3}$ in cores), the collisional mean free path $l = (n\sigma)^{-1}$ is $\sim 10^{11}$ cm (or 10^9 cm in cores), which is much smaller than the length scale of the system (cloud size L). Therefore, the diffuse ISM clouds can effectively be treated as fluids (as $l \ll L$). Moreover, because of the presence of the magnetic field, the charged particles gyrates about the field lines with a gyro-frequency $w_L = eB/mc$ (also known as Larmor frequency). So, in molecular clouds with average thermal speed $v_{\mathrm{th}} \sim 10^{-1}\,\mathrm{km/s}$,

the Larmor radius $a_L = v_{\rm th}/w_L$ (or radius of gyration) is even smaller and can act as an effective mean free path. For example, Larmor frequency for an electron $w_L \sim 1$ Hz, and Larmor radius is $\sim 10^5$ cm $\sim 10^{-13}$ pc ($\ll L$) that validates the fluid theory. In the MHD theory of the ISM, the astrophysical community impose charge neutrality of the fluid by doing a basic approximation that the evolutionary time is much longer than that of plasma oscillations. High frequency plasma behaviour are not considered to be followed as it leads to charge separation. In addition, slow-time variations of MHD theory also allows us to modify the equation of Maxwell's theory of electrodynamics (see equations in Chapter 2) by dropping the displacement current term that corresponds to high frequency phenomena. For astrophysically realistic circumstances, the fluid is treated as neutral assuming that collisions occur frequently enough to mechanically couple the three constituents of the gas i.e., electrons, ions, and neutrals. Later, in Chapter 2, 3 we study the nonideal MHD effect in the gravitational collapse and disk evolution. Nonideal MHD effects result in the dissipation and diffusion of magnetic flux, which arises from the relative drift between neutrals and charged species (either ions or both electrons and ions) as described later in Chapter 1.3.2.1. To better interpret and understand the observational results, nonideal MHD effects (arise due to the imperfect coupling between charged species and neutrals) have been considered to be imperative in the star formation process.

1.2.2 Tracers of the Molecular cloud

The observations of molecular/spectral line emission are an excellent probe to study the physical properties and kinematics of molecular clouds as well as the ongoing chemistry within. Observations show that the less dense-regions of molecular clouds having number densities $n_{\rm H_2} \sim 100\,{\rm cm}^{-3}$ exhibit supersonic linewidths, whereas dense prestellar (starless) cores have densities $n_{\rm H_2} \sim 10^6 - 10^7$ cm^{-3} and the gas appears to have subsonic velocities (Goodman et al., 1998). Molecular hydrogen can be probed at mid/near IR (vibration-rotation) or UV (electronic) wavelengths. Note that the absence of dipole moment of the H_2 molecule gives rise to weak emission, which is caused by the weak quadrupole transitions. Thermal excitations of H_2 molecules requires temperature $\gtrsim 100$ K (see Juvela et al., 2012, for a recent survey). However, the mean temperature of molecular clouds ($T \sim 10$ K) is very low for any electronic, vibrational, and rotational excitations of H_2 molecules. CO, the second most abundant species having an

abundance of 10^{-4} relative to the fraction of molecular hydrogen, is often used as main tracer (a proxy for H_2) of molecular gas. For CO, the ground state rotational transition $J = 1 \rightarrow 0$ corresponds to a wavelength 2.6 mm ($\sim$ 115 GHz), whilst the 1 – 0 vibrational transition is associated with a wavelength of 4.7 μm. CO has a small but finite dipole moment. The energy associated with the allowed rotational transition can be calculated as $E = \hbar^2 J(J+1)/(2\mu r^2) \equiv k_B T_{ex}$, where $\hbar$ is the reduced Planck's constant ($\hbar = h/(2\pi)$ where h is Planck's constant), J is the quantum number for total rotational angular momentum, μ is the reduced mass of the diatomic molecule, T_{ex} is defined as the excitation temperature, and r is the mean separation of the molecule. The molecules can also be observed in isotopologues: ^{13}CO, ^{12}C^{16}O, ^{12}C^{18}O, and ^{13}C^{16}O, which have different optical depths[1]. ^{13}CO emission lines are very useful to measure the column density of gas along the line of sight as such an emission line is optically thin i.e., ^{13}CO emission line comes out from all the layers because of its very low abundance.

To map the column density in molecular clouds, one of the widely used methods is the dust extinction mapping in near-infrared (Lada et al., 1994, 1999). The extinction is empirically proportional to the column density[2] of the cloud. The typical value of dust-to-gas mass ratio is 1 : 100 (Goldsmith et al., 1997). Clumps generally have a higher ionization fraction, on the order of 10^{-4} (Ruffle et al., 1998) and exhibit a visual extinction corresponding to a column density of $\sim 3 \times 10^{21}$ cm^{-2}. Whereas, cores have a lower ionization fraction, on the order of 10^{-7} and exhibit a visual extinction corresponding to a column density of $\sim 8 \times 10^{21}$ cm^{-2} as these regions are self-shielded from incoming UV radiation. Dust (of typical size of $\sim$ 0.1 micron and primarily made up of silicates and graphites) also plays an extremely pivotal role to determine the column density and the mass of the embedded dense cores along the line of slight. Dust absorbs photons emitted by young stars embedded in the cloud and re-radiates these photons at longer wavelengths. Dust thermal radiation peaks at a submillimeter wavelength $\lambda \sim 100 - 300\,\mu$m and radiates as a modified black body. However, the dust continuum emission (in millimeter- submillimeter wavelengths) provides no kinematic information. The CO traces the large-scale density and velocity dispersion of molecular gas. Dust is a major coolant of molecular clouds, along with the line emission from CO, C^+, and other molecules and atoms.

[1] Optical depth is a measure of how much absorption of the line occurs as it passes through the cloud.

[2] It is a measure of the integrated amount of matter per unit area in the object of interest along a particular line-of-sight.

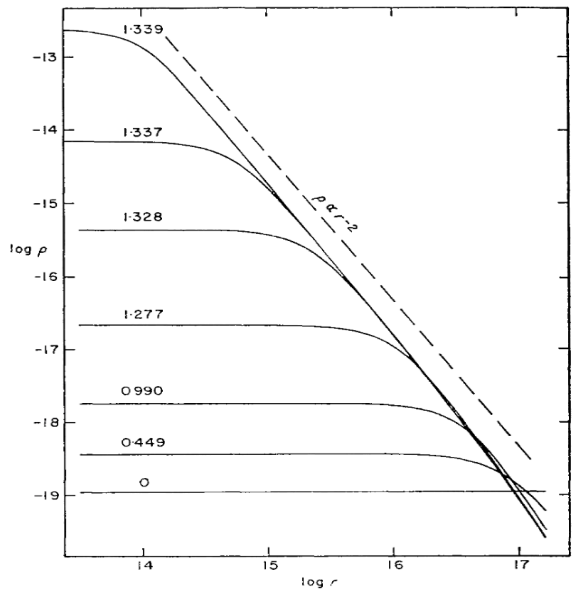

Figure 1.1: The variation of the density distribution in the collapsing cloud with radial distance at different times (cgs units). The curves are labelled with the times in units of 10^{13} sec $\approx$ 0.3 Myr since the beginning of the collapse. Note that the density distribution closely approaches the form $\rho \propto r^{-2}$ (Larson, 1969).

Nevertheless, CO is a good tracer for number densities near and below $\sim 10^3$ cm^{-3}. For tracking down the dense star-forming cores ($n \gtrsim 10^4$ cm^{-3}), nitrogen bearing species, such as NH_3 and N_2H^+, are much preferred as these molecules are excited at such high densities and low temperatures ($T \leq 20$ K).

1.3 Microphysics of star formation

Molecular clouds are highly non-linear systems with many ongoing physical processes e.g., self-gravity, magnetic fields, nonideal magnetohydrodynamic effects (i.e., dissipation mechanisms of magnetic fields), thermal pressure, turbulence, interstellar radiation field, etc. In this section, we briefly discuss the current understanding of how stars form.

1.3.1 Gravitational collapse to star-forming cores

Star formation starts when some of the clumps (over-dense regions of GMCs) reach a critical mass e.g., Jeans mass $M_{\rm J} \equiv c_s^3/\sqrt{G^3\rho}$ (Jeans, 1929), such that sound wave crossing time becomes greater than the free-fall time $t_{\rm ff} \equiv 1/\sqrt{G\rho}$, thus allowing it to collapse under their own gravity, where c_s, G, and ρ denote the sound speed, gravitational constant, and density of the background medium, respectively. The cause of collapse could be as simple as random

fluctuations of density within the cloud, or due to an outside influence such as collisions with other clouds, a supernova, etc. The disturbance in the background medium compresses the gas and dust to the point where it has enough gravity to collect more material onto itself. Jeans theory states that this critical mass corresponds to the shortest wavelength for gravitational fragmentation, which is known as the Jeans length $\lambda_J \equiv c_s/(\sqrt{G\rho})$. In simple words, any region of lengthscale greater than Jeans length λ_J (or equivalently, mass greater than Jeans mass M_J), is more likely to collapse under its self-gravity unless there are some other stabilizing forces present in molecular clouds (as discussed in the following sections 1.3.2 and 1.3.3). According to Jeans theory, the clouds are initialized with a uniform density and temperature, infinite spatial extent (e.g., no defined boundaries), which is not the case in a real scenario. An alternative to an isothermal uniform system is that of a thin sheet. The thin disk approximation yields a vertical half-thickness (as measured above and below the midplane of the thin sheet) at which thermal pressure can halt further one-dimensional compression. In this thesis, we explore the thin-disk approximation in Chapter 2 and 3.

In the current framework of star formation, it is realized that the isothermal cores undergoing gravitational collapse develop a density profile $\rho \propto r^{-2}$ (Larson, 1969; Bodenheimer & Sweigart, 1968, see also Figure 1.1). The modern standard picture of isolated star formation is introduced by Shu (1977); Shu et al. (1987). Typically collapse of a prestellar core is self-similar with an initial singular isothermal sphere (SIS) with a density $\rho = c_s^2/(2\pi G r^2)$. The innermost densest part collapses faster due to free-fall, while the outer region follows $\rho \propto r^{-2}$. If a self-gravitating isothermal gas cloud evolves subsonically before undergoing collapse which denotes it is not very far from the hydrostatic equilibrium, the outer region of such a cloud can tend to retain similar density profiles ($\rho \propto r^{-2}$) as that of an equilibrium state. As the density of the inner region increases, the opacity increases as well. Finally, when the temperature of the central region rises enough so that the internal energy is sufficient to halt the collapse. This is the formation of the first hydrostatic core (or first protostellar core of $n{\sim}10^{10}\,\mathrm{cm}^{-3}$, $M{\sim}10^{-2}\,M_\odot$, $R \leq 10^{14}\,\mathrm{cm} \sim 10^4\,R_\odot$), which is mostly composed of hydrogen molecules. After the first core forms, the outer mass shells continue to fall in at a velocity corresponding to free-fall i.e., $|v| \equiv (2GM/r)^{1/2}$. Just after the hydrostatic core forms, an expansion wave moves outward at the speed of sound speed and the gas behind it undergoes free-fall onto the collapsed

core. Later on, Terebey et al. (1984) extended the self-similar SIS model, adding rotation, while Galli & Shu (1993a,b) studied the case with magnetic fields but for a non-rotating core. The central hydrostatic core steadily builds up its mass from the surrounding infalling envelope and has a steady-state accretion rate $\dot{M} = 4\pi\rho r^2|v| \simeq 0.975 c_s^3/G$ (Shu, 1977). The density profile within the expansion wave acquires $\rho \propto r^{-3/2}$. When the temperature of the hydrostatic core reaches $\gtrsim 2000\,\mathrm{K}$, it triggers the dissociation of H_2 molecules. So, the hydrostatic core loses internal energy and pressure due to the dissociation of H_2 and the self-gravity takes over once again. This is called second collapse, which is the birth of a protostar. Observations indicate that the angular momentum, or equivalently, the rotational energy, of cores is indeed small and is often characterized by the ratio of the rotational energy to the gravitational binding energy, often defined as $\beta_{\rm rot} \equiv \Omega_{\rm rot}^2 R^3/(3GM)$ (typical median value is $\beta_{\rm rot} = 0.02$ for a uniformly rotating, constant density sphere as found by Goodman et al., 1993), where $\Omega_{\rm rot}$ is the rotational speed of the core, R and M are the radius and mass of the core, respectively. During the second collapse, most of the gas in the first core is distributed around the newly born protostar with angular momentum that is sufficient to allow the centrifugal force to balance gravity. Therefore, most of gas in the first core quickly transforms into a rotationally supported disk. Later, in Section 1.4, we discuss the formation and evolution of the star-disk system in detail.

1.3.2 Magnetic fields

The role of the magnetic field in regulating efficiency of star formation in molecular clouds has been greatly explored over the decades. Magnetic pressure and tension forces can provide support against the self-gravity of the cloud. The ratio of mass to magnetic flux (M/Φ) determines the relative importance of magnetic and gravitational field strength in the evolution of molecular clouds and their star-forming cores. Various authors (Mestel & Spitzer, 1956; Strittmatter, 1966; Mouschovias & Spitzer, 1976; Nakano & Nakamura, 1978) have shown that there exists a critical mass-to-flux ratio $(M/\Phi)_{\rm crit}$ $(= (2\pi G^{1/2})^{-1}$. For clouds with $(M/\Phi) < (M/\Phi)_{\rm crit}$ (i.e., normalized mass-to-magnetic flux ratio $\mu = (M/\Phi)/(M/\Phi)_{\rm crit} < 1$) are called subcritical clouds. The subcritical clouds are magnetically dominated and cannot collapse as long as flux-freezing prevails. However, clouds with $(M/\Phi) > (M/\Phi)_{\rm crit}$ (or $\mu > 1$) are supercritical clouds and are gravitationally unstable and prone to collapse even under flux-freezing. The

subcritical clouds are thought to be flattened with the long axis perpendicular to the direction of the background magnetic field and are stable against fragmentation as the magnetic pressure is sufficiently strong to halt the gravitational collapse.

Most of the interstellar medium is composed of neutral atoms/molecules. However, the magnetic force is felt only by the charged species (e.g., ions, electrons, charged dust grains) that are gyrating around the magnetic field lines. The typical observed ionization fraction (primarily cosmic-ray ionization) in molecular clouds can be parameterized as $10^{-7}\,(n_n/10^4\,\mathrm{cm}^{-3})^{-1/2}$, where n_n is the neutral number density ($n_n \simeq n$, where n is total number density including all charged and neutral species). In the deep interiors of GMCs and/or in the protostellar disks, the ionization fraction is fairly low, typically of the order of $\sim 10^{-10}$ to 10^{-12} i.e., the abundance of charged species is extremely low. So, why the magnetic field is even relevant at all in an overwhelmingly neutral gas? A charged species is able to induce a dipole moment on the neutral via interaction potential $V(r) = -Z\alpha_n e^2/(2r^4)$, where α_n is the polarizability of the neutral, e is the electron charge, Z is the atomic number, and r is the distance between the charged and neutral species (Draine, 2011). Thus the charged species increases the effective collisional cross-section (calculated in the Langevin approximation) and by imparting a dipole moment on the neutral. So, collisions between neutrals and charged species is what makes the neutrals feel the Lorentz force. In the astrophysical community, the ideal MHD approximation (or flux-freezing) corresponds to such a state when the magnetic field lines are completely frozen into the matter, i.e., the neutrals are fully coupled to the charged species. For the astrophysical gas in ISM to be in the ideal MHD limit, it has to be sufficiently ionized and it behaves as a perfect conductor (with infinite conductivity). In the infinite conductivity limit, the self-inductance keeps the magnetic flux within any comoving contour fixed, so we can think the particles as moving with the field lines. In the ideal-MHD limit, the neutrals collide often enough with the charged particles such that they are also perfectly tied (comoving) with the field lines. If the collision rate of neutrals with ions is not so high, then the nonideal MHD effect of the ambipolar diffusion will occur (see Section 1.3.2.1).

Despite substantial progress both theoretically and observationally, the debate still persists as to how magnetic support (Mouschovias, 1991) can limit the star formation efficiency, or how magnetic flux can be redistributed (via nonideal MHD effects) such that the star formation can

take place. The best way to converge to a unique answer to this long-standing controversy is to directly measure the magnetic fields inside molecular clouds, which is not easy (as discussed in Section 1.3.2.2). So, the dynamical importance of the magnetic field in evolution of the clouds can be debated. Hence, the astronomers need to observe the indirect tracers of magnetic fields and compare with theoretical predictions.

1.3.2.1 Nonideal magnetohydrodynamic effects

Nonideal MHD effects result from the imperfect coupling between charged species and neutrals[3] when the gas is very weakly ionized. The ISM plasma consists of electrons, ions, and charged dust grains. However, in this thesis we keep aside the nonideal MHD effects of the dust grains. Interestingly, in molecular clouds, inter-species collisions are strong enough that the friction forces are primarily due to elastic collisions with the collision timescales as follows:[4],

$$\tau_{en} = \tau_{ne}\frac{\rho_e}{\rho_n} = 1.21\,\frac{(m_e + m_n)}{\rho_n\langle\sigma w\rangle_{en}}\,, \tag{1.1}$$

and

$$\tau_{in} = \tau_{ni}\frac{\rho_i}{\rho_n} = 1.23\,\frac{(m_i + m_n)}{\rho_n\langle\sigma w\rangle_{in}}\,, \tag{1.2}$$

where $\langle\sigma w\rangle_{sn}$ is the average collision rate between charged species 's' e.g., electrons of mass m_e and ions of mass m_i (singly ionized Na and HCO of mass 23 and 25 amu respectively, where 1 amu = 1.6726×10^{-24} g) with neutrals (H_2 molecules) of mass m_n. The reduced mass $\mu = m_s m_n/(m_s + m_n)$. Here, ρ_i, ρ_e, and ρ_n denote density of ions, electrons, and neutrals, respectively. The pre-factors of order unity in Equations (1.1) and (1.2) account for the presence of the He molecule which has a lower polarizability that prolongs the slowing-down time relative to the value what it would have if only $s - H_2$ collisions are considered. Also, it is worth noting that, the density of the charged species (electrons and ions) $\rho_i + \rho_e \simeq \rho_i$ is many orders of magnitude smaller than the neutral density ρ_n, so its contribution to self-gravity can be neglected. Assuming the force balance between the Lorentz force and collisions with neutrals, conductivity becomes a tensor (having non-zero off diagonal components) (Norman & Heyvaerts, 1985;

[3]Here, i and e represent charged species: ion and electron, respectively; n represent neutral species.

[4]Note that the timescale of ion-neutral collision is typically many orders of magnitude smaller than that of neutral-ion collision τ_{ni}. Similarly, the electron-neutral collision timescale is also smaller than that of neutral-electron collision by many orders of magnitude.

Wardle & Ng, 1999; Wardle, 2007; Dapp et al., 2012) in the nonideal MHD limit. Thereby, it gives rise to three nonideal MHD effects, namely, Ohmic dissipation (OD), Hall effect, and ambipolar diffusion (AD). In principle, all three nonideal MHD terms can be mathematically derived from the generalized form of Faraday's law (see details in Pandey & Wardle, 2008) which states the evolution of magnetic field as follows:

$$\frac{\partial \boldsymbol{B}}{\partial t} = \boldsymbol{\nabla} \times \left[(\boldsymbol{v} \times \boldsymbol{B}) - \eta_{\rm OD}(\boldsymbol{\nabla} \times \boldsymbol{B}) - \eta_{\rm H} \left[(\boldsymbol{\nabla} \times \boldsymbol{B}) \times \frac{\boldsymbol{B}}{B} \right] + \eta_{\rm AD} \left[(\boldsymbol{\nabla} \times \boldsymbol{B}) \times \frac{\boldsymbol{B}}{B} \right] \times \frac{\boldsymbol{B}}{B} \right] . \quad (1.3)$$

Here, $\boldsymbol{v}$ is the bulk velocity such that $\boldsymbol{v} = (\rho_i \boldsymbol{v}_i + \rho_n \boldsymbol{v}_n)/\rho$, where $\rho = \rho_i + \rho_e + \rho_n \simeq \rho_n$ is the bulk density; v_i, v_e, v_n denote the ion, electron, and neutral velocity, respectively, and B is the magnetic field strength. The first term on RHS of Equation (1.3) represents the advective term. If all the other terms are zero then Equation (1.3) expresses magnetic flux conservation within any moving fluid element. The second, third, and fourth terms represent the three nonideal MHD terms: Ohmic dissipation (OD), Hall effect (H), and ambipolar diffusion (AD), respectively. The current density can be defined as $\boldsymbol{J} = c\boldsymbol{\nabla} \times \boldsymbol{B}/(4\pi)$, where c is the speed of light. The magnetic diffusivities for Ohmic dissipation, Hall effect, and ambipolar diffusion are as follows:

$$\eta_{\rm OD} = \frac{c^2}{4\pi\sigma_c} \ , \eta_{\rm H} = \frac{cB}{4\pi e n_e} \ , \eta_{\rm AD} = v_{\rm A}^2 \tau_{ni} = \frac{B^2 \tau_{ni}}{4\pi\rho_n} , \quad (1.4)$$

respectively, where n_e, e, and $v_{\rm A} = B/\sqrt{4\pi\rho}$ are the electron number density, electron charge, and Alfvén wave speed and all the parameters are described earlier. Here, the Ohmic conductivity can be calculated as $\sigma_c = \sum_{s=e,i} \sigma_s$, where $\sigma_s = n_s q_s^2 \tau_{sn}/m_s$. Here, n_s is the number density of each charged species ($n_e \approx n_i$ due to charge neutrality), q_s is the charge of each species, m_s is the mass of each species, and τ_{sn} is the collision time of each charged species with neutrals (see later in Section 2.2.1 and 2.6.2).

To grasp the physics behind the nonideal MHD effects, we need to intuitively understand the microscopic velocity drifts between species. The tiny electron-ion velocity drift $|v_e - v_i|$ that maintains the magnetic field, is typically of the order of $10^{-6}\,{\rm km\,s^{-1}}$ that is much smaller than the characteristic speed in the molecular cloud, for example the sound speed c_s is typically of the order of $10^{-1}\,{\rm km\,s^{-1}}$. Therefore, the plasma consisting of ions and electrons can be treated as single fluid. The electron-neutral collisions are the primary drivers to the Ohmic resistivity

which knocks the electrons and the electrostatically bound ions off from their gyration around the twisted field lines and causes dissipation of current. In the case of Ohmic dissipation, there is no species left which is frozen in the field unlike the other two cases where there is always at least one species that is still partially frozen in the field lines (for example, electrons for Hall effect; ions[5] and electrons for AD). In the case of ambipolar diffusion, ions can efficiently interact with neutrals despite the low ionization fraction because their electromagnetic cross-section is much bigger than the actual geometric cross-section as discussed in the earlier section. The neutrals exert a collisional force to ions and exchange momentum with them (while momentum exchange to the electrons is negligible because of electron's low inertia). So, there exists a drift velocity between ions and neutrals, $|v_i - v_n|$ (given that $v_i \simeq v_e$ is assumed and OD is negligible on the scales of interest), that reaches a terminal state when the collisional force felt by ions balances the magnetic forces on ions. The neutrals slip past the ions which are gyrating around the field line, and fall towards center of gravity. This is known as ambipolar diffusion. Whereas, the magnetic field moves (at the speed of ions) in by a lesser amount. It is called diffusion because the magnetic field is diffusing outward relative to the neutrals. Lastly, the Hall effect (Kunz & Mouschovias, 2009) is caused by the drift between the positively and negatively charged species (including dust). Here, for the completeness, we briefly discuss the Hall effect. However, this thesis only includes the study of Ohmic dissipation and ambipolar diffusion. In the context of a rotating collapsing core, the Hall current $j_{\rm H} = n_e e|v_i - v_e|$ induces a toroidal magnetic field depending on whether the mean field is parallel or anti-parallel to the rotation axis of the collapsing core. The Hall effect is not really diffusion in the usual dissipative sense. The Hall effect only rotates the magnetic-field fluctuations (arising due to oppositely charged species caused by their disparate inertia) about the mean field and does not damp the magnetic energy.

The relative significance between the Lorentz force and the neutral drag is characterized by the Hall parameter, which is the ratio between the gyrofrequency of the charged species and its momentum exchange rate with neutrals, having the following form:

$$\beta_s = \frac{|Z_s| eB}{m_s c \gamma_s \rho_n} \,, \tag{1.5}$$

[5] Although ions are less likely to be frozen in the field than the electrons due to their larger inertia.

where $s = i, e$ for ions, electrons, $|Z_s|$ is the atomic number of the charged species, m_s is the mass, e the is electron charge, B is the magnetic field strength, c is the speed of light, ρ_n is neutral number density. Here, γ_s is rate coefficient of momentum transfer either between ion and neutral or electron and neutral as follows:

$$\gamma_s = \frac{\langle \sigma w \rangle_{sn}}{(m_n + m_s)} , \tag{1.6}$$

where $\langle \sigma w \rangle_{ns}$ is the collision rate[6]. Note that

$$\gamma_i = 1/(\rho_i \tau_{ni}) = 1/(\rho_n \tau_{in}) , \tag{1.7}$$

$$\gamma_e = 1/(\rho_n \tau_{en}) = 1/(\rho_e \tau_{ne}) . \tag{1.8}$$

Additionally, it follows that

$$\frac{\eta_{\rm H}}{\eta_{\rm OD}} = \beta_e , \qquad \frac{\eta_{\rm AD}}{\eta_{\rm H}} = \beta_i . \tag{1.9}$$

The definitions of Ohmic and ambipolar diffusivities in terms of γ_s follows:

$$\eta_{\rm OD} = \frac{c^2 m_e \gamma_e \rho_n}{4\pi e^2 n_e} \quad , \quad \eta_{\rm AD} = \frac{B^2}{4\pi \gamma_i \rho_i \rho_n} , \tag{1.10}$$

which can be derived from Equation 1.4 using Equation 1.1, 1.2, 1.8, and 1.7. The physical significance of the Hall parameter β_s is that charged species 's' is strongly coupled with neutrals if $\beta_s \ll 1$, and on the other hand, is strongly tied to magnetic fields when $\beta_s \gg 1$. As electrons are much more mobile than the ions because of inertia, implying $\beta_e \gg \beta_i$. Therefore, Ohmic resistivity is the dominant nonideal MHD effect when $\beta_i \ll \beta_e \ll 1$, where both electrons and ions are coupled to the neutrals (complete break-down of flux-freezing). The Hall effect dominates when $\beta_i \ll 1 \ll \beta_e$, where electrons are coupled to (frozen in) the magnetic field and ions are coupled to the neutrals. Whereas, AD dominates when $1 \ll \beta_i \ll \beta_e$, where both electrons and ions are coupled to the magnetic field. Since the Hall parameter $\beta_s \propto B/\rho$, we see that Ohmic resistivity dominates in high density regions with weak field, ambipolar diffusion

[6]Note that the collision rate takes into account of the polarization effects. For example, $\langle \sigma w \rangle_{sn} = 2\pi Z_s e (\alpha_N/\mu)^{1/2}$, where α_N is the polarizability coefficient (Osterbrock, 1961; Draine, 2011)

dominates in low density regions with relatively stronger field. Lastly, the Hall regime lies in between. Keeping in mind, if the coupling becomes perfect such that it possesses infinite conductivity ($\sigma_c \to \infty$) or negligible drift velocities ($\tau_{ni}, \tau_{en} \to 0$), the nonideal MHD regime returns to the ideal-MHD case.

In the context of star formation, as the gravitational collapse proceeds and the thermal pressure supported first hydrostatic core (of density around $\rho \gtrsim 10^{-13}\,\mathrm{g\,cm^{-3}}$ or $n \gtrsim 10^{10}\,\mathrm{cm^{-3}}$) forms. The magnetic resistivity appreciably increases within the first core due to its high density In the first core, without magnetic diffusion (as seen in the ideal MHD simulations) the typical value of plasma-$\beta = 8\pi\rho c_s^2/B^2$ is ~ 10 (strong magnetic field which is inherited from the prestellar core). Whereas for the nonideal MHD simulations, β becomes of the order of $\sim 10^4$. Later on, when the density further increases (ionization fraction decreases) during the second collapse (formation of Class 0 protostar), most of the gas in the first core is distributed around the protostar and forms a rotationally supported disk. The ambipolar diffusion is dominant nonideal MHD term for $10^{10} < n < 10^{12}\,\mathrm{cm^{-3}}$. The Ohmic dissipation becomes dominant at $n \sim 10^{12} - 10^{15}\,\mathrm{cm^{-3}}$, especially within protostellar/protoplanetary (PD/PPD) disks. However, the ambipolar diffusion is still not negligible in this regime. The Hall effect is important in between these two regimes of a protoplanetary disk, particularly $\sim 1 - 10\,\mathrm{au}$ from the central protostar (Kunz & Mouschovias, 2009, 2010). Nonideal MHD effects are unavoidable for the evolution of a PPD, as the gas is weakly ionized ($\sim 10^{-6} - 10^{-9}$) in the densest regions of molecular cloud cores (Caselli et al., 1998, 2002). We cannot explore the deep nonlinear physics in the inner and outer disk without inclusion of the nonideal MHD effects (dissipation and diffusion of magnetic flux) on the magnetic field. For the case of a PPD, all three nonideal MHD effects: ambipolar diffusion, the Hall effect, and Ohmic dissipation are important. Because the PPD possesses a wide variety of ionization sources, temperatures, and densities, which lead to a wide diversification of ionization fractions, collision rates, and plasma–β. We still have very limited knowledge about the early protostellar stages of circumstellar disks. Observations of these very early stages of disk formation are challenging because such collapsing cores are surrounded by a dusty envelope. Future three dimensional nonideal MHD global simulations are required to be carried out to explore its effect on the star formation and disk evolution. The relative strengths of the nonideal MHD effects determine the fate of protostellar

disk formation, as well as the long-term evolution of the disk. The Chapter 2 and 3 of this thesis present the consequences of Ohmic dissipation and ambipolar diffusion in core formation and disk evolution.

1.3.2.2 Measurements of magnetic fields

The magnetic fields in the dense ISM can be measured in two primary ways. The first one is using the Zeeman splitting of spectral lines of paramagnetic species (having an unpaired electron). The line shift induced by Zeeman effect $\Delta\nu_z \propto \mu_B B/h$, where μ_B is the Bohr magneton, can be observed either in absorption or emission spectra (Crutcher & Kemball, 2019) of HI (densities $\sim 1 - 100\,\mathrm{cm}^{-3}$), OH (densities $\sim 10^2 - 10^4\,\mathrm{cm}^{-3}$), and CN (densities $\sim 10^5 - 10^6\,\mathrm{cm}^{-3}$). In principle, the Zeeman effect can measure both the line-of-sight ($B_{\rm LOS}$ or $B_\parallel$) and plane-of-sky ($B_{\rm POS}$ or $B_\perp$) components[7]. The splitting in the $B_{\rm LOS}$ component is seen in Stokes parameter V (circular polarizations of π lines) associating with amplitude $\propto (\Delta\nu_z/\Delta\nu)B_{\rm LOS}$, where $\Delta\nu$ is the full line width at half intensity (or the characteristic width of the spectral line). Whereas the splitting in $B_{\rm POS}$ component is seen in Stokes parameters Q and U (linear polarizations) with an amplitude $\propto (\Delta\nu_z/\Delta\nu)^2 B_{\rm POS}$ (as described in the reviews by Crutcher & Kemball, 2019); (see also the discussions on Stokes parameters in Tinbergen, 1996). However, the splitting $\Delta\nu_z$ due to Zeeman effect is observationally unmeasurable since $\Delta\nu_z \ll \Delta\nu$. So, only the LOS field strength and direction can be observationally recovered from the line splitting, which is more like a first-order effect. However, for an emission line with a large velocity width either due to thermal or dynamic broadening, the Zeeman effect widens the line width (or in other words the splitting is veiled under the broadened linewidth), and the strength of the magnetic field $B_\parallel$ can be inferred from the polarization measurements of Stokes parameter V (Crutcher et al., 1993; Robishaw, 2008; Han, 2017; Crutcher & Kemball, 2019). This is like a second-order effect. Since the Zeeman effect is detected using the Stokes V spectrum, a precise definition of this parameter is necessary to be carried out in order to correctly assign the direction of the probed line-of-sight magnetic field (see Robishaw, 2008, and references therein). The polarized maser emission arises from the dense regions with high brightness temperature (due to population inversion) and densities e.g., OH emission from the ultra compact HII regions, H_2O from outflow shocks and protostellar disks, and CH_3OH

[7]LOS and POS mean line-of-sight and plane-of-sky, respectively.

found in the shocks from high-mass star forming regions (Class I and II) (Caswell et al., 2011; Cyganowski et al., 2009; Vlemmings et al., 2006). Another way is to measure the plane of sky component of the magnetic field $B_\perp$ using the Chandrasekhar-Fermi (CF) method (Davis, 1951; Chandrasekhar & Fermi, 1953), by comparing the fluctuations in the direction of $B_\perp$ with those in the velocity field $\delta B/B_0 \propto \delta v/v_\mathrm{A}$, which leads to $B_\mathrm{POS} = f\sqrt{4\pi\rho}\,\delta v_\mathrm{N,T}/\delta\theta$ (see the reviews by Heiles & Crutcher, 2005), where B_0 is the background magnetic field and v_A is Alfvén speed, $\delta v_\mathrm{N,T}$ is the non-thermal linewidth in gas species taken to trace the regions of similar density from the dust polarization, $\delta\theta$ is the dispersion in polarization angle, f is typically 0.5 used as a correction factor (Ostriker et al., 2001) due to integration effects. Interstellar dust polarization is another key mechanism to trace the magnetic field. According to the magnetic alignment mechanism (Davis & Greenstein, 1951; Purcell, 1979), elongated (non-spherical) dust grains spin around the axes parallel to the background magnetic field (i.e., perpendicular to its major axis). The alignment of dust grains (see Figure 1.2) leads to dust thermal emission (in sub-millimeter wavelengths) and absorption (in near infrared wavelengths) with electric field (net polarization) perpendicular and parallel to the local magnetic field, respectively. Although the polarization maps reveal a large scale, ordered magnetic field direction in the plane of sky, they provide no useful information on the field strength. The CF method is a means of estimating B_POS from the polarization maps of the dust emission or extinction. Emission line (non-maser lines) polarization in the ISM can also arise from the Goldreich-Kylafis (GK) effect (Goldreich & Kylafis, 1981), which causes the molecular line emission to be linearly polarized either parallel or perpendicular to the plane-of-sky component of magnetic field. However, the ambiguity on polarization direction complicates the interpretation. In the diffuse ISM, magnetic field strengths are also obtained by Faraday rotation with results consistent with Zeeman observations. Faraday rotation is the rotation of linear polarization due to interaction with the electrons along the line-of-sight is widely used to study galactic magnetic fields using linearly polarized emission from pulsars and extragalactic compact sources (e.g., Brown et al., 2007; Van Eck et al., 2011) or the magnetic field of strongly ionized regions within the Galaxy (Harvey-Smith et al., 2011). However, the use of this method for the case of star-forming clouds is quite rare as the rotation measure of the Faraday effect is extremely small due to low abundance of free electrons in the dense molecular cloud core.

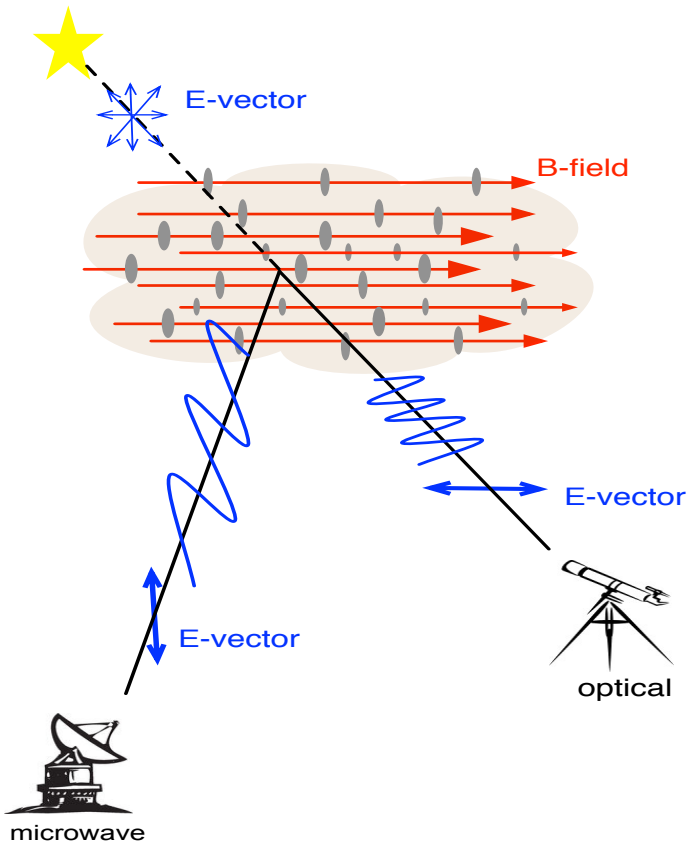

Figure 1.2: Polarization of dust emission in the microwaves and of starlight at optical wavelengths resulting from the alignment of the dust grains with the long (major) axis perpendicular the direction of the magnetic field (Tassis et al., 2018).

1.3.2.3 Density scaling of magnetic fields

For gravitationally contracting interstellar clouds and star-forming cores, the relation between magnetic field strength (B) and gas density (ρ) of the cloud can provide key insights to the dynamical importance of magnetic fields in the evolution of molecular clouds and star formation. The $B-\rho$ relation allows us to study formation mechanisms of the cores (Crutcher et al., 2010; Das et al., 2021; Myers & Basu, 2021; Auddy et al., 2022) whose observed form could be interpreted in terms of effective flux-freezing at higher densities and significant neutral-ion drift (breakdown of flux-freezing) at low densities. Due to a significant electrical conductivity of the interstellar gas (Mestel & Spitzer, 1956) the magnetic flux is frozen in the matter and can prevent fragmentation and spherical collapse. There is still persisting debate on the testable predictions of the $B-\rho$ relation in the flux-freezing limit (i.e. conservation of magnetic flux)

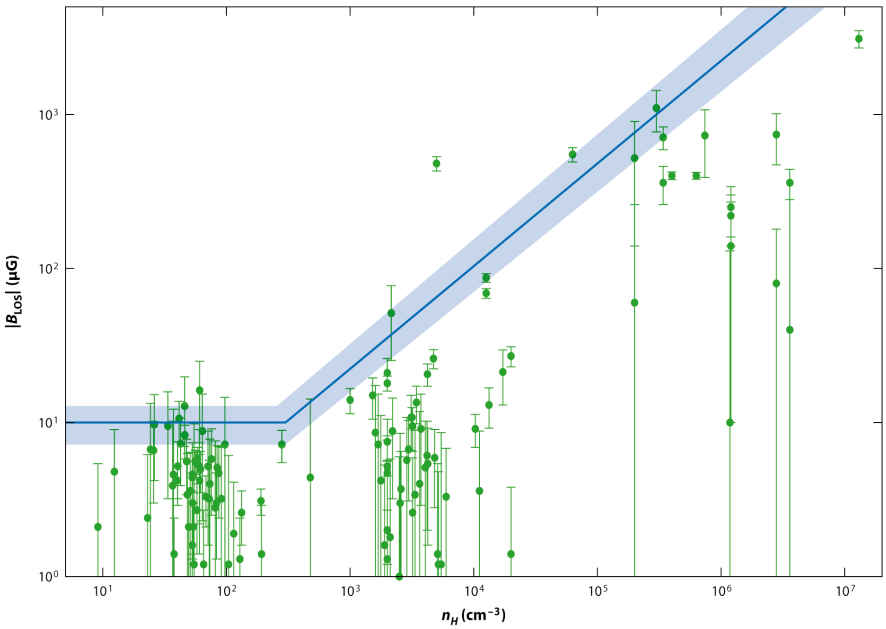

Figure 1.3: Set of diffuse cloud and molecular cloud Zeeman measurements of the magnitude of the line-of-sight (LOS) component of magnetic field strength B_z plotted against number density of gas $n(\mathrm{H}) = n(\mathrm{H_1})$ or $2n(\mathrm{H_2})$ for $\mathrm{H_1}$ and molecular clouds, respectively. The solid blue line shows the most probable maximum values for $B_{\mathrm{tot}}(n_{\mathrm{H}})$ determined from the plotted values of B_{LOS} of Crutcher et al. (2010). The light blue shading above and below the solid blue line represents the ranges given by acceptable alternative model parameters to indicate the uncertainty in the model (see more details in Crutcher, 2012).

for a self-gravitating magnetic cloud. According to theory argued by Mestel (1965), if a weakly magnetized self-gravitating cloud collapsing spherically and isotropically, the scaling between the field strength and the density follows $B \propto \rho^{2/3}$. The above is true for a quasi-spherical collapse where both the mass M and the magnetic flux Φ are conserved i.e., $M \propto \rho R^3$ = constant, $\Phi \propto BR^2$ = constant, implying $M \propto \Phi$, given that R defines the cloud size. Tritsis et al. (2015) also emphasized that $B \propto \rho^{2/3}$ can only be realized under isotropic contraction and is unique for a spherical core. However, Mouschovias (1976a,b) presented a more self-consistent theory of non-homologous quasistatic isothermal contraction of a self-gravitating isothermal interstellar cloud bounded within a hot and tenuous medium and tied with a dynamically important magnetic field. According to this theory, the plasma$-\beta = 8\pi\rho c_s^2/B^2$, i.e., the ratio of thermal pressure to magnetic pressure, remains constant during contraction. Eventually, the cloud flattens due to self-gravity along the field lines and settles itself into a vertical hydrostatic equilibrium to form a thin-sheet like structure. The extent of the flattened sheet of surface density Σ depends on the strength of the magnetic field, gravitational force, and external pressure. Hence, for such a non-homologous collapse, mass M ($\propto \Sigma R^2$) and the magnetic flux Φ ($\propto BR^2$) are conserved, which implies $B \propto \Sigma$. Also, note that for such an isothermal self-gravitating sheet in vertical hydrostatic equilibrium, $\rho c_s^2 \propto \pi G\Sigma^2/2$ implies $\Sigma \propto \rho^{1/2}$. It is straightforward to show that this yields $B \propto \rho^{1/2}$ for such a non-spherical isothermal contraction tied with relatively strong fields. Later on, Crutcher et al. (2010) presented a revised $B - \rho$ relation for a larger sample of both low-density diffuse clouds and high-density molecular clouds with the magnetic field values ranging from a few μG to mG obtained from the Zeeman surveys of HI (atomic hydrogen), OH, and CN spectral lines. Figure 1.3 shows the Zeeman measurements of the line-of-sight component of B and the corresponding uncertainty of 1σ magnitude plotted against the number density, combining the atomic hydrogen density n(HI) and molecular hydrogen density n(H_2) (Crutcher et al., 2010). The curve in Figure 1.3 consists of a flat part i.e., $B \propto \rho^0$ at low-density ($1\,\mathrm{cm^{-3}} \lesssim n_\mathrm{H} \lesssim 300\,\mathrm{cm^{-3}}$), and a power-law scaling $B \propto \rho^{2/3}$ at high density ($10\,\mathrm{cm^{-3}} \lesssim n_\mathrm{H} \lesssim 10^7\,\mathrm{cm^{-3}}$). Crutcher et al. (2010) interprets that the approximated flat region represents the initial accumulation of the gas along field lines, which results in a gradual increase in density while keeping the magnetic field unchanged until it reaches a certain density (break-point) where the two different profiles of power-law join. Eventually,

when the gas accumulates enough mass that is sufficient to undergo a self-gravitating collapse, it leads to a more isotropic spherical contraction with the density scaling of the flux-frozen field as $B \propto \rho^{2/3}$. The magnetic field is therefore considered to be too weak to affect the spherical morphology of the collapse.

Li et al. (2015) carried out three-dimensional supersonic turbulent (see Section 1.3.3) ideal MHD simulations with weak and strong magnetic fields to justify the $B \propto \rho^{\kappa}$ scaling. Li et al. (2015) found that their simulated values of κ are 0.70 ± 0.06 and 0.57 ± 0.05 for the strong and weak field models, respectively. Nonideal MHD effects also have a influence on the $B - \rho$ relation of star-forming cores. Numerical simulations (Fiedler & Mouschovias, 1993; Ciolek & Mouschovias, 1994; Tritsis et al., 2022) of ambipolar diffusion driven gravitational collapse predict $\kappa < 1/2$. Such simulations impose a dynamically important magnetic field that leads to flattening along the magnetic field direction, and subsequent evolution primarily perpendicular to the field. In the astrophysical community, the more expected conclusion is that for the weak magnetic field the density dependence is somewhat closer to $\kappa = 2/3$ as predicted by the weak field spherical collapse theory (Mestel, 1965, 1966) and for the case of moderately strong large-scale magnetic fields it is $B \propto \rho^{1/2}$. In Chapter 3, we explore the magnetic field and density relation for the prestellar cores that essentially links the theoretical prediction and observational findings and shows the imprints of the effect of nonideal MHD on core formation.

1.3.3 Effects of turbulence

In the field of star formation, there has been an ongoing debate over which mechanism between magnetic field and turbulence is more important for driving the fragmentation of molecular clouds and formation of stars. In simple words, turbulence means disruption in the laminar or streamlined flow of a fluid. Quantitatively, turbulence is characterized by the Reynolds number, R which is essentially the ratio of the inertial to viscous forces, and can be written as $R \equiv LV/\nu$, where L and V are the characteristic length and velocity scales of the flow and ν is its kinematic viscosity (Frisch, 1995). If the Reynolds number increases either due to a sufficiently small viscosity and or a sufficiently large combination of characteristic length and velocity scale, the flow can become turbulent or chaotic. As a result, it forms turbulent eddies of various lengthscales within the fluid. Within turbulence, the energy is generally injected on

the largest scales (big whirls) and then the energy flow cascades down to the smallest scales (small whirls) via nonlinear interaction between different size eddies. The smallest eddies are affected by molecular diffusion and viscous dissipation (which converts the kinetic energy of turbulence to thermal energy) when the inertial length scale of an eddy becomes comparable to the viscous dissipation scale. There have been many theories on the turbulence-regulated star formation (Elmegreen & Scalo, 2004; Hartmann, 2001; Palla & Stahler, 2002; Federrath & Klessen, 2012; Padoan & Nordlund, 2002), which consider that turbulence is a key physical parameter in the star formation process. Such large-scale turbulent motions are ubiquitous in stellar outflows and jets, and within the interstellar medium (Elmegreen & Scalo, 2004), and molecular clouds and can be either supersonic or subsonic. Generally, the Mach number is used to quantitatively define a supersonic (Mach number $\gtrsim$ 1) and subsonic (Mach number $\lesssim$ 1) flow. Supersonic turbulence generally decays within a dynamical time scale, whereas the subsonic one sustains over a few dynamical timescales. The fundamental question is whether turbulence induces or inhibits the star formation process. The answer is turbulence can act in both ways. If the turbulent motions within a supercritical cloud are able to provide sufficient balance (just like an internal pressure) against gravity, then the supercritical cloud will remain stable against collapse within the free-fall time. However, a supercritical cloud would collapse if the turbulence dissipates (typical dissipation time scale $\approx d/v_{\rm los}$, where $v_{\rm los}$ is line-of-sight velocity and d is diameter of the molecular cloud) within a single crossing time of eddy-like structures traversing the diameter of the molecular cloud (Mestel & Spitzer, 1956). The supersonic turbulent motions induce compressions that gives rise to high density fluctuations and radiative shocks that drain its energy. On the other hand, large scale turbulence with subsonic motions acts like an external pressure and provides global support by stabilizing the cloud against collapse.

Generally, large-scale flows in the ISM (Hartmann, 2001), supernovae (Klessen et al., 2005), and stellar feedback (Hayward & Hopkins, 2017) are considered to provide the driving energy for turbulence in the system. Nonetheless, one major drawback of such turbulence driven star formation models is the requirement of some continuous physical kinetic energy input which will drive the turbulence in a system. Realistically such source of constantly producing kinetic energy is not sustainable. If the cloud is filamentary (for the case of weak

magnetic field) as a result of compression primarily due to shocks, it is thought that turbulence might play an important role in star formation. However, if the cloud is wide enough, then magnetic field might be more relevant than turbulence in the process of star formation. In addition, numerical simulations show that turbulence can have an effect on the magnetic field itself. Specifically, the models of Fatuzzo & Adams (2002); Zweibel (2002) show that turbulence acts to decrease the ambipolar diffusion timescale within a molecular cloud irrespective of subcritical or supercritical cloud.

1.4 Collapse to a star-disk system

Protostellar disks are formed almost immediately after the collapse of a molecular cloud core as a natural byproduct of the angular momentum conservation (as described in the reviews by Bodenheimer, 1991; Larson, 2010). A PPD is generally a flattened rotating accretion disk around almost all low-mass young stars shortly after their birth. The disk extends for tens to hundreds of au and is composed of gas and dust particles, and continues to feed its central star through accretion. The mass accretion rate $\dot{M}$ from disk to star can be inferred from the accretion luminosity measured by the UV excess that suppresses the intrinsic photospheric spectrum of a YSO. Moreover, the accretion luminosity originates due to the accretion shock formed at the stellar surface, which converts the gravitational energy into the heat and radiation (Calvet & Gullbring, 1998; Gullbring et al., 2000) as discussed later in Chapter 4. In practice, the accretion rate is commonly inferred from emission line profiles, in particular the Hα line, whose strength correlates with the accretion luminosity (Muzerolle et al., 1998, 2001). The inner disk is initially warm and cools later in the "classical T Tauri Star (CTTS)" stage by possible formation of small dust grains made up of silicates smaller than 0.1μm, along with graphite and polycyclic aromatic hydrocarbons (PAHs). In the disk, the dust grains agglomerate through collisions. The dust emission from the interferometric and (sub-)millimeter (e.g., ALMA, SMA, etc.) observations is the primary diagnostic of PPD structure, for example disk surface density, disk mass, disk size, and chemical compositions. Constraining the disk mass from observations is subject to the inaccurate estimation because of the possible presence of the optically thick dust (emission is self-absorbed) along the line-of-sight (Ko et al., 2020, and references therein). If the disk emission is not optically thin (transparent), it predicts the lower

limit of the disk mass, leading to an underestimate of the masses for most disks (Galván-Madrid et al., 2018; Zhu et al., 2019).

By surveying spectral energy distributions (SEDs) from *Spitzer* and *Herschel* observations in nearby star-forming regions, evolutionary phases of the pre-main sequence stars can be classified from Class 0 to Class III objects. Any of the objects belonging to any of these phases are collectively referred as to young stellar objects (YSOs). SEDs suggest that the near-IR and mid-IR excess emission from the YSOs is essentially an indication of a dusty disk surrounding a YSO. The fraction of such YSOs containing excess IR emission decreases with the age of the star-forming region (see reviews by Williams & Cieza, 2011). Class 0 is the initial phase (age $\sim 10^4$ yr), for which the SED peaks at $> 100\,\mu m$ (sub-mm region) with no IR excess (Andre et al., 1993). Most of the Class 0 objects are detected through their vigorous outflows, which indirectly reflects the presence of a protostellar disk, as the disk itself at this phase is too small ($\lesssim 50$ au) to be observed and also shrouded by a dusty envelope. During the Class I phase (age $\sim 10^5$ yrs), the SED is approximately flat or rising into the mid-IR and the protostar is still veiled by an optically thick residual envelope. Observations suggest that very young embedded clusters (age ≤ 1 Myr) show disk fractions of the order 70% to 80% (Gutermuth et al., 2008). During the Class II phase (age $\leq 10^6$ yrs, $M_{\rm disk} \sim 0.01\,M_\odot$), optical emission starts to come out and this is the birth line of the pre-main sequence stars (also known as classical T Tauri phase). The central T-Tauri star is still surrounded by an optically thick PPD with SED decreasing into the mid-IR. Stellar black body emission is not yet completely unveiled. Thereafter, the disk fraction reduces to about 40% to 50% (Lada et al., 2006) for clusters with ages ranging from $2-3$ Myr. Finally, Class III is the phase (age $\gtrsim 10^6$ yrs, $M_{\rm disk} \sim 0.001\,M_\odot$) of evolved T Tauri stars, or in other words weak-line T Tauri stars (WTTS), with the SED showing little or no excess IR fraction. This means that accretion is substantially halted. Class III objects might not have a detectable circumstellar disk as they might be lost due to accretion or dispersal as the star approaches the main sequence. The disk fraction eventually drops below 20% for about a 5 Myr old cluster, and by $\sim 8-10$ Myr, excess IR emission ($\sim 5\%$) become exceedingly rare (Sicilia-Aguilar et al., 2006). During this evolution timeline some material accretes onto the star, some is lost through outflows and photoevaporation, and some condenses into centimeter-kilometer sized planetesimals which leads to first steps toward the planet formation.

1.4.1 Origin of episodic bursts in the early stages of star-formation

In order to understand the evolution of a disk and protostar, it is important to understand the ongoing physical processes that lead to the protostar and disk growth. In our present view of low-mass star formation, a protostar in the early stages (in the so-called Class 0 and Class I phases) is surrounded by a protostellar disk that is deeply embedded in an infalling envelope from the collapse of a rotating prestellar cloud core. The bolometric luminosity found from the observations of Class 0 and Class I objects appears to be around one to two orders of magnitude smaller than that predicted by the infall rate during the embedded phase. This is known as the “luminosity problem". On top of that, low luminosities of Class 0 and Class I objects imply that these protostars have low mass accretion rates, and hence it is difficult to accumulate a typical final stellar mass of $\sim 1\,M_{\odot}$ within the short embedded timescale $\sim$ few 10^5 yr, provided by embedded source statistics. Kenyon et al. (1990) suggested that this disagreement between the accretion rates inferred from bolometric luminosities and the theoretical embedded phase could be reconciled if the young stars accumulate most of their material in a time that is short compared to the lifetime of the embedded phase. The general picture of evolution of pre-main sequence accretion suggests that much of the material added to the central star from the surrounding disk is done through a series of eruptive bursts (in an irregular periodic fashion) interrupted by the long periods of relative quiescence (i.e., time span between two successive accretion bursts), which is known as episodic accretion by the astrophysical community. Theoretical and numerical models indicate that the episodic bursts occur at all early stages of star formation as soon as the star-disk system forms. However, it becomes observable only when the protostellar envelope thins out (essentially from the T Tauri phase).

Recent evidence shows that flares of methanol masers that are the signposts of massive YSOs, are driven by accretion bursts (e.g., SOFIA observations by Stecklum et al., 2021). The energetic protostellar jets (of typical speed $\sim 100\,\mathrm{km\,s^{-1}}$) might be used to trace back the history of protostellar accretion. Shocked gas from the collimated high-velocity jets can survive for thousands of years and often propagate even up to a few pc from their driving source and are powered by disk accretion (Reipurth & Cernicharo, 1995; Reipurth & Aspin, 1997). Such jets were first observed as a sequence of knots, seen at optical wavelengths, and such objects are known as Herbig-Haro (HH) objects (e.g., Herbig, 1966, 1977). The origin of the

chain of knots as found in jets can be attributed to the episodic variation in the mass-accretion rate (Arce et al., 2007). Vorobyov et al. (2018) show the potential link between the knotty jet structure in CARMA 7, a young Class 0 protostar in the Serpens South cluster observed by Plunkett et al. (2015) using ALMA, and episodic accretion in young protostellar disks. Note that the molecular outflows of typical speed $\sim 10\,\mathrm{km}\,s^{-1}$, launching radius of $10-100$ au (e.g., Alves et al., 2017; Hirota et al., 2017) have a much broader opening angle than jets of typical speed $\sim 100\,\mathrm{km}\,s^{-1}$, launching radius of $0.5-7$ au (e.g., Chen et al., 2016; Lee et al., 2017) and are detected through sub-mm emission. This thesis is not focused on the molecular outflows and jets, rather on the episodic accretion. The prototypical sample of bursts are known as FUor eruptions (named after the first known example of this kind originated from the FU Orionis system, e.g., Herbig, 1966, 1977) and EXor (EX Lupi-type) eruptions (e.g., Herbig, 1989, 2008). In one picture of pre-main sequence accretion, FUors and EXors are part of a continuum of bursts. The physical mechanism of driving these two types of bursts can be different. FUors are thought to occur mainly in the embedded Class 0/I phase (i.e. protostars with disk and envelope). EXors would be associated with the disks of T Tauri stars (Class II YSOs). The FUor bursts are relatively longer and stronger compared to EXor bursts. FUors have an average duration of ~ 100 yrs and luminosity of $\sim 100-300\,\mathrm{L}_\odot$ during their outbursts. The prototype of this class, the star FU Ori; is slowly fading out since its 1936 outburst (Kenyon et al., 1990, 2000), and it is still in a relatively high state (with high brightening magnitude similar to its outburst time) at present. Whereas, EXors have a duration of only $\sim 1-2$ yrs and luminosity of $\sim$ few to $10\,\mathrm{L}_\odot$ during outbursts (Lorenzetti et al., 2006; Audard et al., 2010), and about $1-2\,\mathrm{L}_\odot$ (Herbig, 2008) in their quiescence (including about $0.3-0.5\,\mathrm{L}_\odot$ of stellar photospheric luminosity; Audard et al. (2014)).

During the continuous infall from the envelope, the surrounding cool disk is highly susceptible to gravitational instability (GI). The gravitational instability is a hydrodynamic instability that arises in a rotationally supported disk when self-gravity of the disk wins over the stabilization due to thermal pressure on small lengthscales and due to shear (differential rotation) on large lengthscales (as discussed in the review by Kratter & Lodato, 2016). The conditions for fragmentation of a low-mass self-gravitating disk can also be written as a function of local (to a first approximation) disk conditions. Quantitatively, the gravitational instability is denoted by

the Toomre-Q parameter (Toomre, 1964) which can be defined as $Q = c_s\kappa/(\pi G\Sigma_{\rm d})$, also often called as Toomre-Q instability. Here, c_s is the sound speed, G is the gravitational constant, $\Sigma_{\rm d}$ is surface density of disk, κ is the epicyclic frequency (i.e., frequency at which a radially displaced fluid element oscillates). In the absence of an external potential, for a Keplerian disk the epicyclic frequency can be written as $\kappa^2 \equiv (2/r)d/dr(r^2\Omega_{\rm d}) \sim {\Omega_{\rm d}}^2$, where $\Omega_{\rm d}$ is the angular speed of the disk (Armitage, 2011). The growth of perturbations due to gravitational instability occurs for $Q \lesssim 1$, though more general disturbances (Papaloizou & Savonije, 1991) can grow whenever Toomre-Q falls below $1 \lesssim Q \lesssim 2$ (e.g., as found from the simulations of Vorobyov & Basu, 2005a, 2006, 2007, and their series of papers). The Toomre-Q criteria is often simplified as $Q = f(H/R_{\rm d})(M_*/M_{\rm d})$ for the case of Keplerian protostellar disks ($\Omega_{\rm d} = \sqrt{GM_*/R_{\rm d}^3}$). In the above expression, M_* and $M_{\rm d}$ denote the star and disk mass, respectively, f is factor of order unity arising from the disk surface density profile, H and $R_{\rm d}$ are the vertical length scale and disk radius, respectively. The surface density can also be rewritten as $\sim M_{\rm d}/R_{\rm d}^2$. For a non-self-gravitating disc in hydrostatic balance, one can use $c_s/\Omega_{\rm d} = H$ (while for a self-gravitating disk $H = c_s^2/(\pi G\Sigma_{\rm d})$). Noting that, an equivalent but approximate local condition for gravitational instability is $M_{\rm d}/M_* \gtrsim H/R_{\rm d}$. In principle, the factor $H/R_{\rm d}$ is ~ 0.1 for PPDs. Gravitational instability is thus likely to occur early, when protoplanetary disks are still massive.

Mass accretion from the envelope onto the protostellar disk takes place in a fairly uniform (albeit generally declining with time) manner. Whereas accretion from the protostellar disk onto the central protostar occurs primarily in short but vigorous episodes during which $\sim 0.01-0.1\,M_\odot$ can be accreted over a time span of $\sim$ 100 yrs. The following section addresses the mechanism of transport of matter from the disk to star. These episodes of vigorous accretion with mass accretion rate $\gtrsim 10^{-4}\,M_\odot{\rm yr}^{-1}$ manifest themselves as FU Orionis variables (FUor). Due to the mismatch between the infall and transport rate, the central protostar mass does not grow at the same rate as the disk mass. Hence, the disk becomes more massive than the central protostar, which leads to gravitational instability (GI) within the protostellar/protoplanetary disk (PD/PPD). Generally, the disk gets fragmented into large spiral arms and gravitationally bound clumps. Afterward, these clumps migrate inward through the spiral arms (e.g., Fig 4 of Vorobyov & Basu, 2006) and fall onto the center, which triggers the vigorous stochastic accretion bursts. Between two successive accretion bursts (which is quiescent phase), a typical

Class 0/Class I protostar is characterized by a low mass accretion rate of $\sim 10^{-7} M_{\odot} \mathrm{yr}^{-1}$. Most of the protostar mass (up to 30% – 40% of the final stellar mass) is accreted during the mass accretion bursts rather than in the quiescent phase between the bursts. The early burst phase terminates when the infalling envelope has lost most of its gas reservoir. The protostar then enters in a T-Tauri phase and its subsequent evolution is characterized by a low-level accretion. To study the effect of gravitational instability extensively in disk evolution, global numerical simulations are required (Laughlin & Bodenheimer, 1994; Vorobyov & Basu, 2005a,b, 2006, 2007, 2008, 2010, 2015). Later in Chapter 4, we present our self-developed semi-analytic model of episodic accretion from the disk to star. In Chapter 5, we discuss the characteristics of episodic accretion bursts as obtained from a global MHD simulation of the star-disk system.

1.4.2 Disk Physics: mechanism of transport

Observations of the classical T Tauri stars (Bouvier et al., 1993) suggest that the specific angular momentum (total angular momentum per unit mass) for such stars is approximately equal to $j \equiv 4\pi R_*^2/(5P) \sim 5.6 \times 10^{16}\ \mathrm{cm^2\,s^{-1}}\,(R_*/2\mathrm{R}_{\odot})^2 (P/10\ \mathrm{days})^{-1}$ using their rotation period ($P = 3 - 10$ days) and radius ($R_* \approx 2\mathrm{R}_{\odot}$), given that star rotates uniformly. On the other hand, Goodman et al. (1993); Jijina et al. (1999); Caselli et al. (2002) find that the specific angular momentum for cloud cores is $\sim 5 \times 10^{21} \mathrm{cm^2\,s^{-1}}\,(R/0.1\,\mathrm{pc})^2\,(\Omega/4\,\mathrm{km\,s^{-1}pc^{-1}})$ provided that core has a density of $\sim 10^4\,\mathrm{cm^{-3}}$, size of ~ 0.1 pc, and velocity gradient of $0.3 - 4\,\mathrm{km\,s^{-1}}$ as found from NH_3 observations. It indicates that the specific angular momentum should be reduced by 5 orders of magnitude when forming a star from the collapse of a molecular cloud core. If the angular momentum is conserved through the collapse, which means the gravity (GM/r^2) should balance the centrifugal acceleration (j^2/r^3) at the centrifugal radius $R_c \equiv j^2/(GM) \sim 0.06\,\mathrm{pc}\,(M/M_{\odot})^{-1}\,(j/5 \times 10^{21}\,\mathrm{cm^2\,s^{-1}})^2$. It points out that if the angular momentum is not sufficiently reduced, it prevents the formation of stellar sized objects (as $R_c \gg R_*$), leading to the overall "angular momentum problem" of star formation (Mestel, 1965; Spitzer, 1978; Tomisaka, 2000). Indeed, disks are observed or inferred around at least some Class 0 and Class I protostars, and mostly T-Tauri (Class II) stars, and even around brown dwarfs (objects with substellar masses). However, the observed mass ratios between the disk and central object are typically ~1 per cent (Andrews & Williams, 2005; Scholz et al., 2006).

This fact implies that there is an efficient mechanism which drives inward accretion of material and outward transport of angular momentum that sets in very early during the life of the disk and even while it is forming. For example, in the case of our solar system, 99.9% of the mass of the system is at the center and 99% of its total angular momentum is in the planetary orbits. The following sections aim to discuss the physical processes (magnetic and non-magnetic) of mass and angular momentum transport during the accretion from disk to star. Disk self-gravity and the magnetorotational instability (MRI) are the most important dynamical processes in protoplanetary disks that have been studied in this thesis.

1.4.2.1 Transport in self-gravitating disk

For a self-gravitating disk, the role of gravitational torques is significant in transporting mass inward and angular momentum outward during different evolutionary stages of a protostellar disk (Vorobyov & Basu, 2007). In the early phase, when the infall from the surrounding envelope is substantial, the disk becomes gravitationally unstable ($Q \lesssim 1$ or in other words the disk-to-star mass ratio exceeds few times 0.1) and gets fragmented into distinct spiral arms and embedded clumps. Gravitational torques associated with the spiral arms trigger the clump infall onto the protostar producing mass accretion bursts that are identified with the observed Fuor eruptions. In the late phase, when the gas reservoir of the envelope is diminished, the clear spiral structures weaken out. GI induced spiral structures are replaced by ongoing irregular non-axisymmetric density perturbations, which further decays with time. Global hydrodynamic simulations of the protostellar disk (Vorobyov & Basu, 2007) reveals that there is typically a residual non-zero gravitational torque from these density perturbations. Although at large radial distances, the gravitational torques are expected to be small due to low gas surface density and effective axial-symmetry in the envelope. In particular, the net gravitational torque in the inner disk tends to be negative during first few one-tenth million years ($\gtrsim 0.5$ Myr) of the evolution, while the outer disk has a net positive gravitational torque (see Vorobyov & Basu, 2007, for more discussions). In the later evolution ($\gtrsim 0.5$ Myr), the spiral distribution of gravitational torques shows an alternating behaviour in the azimuthal direction such that local gas patches with positive torque if followed by patches with negative torque. These patches with the positive and negative torques fluctuate with time. Even though the net global effect of positive and negative torques appears to exactly cancel out globally, there is in fact a residual

negative gravitational torque that arises from the density inhomogeneities (i.e.,their effects do not exactly cancel out) at least within the inner disk (Vorobyov & Basu, 2007).

Numerical simulations of Vorobyov & Basu (2007) suggest that any slight deviation from axial symmetry due to density fluctuations in a protostellar disk can give rise to gravitational torques. Observations show the existence of a pronounced non-axisymmetry in disks that are several Myr old, (e.g., around AB Aurigae, Fukagawa et al., 2004) and (HD 100546, Grady et al., 2001). Larson (1984) pointed out even a tiny density fluctuation of the order of a few percent in a self-gravitating disk can generate gravitational torques that can further drive the sufficient angular momentum transport comparable to what is often obtained via disk viscosity generated by turbulence. It is an alternative mechanism for transporting angular momentum through the disk using a simple $\alpha-$ viscosity parametrization as prescribed by Shakura & Sunyaev (1973). The disk kinematic viscosity (dynamic viscosity per unit volume density) is proportional to its temperature that can be written as $\nu = \alpha c_s^2/\Omega = \alpha c_s H$, where α is a dimensionless viscosity parameter, given that the turbulence is subsonic, Ω is the Keplerian orbital angular velocity, and the disk height H as an upper limit for the size of the eddies generated due to turbulence in disk gas (Vorobyov et al., 2020). The direct proportionality between viscosity and sound speed implies that an increase in disk temperature causes a higher rate of mass accretion due to an enhanced viscous mass transfer (and vice versa). Global hydrodynamic simulations of Vorobyov & Basu (2010) show that a higher rate of mass infall onto the disk rather than that onto the star (Toomre-Q instability) is a necessary but not a sufficient condition for disk susceptibility to fragmentation. In regions of a disk where radiative cooling and heating process occur, the local heating/cooling time also needs to be shorter than a few times the local dynamical time ($\sim \Omega^{-1}$) such that fragmentation can occur. Heating due to stellar and background irradiation is quantitatively treated in a way that is opposite to that of radiative cooling, i.e., radiation from the central star and natal molecular cloud hits the surface and diffuses down to the midplane where it transforms into heat. The cooling time can be parameterized as $t_{\rm cool} = \beta\,\Omega_k^{-1}$, where β is dimensionless parameter of order unity, typically depends on the conditions in the disk, e.g., disk thickness, chemical composition, dust content, etc as found from the local hydrodynamic simulations of disks (Gammie, 2001; Rice et al., 2003; Mejía et al., 2005). The above condition of disk fragmentation is often termed as $\beta-$ cooling

criterion. Short cooling times allow the disk to radiate away the energy provided by shocks or turbulent dissipation, such that neither pressure support nor shear suffices to preclude gravitational collapse. Within $\sim$ 50 AU, the cooling time becomes short enough such that it can induce fragmentation (see Kratter & Lodato, 2016, and references therein). While at distances of the order of tens of au, the cooling time is relatively longer than dynamical time. Hence, the disk might survive in a self-regulated state (in other words, gravitationally stable). Global models of a self-consistently formed disk by Vorobyov & Basu (2007) shows that it is also self-regulated in the late phase, so that it is near the Toomre stability limit, with $Q \approx 1.5 - 2.0$. Detailed studies of the disk fragmentation and gravitational torques motivated by recent discoveries are discussed extensively in the literature (e.g., Vorobyov & Basu, 2006, 2010; Kratter & Lodato, 2016).

1.4.2.2 Magnetic field as a source of transport

A protostellar accretion disk that is dynamically coupled to a weak magnetic field in the sense that thermal energy exceeds the magnetic energy density i.e., $B_z^2/(8\pi) \lesssim \rho c_s^2$, where B_z, c_s, and ρ represent the vertical magnetic field, sound speed, and disk density, respectively. Such a Keplerian disk (where angular speed Ω decreases as orbital radius of the disk increases) is subject to an instability of shear flows that can likely initiate MHD turbulence. This instability is often called the magnetorotational instability or MRI (Balbus & Hawley, 1991). Intuitively, the magnetorotational instability can be understood in the following way. Consider a vertical magnetic field of the disk that is slightly perturbed radially with a vertical wavelength such that the radial perturbation varies with height (see also Figure 18 of Armitage, 2015). Thereby, it now links the fluid elements in the disk at different radii, then the fluid parcel closer to the central star orbits faster than the fluid parcel further out, which induces a toroidal field component. For a fixed magnetic field strength, the disk becomes MRI unstable (Armitage, 2015) when the separation between two fluid elements exceeds the critical lengthscale of separation $\lambda_{\rm crit,MRI} = 2\pi v_{\rm A}/(\sqrt{3}\Omega)$, where $v_{\rm A} = B_z/\sqrt{(4\pi\rho)}$ is the Alfvén speed. The magnetic tension in the string like magnetic field line joining two fluid parcels imparts azimuthal forces to both the inner and outer fluid parcels such that the inner fluid parcel then moves further inward and the outer fluid parcel moves further outward. This destabilizes the disk. However, the fluid element going inward does not necessarily fall onto the central star. If we think of the global picture,

then the collective influence of all these different parcels moving back and forth triggers the turbulent eddies in the disk. Each individual eddy scale acts like an effective mean free path. Once there are sufficient number of turbulent eddies, these can exchange angular momentum between the fluid parcels, which makes the inner fluid element rotate more rapidly and outer fluid element rotate more slowly, just the way friction does. The resulting MHD turbulence (in the form of eddies) often generates Maxwell stress tensor that result in angular momentum transport (see reviews by Balbus & Hawley, 1998). That effective friction or turbulent viscosity is the possible reason that drives the some fluid parcels inward eventually by reducing their angular momentum. When these parcels are accreted rapidly onto the star, it gives rise to an MRI outburst.

Observations suggest that the thermal ionization in most parts of T-Tauri disks is too low to allow sufficient magnetic coupling for the MRI to operate. This problem might be mitigated by invoking non-thermal ionization by cosmic rays (Gammie, 1996), or X-rays from the central star (Glassgold et al., 1997). However, such a weakly magnetized disk is optically thick to cosmic rays at a critical surface density of $100\,\mathrm{g\,cm^{-2}}$. Therefore, the cosmic rays can only penetrate up to a smaller column density and ionize the photons only at those upper layers of the disk. Thus the outer layers of the disk can remain ionized and magnetically coupled nearly at all radii. However, the dense inner (near the midplane) region of low ionization fractions becomes a so-called "dead zone" (MRI-inactive) where there is no obvious mechanism for mass and angular momentum transport (Gammie, 1996). Generally in Class I disks, it seems that the bulk of the disk mass might comprise these dead zones. Within such dead zones, due to adiabatic compression, the temperature gradually increases. When the temperature becomes $\gtrsim 1300\,\mathrm{K}$, ionization of alkaline metals begins. Then the dead zone has increased magnetic coupling and gets converted into MRI-active region which gives rise to a vigorous MRI burst by further allowing the outward transport of angular momentum. To date no observation shows the direct evidence either for or against the existence of dead zones. Theoretical calculations, however, continue to suggest that it is more likely that the PPDs develop a dead zone at radii of ~ 1 AU (Salmeron & Wardle, 2008; Terquem, 2008; Bai & Goodman, 2009; Turner & Drake, 2009; Turner et al., 2010). Nevertheless, future global nonideal MHD simulations of disks are required to be carried out to investigate the disk formation and evolution at very early times.

The primary obstacle for the MRI under the ideal MHD assumption of flux-freezing is that the disk must remain sufficiently ionized. In the case of nonideal MHD, if the disk resistivity/diffusivity is too high, then the MRI will not operate as the field will diffuse out of a fluid parcel much faster than the actual MRI growth timescale. In most of the astrophysical accretion disks that are non self-gravitating, the MRI may be the main source of angular momentum transport. These include the non-self-gravitating disks for example, disks around white dwarfs, neutron stars, and black holes. For example, disks around black holes are likely to be thermally ionized, the ionization fraction of the gas is not a concern. However, at larger distances from a central star, from a few to tens of au, the disk becomes colder and denser and the penetration of ionizing photons drops. While dead zones in the PPDs pose a hindrance to mass accretion, they may enable another important process in protostellar disks i.e., planet formation. The Chapter 5 of this thesis discusses the consequences of our results on episodic accretion and disk evolution in this context.

1.5 Chapter review

In this thesis, we carry out a detailed study of the different physical processes that are possibly responsible for star formation in molecular clouds. In Chapter 2, we provide a comprehensive study on the fragmentation of the protostellar disk during the early embedded phase) in terms of lengthscale, timescale, and mass scale, in the presence of nonideal MHD effects. In Chapter 3, we show a similar study of fragmentation, but for the case of a molecular cloud and discuss the consequences of nonideal MHD on the observed features e.g., prestellar core lifetime, mass, etc. Thereafter, in Chapter 4, we study the effects of episodic accretion in the disk evolution and in the observed luminosities using a semi-analytic model of mass accretion. In Chapter 5, we conduct numerical magnetohydrodynamic global simulations of a disk to investigate the physical mechanism causing the episodic bursts and their detailed physical characteristics. We compare these characteristics with the observational signatures of bursts. Finally, we quantify their role of bursts in formation and long-term global evolution of protostellar disks and the onset of giant-planet formation.

Bibliography

Alves F. O., Girart J. M., Caselli P., Franco G. A. P., Zhao B., Vlemmings W. H. T., Evans M. G., Ricci L., 2017, A&A, 603, L3

Andre P., Ward-Thompson D., Barsony M., 1993, ApJ, 406, 122

Andrews S. M., Williams J. P., 2005, ApJ, 631, 1134

Arce H. G., Shepherd D., Gueth F., Lee C. F., Bachiller R., Rosen A., Beuther H., 2007, in Reipurth B., Jewitt D., Keil K., eds, Protostars and Planets V. p. 245 (arXiv:astro-ph/0603071)

Armitage P. J., 2011, ARA&A, 49, 195

Armitage P. J., 2015, arXiv e-prints, p. arXiv:1509.06382

Arzoumanian D., et al., 2011, A&A, 529, L6

Audard M., et al., 2010, A&A, 511, A63

Audard M., et al., 2014, in Beuther H., Klessen R. S., Dullemond C. P., Henning T., eds, Protostars and Planets VI. p. 387 (arXiv:1401.3368), doi:10.2458/azu_uapress_9780816531240-ch017

Auddy S., Basu S., Kudoh T., 2022, ApJ, 928, L2

Bai X.-N., Goodman J., 2009, ApJ, 701, 737

Balbus S. A., Hawley J. F., 1991, ApJ, 376, 214

Balbus S. A., Hawley J. F., 1998, Reviews of Modern Physics, 70, 1

Bodenheimer P., 1991, in Catalano S., Stauffer J. R., eds, NATO Advanced Study Institute (ASI) Series C Vol. 340, Angular Momentum Evolution of Young Stars. p. 1

Bodenheimer P., Sweigart A., 1968, ApJ, 152, 515

Bouvier J., Cabrit S., Fernandez M., Martin E. L., Matthews J. M., 1993, A&A, 272, 176

Brown J. C., Haverkorn M., Gaensler B. M., Taylor A. R., Bizunok N. S., McClure-Griffiths N. M., Dickey J. M., Green A. J., 2007, ApJ, 663, 258

Calvet N., Gullbring E., 1998, ApJ, 509, 802

Caselli P., Walmsley C. M., Terzieva R., Herbst E., 1998, ApJ, 499, 234

Caselli P., Benson P. J., Myers P. C., Tafalla M., 2002, ApJ, 572, 238

Caswell J. L., Kramer B. H., Reynolds J. E., 2011, MNRAS, 414, 1914

Chandrasekhar S., Fermi E., 1953, ApJ, 118, 116

Chen X., Arce H. G., Zhang Q., Launhardt R., Henning T., 2016, ApJ, 824, 72

Chomiuk L., Povich M. S., 2011, AJ, 142, 197

Ciolek G. E., Mouschovias T. C., 1994, ApJ, 425, 142

Crutcher R. M., 2012, ARA&A, 50, 29

Crutcher R. M., Kemball A. J., 2019, Frontiers in Astronomy and Space Sciences, 6, 66

Crutcher R. M., Troland T. H., Goodman A. A., Heiles C., Kazes I., Myers P. C., 1993, ApJ, 407, 175

Crutcher R. M., Wandelt B., Heiles C., Falgarone E., Troland T. H., 2010, ApJ, 725, 466

Cyganowski C. J., Brogan C. L., Hunter T. R., Churchwell E., 2009, ApJ, 702, 1615

Dapp W. B., Basu S., Kunz M. W., 2012, A&A, 541, A35

Das I., Basu S., André P., 2021, A&A, 649, L13

Davis L., 1951, Physical Review, 81, 890

Davis Leverett J., Greenstein J. L., 1951, ApJ, 114, 206

Dobbs C. L., et al., 2014, in Beuther H., Klessen R. S., Dullemond C. P., Henning T., eds, Protostars and Planets VI. p. 3 (arXiv:1312.3223), doi:10.2458/azu_uapress_9780816531240-ch001

Draine B. T., 2011, Physics of the Interstellar and Intergalactic Medium

Elmegreen B. G., Scalo J., 2004, ARA&A, 42, 211

Evans Neal J. I., et al., 2009, ApJS, 181, 321

Fatuzzo M., Adams F. C., 2002, ApJ, 570, 210

Federrath C., Klessen R. S., 2012, ApJ, 761, 156

Fiedler R. A., Mouschovias T. C., 1993, ApJ, 415, 680

Frisch U., 1995, Turbulence. The legacy of A.N. Kolmogorov

Fukagawa M., et al., 2004, ApJ, 605, L53

Galli D., Shu F. H., 1993a, ApJ, 417, 220

Galli D., Shu F. H., 1993b, ApJ, 417, 243

Galván-Madrid R., Liu H. B., Izquierdo A. F., Miotello A., Zhao B., Carrasco-González C., Lizano S., Rodríguez L. F., 2018, ApJ, 868, 39

Gammie C. F., 1996, ApJ, 457, 355

Gammie C. F., 2001, ApJ, 553, 174

Glassgold A. E., Najita J., Igea J., 1997, ApJ, 480, 344

Goldreich P., Kylafis N. D., 1981, ApJ, 243, L75

Goldsmith P. F., Bergin E. A., Lis D. C., 1997, ApJ, 491, 615

Goodman A. A., Benson P. J., Fuller G. A., Myers P. C., 1993, ApJ, 406, 528

Goodman A. A., Barranco J. A., Wilner D. J., Heyer M. H., 1998, ApJ, 504, 223

Grady C. A., et al., 2001, AJ, 122, 3396

Gullbring E., Calvet N., Muzerolle J., Hartmann L., 2000, ApJ, 544, 927

Gutermuth R. A., et al., 2008, ApJ, 674, 336

Han J. L., 2017, ARA&A, 55, 111

Hartmann L., 2001, AJ, 121, 1030

Harvey-Smith L., Madsen G. J., Gaensler B. M., 2011, ApJ, 736, 83

Hayward C. C., Hopkins P. F., 2017, MNRAS, 465, 1682
Heiles C., Crutcher R., 2005, in Wielebinski R., Beck R., eds, , Vol. 664, Cosmic Magnetic Fields. p. 137, doi:10.1007/11369875_7
Herbig G. H., 1966, Vistas in Astronomy, 8, 109
Herbig G. H., 1977, ApJ, 217, 693
Herbig G. H., 1989, in European Southern Observatory Conference and Workshop Proceedings. pp 233–246
Herbig G. H., 2008, AJ, 135, 637
Heyer M., Dame T. M., 2015, ARA&A, 53, 583
Hirota T., Machida M. N., Matsushita Y., Motogi K., Matsumoto N., Kim M. K., Burns R. A., Honma M., 2017, Nature Astronomy, 1, 0146
Jeans J. H., 1929, The universe around us
Jijina J., Myers P. C., Adams F. C., 1999, ApJS, 125, 161
Juvela M., et al., 2012, A&A, 541, A12
Kenyon S. J., Hartmann L. W., Strom K. M., Strom S. E., 1990, AJ, 99, 869
Kenyon S. J., Kolotilov E. A., Ibragimov M. A., Mattei J. A., 2000, ApJ, 531, 1028
Klessen R. S., Ballesteros-Paredes J., Vázquez-Semadeni E., Durán-Rojas C., 2005, ApJ, 620, 786
Ko C.-L., Liu H. B., Lai S.-P., Ching T.-C., Rao R., Girart J. M., 2020, ApJ, 889, 172
Kratter K., Lodato G., 2016, ARA&A, 54, 271
Kunz M. W., Mouschovias T. C., 2009, MNRAS, 399, L94
Kunz M. W., Mouschovias T. C., 2010, MNRAS, 408, 322
Lada C. J., Lada E. A., Clemens D. P., Bally J., 1994, ApJ, 429, 694
Lada C. J., Alves J., Lada E. A., 1999, ApJ, 512, 250
Lada C. J., et al., 2006, AJ, 131, 1574
Lada C. J., Lombardi M., Alves J. F., 2010, ApJ, 724, 687
Larson R. B., 1969, MNRAS, 145, 271
Larson R. B., 1981, MNRAS, 194, 809
Larson R. B., 1984, MNRAS, 206, 197
Larson R. B., 2010, Reports on Progress in Physics, 73, 014901
Laughlin G., Bodenheimer P., 1994, ApJ, 436, 335
Lee C.-F., Ho P. T. P., Li Z.-Y., Hirano N., Zhang Q., Shang H., 2017, Nature Astronomy, 1, 0152
Li P. S., McKee C. F., Klein R. I., 2015, MNRAS, 452, 2500
Lorenzetti D., et al., 2006, A&A, 453, 579
McKee C. F., Williams J. P., 1997, ApJ, 476, 144

Mejía A. C., Durisen R. H., Pickett M. K., Cai K., 2005, ApJ, 619, 1098

Mestel L., 1965, QJRAS, 6, 265

Mestel L., 1966, MNRAS, 133, 265

Mestel L., Spitzer L. J., 1956, MNRAS, 116, 503

Mouschovias T. C., 1976a, ApJ, 206, 753

Mouschovias T. C., 1976b, ApJ, 207, 141

Mouschovias T. C., 1991, ApJ, 373, 169

Mouschovias T. C., Spitzer L. J., 1976, ApJ, 210, 326

Muzerolle J., Hartmann L., Calvet N., 1998, AJ, 116, 455

Muzerolle J., Calvet N., Hartmann L., 2001, ApJ, 550, 944

Myers P. C., Basu S., 2021, arXiv e-prints, p. arXiv:2104.02597

Myers P. C., Dame T. M., Thaddeus P., Cohen R. S., Silverberg R. F., Dwek E., Hauser M. G., 1986, ApJ, 301, 398

Nakano T., Nakamura T., 1978, PASJ, 30, 671

Norman C., Heyvaerts J., 1985, A&A, 147, 247

Osterbrock D. E., 1961, ApJ, 134, 347

Ostriker E. C., Stone J. M., Gammie C. F., 2001, ApJ, 546, 980

Padoan P., Nordlund Å., 2002, ApJ, 576, 870

Palla F., Stahler S. W., 2002, ApJ, 581, 1194

Pandey B. P., Wardle M., 2008, MNRAS, 385, 2269

Papaloizou J. C., Savonije G. J., 1991, MNRAS, 248, 353

Planck Collaboration et al., 2015, A&A, 576, A106

Planck Collaboration et al., 2016, A&A, 586, A138

Plunkett A. L., Arce H. G., Mardones D., van Dokkum P., Dunham M. M., Fernández-López M., Gallardo J., Corder S. A., 2015, Nature, 527, 70

Pokhrel R., et al., 2018, ApJ, 853, 5

Purcell E. M., 1979, ApJ, 231, 404

Reipurth B., Aspin C., 1997, AJ, 114, 2700

Reipurth B., Cernicharo J., 1995, in Lizano S., Torrelles J. M., eds, Revista Mexicana de Astronomia y Astrofisica Conference Series Vol. 1, Revista Mexicana de Astronomia y Astrofisica Conference Series. p. 43

Rice W. K. M., Armitage P. J., Bate M. R., Bonnell I. A., 2003, MNRAS, 339, 1025

Ridge N. A., et al., 2006, AJ, 131, 2921

Robishaw T., 2008, PhD thesis, University of California, Berkeley

Robitaille T. P., Whitney B. A., 2010, ApJ, 710, L11

Ruffle D. P., Hartquist T. W., Rawlings J. M. C., Williams D. A., 1998, A&A, 334, 678

Sadavoy S. I., et al., 2014, ApJ, 787, L18
Salmeron R., Wardle M., 2008, MNRAS, 388, 1223
Scholz A., Jayawardhana R., Wood K., 2006, ApJ, 645, 1498
Shakura N. I., Sunyaev R. A., 1973, A&A, 500, 33
Shu F. H., 1977, ApJ, 214, 488
Shu F. H., Adams F. C., Lizano S., 1987, ARA&A, 25, 23
Sicilia-Aguilar A., et al., 2006, ApJ, 638, 897
Spitzer L., 1978, Physical processes in the interstellar medium. John Wiley and Sons, USA, doi:10.1002/9783527617722
Stecklum B., et al., 2021, A&A, 646, A161
Strittmatter P. A., 1966, MNRAS, 132, 359
Tassis K., et al., 2018, arXiv e-prints, p. arXiv:1810.05652
Terebey S., Shu F. H., Cassen P., 1984, ApJ, 286, 529
Terquem C. E. J. M. L. J., 2008, ApJ, 689, 532
Tinbergen J., 1996, Astronomical Polarimetry
Tomisaka K., 2000, ApJ, 528, L41
Toomre A., 1964, ApJ, 139, 1217
Tritsis A., Panopoulou G. V., Mouschovias T. C., Tassis K., Pavlidou V., 2015, MNRAS, 451, 4384
Tritsis A., Federrath C., Willacy K., Tassis K., 2022, MNRAS, 510, 4420
Turner N. J., Drake J. F., 2009, ApJ, 703, 2152
Turner N. J., Carballido A., Sano T., 2010, ApJ, 708, 188
Van Eck C. L., et al., 2011, ApJ, 728, 97
Vlemmings W. H. T., Diamond P. J., van Langevelde H. J., Torrelles J. M., 2006, A&A, 448, 597
Vorobyov E. I., Basu S., 2005a, MNRAS, 360, 675
Vorobyov E. I., Basu S., 2005b, ApJ, 633, L137
Vorobyov E. I., Basu S., 2006, ApJ, 650, 956
Vorobyov E. I., Basu S., 2007, MNRAS, 381, 1009
Vorobyov E. I., Basu S., 2008, ApJ, 676, L139
Vorobyov E. I., Basu S., 2010, ApJ, 719, 1896
Vorobyov E. I., Basu S., 2015, ApJ, 805, 115
Vorobyov E. I., Elbakyan V. G., Plunkett A. L., Dunham M. M., Audard M., Guedel M., Dionatos O., 2018, A&A, 613, A18
Vorobyov E. I., Khaibrakhmanov S., Basu S., Audard M., 2020, A&A, 644, A74
Wardle M., 2007, Ap&SS, 311, 35

Wardle M., Ng C., 1999, MNRAS, 303, 239

Williams J. P., Cieza L. A., 2011, ARA&A, 49, 67

Zhu Z., et al., 2019, ApJ, 877, L18

Zuckerman B., Palmer P., 1974, ARA&A, 12, 279

Zweibel E. G., 2002, ApJ, 567, 962

di Francesco J., Evans N. J. I., Caselli P., Myers P. C., Shirley Y., Aikawa Y., Tafalla M., 2007, in Reipurth B., Jewitt D., Keil K., eds, Protostars and Planets V. p. 17 (arXiv:astro-ph/0602379)

Chapter 2

Linear Stability Analysis of a Magnetic Rotating Disk with Ohmic Dissipation and Ambipolar Diffusion

A version of this chapter has been published in the Astrophysical Journal as Das I. and Basu S. 2021 ApJ, 910, 163, DOI:10.3847/1538-4357/abdb2c

2.1 Introduction

For decades, theoretical studies have suggested that magnetic fields play an indispensable role in the formation and evolution of interstellar clouds, cloud cores, and protostellar disks (Mestel & Spitzer, 1956; Mouschovias, 1978; Shu et al., 1987, 1999; Mouschovias & Ciolek, 1999; Wurster & Li, 2018). Recent observations by the *Planck* satellite (Planck Collaboration et al., 2015, 2016) have convincingly emphasized the importance of the magnetic field to the density structures on physical scales ranging from tens of parsecs to approximately one parsec in the nearby ($d < 450$ pc) well-known molecular clouds. They statistically evaluated the relative orientation between the magnetic field projected on the plane of sky obtained from the polarized thermal emission (353 Hz) of magnetically-aligned dust grains with the maps of gas column density $N_{\rm H}$ and found that the magnetic field became oriented more nearly perpendicular to the elongations in column density maps when $N_{\rm H} \gtrsim 10^{22}$ cm^{-2}. This is consistent with self-gravity becoming important at these column densities but being not so important at lower column den-

sities. By using the Davis-Chandrasekhar-Fermi (DCF) method (Davis, 1951; Chandrasekhar & Fermi, 1953) to estimate the magnetic field strength, they also found that the large-scale (low density) magnetic field is quite strong relative to turbulence and self-gravity, with estimations that the turbulence is sub-Alfvénic (or close to Alfvénic) and the mass-to-flux ratio is subcritical (see Table D.1 in Planck Collaboration et al., 2016). Pattle et al. (2017) used polarimetry to estimate a subcritical mass-to-flux ratio (~ 0.4) on the large scale in the Orion A filament.

Fiedler & Mouschovias (1993) carried out a two-dimensional (r, z in cylindrical coordinates) simulation of core formation and prestellar collapse in a molecular cloud with an initial subcritical mass-to-flux ratio. In this situation, ambipolar diffusion, the drift of neutrals through the plasma and magnetic field lines because of the imperfect coupling between the neutrals and charged species, can lead to core formation. The cloud has time to settle into a flattened structure with minor axis parallel to the background magnetic field. Based on this result, Ciolek & Mouschovias (1993, 1994) and Basu & Mouschovias (1994, 1995a,b) studied ambipolar-diffusion-driven protostellar core formation and collapse using the "thin-sheet" approximation, with axially symmetric disks threaded by a vertical magnetic field, with hydrostatic equilibrium maintained along field lines at all times.

The thin-sheet approximation was subsequently used by Basu & Ciolek (2004, see also Indebetouw & Zweibel (2000)) for models of nonaxisymmetric, gravitationally collapsing cores in subcritical and supercritical clouds. Ciolek & Basu (2006, see also Morton (1991)) presented a linear stability analysis of isothermal, partially ionized, magnetic, self-gravitating sheets using the thin-sheet approximation. The preferred fragmentation scale typically has the largest super-Jeans value at transcritical (but mildly supercritical) values of the mass-to-flux ratio. The predicted preferred fragmentation length scales obtained from this linear analysis were verified to agree with the average fragmentation scales of a large suite of nonlinear evolution calculations in the thin sheet approximation (Basu et al., 2009a). Three-dimensional simulations of fragmentation including ambipolar diffusion (Kudoh et al., 2007; Kudoh & Basu, 2011) showed that the general trends are robust.

Gravitational instability (hereafter GI) is also thought to be important in protostellar disks, as a pathway for the formation of stellar companions, brown dwarfs, or giant planets (see review by Kratter & Lodato, 2016). Global numerical simulations of disks show that it can

produce clumps of the appropriate masses (e.g., Stamatellos & Whitworth, 2009; Vorobyov & Basu, 2010a; Basu & Vorobyov, 2012; Vorobyov, 2016). Simulations of the self-consistent formation of disks from the collapse of a prestellar core generally show that the disk mass is comparable to the central protostar mass in the early evolution of disks, making them susceptible to GI (Vorobyov & Basu, 2006, 2010b, 2015).

Interest in the early (possibly GI dominated or influenced) evolution of disks has increased due to recent ALMA observations showing that they exist in the early class 0 stage of star formation (Sakai et al., 2014; Ohashi et al., 2014; Lefloch et al., 2015; Plunkett et al., 2015; Ching et al., 2016; Tokuda et al., 2016; Aso et al., 2017; Lee et al., 2017, 2018). ALMA has also clarified the properties of disk structure in the later class I and II stages (Aso et al., 2015; Bjerkeli et al., 2016; Pérez et al., 2016; Alves et al., 2017), including a vast array of substructure like gaps, rings, and spiral arms revealed by the DSHARP project (see Andrews et al., 2018; Huang et al., 2018). These observations show that the process of planet formation is well underway soon after protostar and disk formation. The required rapid planet formation implies a possible important role for GI during the early embedded phase of disks.

Despite extensive work to date on hydrodynamic modeling and observations of disks, the complex role of magnetic fields is just beginning to be explored. Observationally, magnetic fields are very difficult to detect in disks. An indirect detection through polarization of dust emission due to elongated magnetically-aligned grains is complicated by the polarization due to scattering that can dominate the signal at mm wavelengths (Kataoka et al., 2015, 2016; Yang et al., 2016a,b).

In order to understand disk formation and subsequent evolution, the nonideal MHD effects (Ohmic dissipation, ambipolar diffusion, Hall effect) are substantially key features. A nascent disk forms in a magnetically subdominant region where the magnetic field is primarily weakened by Ohmic dissipation (hereafter OD) and ambipolar diffusion (hereafter AD) (e.g., Dapp & Basu, 2010; Dapp et al., 2012; Tomida et al., 2015; Masson et al., 2016; Tsukamoto et al., 2018; Tsukamoto, 2016; Wurster et al., 2018; Hirano & Machida, 2019; Hirano et al., 2020). Without the OD that becomes the dominant form of magnetic dissipation at number densities above 10^{12} cm^{-3}, a disk may not even form (e.g., Allen et al., 2003; Galli et al., 2006; Mellon & Li, 2008; Li et al., 2014); the so-called “magnetic braking catastrophe”.

In general then, a rotationally-supported circumstellar disk is formed around a newly born star in a relatively high density region where OD becomes important. In the Ohmic regime, the inductive effect of the plasma is restricted by the collisions that the charge carriers encounter (i.e., the resistivity), primarily with neutral particles in the partially ionized environment. The OD must then regulate the different (stable and unstable) modes that occur in the high density environment of protostellar disks. Thus it is important to study the effect of nonideal MHD in a rotating self-gravitating environment that is most applicable to the early evolution of disks. The Toomre criterion is modified due to magnetic fields (Lizano et al., 2010). OD and AD will modify it further still. The effect of GI in inducing giant planet formation (e.g., Bodenheimer, 1995; Saigo & Tomisaka, 2006; Lizano et al., 2010; Machida et al., 2016) will be modified by these effects. Furthermore, the marginal state of instability described by the Toomre criterion is known to introduce low-amplitude fluctuations in global disk models (Vorobyov & Basu, 2007) that can drive the angular momentum transport. Therefore, the effect of nonideal MHD on marginally stable modes is also important to clarify. Three-dimensional MHD simulations of disk formation starting from a prestellar core tend to show that the early evolution of disks is characterized by a significant magnetic field strength such that the mass-to-flux ratio is only mildly supercritical (Hirano et al., 2020).

In this paper, we present a linear stability analysis to explore the gravitational instability in protostellar disks. We adopt a sheetlike model that is isothermal, self-gravitating, weakly ionized, magnetic, and rotating. We investigate two nonideal MHD effects: Ohmic dissipation (OD) and ambipolar diffusion (AD). The interplay of OD and rotation are particularly interesting extensions of the analysis presented by Ciolek & Basu (2006).

Our paper is structured as follows. In Section 2.2.1 and 2.2.2, we describe the fundamental assumptions and derive the necessary system of governing equations for a model cloud. From Section 2.2.3 to Section 2.2.7, we describe the stability of the model cloud by linearizing and Fourier analyzing the governing equations, and present some results including the generalized (magnetically dependent) Toomre criterion and the stationary magnetic field limit. In Section 5.3 we present numerical results of our model, and in Section 2.4 we relate our results to observations and models of protostellar disks. Finally, in Section 2.5, we summarize and conclude the consequences of our findings. In the interest of completeness, this paper contains

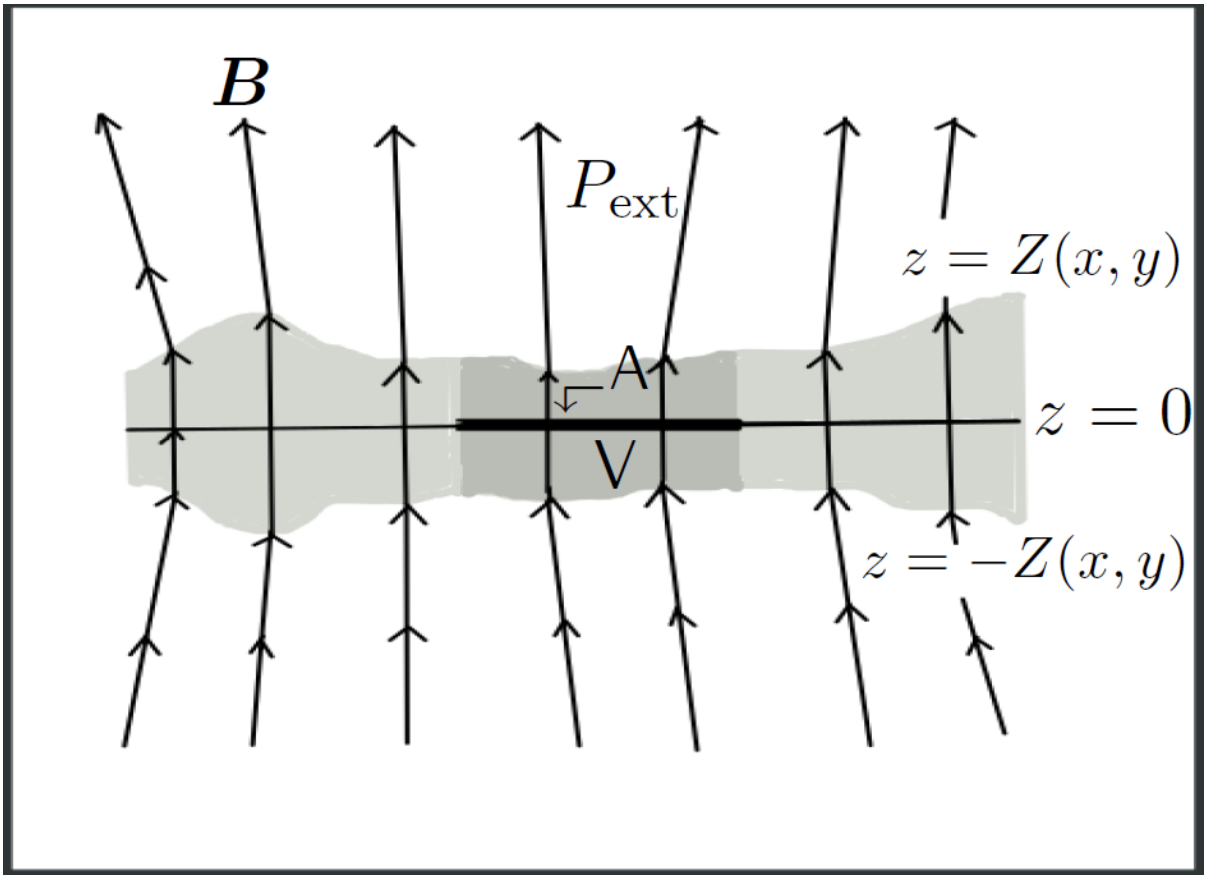

Figure 2.1: Schematic diagram of the thin-disk model. An area A is indicated by the thick dark line and can be seen edge-on in the $z = 0$ plane. The associated volume V is shown by dark shaded region, and adjacent lightly shaded regions are bounded by the curves $z = Z$ and $z = -Z$ and a hot, tenuous medium with external pressure $P_{\rm ext}$. The lines with arrows represent the magnetic field.

many equations and derivations. Note that every parameter written with a 'prime' or 'tilde' denotes their dimensionless form.

2.2 Analytic Considerations

2.2.1 Physical Formulation

We formulate model clouds as rotating, self-gravitating, partially ionized, isothermal, magnetic, planar thin sheets with infinite extent in the x- and y- directions and a local vertical half-thickness $Z(x, y, t)$. Our model follows a similar kind of formulation as adopted and described by Ciolek & Basu (2006) and Basu et al. (2009a,b), but with further interesting physics.

The configuration of the magnetic field threading such a cloud is

$$\begin{aligned}\boldsymbol{B}(x,y,z,t) &= B_{z,\mathrm{eq}}(x,y,t)\hat{\boldsymbol{z}} \quad \text{for } |z| \le Z(x,y,t),\\ &= \Big[B_z(x,y,z,t)\hat{\boldsymbol{z}} + B_x(x,y,z,t)\hat{\boldsymbol{x}}\\ &+ B_y(x,y,z,t)\hat{\boldsymbol{y}}\Big] \quad \text{for } |z| > Z(x,y,t),\end{aligned} \tag{2.1}$$

where $B_{z,\mathrm{eq}}$ is the magnetic field strength in the equatorial plane ($z = 0$) of the cloud (see Figure 2.1). In the limit $|z| \to \infty$, $\boldsymbol{B} \to B_{\mathrm{ref}}\hat{\boldsymbol{z}}$, where B_{ref} is a uniform reference magnetic field very far away from the sheet. From now on, all physical quantities are understood to be a function of time t.

The unit normal vectors to the upper and lower surfaces of the sheet are given by

$$\hat{\boldsymbol{n}} = \frac{\pm\hat{\boldsymbol{z}} \mp \left[(\partial Z/\partial x)\,\hat{\boldsymbol{x}} + (\partial Z/\partial y)\,\hat{\boldsymbol{y}}\right]}{\left[1 + (\partial Z/\partial x)^2 + (\partial Z/\partial y)^2\right]^{1/2}}, \tag{2.2}$$

where the upper sign refers to the upper surface and the lower sign to the lower surface.

Using the integral form of Gauss's law yields that the normal components of the magnetic field across the upper and lower surfaces of the sheet are continuous. This leads to

$$\begin{aligned}B_z\,(x,y,\pm Z) - \; & B_x\,(x,y,\pm Z)\,\frac{\partial Z}{\partial x}\\ - \; & B_y\,(x,y,\pm Z)\,\frac{\partial Z}{\partial y} = B_{z,\mathrm{eq}}(x,y).\end{aligned} \tag{2.3}$$

In our model, we adopt a velocity unit of c_s, the isothermal sound speed, and a column density unit of $\sigma_{n,0}$, the initial uniform column density. The length unit is $L_0 = c_s^2/(2\pi G\sigma_{n,0})$, leading to a time unit $t_0 = c_s/(2\pi G\sigma_{n,0})$, where G is the universal gravitational constant. The mass unit is $M_0 = c_s^4/(4\pi^2 G^2\sigma_{n,0})$ and the unit of acceleration is $2\pi G\sigma_{n,0}$, which is the magnitude of the vertical gravitational acceleration above the planar sheet. The magnetic field strength unit is $B_0 = 2\pi G^{1/2}\sigma_{n,0}$. See Section 2.6.1 for the numeric values of all these free parameters.

Vertical pressure equilibrium arises from a balance between thermal pressure and the combined contribution from self-gravitational pressure, magnetic pressure and any other external

pressure, which yields

$$\rho_n c_s^2 = \frac{\pi}{2} G\sigma_n^2 + P_{\rm ext} + \frac{1}{8\pi}\left[B_{x,Z}^2 + B_{y,Z}^2 + \left\{B_{x,Z}\left(\partial Z/\partial x\right) + B_{y,Z}\left(\partial Z/\partial y\right)\right\}^2\right], \tag{2.4}$$

where $B_{x,Z} \equiv B_x(x, y, +Z)$, $B_{y,Z} \equiv B_y(x, y, +Z)$, and ρ_n and σ_n are the volume and column mass density of neutrals, respectively. The calculation of $B_{x,Z}$ and $B_{y,Z}$ is discussed in Ciolek & Basu (2006). Note that in molecular clouds, $\rho_n \gg \rho_i$, where ρ_i is the ion density. Furthermore, $c_s = (k_B T/m_n)^{1/2}$ is the isothermal sound speed, k_B is the Boltzmann constant, T is the temperature and m_n is the mean mass of a neutral particle ($m_n = 2.33$ amu). The evolution equations of our model include the effect of AD and OD. Because of AD, neutrals can stay at least partially coupled to the magnetic field via neutral-ion collisions. This is quantified by the time scale for collisions between neutrals and ions (e.g., Basu & Mouschovias, 1994, and references within):

$$\tau_{ni} \equiv 1.4\frac{m_i + m_n}{m_i}\frac{1}{n_i\langle\sigma w\rangle_{i\mathrm{H}_2}}, \tag{2.5}$$

where $\langle\sigma w\rangle_{i\mathrm{H}_2}$ is the average collision rate between ions of mass m_i (singly ionized Na, Mg, and HCO, for which we adopt a typical mass of 25 amu) and neutrals of mass m_n. We adopt a neutral-ion collision rate between H_2 and HCO^+ as $1.69 \times 10^{-9}\,\mathrm{cm^3\,s^{-1}}$ (McDaniel & Mason, 1973). These collisions transport knowledge of the magnetic field to the neutral particles via ions that are tied to the field lines. The factor 1.4 arises because the inertia of helium is neglected in calculating the slowing-down time of the neutrals by collisions with ions (Ciolek & Basu, 2006; Mouschovias & Ciolek, 1999).

We adopt a constant power-law approximation for calculating the ion number density (n_i) in terms of the neutral number density (n_n):

$$n_i = \kappa\left(\frac{n_n}{10^5\ \mathrm{cm^{-3}}}\right)^k, \tag{2.6}$$

where $\kappa\,(= 3 \times 10^{-3}\mathrm{cm^{-3}})$ and $k\,(= 1/2)$ are constants (see Ciolek & Basu, 2006; Ciolek &

Mouschovias, 1998) . So, the ionization fraction (χ_i) can be written as

$$\chi_i = \frac{n_i}{n_n} \approx 10^{-5}\, n_n^{-1/2}, \tag{2.7}$$

and is typically a very small number, $\approx 10^{-7}$ when $n_n = 10^4$ cm^{-3}. Molecular clouds are weakly ionized yet retain a relatively good (though imperfect) coupling between plasma and neutrals due to the enhanced Langevin cross section for ion-neutral collisions (see Shu, 1992, § 27).

In our formulation we include the additional nonideal MHD effect of OD. It is a measure of the decoupling of the charged species from the magnetic field, due to resistivity arising from collisions of the charge carriers with neutrals. Collisions of the charged species with each other is neglected as we are studying a weakly ionized plasma. The conductivity for each charged species $s = e, i$ can be written as

$$\sigma_s = \frac{n_s q_s^2 \tau_{sn}}{m_s}, \tag{2.8}$$

where n_s is the number density of each charged species (we can assume $n_e \approx n_i$ due to charge neutrality), q_s is the charge of each species, m_s is the mass of each species, and τ_{sn} is the mean collision time of each charged species with neutrals (see Section 2.6.2). We define conductivity $\sigma_c = \sum_{s=e,i} \sigma_s$, and the electron contribution is expected to dominate. So, finally, the expression of Ohmic diffusivity ($\eta_{\rm OD}$) can be written as

$$\eta_{\rm OD} = \frac{c^2}{4\pi\sigma_c}, \tag{2.9}$$

where c is the speed of the light. Note that $(4\pi\eta_{\rm OD})/c^2$ is the Ohmic resistivity, i.e., the inverse of the conductivity, and leads to the well-known form of Ohm's law:

$$\boldsymbol{E}_n = \frac{4\pi\eta_{\rm OD}}{c^2}\boldsymbol{j}, \tag{2.10}$$

where $\boldsymbol{j}$ is the electric current density and $\boldsymbol{E}_n$ is the electric field in the reference frame of the neutrals (for more details, see Dapp et al., 2012).

2.2.2 Fundamental Equations

The system of equations for the model cloud are derived (see Ciolek & Basu, 2006) by integrating the fundamental MHD equations over the vertical direction (i.e., from $z_{\rm lower} = -Z(x,y)$ to $z_{\rm upper} = Z(x,y)$). Doing the same for the equation of mass continuity yields

$$\frac{\partial \sigma_n}{\partial t} + \boldsymbol{\nabla}_p \cdot (\sigma_n \, \boldsymbol{v}_n) = 0, \tag{2.11}$$

where $\sigma_n(x,y) = \int_{-Z}^{Z} \rho_n(x,y) dz$. Next, we consider the equation of force using the total stress tensor (thermal plus Maxwell)

$$\boldsymbol{T} = -\left[\rho_n c_s^2 + \frac{B^2}{8\pi}\right]\mathbf{1} + \frac{\boldsymbol{B}\boldsymbol{B}}{4\pi}, \tag{2.12}$$

here, $\mathbf{1}$ is identity tensor. The force equation (per unit area) in the rotating frame of reference for the neutrals is given by,

$$\begin{aligned}\frac{\partial}{\partial t}(\sigma_n \, \boldsymbol{v}_n) + \boldsymbol{\nabla}_p \cdot \, (\sigma_n \boldsymbol{v}_n \, \boldsymbol{v}_n) = \boldsymbol{F}_T + \boldsymbol{F}_{\rm Mag} \\ + \sigma_n \left[\boldsymbol{g}_p - 2(\boldsymbol{\Omega} \times \boldsymbol{v}_n) + \boldsymbol{\Omega} \times (\boldsymbol{\Omega} \times \boldsymbol{r})\right],\end{aligned} \tag{2.13}$$

where

$$\boldsymbol{F}_T = -C_{\rm eff}^2 \boldsymbol{\nabla}_p \sigma_n, \tag{2.14}$$

$$\boldsymbol{F}_{\rm Mag} = \frac{B_{z,\rm eq}}{2\pi}\left(\boldsymbol{B}_p - Z\nabla_p B_{z,\rm eq}\right) + O\left(\boldsymbol{\nabla}_p Z\right), \tag{2.15}$$

$$Z = \frac{\sigma_n}{2\rho_n}, \tag{2.16}$$

$$\boldsymbol{g}_p = -\nabla_p \psi, \tag{2.17}$$

$$\psi = \mathcal{F}^{-1}\left[-2\pi G \frac{\mathcal{F}(\sigma_n)}{k}\right], \tag{2.18}$$

$$\boldsymbol{B}_p = -\nabla_p \Psi, \tag{2.19}$$

$$\Psi = \mathcal{F}^{-1}\left[\frac{\mathcal{F}\left(B_{z,\mathrm{eq}} - B_{\mathrm{ref}}\right)}{k}\right], \tag{2.20}$$

$$C_{\mathrm{eff}}^2 = \frac{\pi}{2} G\sigma_n^2 \frac{\left[3P_{\mathrm{ext}} + \frac{\pi}{2}G\sigma_n^2\right]}{\left[P_{\mathrm{ext}} + \frac{\pi}{2}G\sigma_n^2\right]^2} c_s^2. \tag{2.21}$$

In the above equations, $\boldsymbol{r} = x\hat{\boldsymbol{x}} + y\hat{\boldsymbol{y}}$, $\boldsymbol{\nabla}_p \equiv \hat{\boldsymbol{x}}\partial/\partial x + \hat{\boldsymbol{y}}\partial/\partial y$ is the planar gradient operator and ψ and Ψ are the gravitational and magnetic potential, respectively. Here, $\mathcal{F}(f)$ and $\mathcal{F}^{-1}(f)$ represent the forward and backward Fourier transform of a function f, respectively. The C_{eff} is the local effective sound speed which includes the effect of an external pressure. In the absence of P_{ext}, C_{eff} is reduced to the isothermal sound speed c_s. The $\boldsymbol{v}_n(x,y) = v_{n,x}(x,y)\hat{\boldsymbol{x}} + v_{n,y}(x,y)\hat{\boldsymbol{y}}$ is the velocity of neutrals in the plane of the sheet. The planar sheet is rotating with an angular velocity Ω about the z-axis, so that $\boldsymbol{\Omega} = \Omega\hat{\boldsymbol{z}}$. The magnetic field and rotation axis are perpendicular to the sheet. Here, $2(\boldsymbol{\Omega}\times\boldsymbol{v}_n)$ and $\boldsymbol{\Omega}\times(\boldsymbol{\Omega}\times\boldsymbol{r})$ are the Coriolis and centrifugal acceleration terms, respectively. A more complete expression of $\boldsymbol{F}_{\mathrm{Mag}}$ can be written showing the $O(\nabla_p Z)$ terms explicitly (see Equation 3.19, 3.20; also Ciolek & Basu (2006)). The vertical z-wavenumber k (> 0) is presented as a function of k_x and k_y, which are the x-, and y-wavenumbers in the plane of the sheet such that $k \equiv k_z = (k_x^2 + k_y^2)^{1/2}$. By a sheet being thin we mean that for any physical quantity $f(x,y,z,t)$, the criterion $f/\nabla_p f \gg Z$ is satisfied.

The advection of magnetic flux for our model is described by the magnetic induction equation,

$$\frac{\partial \boldsymbol{B}_{z,\mathrm{eq}}}{\partial t} = \boldsymbol{\nabla}_p \times \left(\boldsymbol{v}_i \times \boldsymbol{B}_{z,\mathrm{eq}}\right) - \boldsymbol{\nabla}_p \times \left(\eta_{\mathrm{OD}}\, \boldsymbol{\nabla}_p \times \boldsymbol{B}_{z,\mathrm{eq}}\right), \tag{2.22}$$

where

$$\boldsymbol{v}_i = \boldsymbol{v}_n + \frac{\tau_{ni}}{\sigma_n}\boldsymbol{F}_{\mathrm{Mag}}. \tag{2.23}$$

In the above equations, η_{OD} and τ_{ni} are the Ohmic diffusivity, neutral-ion collision time, respectively. The $\boldsymbol{v}_i(x,y)$ is the ion velocity such that $\boldsymbol{v}_i(x,y) = v_{i,x}(x,y)\hat{\boldsymbol{x}} + v_{i,y}(x,y)\hat{\boldsymbol{y}}$. Finally, we obtain a simplified form of these equations by separating the x- and y- components. Doing that

for Equation 2.11, Equation 2.13, Equation 2.15, and Equation 2.22, yields

$$\frac{\partial \sigma_n}{\partial t} + \frac{\partial}{\partial x}(\sigma_n v_{n,x}) + \frac{\partial}{\partial y}(\sigma_n v_{n,y}) = 0, \tag{2.24}$$

$$\begin{aligned}\frac{\partial}{\partial t}(\sigma_n v_{n,x}) + \frac{\partial}{\partial x}(\sigma_n v_{n,x}^2) + \frac{\partial}{\partial x}(\sigma_n v_{n,x} v_{n,y}) \\ = \sigma_n\, g_x - C_{\rm eff}^2 \frac{\partial \sigma_n}{\partial x} + F_{{\rm Mag},x} + 2\sigma_n \Omega v_{n,y},\end{aligned} \tag{2.25}$$

$$\begin{aligned}\frac{\partial}{\partial t}(\sigma_n v_{n,y}) + \frac{\partial}{\partial y}(\sigma_n v_{n,x} v_{n,y}) + \frac{\partial}{\partial y}(\sigma_n v_{n,y}^2) \\ = \sigma_n\, g_y - C_{\rm eff}^2 \frac{\partial \sigma_n}{\partial y} + F_{{\rm Mag},y} - 2\sigma_n \Omega v_{n,x},\end{aligned} \tag{2.26}$$

$$\begin{aligned}F_{{\rm Mag},x} = \frac{B_{z,{\rm eq}}}{2\pi}\left(B_{x,Z} - Z\,\frac{\partial B_{z,{\rm eq}}}{\partial x}\right) \\ + \frac{1}{4\pi}\frac{\partial Z}{\partial x}\Bigg[B_{x,Z}^2 + B_{y,Z}^2 + 2B_{z,{\rm eq}}\left(B_{x,Z}\frac{\partial Z}{\partial x} + B_{y,Z}\frac{\partial Z}{\partial y}\right) \\ + \left(B_{x,Z}\frac{\partial Z}{\partial x} + B_{y,Z}\frac{\partial Z}{\partial y}\right)^2\Bigg],\end{aligned} \tag{2.27}$$

$$\begin{aligned}F_{{\rm Mag},y} = \frac{B_{z,{\rm eq}}}{2\pi}\left(B_{y,Z} - Z\,\frac{\partial B_{z,{\rm eq}}}{\partial y}\right) \\ + \frac{1}{4\pi}\frac{\partial Z}{\partial y}\Bigg[B_{x,Z}^2 + B_{y,Z}^2 + 2B_{z,{\rm eq}}\left(B_{x,Z}\frac{\partial Z}{\partial x} + B_{y,Z}\frac{\partial Z}{\partial y}\right) \\ + \left(B_{x,Z}\frac{\partial Z}{\partial x} + B_{y,Z}\frac{\partial Z}{\partial y}\right)^2\Bigg],\end{aligned} \tag{2.28}$$

$$\begin{aligned}\frac{\partial B_{z,{\rm eq}}}{\partial t} = -\frac{\partial}{\partial x}\left(B_{z,{\rm eq}} v_{i,x}\right) - \frac{\partial}{\partial y}\left(B_{z,{\rm eq}} v_{i,y}\right) \\ + \left[\frac{\partial}{\partial x}\left(\eta_{\rm OD}\frac{\partial B_{z,{\rm eq}}}{\partial x}\right) + \frac{\partial}{\partial y}\left(\eta_{\rm OD}\frac{\partial B_{z,{\rm eq}}}{\partial y}\right)\right].\end{aligned} \tag{2.29}$$

Note that in the force equations we no longer consider the centrifugal term $[\boldsymbol{\Omega} \times (\boldsymbol{\Omega} \times \boldsymbol{r}) = -\Omega^2(x\hat{\boldsymbol{x}} + y\hat{\boldsymbol{y}})]$. This is because we assume that the centrifugal force is balanced in the background state by a gravitational force produced by an unspecified mass distribution. This is a form of the "Jeans swindle", to rely on a force balance in the uniform background state (see Binney & Tremaine, 2008, § 5.6.1).

2.2.3 Stability of the model: Linearization and Analysis

Starting with a static uniform background, any physical quantity of the thin-sheet equations can be expanded by writing it via

$$f(x, y, t) = f_0 + \delta f_a e^{i\left(k_x x + k_y y - \omega t\right)}, \tag{2.30}$$

where f_0 is the unperturbed background state, δf_a is the amplitude of the perturbation. k_x, k_y, and k are the x-, y-, and z- wavenumbers, respectively, and ω is the complex angular frequency. With this Fourier analysis, $\partial/\partial t \rightarrow -i\omega$, $\partial/\partial x \rightarrow ik_x$, and $\partial/\partial y \rightarrow ik_y$. For assumed small-amplitude perturbations such that $|\delta\, f_a| \ll f_0$, and retaining the linearized form of the perturbed quantities from Eqs. 3.16, 3.17, 3.18 and 3.21, the following equations are obtained

$$\omega\, \delta\sigma'_n = k_x\, c_s\, \delta v'_{n,x} + k_y\, c_s\, \delta v'_{n,y} \ , \tag{2.31}$$

$$\begin{aligned} \omega\, c_s\, \delta v'_{n,x} = {} & \frac{k_x}{k} \left[C^2_{\mathrm{eff},0}\, k - 2\pi G \sigma_{n,0} \right] \delta\sigma'_n + i\, 2\Omega c_s \delta v'_{n,y} \\ & + \frac{k_x}{k} \left[\, 2\pi G \sigma_{n,0}\, \mu_0^{-1} + k\, V^2_{A,0}\, \mu_0 \, \right] \delta B'_{z,\mathrm{eq}} \ , \end{aligned} \tag{2.32}$$

$$\begin{aligned} \omega\, c_s\, \delta v'_{n,y} = {} & \frac{k_y}{k} \left[C^2_{\mathrm{eff},0}\, k - 2\pi G \sigma_{n,0} \right] \delta\sigma'_n - i\, 2\Omega c_s \delta v'_{n,x} \\ & + \frac{k_y}{k} \left[\, 2\pi G \sigma_{n,0}\, \mu_0^{-1} + k\, V^2_{A,0}\, \mu_0 \, \right] \delta B'_{z,\mathrm{eq}} \ , \end{aligned} \tag{2.33}$$

$$\begin{aligned} \omega\, \delta B'_{z,\mathrm{eq}} = {} & \frac{k_x}{\mu_0}\, c_s\, \delta v'_{n,x} + \frac{k_y}{\mu_0}\, c_s\, \delta v'_{n,y} \\ & - i \left[\eta_{\mathrm{OD},0}\, k^2 + \, \tau_{ni,0} \, \left(2\pi G \sigma_{n,0} \mu_0^{-2} k + k^2\, V^2_{A,0} \right) \right] \delta B'_{z,\mathrm{eq}}, \end{aligned} \tag{2.34}$$

where the perturbed eigenfunctions $\delta\sigma_n$, $\delta v_{n,x}$ (and $\delta v_{n,y}$), $\delta B_{z,\mathrm{eq}}$ are normalized by $\sigma_{n,0}$, c_s and B_0 ($= 2\pi G^{1/2} \sigma_{n,0}$), respectively such that $\delta\sigma'_n = \delta\sigma_n/\sigma_{n,0}$, $\delta v'_{n,x} = \delta v_{n,x}/c_s$, $\delta v'_{n,y} = \delta v_{n,y}/c_s$, and $\delta B'_{z,\mathrm{eq}} = \delta B_{z,\mathrm{eq}}/B_0$. Here, $\tau_{ni,0}$, $\eta_{\mathrm{OD},0}$, $C_{\mathrm{eff},0}$, and $\sigma_{n,0}$, $\rho_{n,0}$ represent the initial uniform component of neutral-ion collision time, the Ohmic diffusivity, the local effective sound speed, the mass column density of the sheet, and the volume density, respectively. The quantities $\tau_{ni,0}$ and $\eta_{\mathrm{OD},0}$ are regarded as measures of AD and OD, respectively. From Equation 2.23 one

obtains

$$v_{i,x} = v_{n,x} + \frac{\tau_{ni,0}}{\sigma_n}\left(\frac{\rho_{n,0}}{\rho_n}\right)^{1/2} F_{\mathrm{Mag},x}, \tag{2.35}$$

$$v_{i,y} = v_{n,y} + \frac{\tau_{ni,0}}{\sigma_n}\left(\frac{\rho_{n,0}}{\rho_n}\right)^{1/2} F_{\mathrm{Mag},y}, \tag{2.36}$$

where $v_{i,x}$, $v_{i,y}$, $v_{n,x}$, $v_{n,y}$ have been discussed earlier. The above equations introduce the normalized initial mass-to-flux ratio of the background reference state,

$$\mu_0 \equiv 2\pi G^{1/2}\frac{\sigma_{n,0}}{B_{\mathrm{ref}}} = \frac{1}{\tilde{B}_{\mathrm{ref}}}, \tag{2.37}$$

where $\tilde{B}_{\mathrm{ref}} = B_{\mathrm{ref}}/B_0$, and $(2\pi G^{1/2})^{-1}$ is the critical mass-to-flux ratio for gravitational collapse in the adopted model (Nakano & Nakamura, 1978; Ciolek & Basu, 2006), and B_{ref} is the magnetic field strength of the background reference state that is equal to the initial uniform component of the magnetic field strength in the equatorial plane of the cloud ($B_{z,\mathrm{eq},0}$). Regions with $\mu_0 < 1$ are defined as subcritical, regions with $\mu_0 > 1$ are defined to be supercritical, and regions with $\mu_0 \approx 1$ are transcritical. Furthermore, $V_{A,0}$ is the initial uniform Alfvén speed,

$$V_{A,0}^2 \equiv \frac{B_{\mathrm{ref}}^2}{4\pi\rho_{n,0}} = 2\pi G\sigma_{n,0}\mu_0^{-2}Z_0 \ . \tag{2.38}$$

The initial uniform component of the ambipolar diffusivity can be expressed as

$$\eta_{\mathrm{AD},0} = V_{A,0}^2\tau_{ni,0} = 2\pi G\sigma_{n,0}\mu_0^{-2}Z_0\tau_{ni,0}. \tag{2.39}$$

The initial vertical half-thickness is

$$Z_0 = \frac{\sigma_{n,0}c_s^2}{\pi G\sigma_{n,0}^2 + 2P_{\mathrm{ext}}}. \tag{2.40}$$

From now on, we use the following form of the pressure balance equation

$$\rho_{n,0}c_s^2 = \frac{\pi}{2}G\sigma_{n,0}^2 + P_{\mathrm{ext}}, \tag{2.41}$$

obtained by linearizing Equation 3.13.

2.2.4 Dispersion Relation

A gravitationally unstable mode occurs if one of the imaginary parts of the complex angular frequency ($\omega_{\rm IM}$) leads to a growing solution, i.e., $\omega_{\rm IM} > 0$. The growth time of such an instability is obtained from the relation $\tau_g = 1/\omega_{\rm IM}$. The dispersion relation is found from the following system of equations:

$$\begin{bmatrix} -\omega & k_x c_s & k_y c_s & 0 \\ \frac{k_x}{k} A_1 & -\omega\, c_s & 2i\Omega c_s & \frac{k_x}{k} A_2 \\ \frac{k_y}{k} A_1 & -2i\Omega c_s & -\omega\, c_s & \frac{k_y}{k} A_2 \\ 0 & \frac{k_x}{\mu_0} c_s & \frac{k_y}{\mu_0} c_s & -[\omega + i(\theta+\gamma)] \end{bmatrix} \begin{bmatrix} \delta\sigma'_n \\ \delta v'_{n,x} \\ \delta v'_{n,y} \\ \delta B'_{z,\rm eq} \end{bmatrix} = 0\,, \tag{2.42}$$

where

$$A_1 = \left(C^2_{\rm eff,0} k - 2\pi G \sigma_{n,0}\right), \tag{2.43}$$

$$A_2 = \left(2\pi G \sigma_{n,0}\, \mu_0^{-1} + k\, V^2_{A,0}\, \mu_0\right), \tag{2.44}$$

$$\gamma = \eta_{\rm OD,0}\, k^2, \tag{2.45}$$

$$\theta = \tau_{ni,0}\left(2\pi G \sigma_{n,0} \mu_0^{-2} k + k^2 V^2_{A,0}\right) = \eta_{\rm AD,0} \frac{(k + Z_0 k^2)}{Z_0}, \tag{2.46}$$

(see Section 2.6.3 for more discussion on $\eta_{\rm AD,0}$ and $\eta_{\rm OD,0}$). Now, solving the determinant of the above matrix, the dispersion relation is

$$\begin{aligned} (\omega + i\,[\theta+\gamma])\,(\omega^2 - C^2_{\rm eff,0}\, k^2 + 2\pi G\sigma_{n,0} k - 4\Omega^2) \\ = \omega\,\left[2\pi G\sigma_{n,0} k \mu_0^{-2} + k^2\, V^2_{A,0}\right]\,. \end{aligned} \tag{2.47}$$

In the limit of flux-freezing ($\tau_{ni,0} \to 0,\ \eta_{\rm OD,0} \to 0$),

$$\begin{aligned} \omega^2 - C^2_{\rm eff,0}\, k^2 + 2\pi G\sigma_{n,0} k - 4\Omega^2 \\ = 2\pi G\sigma_{n,0} k \mu_0^{-2} + k^2\, V^2_{A,0}\,. \end{aligned} \tag{2.48}$$

In the limit of OD only ($\tau_{ni,0} \to 0$),

$$\begin{aligned}(\omega + i\,\gamma)\,(\omega^2 - C_{\rm eff,0}^2\,k^2 + 2\pi G\sigma_{n,0}k - 4\Omega^2) \\ = \omega\,\left(2\pi G\sigma_{n,0}k\mu_0^{-2} + k^2\,V_{A,0}^2\right)\,.\end{aligned} \tag{2.49}$$

In the limit of AD only ($\eta_{\rm OD,0} \to 0$),

$$\begin{aligned}(\omega + i\,\theta)\,(\omega^2 - C_{\rm eff,0}^2\,k^2 + 2\pi G\sigma_{n,0}k - 4\Omega^2) \\ = \omega\,\left(2\pi G\sigma_{n,0}k\mu_0^{-2} + k^2\,V_{A,0}^2\right)\,.\end{aligned} \tag{2.50}$$

In the limit of flux-freezing, the gravitationally unstable mode corresponds to one of the roots of $\omega^2 < 0$ and occurs for $\mu_0 > 1$. The growth time for this mode becomes a function of Ω and μ_0 and can be written as

$$\tau_g = \frac{\lambda}{2\pi\left[G\sigma_{n,0}(1-\mu_0^{-2})(\lambda - \lambda_{MS}) - \frac{\Omega^2\lambda^2}{\pi^2}\right]^{1/2}}\,, \tag{2.51}$$

for $\lambda \geq \lambda_{MS}$, where

$$\lambda_{\rm MS} = \frac{\left(C_{\rm eff,0}^2 + V_{A,0}^2\right)}{G\sigma_{n,0}\left(1-\mu_0^{-2}\right)}. \tag{2.52}$$

The minimum growth time for the unstable mode occurs at the preferred magnetosonic length scale $\lambda_{\rm MS,m} = 2\lambda_{\rm MS}$. As $\mu_0 \to \infty$, this implies negligible magnetic support ($\tilde{B}_{\rm ref} \to 0$). In this regime, the growth time $\tau_{g,T}$ is dependent on the critical thermal length scale ($\lambda_{\rm T} \equiv C_{\rm eff,0}^2/(G\sigma_{n,0})$) as follows:

$$\tau_{g,T} = \frac{\lambda}{2\pi\left[G\sigma_{n,0}\,(\lambda - \lambda_{\rm T}) - \frac{\Omega^2\lambda^2}{\pi^2}\right]^{1/2}}\,. \tag{2.53}$$

In this regime ($\mu_0 \gg 1$), the minimum growth time for the unstable mode occurs at the preferred thermal length scale $\lambda_{T,m} = 2\lambda_{\rm T}$.

After including the nonideal MHD effects, i.e., OD and AD, the gravitationally unstable mode still corresponds to one of the roots of the full dispersion relation (Equation 3.4) and all of them are obtained numerically. Because it is a cubic equation, an analytic expression of the

growth time cannot be written down as simply as Equation 2.53.

2.2.5 Normalization

The model we use can be characterized by several dimensionless free parameters in addition to μ_0 (see Equation 3.3). We normalize all length scales by L_0 and timescales by t_0, mass by M_0, column densities by $\sigma_{n,0}$, magnetic field strength by B_0. We define a dimensionless form of the initial neutral-ion collision time $\tilde{\tau}_{ni,0} = \tau_{ni,0}/t_0 = \left(2\pi G\sigma_{n,0}\tau_{ni,0}\right)/c_s$ and a dimensionless external pressure $\tilde{P}_{\rm ext} \equiv (2P_{\rm ext})/(\pi G\sigma_{n,0}^2)$. The dimensionless local effective sound speed is

$$\tilde{C}_{\rm eff,0} = \frac{C_{\rm eff,0}}{c_s} = \frac{\left(1+3\tilde{P}_{\rm ext}\right)^{\frac{1}{2}}}{\left(1+\tilde{P}_{\rm ext}\right)}. \tag{2.54}$$

The dimensionless Alfvén wave speed is

$$\tilde{V}_{A,0} = \frac{V_{A,0}}{c_s} = \tilde{Z}_0^{1/2}\tilde{B}_{\rm ref} = \tilde{Z}_0^{1/2}\mu_0^{-1}, \tag{2.55}$$

We define the normalized ambipolar diffusivity

$$\tilde{\eta}_{\rm AD,0} = \eta_{\rm AD,0}\left(t_0/L_0^2\right) = \tilde{V}_{A,0}^2\tilde{\tau}_{ni,0} = \tilde{Z}_0\mu_0^{-2}\tilde{\tau}_{ni,0}, \tag{2.56}$$

and a normalized Ohmic diffusivity $\tilde{\eta}_{\rm OD,0} = \eta_{\rm OD,0}\left(t_0/L_0^2\right)$. Here, $\tilde{Z}_0$ is the normalized local vertical half-thickness and is written as

$$\tilde{Z}_0 = \frac{Z_0}{L_0} = \frac{2}{\left(1+\tilde{P}_{\rm ext}\right)}, \tag{2.57}$$

(note that $\tilde{Z}_0 = 2$ with no external pressure). See Section 2.6.4 for more discussion on $\tilde{C}_{\rm eff,0}$ and $\tilde{Z}_0$. The normalized isothermal magnetosonic speed in our units is written as

$$\tilde{V}_{\rm MS,0} = \left(\tilde{C}_{\rm eff,0}^2 + \tilde{V}_{A,0}^2\right)^{\frac{1}{2}} = \tilde{C}_{\rm eff,0}\left[1+\frac{2}{\mu_0^2}\frac{(1+\tilde{P}_{\rm ext})}{(1+3\tilde{P}_{\rm ext})}\right]^{\frac{1}{2}}. \tag{2.58}$$

The normalized form of governing equations (see Equations (3.25) to (3.28)) are following

$$\omega' \, \delta\sigma'_n = k'_x \, \delta v'_{n,x} + k'_y \, \delta v'_{n,y} \ , \tag{2.59}$$

$$\begin{aligned} \omega' \, \delta v'_{n,x} = \frac{k'_x}{k'} \left[\tilde{C}^2_{\mathrm{eff},0} \, k' - 1\right] \delta\sigma'_n + \ i \, Q \delta v'_{n,y} \\ + \ \frac{k'_x}{k'} \, \mu_0^{-1} \left[1 + \tilde{Z}_0 k'\right] \delta B'_{z,\mathrm{eq}} \ , \end{aligned} \tag{2.60}$$

$$\begin{aligned} \omega' \, \delta v'_{n,y} = \frac{k'_y}{k'} \left[\tilde{C}^2_{\mathrm{eff},0} \, k' - 1\right] \delta\sigma'_n - \ i \, Q \delta v'_{n,x} \\ + \ \frac{k'_y}{k'} \, \mu_0^{-1} \left[1 \ + \tilde{Z}_0 k'\right] \delta B'_{z,\mathrm{eq}} \ , \end{aligned} \tag{2.61}$$

$$\omega' \, \delta B'_{z,\mathrm{eq}} = \frac{k'_x}{\mu_0} \, \delta v'_{n,x} + \frac{k'_y}{\mu_0} \, \delta v'_{n,y} \ - i \left[\tilde{\gamma} + \tilde{\theta}\right] \delta B'_{z,\mathrm{eq}} \ . \tag{2.62}$$

So, the normalized form of the dispersion relation is

$$\begin{aligned} \left(\omega' + i[\tilde{\theta} + \tilde{\gamma}]\right)(\omega'^2 - \tilde{C}^2_{\mathrm{eff},0} k'^2 + k' - Q^2) \\ = \omega' \, \left(k' \mu_0^{-2} + \tilde{Z}_0 k'^2 \mu_0^{-2}\right) \ , \end{aligned} \tag{2.63}$$

where $k' = kL_0$, $\omega' = \omega t_0$, and

$$\tilde{\gamma} = \gamma t_0 = \tilde{\eta}_{\mathrm{OD},0} \, k'^2, \tag{2.64}$$

$$\tilde{\theta} = \theta t_0 = \tilde{\tau}_{ni,0} \, \mu_0^{-2} \, \left(k' + \tilde{Z}_0 k'^2\right) = \tilde{\eta}_{\mathrm{AD},0} \frac{\left(k' + \tilde{Z}_0 k'^2\right)}{\tilde{Z}_0}. \tag{2.65}$$

In the limit of flux-freezing ($\tilde{\tau}_{ni,0} \to 0$, $\tilde{\eta}_{\mathrm{OD},0} \to 0$),

$$\omega'^2 - \tilde{C}^2_{\mathrm{eff},0} k'^2 + k' - Q^2 = k' \mu_0^{-2} + \tilde{Z}_0 k'^2 \mu_0^{-2}. \tag{2.66}$$

In the limit of OD only ($\tilde{\tau}_{ni,0} \to 0$),

$$\begin{aligned} (\omega' + i\tilde{\gamma}) \ (\omega'^2 - \tilde{C}^2_{\mathrm{eff},0} k'^2 + k' - Q^2) \\ = \omega' \, \left(k' \mu_0^{-2} + \tilde{Z}_0 k'^2 \mu_0^{-2}\right) \ . \end{aligned} \tag{2.67}$$

In the limit of AD only ($\tilde{\eta}_{\rm OD,0} \rightarrow 0$),

$$\begin{aligned}\left(\omega' + i\tilde{\theta}\right)\left(\omega'^2 - \tilde{C}^2_{\rm eff,0}k'^2 + k' - Q^2\right) \\ = \omega'\left(k'\mu_0^{-2} + \tilde{Z}_0 k'^2 \mu_0^{-2}\right) .\end{aligned} \tag{2.68}$$

Here, we represent the effect of rotation in terms of the Toomre parameter

$$Q \equiv \frac{c_s \Omega}{\pi G \sigma_{n,0}} \tag{2.69}$$

(Toomre, 1964).

Similarly, under flux-freezing the normalized form of the growth time of the gravitationally mode can be written as

$$\tau'_g = \frac{\lambda'}{\left[2\pi\left(1-\mu_0^{-2}\right)\left(\lambda' - \lambda'_{\rm MS}\right) - \ Q^2\lambda'^2\right]^{1/2}} , \tag{2.70}$$

for $\lambda' \geq \lambda'_{MS}$ and for $\mu_0 > 1$,

$$\lambda'_{\rm MS} = 2\pi \frac{\left(\tilde{C}^2_{\rm eff,0} + \tilde{Z}_0\mu_0^{-2}\right)}{\left(1-\mu_0^{-2}\right)} . \tag{2.71}$$

The minimum growth time for the unstable mode occurs at $\lambda'_{\rm MS,m} = 2\lambda'_{\rm MS}$. Note that, $k'_{\rm MS,m} = k'_{\rm MS}/2$. The dimensionless thermal growth time ($\tau'_{g,T}$) is

$$\tau'_{g,T} = \frac{\lambda'}{\left[2\pi(\lambda' - \lambda'_{\rm T}) - \ Q^2\lambda'^2\right]^{\frac{1}{2}}} , \tag{2.72}$$

where the dimensionless critical thermal length scale is defined as

$$\lambda'_{\rm T} = 2\pi\tilde{C}^2_{\rm eff,0} = \pi\frac{\left(1+3\tilde{P}_{\rm ext}\right)}{\left(1+\tilde{P}_{\rm ext}\right)}\tilde{Z}_0 . \tag{2.73}$$

Interestingly, we notice that in the flux-frozen case the normalized shortest growth timescale is different for each different normalized rotation rate Q, as obtained in Equation 2.70 and 2.72. However, we find that the corresponding normalized preferred length scale remains the same irrespective of any rotation as shown in Equation 2.71 and 2.73 (see also Figure 2.9 for relevant

discussion). When $\mu_0 \to \infty$ and $Q = 0$, the minimum growth time for the unstable mode occurs at $\lambda'_{\rm T,m} = 2\lambda'_{\rm T}$ and it yields a growth time

$$\tau'_{g,T,m} = \left(\frac{2\lambda'_{\rm T}}{\pi}\right)^{1/2} = 2\,\tilde{C}_{\rm eff,0}\,, \tag{2.74}$$

which is the same as the dimensionless dynamical (free-fall) timescale ($t'_{\rm d} = t_{\rm d}/t_0 = \tilde{Z}_0$, or $t_{\rm d} = Z_0/c_s$) when $\tilde{P}_{\rm ext} = 0$. For the highly supercritical regime ($\mu_0 \gg 1$), under the asymptotic limit ($\lambda' \gg \lambda'_{\rm T}$),

$$\tau'_g \;\to\; \left(\frac{\lambda'}{2\pi}\right)^{1/2}, \tag{2.75}$$

as obtained from Equation 2.70 for the case of no rotation ($Q = 0$). This behavior is seen in Figure 2.5(a) and Figure 2.6 for very large length scales and $\mu_0 > 1$. These results show that in the limit $Q = 0$, the isothermal sheet has a thermal length scale ($\lambda'_{\rm T} = 2\pi\tilde{C}^2_{\rm eff,0}$, effectively the "Jeans length") and a preferred thermal length scale $\lambda'_{\rm T,m} = 4\pi\tilde{C}^2_{\rm eff,0}$. Similarly, in the limit $\tilde{P}_{\rm ext} \to 0$, it becomes $\lambda_{\rm T,m} = 4\pi\ L_0 = 2\pi Z_0$) and thermal (Jeans) timescale $\tau'_{\rm T,m} = 2$ (similarly, $\tau_{\rm T,m} = 2L_0/c_s = Z_0/c_s$). We use λ' as an independent variable since the characteristic dispersion relation for our eigensystem is only a function of $k' \equiv k'_z = (k'^2_x + k'^2_y)^{1/2}$. Under this approximation, all the perturbations are independent of the planar angle of propagation α ($= \tan^{-1}[k'_y/k'_x]$).

2.2.6 Generalized Toomre Criterion

We derive a generalized Toomre criterion in terms of a generalized rotation parameter ($Q_{\rm eff}$) that includes a magnetic dependence (see Section 2.6.5). In the limit of flux-freezing, the expression is

$$Q_{\rm eff} = \Omega\frac{\left(C^2_{\rm eff,0} + V^2_{A,0}\right)^{1/2}}{\pi G\sigma_{n,0}\left(1-\mu_0^{-2}\right)} = Q\frac{\left(\tilde{C}^2_{\rm eff,0} + \tilde{Z}_0\,\mu_0^{-2}\right)^{1/2}}{\left(1-\mu_0^{-2}\right)} \tag{2.76}$$

(see Lizano et al. (2010) for a similar expression). The above equation shows that $Q_{\rm eff}$ has a direct dependence on the mass-to-flux-ratio (μ_0) as well as on the isothermal magnetosonic speed $\left(C^2_{\rm eff,0} + V^2_{A,0}\right)^{1/2}$ (see Equation 2.58).

In the regime where the normalized mass-to-flux ratio approaches infinity, implying negli-

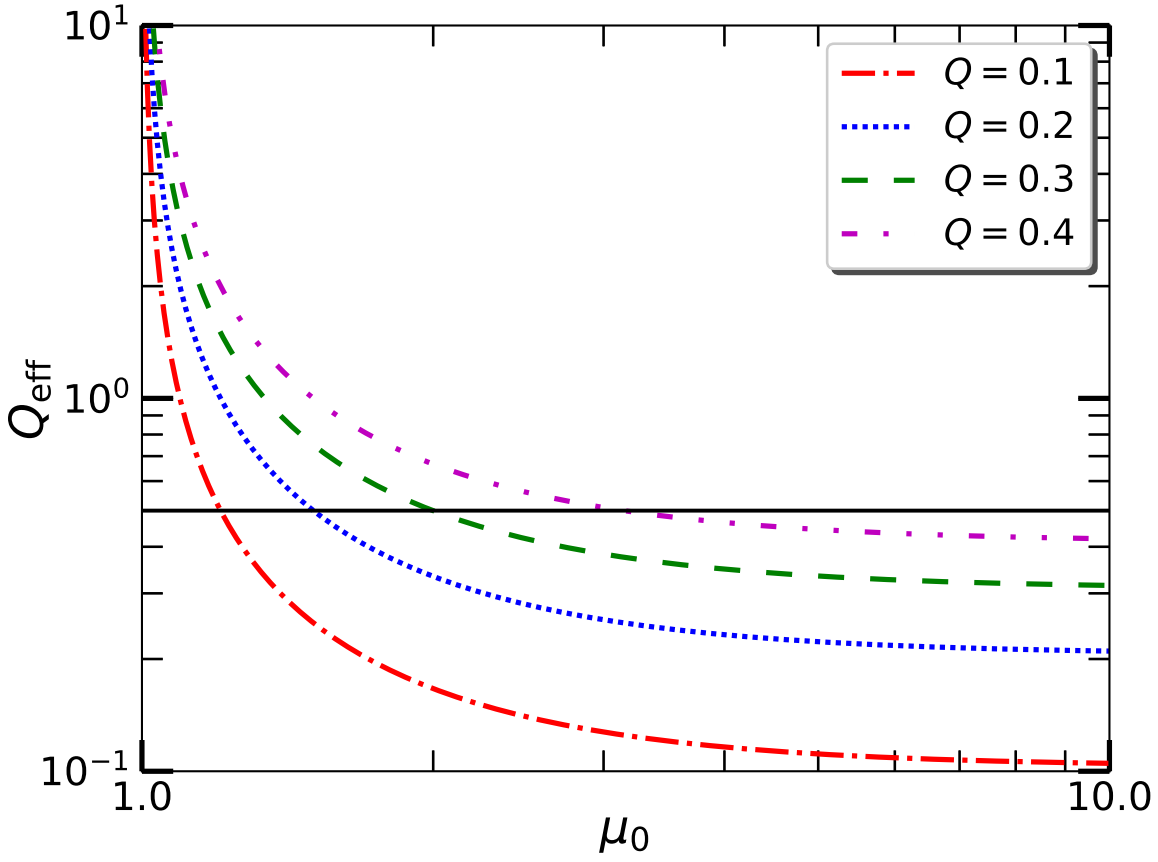

Figure 2.2: Normalized generalized rotation parameter ($Q_{\rm eff}$) as a function of μ_0 for different values of $Q = 0.1$ (red), 0.2 (blue), 0.3 (green), 0.4 (magenta) with flux-freezing. The black solid line represents the instability cutoff and occurs at $Q_{\rm eff} = 1/2$ under flux-freezing.

gible magnetic support, and for no external pressure (i.e., $C_{\rm eff,0} = c_s$) one can show that

$$Q_{\rm eff} \rightarrow \frac{c_s \Omega}{\pi G \sigma_{n,0}} = Q. \tag{2.77}$$

We evaluate the generalized Toomre instability criterion that yields

$$Q_{\rm eff} < \frac{1}{2}, \tag{2.78}$$

or, equivalently,

$$Q < Q_{\rm crit,m} = \frac{1}{2} \frac{\left(1 - \mu_0^{-2}\right)}{\left(\tilde{C}_{\rm eff,0}^2 + \tilde{Z}_0 \mu_0^{-2}\right)^{1/2}}. \tag{2.79}$$

See the derivation in Section 2.6.5.

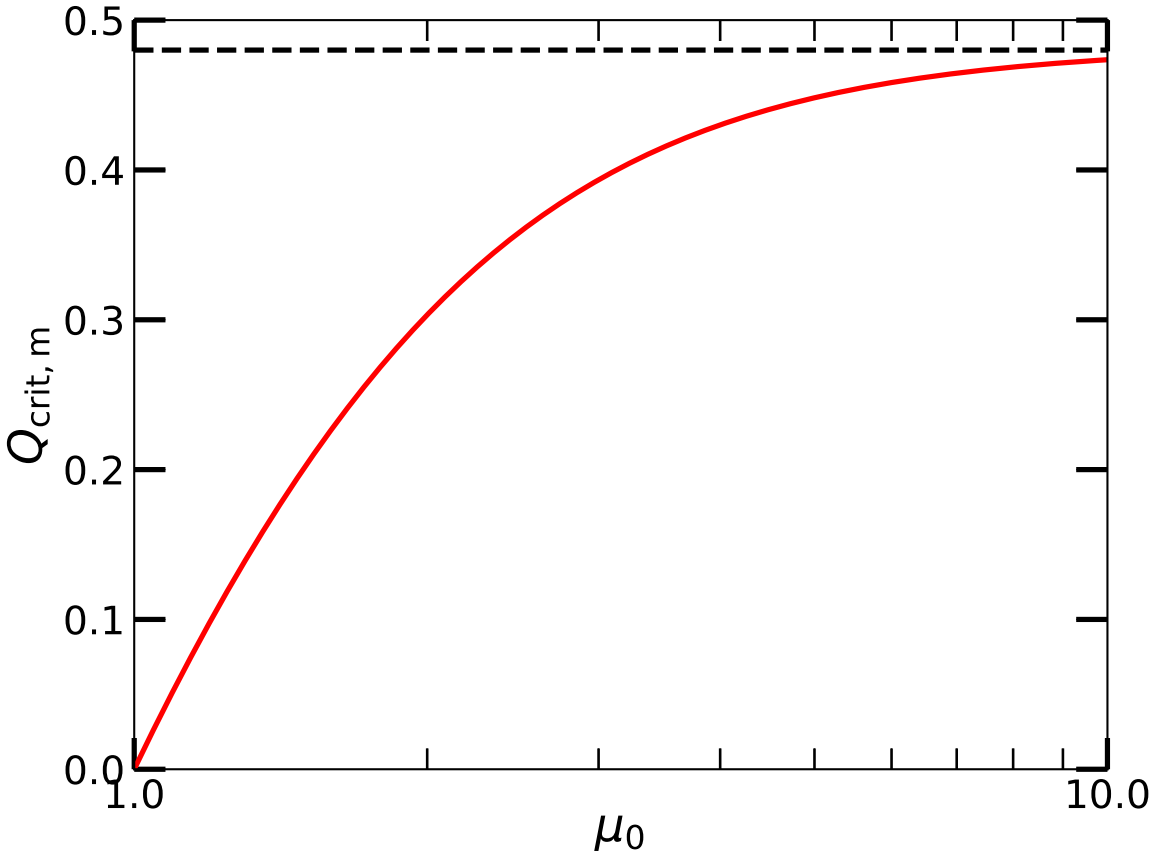

Figure 2.3: Modified critical rotation parameter $Q_{\rm crit,m}$ (that has a magnetic dependence) as a function of μ_0. The solid line shows the case for flux-freezing such that instability occurs for $Q < Q_{\rm crit,m}$. The dashed line shows critical value of instability in the hydrodynamic limit (i.e., $Q_{\rm crit,m} \to 1/(2\tilde{C}_{\rm eff})$; see Equation 2.79.

Figure 2.2 shows the normalized magnetic Toomre Q factor ($Q_{\rm eff}$) as a function of normalized mass-to-flux ratio (μ_0) in the flux-freezing limit for four different values $Q = 0.1, 0.2, 0.3, 0.4$. The solid line represents the cutoff value of $1/2$ that implies no unstable mode can occur for those values of μ_0 for which $Q_{\rm eff} \geq 1/2$, as long as flux-freezing prevails.

One can show (see Figure 2.3 and also Table 2.1) that in the hydrodynamic limit with no external pressure ($\tilde{C}_{\rm eff,0} = 1$), $Q_{\rm crit,m}$ reduces to the critical Toomre instability limit. Figure 2.3 presents the magnetic critical limit of Q (i.e., $Q_{\rm crit,m}$) obtained under the limit of flux-freezing as a function of μ_0. The dotted line represents the critical boundary in the hydrodynamic limit for a nonzero $\tilde{P}_{\rm ext}$, which is $1/(2\tilde{C}_{\rm eff})$ (see Equation 2.79). We also show that the magnetic dependent critical bound ($Q_{\rm crit,m}$) goes back to the hydrodynamic value in the regime $\mu_0 \gg 1$.

This above criteria can easily be acquired from the following dispersion relation

$$\begin{aligned} \omega^2 &= C_{\rm eff,0}^2 k^2 - 2\pi G\sigma_{n,0} k + 4\Omega^2, \\ \text{or,}\quad \omega'^2 &= k'^2 - k' + Q^2, \end{aligned} \tag{2.80}$$

which is same as the dispersion relation (Equation 2.48 or Equation 2.66) for an isothermal planar sheet in the hydrodynamic limit.

We discuss the effect of rotation on the lower and upper limits of the unstable range of wavelengths. From the dispersion relation under flux-freezing (Equation 2.66), setting $\omega'^2 = 0$ we obtain

$$k'_{\pm,\rm Q} = k'_{\rm MS,m}\left[1 \pm \sqrt{1 - 4Q_{\rm eff}^2}\right], \tag{2.81}$$

where

$$k'_{\rm MS,m} = \frac{2\pi}{\lambda'_{\rm MS,m}} = \frac{(1-\mu_0^{-2})}{2(\tilde{C}_{\rm eff,0}^2 + \tilde{V}_{A,0}^2)}\,, \tag{2.82}$$

see Section 2.2.5 for a detailed discussion on $\lambda'_{\rm MS,m}$. Here, $'+'$ and $'-'$ signs belong to the minimum (maximum, i.e., $\lambda'_{\rm Q,max}$) and maximum (minimum, i.e., $\lambda'_{\rm Q,min}$) wavenumbers (wavelengths) for rotationally modulated instability, respectively. Under the approximation $4Q_{\rm eff}^2 \ll 1$, $\lambda'_{\rm Q,min}$ and $\lambda'_{\rm Q,max}$ can be obtained from the above relation. It follows that

$$\lambda'_{\rm Q,min} = \frac{2\pi}{\left(1 - Q_{\rm eff}^2\right)} \frac{\left(\tilde{C}_{\rm eff,0}^2 + \tilde{Z}_0\mu_0^{-2}\right)}{\left(1-\mu_0^{-2}\right)} = \frac{\lambda'_{\rm MS}}{\left(1 - Q_{\rm eff}^2\right)}\,, \tag{2.83}$$

$$\lambda'_{\rm Q,max} = \frac{2\pi}{Q_{\rm eff}^2} \frac{\left(\tilde{C}_{\rm eff,0}^2 + \tilde{Z}_0\mu_0^{-2}\right)}{\left(1-\mu_0^{-2}\right)} = \frac{\lambda'_{\rm MS}}{Q_{\rm eff}^2}\,. \tag{2.84}$$

We see that the lower and upper limits of unstable wavelengths gradually increase and decrease for higher rotation, as seen from Figure 2.4(a) and (b), respectively. This suggests that rotation stabilizes not only the longer wavelengths but also the smaller wavelengths. Hence, when adding rotation, the total range of unstable length scales is reduced.

In the hydrodynamic limit ($\tilde{B}_{\rm ref} \to 0\,;\, \mu_0 \to \infty$), Equation 2.81 reduces to

$$k'_{\pm,\rm Q} = \frac{1}{2\tilde{C}_{\rm eff,0}^2}\left[1 \pm \sqrt{1 - 4Q^2\tilde{C}_{\rm eff,0}^2}\,\right]. \tag{2.85}$$

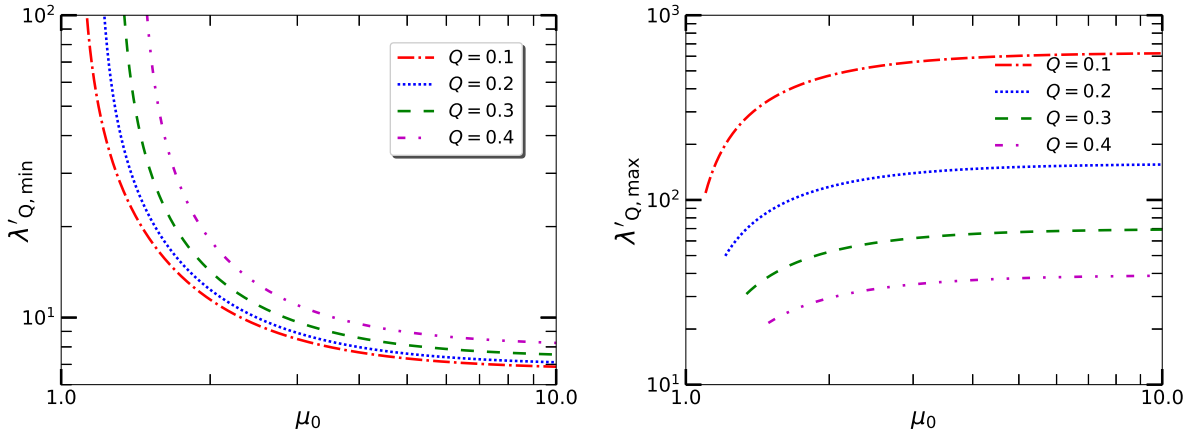

(a) (b)

Figure 2.4: Normalized maximum and minimum wavelength for rotationally modulated instability as a function of μ_0. (a) is for minimum wavelength, $\lambda'_{Q,min}$ (see Equation 2.83) and (b) is for maximum wavelength, $\lambda'_{Q,max}$ (see Equation 2.84).

Similarly, under the approximation $4Q^2\tilde{C}^2_{eff,0} \ll 1$ in the hydrodynamic limit, we find

$$\lambda'_{Q,min} = \frac{2\pi}{\left(1 - Q^2\tilde{C}^2_{eff,0}\right)}\tilde{C}^2_{eff,0}, \tag{2.86}$$

$$\lambda'_{Q,max} = \frac{2\pi}{Q^2}, \tag{2.87}$$

which are similar to Equation 2.83 and Equation 2.84 for $\mu_0 \to \infty$. In the limit $\tilde{P}_{ext} \to 0$, Equation 2.85 becomes

$$k'_{\pm,Q} = \frac{1}{2}\left[1 \pm \sqrt{1 - 4Q^2}\right], \tag{2.88}$$

which can be directly obtained from Equation 2.80. Now, under the approximation $4Q^2 \ll 1$, we get

$$\lambda'_{Q,min} = \frac{2\pi}{1 - Q^2}, \tag{2.89}$$

$$\lambda'_{Q,max} = \frac{2\pi}{Q^2}, \tag{2.90}$$

which are counterparts to Equation 2.86 and Equation 2.87 in the limit $\tilde{P}_{ext} \to 0$ (i.e., $\tilde{C}_{eff,0} = 1$).

2.2.7 Stationary Magnetic Field Limit

In the limit of stationary magnetic field, $\omega\delta B'_{z,\mathrm{eq}} \to 0$, we discuss the respective cases of Ohmic dissipation (OD) and ambipolar diffusion (AD). Under the stationary magnetic field limit, we obtain the normalized dispersion relation for the case of only OD ($\tilde{\tau}_{ni,0} = 0,\ Q = 0$) is

$$\omega'^2 + \omega' \frac{i}{\tilde{\eta}_{\mathrm{OD},0}} \frac{\left(1 + \tilde{Z}_0 k'\right)}{k'\mu_0^2} - \left(\tilde{C}^2_{\mathrm{eff},0} k'^2 - k'\right) = 0 \ , \tag{2.91}$$

which yields a growth timescale of OD

$$\tau'_{g,\mathrm{OD}} = \frac{2\tilde{\eta}_{\mathrm{OD},0}\lambda'}{\left[\left(\frac{\lambda'\left(\lambda'+2\pi\tilde{Z}_0\right)}{2\pi\mu_0^2}\right)^2 + 8\pi\tilde{\eta}^2_{\mathrm{OD},0}\left(\lambda' - \lambda'_{\mathrm{T}}\right)\right]^{\frac{1}{2}} - \left(\frac{\lambda'\left(\lambda'+2\pi\tilde{Z}_0\right)}{2\pi\mu_0^2}\right)} \ . \tag{2.92}$$

See Section 2.6.6 for a derivation of Equation 2.91. Minimizing $\tau'_{g,\mathrm{OD}}$ of Equation 2.92 with respect to λ' yields

$$\lambda'_{\mathrm{preferred,OD}} = \lambda'_{\mathrm{T}}. \tag{2.93}$$

Furthermore, one obtains

$$\tau'_{g,\mathrm{OD}} \to \infty \quad \text{at } \lambda'_{\mathrm{preferred,OD}} = \lambda'_{\mathrm{T}}, \tag{2.94}$$

and this feature is illustrated later in Figure 2.8(a) and (b). The remnant thermal pressure makes the timescale of the contraction driven by OD to be infinitely long in the regime $\mu_0 \ll 1$.

Under a similar approximation in the regime of only AD ($\tilde{\eta}_{\mathrm{OD},0} = 0,\ Q = 0$), the resulting normalized dispersion relation is

$$\omega'^2 + \omega' \frac{i}{\tilde{\tau}_{ni,0}} - \left(\tilde{C}^2_{\mathrm{eff},0} k'^2 - k'\right) = 0, \tag{2.95}$$

(see also Ciolek & Basu, 2006). From the above relation of AD, one finds that an unstable mode exists for $\lambda' > \lambda'_{\mathrm{T}}$, and has a growth timescale of AD

$$\tau'_{g,\mathrm{AD}} = \frac{2\tilde{\tau}_{ni,0}\lambda'}{\left[\lambda'^2 + 8\pi\tilde{\tau}^2_{ni,0}(\lambda' - \lambda'_{\mathrm{T}})\right]^{\frac{1}{2}} - \lambda'} \ . \tag{2.96}$$

See Section 2.6.6 for a derivation of Equation 2.95. We further carried out the following cal-

culation by minimizing $\tau'_{g,\mathrm{AD}}$ from Equation 2.96 with respect to λ' which yields

$$\lambda'_{\mathrm{preferred,AD}} = 2\lambda'_{\mathrm{T}} \, . \tag{2.97}$$

Furthermore, we obtain

$$\tau'_{g,\mathrm{AD}} = \frac{4\tilde{\tau}_{ni,0}\lambda'_{\mathrm{T}}}{\left[4\lambda'^{2}_{\mathrm{T}} + 8\pi\tilde{\tau}^{2}_{ni,0}\lambda'_{\mathrm{T}}\right]^{\frac{1}{2}} - 2\lambda'_{\mathrm{T}}} \quad \text{at} \;\; \lambda'_{\mathrm{preferred,AD}} = 2\lambda'_{\mathrm{T}}, \tag{2.98}$$

and this value is independent of μ_0, which is illustrated later in Figure 2.8(c) and (d).

In the asymptotic limit ($\lambda' \gg \lambda'_{\mathrm{T}}$) from Equation 2.92 and Equation 2.96 we deduce

$$\tau'_{g,\mathrm{OD}} = \frac{2\tilde{\eta}_{\mathrm{OD},0}}{\frac{(\lambda'+2\pi\tilde{Z}_0)}{2\pi\mu_0^2}\left[\left\{1 + \frac{8\pi\tilde{\eta}^{2}_{\mathrm{OD},0}(\lambda'-\lambda'_{\mathrm{T}})}{\left(\frac{\lambda'(\lambda'+2\pi\tilde{Z}_0)}{2\pi\mu_0^2}\right)^{2}}\right\}^{\frac{1}{2}} - 1\right]} \rightarrow \frac{\lambda'^{2}}{4\pi^2\mu_0^2\tilde{\eta}_{\mathrm{OD},0}}, \tag{2.99}$$

$$\tau'_{g,\mathrm{AD}} = \frac{2\tilde{\tau}_{ni,0}}{\left[\left\{1 + \frac{8\pi\tilde{\tau}^{2}_{ni,0}(\lambda'-\lambda'_{\mathrm{T}})}{\lambda'^{2}}\right\}^{\frac{1}{2}} - 1\right]} \rightarrow \frac{\lambda'}{2\pi\tilde{\tau}_{ni,0}}, \tag{2.100}$$

respectively, (using $(1+x)^{1/2} \approx 1 + x/2$ for $x \ll 1$). This behavior of the growth timescales is seen in Figure 2.6 for very large length scales and $\mu_0 < 1$. In this figure we see the slope of the curves for OD are steeper than the case for AD. Also we see that as $\tilde{\eta}_{\mathrm{OD},0} \rightarrow \infty$, $\tau'_{g,\mathrm{OD}} \rightarrow \lambda' / \left[2\pi\left(\lambda' - \lambda'_{\mathrm{T}}\right)\right]^{1/2}$, and when $\tilde{\tau}_{ni,0} \rightarrow \infty$, $\tau'_{g,\mathrm{AD}} \rightarrow \lambda' / \left[2\pi\left(\lambda' - \lambda'_{\mathrm{T}}\right)\right]^{1/2}$. This is identical to Equation 2.72 when $\mu_0 \rightarrow \infty$, i.e., when $\tilde{B}_{\mathrm{ref}} \rightarrow 0$ and $Q = 0$. In the regime $\mu_0 \ll 1$, the minimum growth time for OD and AD occur at the preferred wavelength λ'_{T} and $2\lambda'_{\mathrm{T}}$, respectively as defined above. The limit $\tilde{\eta}_{\mathrm{OD},0} \rightarrow \infty$ corresponds to an extremely high rate of collisions encountered by the charged particles such that they become decoupled from the magnetic field. On the other hand, $\tilde{\tau}_{ni,0} \rightarrow \infty$ corresponds to the case when there is no collisional coupling between the neutrals and the ions (and hence with the magnetic field). The ions are completely "invisible" to the neutrals in this situation, and there is no transmission of magnetic force to neutrals via neutral-ion collisions.

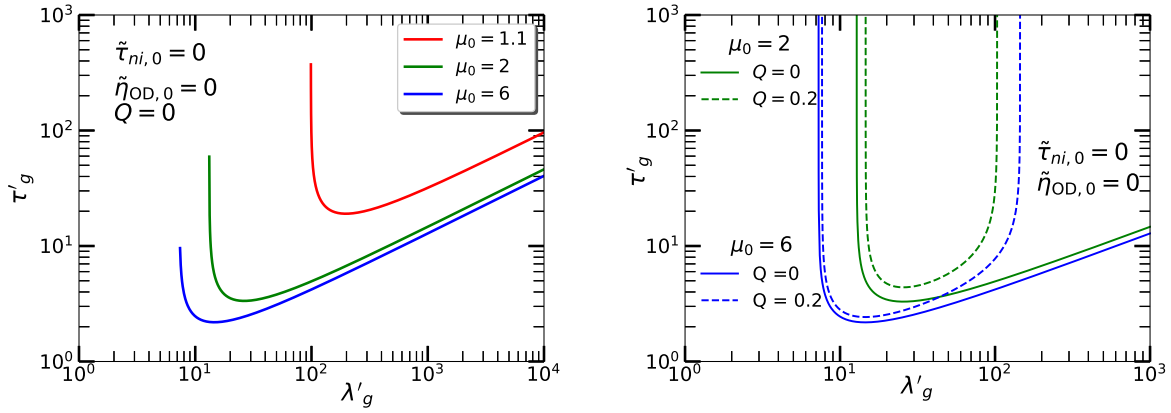

(a) (b)

Figure 2.5: Normalized growth time of the gravitationally unstable mode ($\tau'_g = \tau_g/t_0$) as a function of normalized wavelength ($\lambda'_g = \lambda_g/L_0$) for flux-frozen models ($\tilde{\eta}_{OD,0} = 0$, $\tilde{\tau}_{ni,0} = 0$) with different values of the normalized mass-to-flux-ratio. The left panel (a) shows the case with $Q = 0$ for fixed $\mu_0 = 1.1$ (red), 2 (green), and 6 (blue). The right panel (b) shows the cases with $Q = 0$ and $Q = 0.2$ for $\mu_0 = 2$ (green) and 6 (blue).

2.3 Numerical Results

In subsequent sections we generate figures based on solutions of the normalized dispersion relation as described in (Section 2.2.5). Henceforth the normalized wavelength λ' is attributed as λ'_g which means $2\pi/k'_g$; "g" corresponds to the "growth mode".

2.3.1 Flux-frozen Model

Figure 2.5 shows the instability growth time τ'_g ($= \tau_g/t_0$) as a function of the wavelength λ'_g ($= \lambda_g/L_0$) for flux-frozen cases. Figure 2.5(a) shows the case without rotation (as obtained by Ciolek & Basu (2006)), whereas Figure 2.5(b) shows the growth time for supercritical clouds with $\mu_0 = 2$ and 6, including rotation (in terms of the Q parameter) as obtained from our model (see Equation 2.66). Here, $Q = 0$ lines serve as a reference point. In the limit of large length scale, τ_g varies as $\lambda_g^{'1/2}$, which can be seen from Equation 2.75. We notice that adding a small rotation ($Q = 0.2$) causes the gravitational collapse timescale to be comparatively longer than the case without rotation. Instability occurs for those length scales that are not stabilized by the thermal, magnetic, and rotational support. We see that rotation plays a significant role to stabilize the longer wavelengths. Furthermore, along with thermal pressure, rotation also helps to stabilize the smaller length scales, as discussed earlier in Section 2.2.6 (see also Figure 2.4).

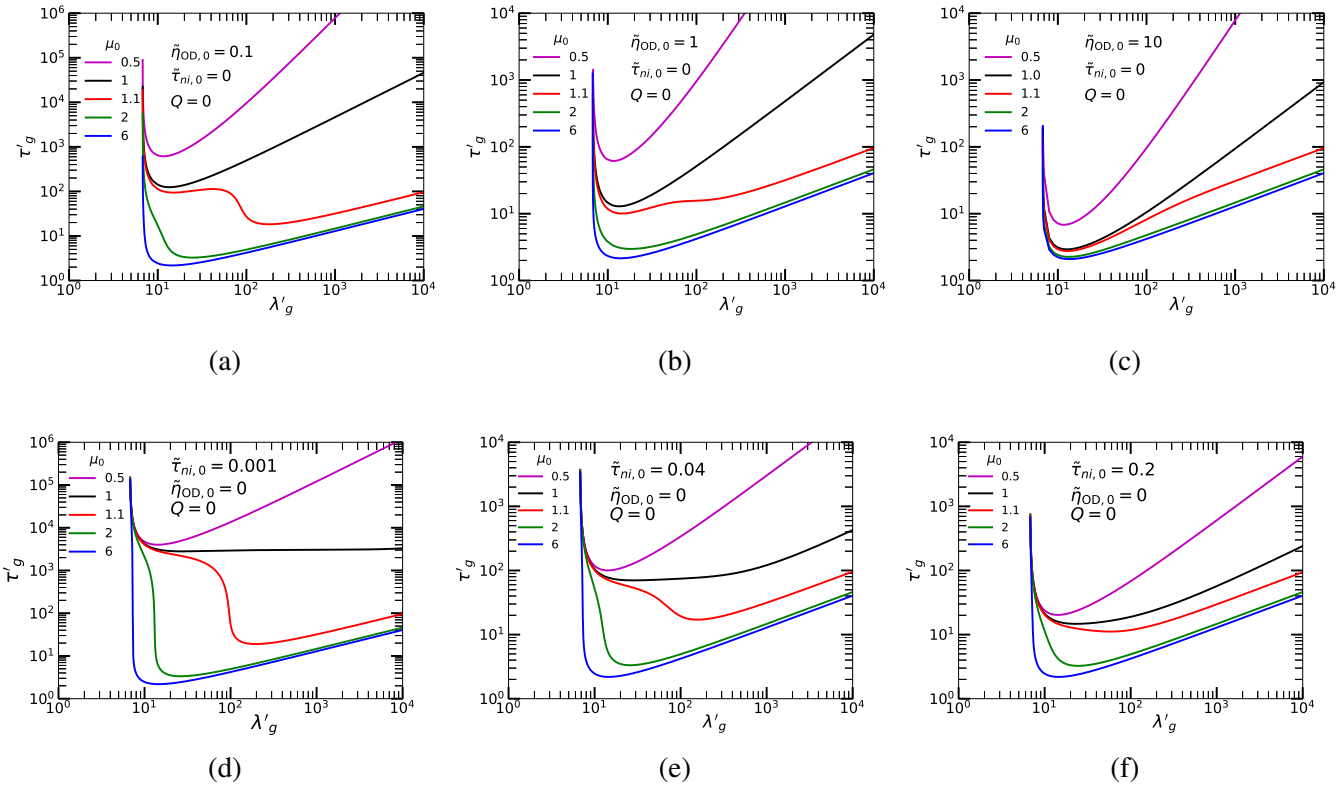

Figure 2.6: Normalized growth time of the gravitationally unstable mode ($\tau'_g = \tau_g/t_0$) as a function of normalized wavelength ($\lambda'_g = \lambda_g/L_0$). Each panel shows a model with a fixed μ_0 = 0.5 (magenta), 1 (black), 1.1 (red), 2 (green), 6 (blue). Figures in the upper panel (a),(b),(c) show the cases for normalized Ohmic diffusivity $\tilde{\eta}_{\rm OD,0}$ = 0.1, 1, and 10, respectively. Figures in the lower panel (d),(e),(f) show the cases for neutral-ion collision time $\tilde{\tau}_{ni,0}$ = 0.001, 0.04, and 0.2, respectively.

Hence, the range (or span) of unstable wavelengths has been reduced from both the left hand side (shorter end of the length scales) and the right hand side (longer side of the length scales). Later, in Section 2.3.5, we discuss the effect of the magnetic field in creating a modified value of the critical rotation parameter.

2.3.2 Theoretical Models with Nonideal MHD

We evaluate the growth timescale and length scale of gravitational instability with nonideal MHD effects. The larger the Ohmic diffusivity ($\tilde{\eta}_{\rm OD,0}$) and/or the neutral-ion collision time ($\tilde{\tau}_{ni,0}$), the greater are the effects of Ohmic dissipation (OD) and ambipolar diffusion (AD), respectively.

Figure 2.6 presents the instability growth time τ'_g (= τ_g/t_0) as a function of the wave-

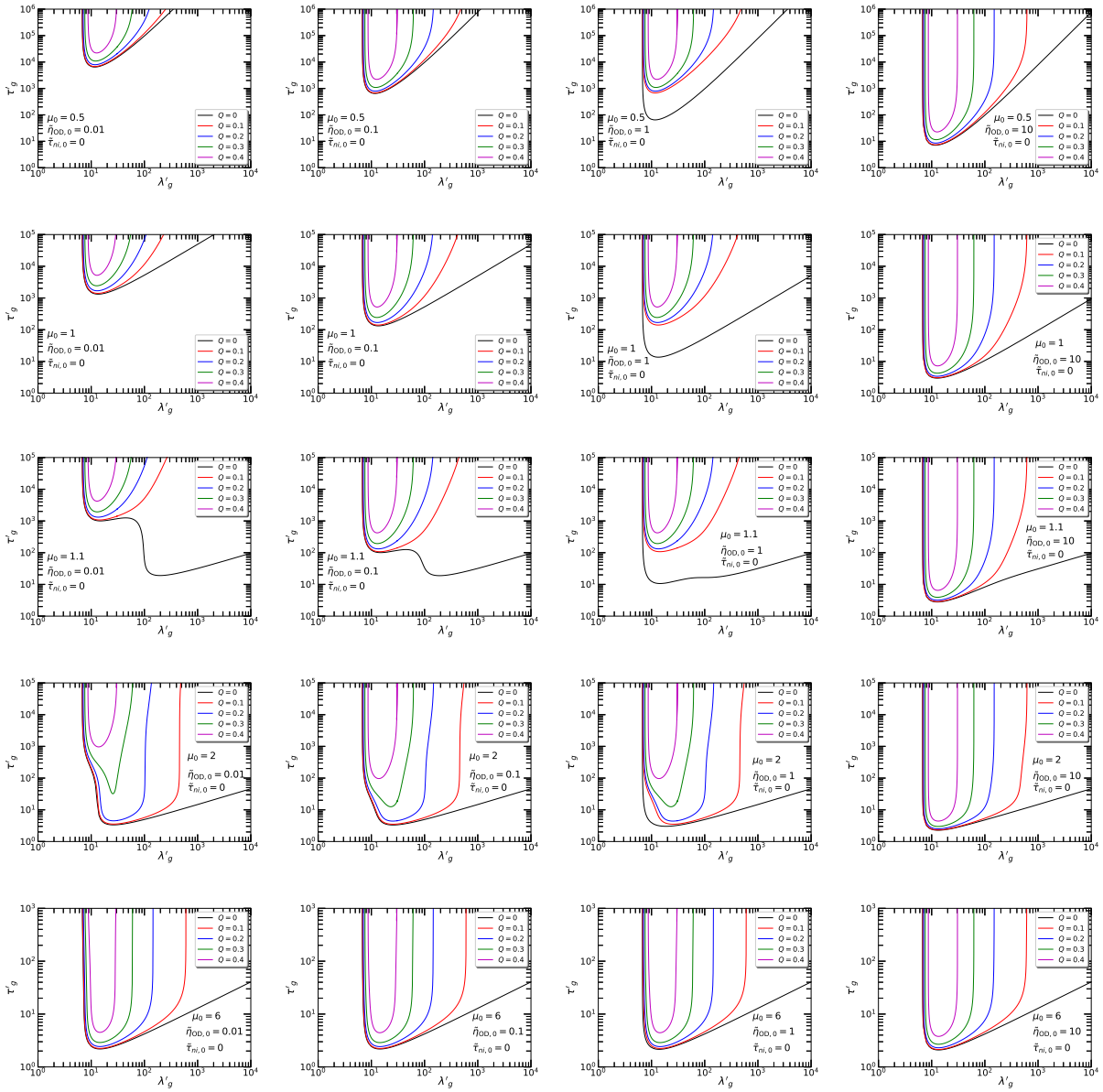

Figure 2.7: Normalized growth time $\tau'_g = \tau_g/t_0$ of gravitationally unstable mode as a function of the normalized wavelength $\lambda'_g = \lambda_g/L_0$. Left to right: For models with different normalized Ohmic diffusivities $\tilde{\eta}_{\rm OD,0} = 0.01$ (1st column), 0.1 (2nd column), 1 (3rd column), 10 (4th column). Top to bottom: For models with different normalized mass-to-flux-ratio $\mu_0 = 0.5$ [1st row: a, b, c, d], $\mu_0 = 1$ [2nd row: e, f, g, h], $\mu_0 = 1.1$ [3rd row: i, j, k, l], $\mu_0 = 2$ [4th row: m, n, o, p], $\mu_0 = 6$ [5th row: q, r, s, t]. Each figure shows timescale curves for models with different normalized rotation $Q = 0$ (black), 0.1 (red), 0.2 (blue), 0.3 (green), and 0.4 (magenta).

length λ'_g ($= \lambda_g/L_0$) for different cases of OD and AD (see also Ciolek & Basu (2006) for AD). Here, the three different cases in the upper panel represent various Ohmic diffusivities: $\tilde{\eta}_{\rm OD,0} = 0.1, 1, 10$. The lower panel represents various areas within a molecular cloud: diffuse

regions with high ionization fractions ($\tilde{\tau}_{ni,0} = 0.001$), dense core forming regions with low ionization fractions ($\tilde{\tau}_{ni,0} = 0.2$) and an intermediate region ($\tilde{\tau}_{ni,0} = 0.04$). Each panel shows the dependence for several labeled values of μ_0 ($= 1/\tilde{B}_{\rm ref}$). Here, $\mu_0 = 0.5$ is a subcritical cloud, $\mu_0 = 1$ is a transcritical cloud, $\mu_0 = 1.1$ is slightly supercritical, $\mu_0 = 2$ is somewhat supercritical, and $\mu_0 = 6$ is highly supercritical. We see that the growth time decreases with greater $\tilde{\eta}_{\rm OD,0}$ and $\tilde{\tau}_{ni,0}$. In the limit of very large length scale, the normalized timescale (τ'_g) for OD and AD asymptotically varies as λ'^2_g and λ'_g, respectively for $\mu_0 < 1$, as derived from Equation 2.99 and Equation 2.100. Whereas, for the supercritical region, τ'_g asymptotically varies as $\lambda'^{1/2}_g$, as derived in Equation 2.75. Hence for this case, the minima of τ'_g vs λ'_g curves look shallower as compared to the subcritical cases. The diffusive-driven instabilities for the subcritical clouds have a sharper minimum (peak) in the growth time.

Figure 2.7 shows the instability growth timescale and length scale with OD as the only nonideal MHD effect. The first, second, third, and fourth column (from left to right) show the cases for $\tilde{\eta}_{\rm OD,0} = 0.01$, $\tilde{\eta}_{\rm OD,0} = 0.1$, $\tilde{\eta}_{\rm OD,0} = 1$, and $\tilde{\eta}_{\rm OD,0} = 10$, respectively. Each column shows five different normalized mass-to-flux-ratios ($\mu_0 = 0.5, 1, 1.1, 2, 6$) and each panel shows five different rotation levels ($Q = 0, 0.1, 0.2, 0.3, 0.4$). For the subcritical case ($\mu_0 = 0.5$, note first row), as the Ohmic diffusivity ($\tilde{\eta}_{\rm OD,0}$) increases by each factor of 10, the instability growth time significantly gets reduced. Since the magnetic flux is being dissipated at a faster rate, it shortens the growth timescale. Changing $\tilde{\eta}_{\rm OD,0}$ from 0.01 to 10, the timescale gets smaller by a factor of 10^3. Also, for the transcritical ($\mu_0 = 1$, note second row) and slightly transcritical ($\mu_0 = 1.1$, note third row) clouds, the growth timescale is lowered down by a similar magnitude when moving from $\tilde{\eta}_{\rm OD,0} = 0.01$ to 10. For the mildly supercritical case ($\mu_0 = 2$, note fourth row), a gradual reduction in the growth timescale is more prominent for the modes with higher rotation. This signifies that in the regime of OD, gravitational collapse is likely to be faster even with the higher rotation speed. Lastly, for the highly supercritical case ($\mu_0 = 6$, note fifth row), since the inward gravitational pull is extremely dominant over the magnetic field and rotation, there is not much appreciable change in the growth modes with the variation of $\tilde{\eta}_{\rm OD,0}$.

Earlier, for the flux-frozen case, we mentioned that there is no unstable, gravitationally collapsing mode for $\mu_0 < 1$, implying that only initially supercritical clouds can collapse. However, the addition of AD and OD (see Figure 2.6 and Figure 2.7) allows for unstable,

gravitationally collapsing modes to exist for both subcritical ($\mu_0 < 1$) and supercritical ($\mu_0 > 1$) regimes. See also Section 2.6.7 for the combined effects of OD and AD. For all these plots and for each case of μ_0 shown, we notice that each curve has a distinct minimum. This minimum represents the shortest growth time (fastest growth rate) and a corresponding preferred length scale for gravitational instability.

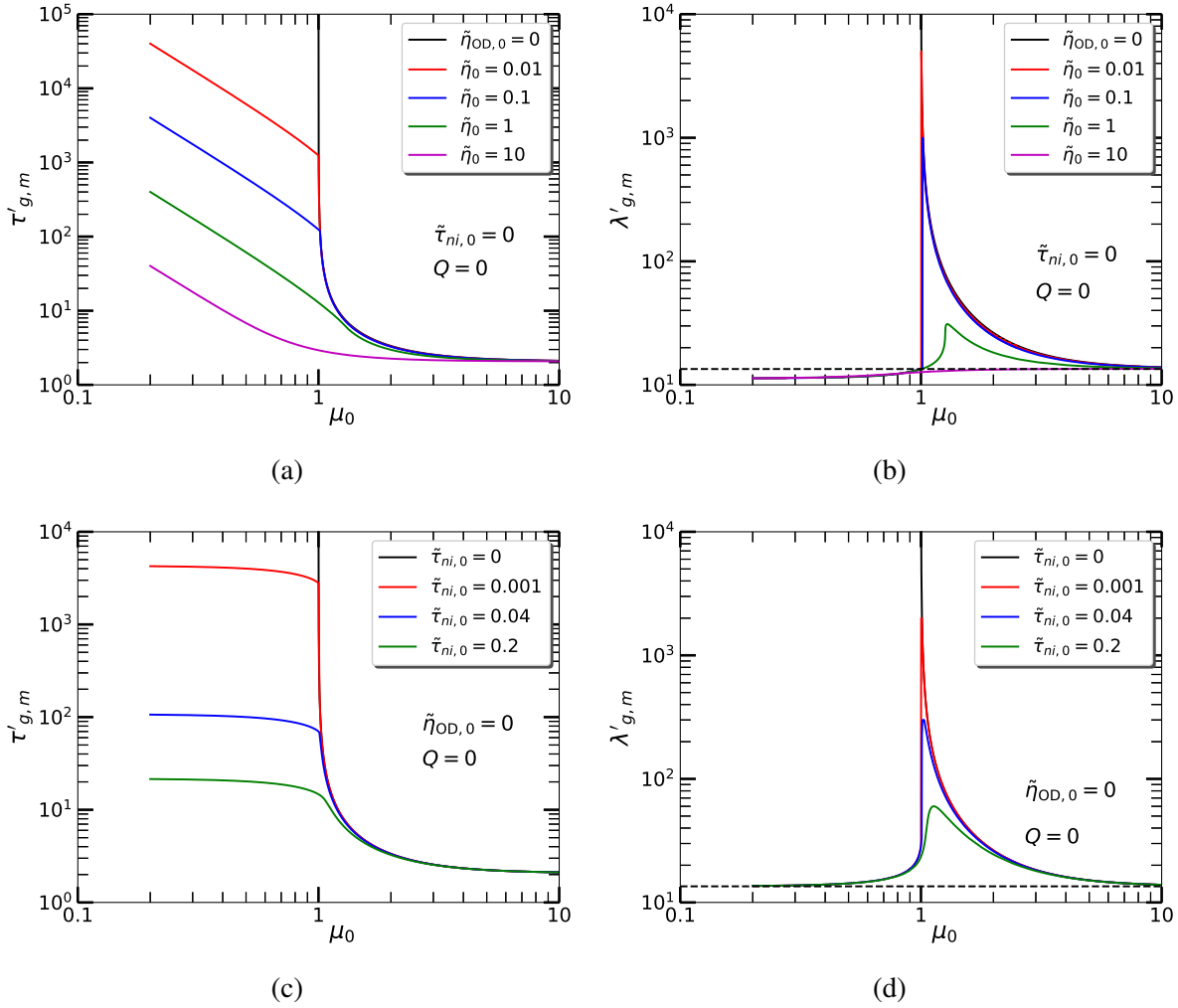

Figure 2.8: Normalized shortest growth timescale $\tau'_{g,m} = \tau_{g,m}/t_0$ and preferred length scale $\lambda'_{g,m} = \lambda_{g,m}/L_0$ of the gravitationally unstable mode as a function of the normalized mass-to-flux ratio μ_0. Upper panel (a and b) shows the case of Ohmic dissipation for models with normalized Ohmic diffusivities $\tilde{\eta}_{OD,0} = 0$ (black), 0.01 (red), 0.1 (blue), 1 (green), and 10 (magenta). Lower panel (c and d) shows the case of ambipolar diffusion for models with normalized neutral-ion collision time $\tilde{\tau}_{ni,0} = 0$ (black), 0.001 (red), 0.04 (blue), 0.2 (green). The black dashed line in (b) and (d) denotes the value $2\lambda'_T$; λ'_T is the normalized thermal length scale.

Figure 2.8 shows the normalized minimum growth time of the gravitationally unstable

mode $\tau'_{g,m}$ ($= \tau_{g,m}/t_0$) and length scale $\lambda'_{g,m}$ ($= \lambda_{g,m}/L_0$) corresponding to this most unstable mode (which we call the preferred length scale) as a function of μ_0. The upper panel of Figure 2.8 shows the case with only OD as obtained from our model. On the other hand, the lower panel of Figure 2.8 shows the same for different amounts of AD, as calculated previously by Ciolek & Basu (2006) and Bailey & Basu (2012). For both nonideal MHD effects, we observe qualitatively similar length scale curves, and timescale curves that are qualitatively similar in the supercritical regime but differ in the subcritical regime.

In the limit of flux-freezing ($\tilde{\eta}_{\rm OD,0} = 0$, $\tilde{\tau}_{ni,0} = 0$), for the supercritical regime ($\mu_0 > 1$), each of the flux-freezing curves in Figure 2.8 shows that the growth time and length scale for instability are short; essentially the timescale and length scale follow the dynamical timescale ($t_{\rm d} = Z_0/c_s$) and preferred thermal length scale ($\lambda_{{\rm T},m}$). Even with nonideal MHD terms included, the growth times are similar in the supercritical regime, since these modes are dominated by gravity. As the normalized mass-to-flux ratio approaches the transcritical value ($\mu_0 = 1$) the growth timescale/length scale for instability becomes infinitely long, since in the flux-frozen case only supercritical clouds can collapse. With the addition of either nonideal MHD effect (OD or AD), the growth timescale in the subcritical regime becomes finite.

In the OD-only regime, Figure 2.8(a) shows that an increasing $\tilde{\eta}_{\rm OD,0}$, which increases the rate of magnetic flux dissipation, makes the growth time tend toward that of thermal collapse $\tau'_{g,T,m}$ ($= \tau_{g,T,m}/t_0$). For $\mu_0 \ll 1$, the preferred length scale attains the thermal length scale as shown in Equation 2.93, hence the corresponding minimum growth timescale goes to infinity as derived in Equation 2.94.

Similarly, in the AD-only case, for a relatively large $\tilde{\tau}_{ni,0} > 0.2$, the growth timescale of the subcritical regime is decreasing toward that of thermal collapse. However, for each value of $\tilde{\tau}_{ni,0}$, it has a plateau for all values of $\mu_0 \ll 1$. This is a distinguishing characteristic of AD in comparison to OD. As seen in Equation 2.39 and Equation 2.56, the ambipolar diffusivity is proportional to the square of the background magnetic field strength, therefore proportional to μ_0^{-2}. Even as μ_0 decreases in the regime $\mu_0 \ll 1$, $\tilde{\eta}_{\rm AD,0}$ increases as μ_0^{-2} and enforces a fixed drift speed of ions and neutrals (see Section 2.6.8 for more details on the eigenfunctions) and thereby in the growth timescale. For a typical normalized neutral-ion collision time as observed in molecular clouds ($\tilde{\tau}_{ni,0} = 0.2$), the timescale for collapse of a subcritical region is ~ 10 times

longer than that of a supercritical region (see Figure 2.8(c)). This leads to the often quoted result that the ambipolar diffusion time is ~ 10 times the dynamical time. However, note that a transcritical region has a growth time that is intermediate to the two plateau values.

The preferred wavelengths for collapse ($\lambda'_{g,m} = \lambda_{g,m}/L_0$) exhibit an interesting dependence on μ_0 (see Figure 2.8(b) and (d)). For a nonzero Ohmic diffusivity or neutral-ion collision time, the wavelength with the minimum growth time remains close to the flux-freezing value for decidedly supercritical clouds, since these are gravity-dominated modes that collapse quickly with little time for significant magnetic diffusion. For transcritical but slightly supercritical clouds, there is a sharp rise in the preferred wavelength, similar to what happens in the flux-frozen case. However, the preferred wavelength does not diverge at $\mu_0 = 1$ as in the flux-frozen case. Instead, the magnetic diffusion caps the preferred wavelength at a finite, but potentially large value that depends on the level of diffusivity. In these hybrid transcritical modes, there is enough magnetic field dragging to create an hourglass shape with a strong curvature force that resists the collapse, so that larger perturbations with more mass can more easily overcome the magnetic support. For subcritical regions, where flux-freezing would allow no instability, modes of diffusion-driven contraction now appear. These modes have very little magnetic field enhancement in the perturbed region (see Section 2.6.8). Given the withdrawal of magnetic support by OD or AD, the preferred scale converges back toward the thermal length scale. The black dashed line in Figure 2.8(b) and (d) denotes the value $2\lambda'_{\rm T}$. Specifically, for OD it converges to $\lambda'_{\rm T}$, the critical thermal length scale, and for AD it converges to $2\lambda'_{\rm T}$ as would be found in the hydrodynamic case. These limits were shown in Equation 2.93 and Equation 2.97 and the difference can be attributed to the stronger wavenumber dependence of the OD term (see Section 2.6.3).

2.3.3 Results for a Protostellar Disk

In this section we focus on the region of parameter space that is most applicable to protostellar disks, i.e., models with significant nonzero values of $\tilde{\eta}_{\rm OD,0}$ and Q, and potentially $\tilde{\tau}_{ni,0}$ as well.

Figure 2.9 shows the shortest growth timescale of the gravitationally unstable mode and corresponding length scale as a function of the critical mass-to-flux ratio (μ_0) for a rotationally-supported protostellar disk in a regime with Ohmic dissipation (OD) only. We study the case

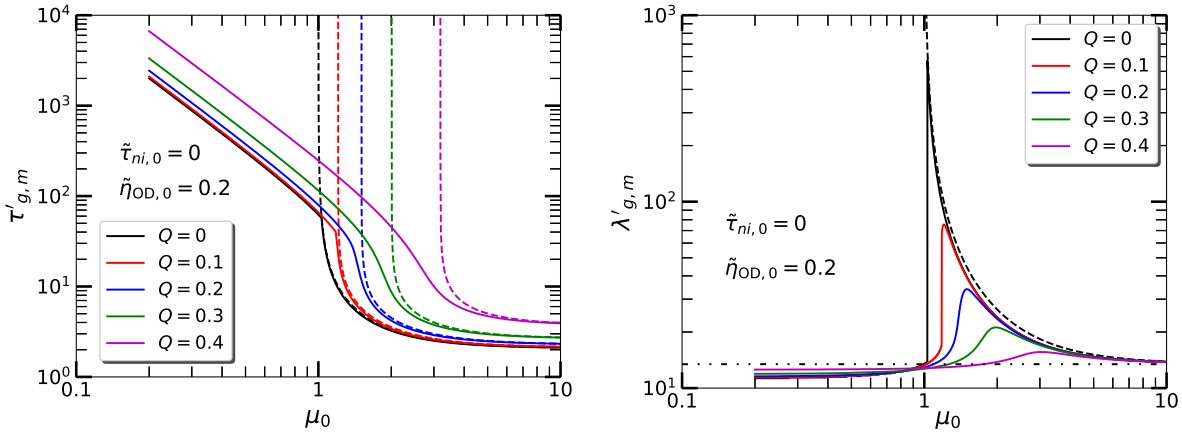

(a) (b)

Figure 2.9: Normalized shortest growth timescale ($\tau'_{g,m} = \tau_{g,m}/t_0$), preferred length scale ($\lambda'_{g,m} = \lambda_{g,m}/L_0$) of the most unstable mode as a function of normalized mass-to-flux ratio (μ_0). This represents a model with a fixed normalized Ohmic diffusivity $\tilde{\eta}_{OD,0} = 0.2$ and without ambipolar diffusion ($\tilde{\tau}_{ni,0} = 0$). Each panel shows preferred timescale and length curves for models with normalized rotation $Q = 0$ (black), 0.1 (red), 0.2 (blue), 0.3 (green), and 0.4 (magenta). The dashed lines in (a) show the corresponding timescale curves for different Q under the limit of flux-freezing. In (b), the dashed line shows the corresponding length scale curves for all Q under flux-freezing. In (b), the dash-dotted line shows the value $2\lambda'_T$.

of $\tilde{\eta}_{OD,0} = 0.2$ corresponding to neutral number density $n_{n,0} = 10^{11}$ cm^{-3}. In Figure 2.9(a), we see that the minimum growth timescale of the disk becomes longer with higher rotation. This indicates that rotation is providing more support together with the magnetic field and thermal pressure against the inward gravitational pull. Overall, the reasoning behind this kind of trend in the timescale and the length scale curves has been explained while discussing Figure 2.8. We find that adding rotation to the flux-freezing case yields different minimum growth timescale curves for each different rotation rate as shown by the dotted lines in Figure 2.9(a). In the highly supercritical regime, the growth timescale for each different rotation rate belongs to a different thermal collapse time for each different rotation. See Equation 2.70 and 2.72 for the calculation. The dynamical time obtained with a higher rotation is longer than that with smaller rotation.

Figure 2.9(b) shows that the preferred wavelength becomes smaller with higher rotation, since the rotation stabilizes the longer length scales. Note that as rotation increases, each respective peak preferred wavelength is gradually shifted to a larger μ_0. This is because for

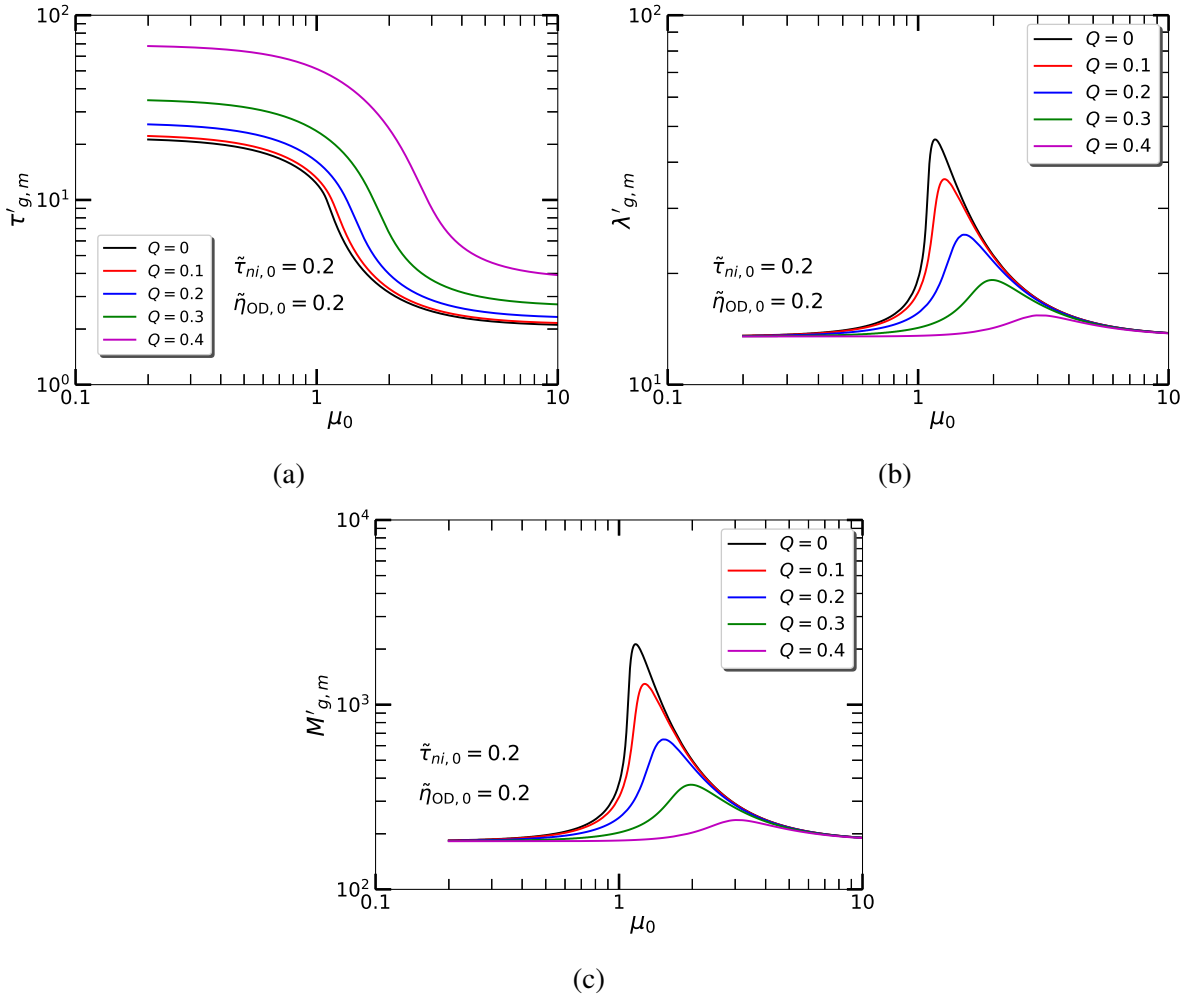

Figure 2.10: Normalized shortest growth timescale ($\tau'_{g,m} = \tau_{g,m}/t_0$), preferred length scale ($\lambda'_{g,m} = \lambda_{g,m}/L_0$) and preferred fragmentation mass ($M'_{g,m} = M_{g,m}/M_0$) of the most unstable mode as a function of normalized mass-to-flux ratio (μ_0). This model is shown for a fixed normalized Ohmic diffusivity ($\tilde{\eta}_{OD,0} = 0.2$) and normalized neutral-ion collision time ($\tilde{\tau}_{ni,0} = 0.2$) corresponding to $n_{n,0} = 10^{11}$ cm^{-3} and $T = 30$ K. Each panel shows instability curves for different normalized rotation $Q = 0$ (black), 0.1 (red), 0.2 (blue), 0.3 (green), and 0.4 (magenta).

an increased Q, the disk attains more support from rotation and becomes more stable against the self-gravitational collapse. The field lines are not dragged in as much, and the (restorative) effect of magnetic field curvature is maximized at progressively greater μ_0, where gravity is more dominant. This causes the peak of $\lambda'_{g,m}$ to move to greater values of μ_0, but have decreased value, as Q increases. Furthermore, we see that for higher rotation $\lambda'_{g,m}$ becomes larger than that for smaller rotation in the regime $\mu_0 < 1$, in contrast to its trend in the regime $\mu_0 \geq 1$. Since rotation helps to stabilize the smaller length scales, an increment in rotation pushes the

lower limit of unstable wavelengths to a larger value. So, the shortest growth time occurs at a relatively larger wavelength for a higher Q in the regime $\mu_0 < 1$. We find that adding rotation to the flux-freezing case yields the exactly same preferred length scale curve for each different rotation rate as shown by the black dotted line in Figure 2.9(b), which is the same as for the $Q = 0$ case. We found that the preferred wavelength is independent of Q for the flux-frozen case (see Equation 2.71 and 2.73). The black dash-dotted line in Figure 2.9(b) shows $2\lambda'_{\rm T}$, as discussed in Figure 2.8.

In Figure 2.10, we present a more realistic case of a rotationally-supported protostellar disk in the hybrid regime where OD and AD are both active. Figure 2.10(a) and 2.10(b) show the minimum growth time of the gravitationally unstable mode $\tau'_{g,m}$ and the corresponding length scale, $\lambda'_{g,m}$, respectively, as a function of μ_0. These are shown for the density $n_{n,0} = 10^{11}$ cm^{-3}, with specific values of normalized Ohmic diffusivity $\tilde{\eta}_{\rm OD,0} = 0.2$ and normalized neutral-ion collision time $\tilde{\tau}_{ni,0} = 0.2$, and adopting different rotational speeds. Interestingly, in such high density regions, the effects of AD are still present and cannot be neglected. Because of the AD, the minimum growth timescale curves get plateaued in the subcritical regime, which are indefinitely long for OD only, as seen in Figure 2.9(a). On the whole, the behavior of $\lambda'_{g,m}$, as shown in Figure 2.10(b), looks similar to the previously discussed length scale plots. The presence of these two nonideal MHD effects together reduces the preferred length scale by an order of 10 as compared to Figure 2.9(b) for the case of no rotation ($Q = 0$). In the subcritical regime, as the magnetic diffusion becomes strong in the presence of AD and OD together, the shortest growth times occur at the same preferred wavelength (that is similar to that of thermal collapse) regardless of the level of rotation.

Continuing with these parameters, Figure 2.10(c) shows the normalized preferred mass $M'_{g,m} = M_{g,m}/M_0$ corresponding to fastest growing mode as a function of normalized mass-to-flux ratio (μ_0) for different values of rotation. We see that the preferred mass for collapse exceeds the Jeans mass by a factor of up to 10 when including OD and/or AD. The influence of the magnetic field on the preferred mass of the most unstable mode can essentially lead to the concept of a modified threshold for the fragmentation mass, as opposed to the Jeans mass alone. This can allow a step forward to the understanding for the formation of clumps within a protostellar disk in the early embedded phase.

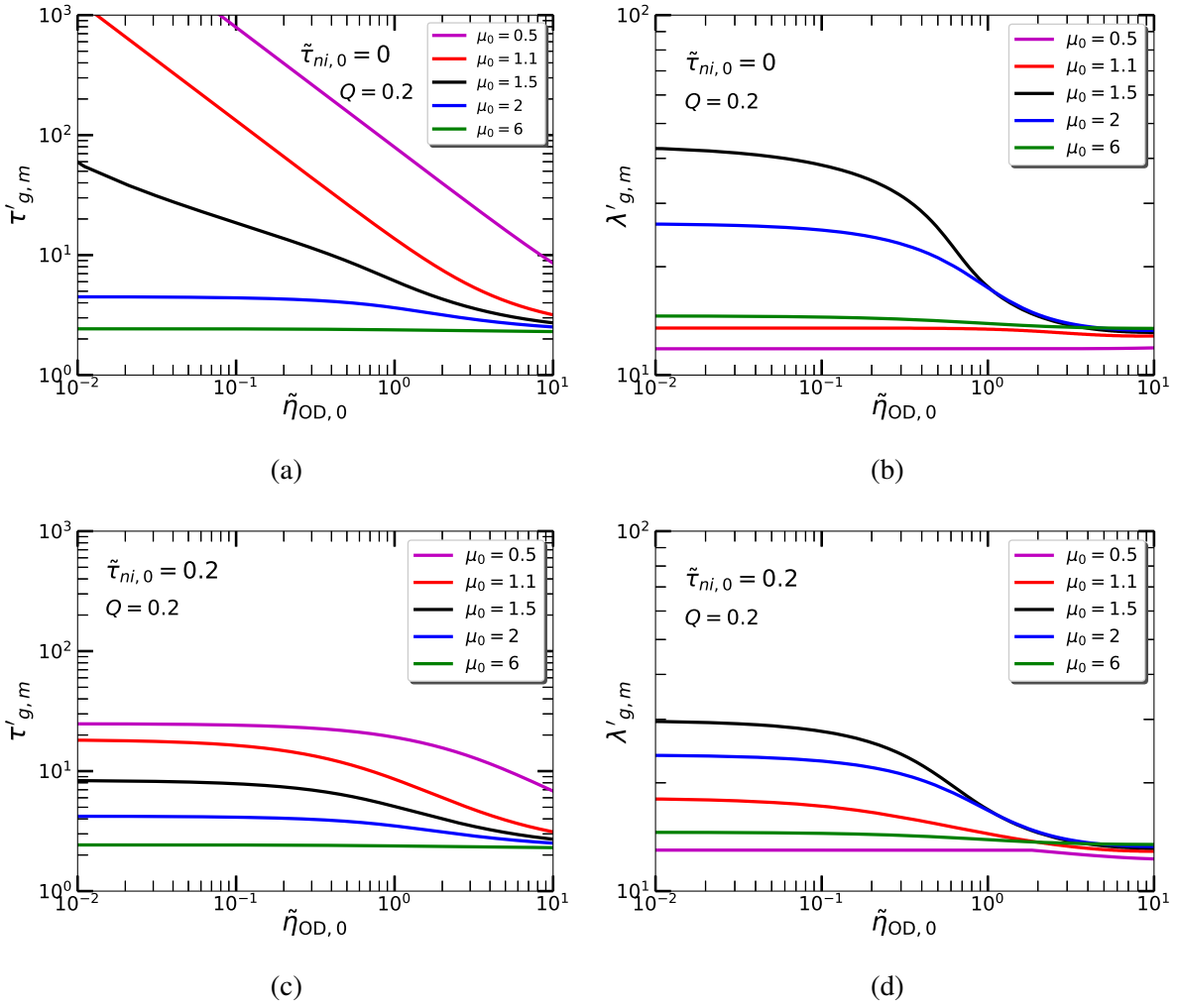

Figure 2.11: Normalized shortest growth time of gravitationally unstable mode ($\tau'_{g,m} = \tau_{g,m}/t_0$) and normalized preferred length scale of most unstable mode ($\lambda'_{g,m} = \lambda_{g,m}/L_0$) as a function of normalized Ohmic diffusivity ($\tilde{\eta}_{OD,0}$) for a fixed normalized rotation $Q = 0.2$. Fig (a) and (b) show the model for (i) $\tilde{\tau}_{ni,0} = 0$. Fig (c) and (d) show the model for (ii) $\tilde{\tau}_{ni,0} = 0.2$.

2.3.4 $\tau'_{g,m}$ and $\lambda'_{g,m}$ as Functions of the Diffusion Parameters

We present an alternative way to look at the minimum growth timescale ($\tau'_{g,m}$) and length scale ($\lambda'_{g,m}$) by studying them as a function of diffusion parameters, i.e., Ohmic diffusivity ($\tilde{\eta}_{OD,0}$) and neutral-ion collision time ($\tilde{\tau}_{ni,0}$), for fixed μ_0. Figure 2.11 shows $\tau'_{g,m}$ and $\lambda'_{g,m}$ as a function of $\tilde{\eta}_{OD,0}$ with a finite rotation $Q = 0.2$. Figure 2.11(a) and (b) represent the case of only Ohmic dissipation (OD) over a range of $\tilde{\eta}_{OD,0}$ from 0.01 to 10. Figure 2.11(a) shows that for a subcritical cloud with $\mu_0 = 0.5$, $\tau'_{g,m}$ falls off with $\tilde{\eta}_{OD,0}$ in almost a linear fashion. For $\mu_0 \approx 1.1$, the growth time decreases at a much faster rate up until $\tilde{\eta}_{OD,0} \approx 1$, after which it settles down

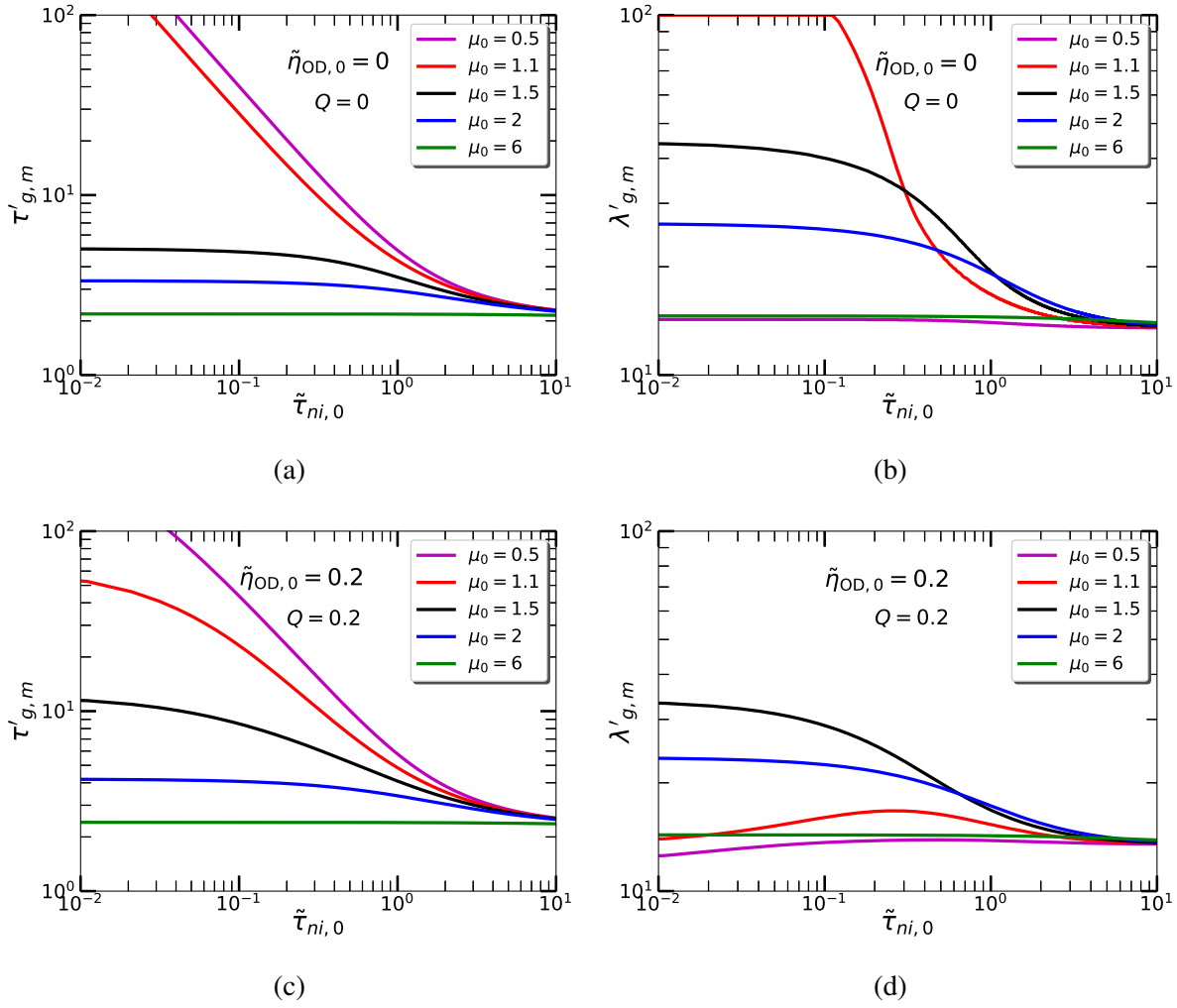

Figure 2.12: Normalized shortest growth time of gravitationally unstable mode ($\tau'_{g,m} = \tau_{g,m}/t_0$) and normalized preferred length scale of most unstable mode ($\lambda'_{g,m} = \lambda_{g,m}/L_0$) as a function of normalized neutral-ion collision time ($\tilde{\tau}_{ni,0}$). Fig (a) and (b) show the model for (i) $\tilde{\eta}_{OD,0} = 0$, $Q = 0$. Fig (c) and (d) show the models for (ii) $\tilde{\eta}_{OD,0} = 0.2$, $Q = 0.2$.

to the thermal collapse time. For $\mu_0 = 2$, the timescale is plateaued for highly ionized regions where the collapse time is longer, while for low ionization fractions the collapse time again attains the thermal collapse time. For a highly supercritical case ($\mu_0 = 6$), the cloud is unstable on the thermal timescale since gravity predominates.

Now, coming to Figure 2.11(b), for $\tilde{\eta}_{OD,0} \lesssim 1$, we see that as μ_0 increases from below unity, $\lambda'_{g,m}$ increases from the thermal wavelength (λ'_T) and becomes maximum at $\mu_0 \gtrsim 1$, and then goes back toward λ'_T for greater values of μ_0. This is due to a sharp resonant-like peak in $\lambda'_{g,m}$ at $\mu_0 \gtrsim 1$ (discussed earlier in Section 2.3.2). On the other hand, for $\tilde{\eta}_{OD,0} \gg 1$, $\lambda'_{g,m}$ drops down

toward $\lambda'_{\rm T}$ as the preferred mode is dominated by OD.

The addition of AD causes a significant reduction in the timescale and length scale curves, as shown in Figure 2.11(c) and (d). Overall, it depicts the interaction of the field lines with two different magnetic diffusion mechanisms and self-gravity. For $\mu_0 \lesssim 1$, Figure 2.11(c) shows that the growth time becomes shorter by an order of about 100. In contrast, for $\mu_0 = 1.5$ (slightly supercritical cloud) this reduction in timescale is relatively smaller and for $\mu_0 = 2$ it is smaller still. As μ_0 increases to a highly supercritical value ($\mu_0 = 6$), self-gravity dominates and the growth time tends to the thermal timescale. Figure 2.11(d) shows that for $\tilde{\eta}_{\rm OD,0} \lesssim 1$ and $\mu_0 = 1.5$ or 2, the $\lambda'_{g,m}$ is shortened by a factor of about $1-2$ compared to the case without AD. Whereas, for $\tilde{\eta}_{\rm OD,0} \gtrsim 1$, all the $\lambda'_{g,m}$ corresponding to different μ_0 become indistinguishable from each other and merge to the thermal scale.

Figure 2.12 shows the variation of the growth time and wavelength as a function of the neutral-ion collision time $\tilde{\tau}_{ni,0}$. The general trend of timescale and length scale curves shown in Figure 2.12 behaves qualitatively in the same way as it does with regards to $\tilde{\eta}_{\rm OD,0}$. However, from a closer look some subtle differences can be seen. For $\mu_0 = 0.5$ and 1, the timescale curves decrease almost linearly until they reach $\tilde{\tau}_{ni,0} \sim 1$, as seen in Figure 2.12(a) (see also Bailey & Basu, 2012). But in Figure 2.12(c), we see that the timescale curves corresponding to these μ_0 values attain the plateau at a much faster rate as they approach toward smaller $\tilde{\tau}_{ni,0}$. Moreover, because of a nonzero rotation, the growth timescale for $\mu_0 = 1.5$ and 2 becomes a little longer in comparison to that seen in Figure 2.12(a).

Moving to Figure 2.12(d), we notice that the maximum wavelength occurs at $\mu_0 = 1.5$ as compared to Figure 2.12(b) where $\mu_0 = 1.1$ corresponds to the maximum wavelength. This again shows that rotation provides an enhanced support even in a nearly transcritical regime, because of which the peak preferred length scale is shifted toward a slightly more supercritical region. Furthermore, on the side of high ionization fractions (i.e., $\tilde{\tau}_{ni,0} \approx 0.01$), the length scale curves for $\mu_0 \lesssim 1$ go to the thermal length scale (as discussed earlier in Section 2.2.7). Also, the length scale curve for $\mu_0 = 0.5$ continues to decrease more rapidly than that for $\mu_0 = 1.1$. This happens entirely because of stronger magnetic diffusion that is essentially lowering down the length scale toward the thermal length scale. Lastly, coming to $\mu_0 = 6$; being highly supercritical it evolves on the thermal length scale and timescale irrespective of any magnetic

effects and the adopted rotation.

2.3.5 Critical Limit of the Generalized Toomre Criterion

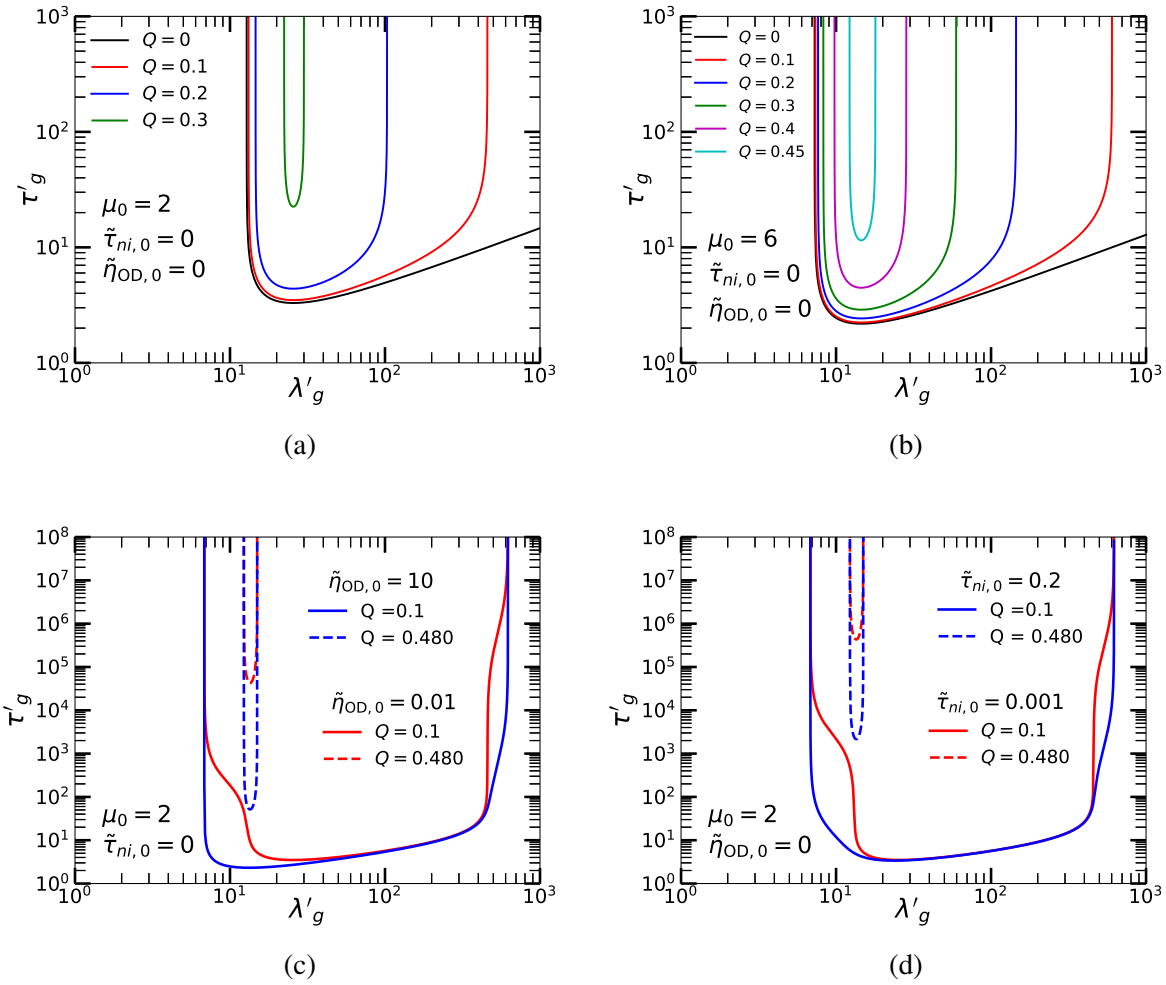

Figure 2.13: Normalized growth time of gravitationally unstable mode ($\tau'_g = \tau_g/t_0$) as a function of normalized wavelength ($\lambda'_g = \lambda_g/L_0$) for the following models. Fig (a) and (b) shows flux-frozen model with fixed normalized mass-to-flux-ratio $\mu_0 = 2$ and $\mu_0 = 6$ respectively. In (a) and (b), the timescale curves are shown for models with normalized rotation $Q = 0$ (black), 0.1 (blue), 0.2 (red), 0.3 (green), and 0.4 (magenta), 0.45 (cyan). Fig (c) shows timescale curves for $\mu_0 = 2$ solely with Ohmic dissipation and $\tilde{\eta}_{\rm OD,0} = 0.01, 10$ (red and blue, respectively). Fig (d) shows timescale curves for $\mu_0 = 2$ solely with ambipolar diffusion [$\tau_{ni,0} = 0.001, 0.2$ (red and blue, respectively)]. Each one of (c) and (d) shows timescale scale curves for $Q = 0.1, 0.480$ (solid line and dashed line for respective color). See also Table 2.1.

We introduced the effect of the magnetic field on Toomre's instability criterion and obtained an analytic expression in the flux-freezing limit (see Section 2.2.6). Here, we investigate the de-

Table 2.1: Feasible Range of Q in Different Regimes. Generalized Toomre Instability criterion ($Q < Q_{\rm crit,m}$), see Figure 2.3, Equation 2.79. see also Figure 2.13 for nonideal MHD cases. Here, HD, FF, OD, and AD present Hydrodynamic, Flux-frozen, ohmic dissipation, and ambipolar diffusion, respectively.

$\tilde{P}_{\rm ext}$	$\tilde{C}_{\rm eff}$	Regime	Nonideal MHD parameters	$\mu_0 = (1/\tilde{B}_{\rm ref})$	$Q_{\rm crit,m}$
0	1	HD	-	∞	0.5
0.1	1.037	HD	-	∞	0.482
		FF	-	6	0.459
			-	5	0.449
			-	4	0.44
			-	3	0.40
			-	2	0.304
			-	1.1	0.054
		OD	$\tilde{\eta}_{\rm OD,0}$ = [0.01, 0.1, 1, 10]	all	0.482
		AD	$\tilde{\tau}_{ni,0}$ = [0.001, 0.04, 0.2]	all	0.482

pendence of the nonideal MHD effects on the rotation parameter by analyzing our numerically obtained results.

Figure 2.13 shows normalized growth timescale as a function of length scales in different MHD regimes (ideal and nonideal). In Figure 2.13(a) and (b), under flux-freezing condition, we see unstable growing modes can be obtained for a larger Q with $\mu_0 = 6$ than that with $\mu_0 = 2$. As the cloud becomes more supercritical, the feasible instability range of Q expands with the increase of μ_0 until it merges with that of the hydrodynamic case (see Table 2.1 and Figure 2.3). When we incorporate any of the nonideal MHD effects (either $\tilde{\eta}_{\rm OD,0}$ or $\tilde{\tau}_{ni,0}$), growing modes can be obtained almost for the entire feasible range of Q as seen in Figure 2.13(c) and (d). These two cases are shown for a slightly supercritical value, $\mu_0 = 2$, to provide a better comparison with respect to Figure 2.13(a). After adding a very small Ohmic diffusivity ($\tilde{\eta}_{\rm OD,0} = 0.01$) or neutral-ion collision time ($\tilde{\tau}_{ni,0} = 0.001$), we obtain an unstable mode even for $Q = 0.480$ when $\mu_0 = 2$, unlike the flux-frozen case in which $Q = 0.480$ corresponds to stable modes. For a fixed value of Q at which an unstable mode exists in the flux-frozen case, introducing a non-zero $\tilde{\eta}_{\rm OD,0}$ or $\tilde{\tau}_{ni,0}$ reduces the growth time of the instability as compared to the flux-frozen case. In our model, an unstable mode occurs for $Q < 0.482$ ($= 1/(2\tilde{C}_{\rm eff,0})$)

when we take $\tilde{P}_{\rm ext} = 0.1$, and for $Q < 0.5$ when $\tilde{P}_{\rm ext} = 0$.

Therefore, in the supercritical regime with magnetic diffusion, the critical instability limit of Q reverts back to the hydrodynamic value. The growth times and wavelengths of preferred unstable modes for low values of diffusivity are however much longer than for higher values of diffusivity.

2.4 Discussion

We calculate some typical numbers based on our model for a rotationally-supported protostellar disk. In the high density environment of a protostellar disk, both Ohmic dissipation (OD) and ambipolar diffusion (AD) are expected to be active. Based on the parameters discussed in Section 2.6.1, we estimate the nonideal MHD parameters using

$$\tau_{ni,0} = 3.74 \times 10^4 \left(\frac{T}{10\,\mathrm{K}}\right)\left(\frac{0.01\ \mathrm{g\ cm^{-2}}}{\sigma_{n,0}}\right)^2 \left(\frac{10^{-7}}{\chi_{i,0}}\right)\left(1+\tilde{P}_{\rm ext}\right)^{-1}\ \mathrm{yr}, \tag{2.101}$$

where the ionization fraction is given by the approximate relation

$$\chi_{i,0} = 10^{-7}\left(\frac{n_{n,0}}{10^4\ \mathrm{cm^{-3}}}\right)^{-1/2}, \tag{2.102}$$

and for OD we use

$$\begin{aligned}\eta_{\rm OD,0} =& C_1\ 1.3 \times 10^{18}\left(\frac{n_{n,0}}{10^{12}\,\mathrm{cm^{-3}}}\right)\left(\frac{T}{10\,\mathrm{K}}\right)^{1/2} \\ &\times\left[1-\tanh\left(\frac{n_{n,0}}{10^{15}\,\mathrm{cm^{-3}}}\right)\right]\ \mathrm{cm^2\ s^{-1}},\end{aligned} \tag{2.103}$$

as used by Machida et al. (2007) based on calculations by Nakano et al. (2002). The term within the square brackets of Equation 2.103 is a cutoff representing the restoration of flux-freezing at high densities due to thermal ionization. The uncertainties in C_1 (adopting a dimensionless scaling parameter whose standard value is unity) hinge largely on the grain properties (e.g., Dapp & Basu, 2010).

The magnetic field is expected to be largely dragged in by the collapse of a prestellar core and there should be significant magnetization at early times. Three-dimensional nonideal MHD simulations that start from a prestellar core show that in the very early embedded phase the disk is only mildly supercritical with normalized mass-to-flux ratio $\mu_0 \gtrsim 3$ if the prestellar core has $\mu_0 = 3$ (Hirano et al., 2020). Observationally, the magnetic field is difficult to detect directly

through the Zeeman effect in small-scale low mass objects like disks (Brauer et al., 2017). Furthermore, the strength of polarized emission from embedded dust cannot be related to a field strength, but an indirect means such as the DCF method could work in principle. However, this has also proven to be challenging, since the spatially resolved polarization vectors detected at mm wavelengths tend to be dominated by dust scattering instead (Kataoka et al., 2015, 2016; Yang et al., 2016a,b). Observations of masers in compact high density regions near massive protostars often reveal polarization that can be used to infer the magnetic field strength through the Zeeman effect. Vlemmings et al. (2010) used methanol (CH_3OH) maser emission around the massive protostar Cepheus A HW2 to infer a large-scale magnetic field of strength ≈ 23 mG in the ≈ 1000 AU circumstellar disk. The field direction was also estimated to be nearly perpendicular to the disk elongation and nearly parallel to the observed outflow. The inferred mass-to-flux ratio was $\mu \approx 1.7$. In regions of low-mass star formation, Gonçalves et al. (2008) and Myers et al. (2020) used the indirect means of fitting the magnetic field morphology to determine the mass-to-flux ratios of the protostellar envelopes on ≈ 1000 AU scales, yielding $\mu \approx 1.7$ and $\mu \approx 1.5$ for NGC 1333 IRAS 4A and BHR71 IRS1, respectively.

To gain insight into the values of the nonideal MHD coefficients, we refer to figure 4 of Dapp et al. (2012), which shows the relative contribution from AD and OD to their respective diffusivity coefficients. Their simulation shows that the diffusion coefficients for AD and OD are nearly the same on the scale of the first core at $r \approx 1$ AU. The contribution of OD continues to increase sharply at higher densities ($n_{n,0} \gtrsim 10^{11}$ cm^{-3}) and significantly exceeds the contribution from AD. At lower densities, the AD coefficient dominates that due to OD but this does not cause a large flux loss since the dynamical time is less than the diffusion time associated with AD during the runaway collapse phase.

Based on the simulations of Vorobyov & Basu (2006, see their figure 4) that follow the self-consistent formation of disks from the collapse of prestellar cores, we infer a typical mid-range neutral number density $n_{n,0} \approx 10^{11}$ cm^{-3} during the early embedded phase of the disk that is characterized by recurrent GI. This is also the density at which both OD and AD contribute significantly to magnetic dissipation, so it makes an interesting reference point to study. Based also on these simulations (Vorobyov & Basu, 2006, 2007), we estimate a typical disk temperature $T = 30$ K. These numbers lead to $\rho_{n,0} = 3.90 \times 10^{-13}$ g cm^{-3}, $\sigma_{n,0} = 59.95$ g cm^{-2},

$L_0 = 2.80$ AU, $t_0 = 41.74$ yr, $M_0 = 5.32 \times 10^{-5}\, M_\odot$, and $\chi_i = 3.16 \times 10^{-11}$. See figure 5 of Dapp et al. (2012) for a comparison of ionization fraction for large number density. Using equations (2.101) and (2.103), we then find that $\eta_{\rm OD,0} = 2.25 \times 10^{17}$ cm^2 s^{-1} and $\tau_{ni,0} = 8.98$ yr, leading to $\tilde{\eta}_{\rm OD,0} = 0.2$ and $\tilde{\tau}_{ni,0} = 0.2$, respectively (see figure 2 of Dapp et al., 2012).

The adopted surface density $\sigma_{n,0} = 59.95\,{\rm g\,cm^{-2}}$ is congruent with a typical value in simulations of the early embedded class 0 phase (Vorobyov & Basu, 2006, see their figure 5). Observationally, Pérez et al. (2016) estimated a surface density $\approx 5\,{\rm g\ cm^{-2}}$ for the disk surrounding Elias 2–27, however that is a class II object representing a later stage of evolution. Our estimated $\sigma_{n,0}$ does not include the inward pressure of an extra vertical squeezing W_* due to the gravity of the central star. This can reduce the value of the surface density for a given volume density. The effect of W_* is calculated quantitatively in Section 2.6.9, and we do not deal with it further here as we are making order of magnitude estimates.

We refer the reader back to Figure 2.10(c) and note that for the values $Q = 0, 0.1, 0.2, 0.3, 0.4$, the peak preferred modes with minimum growth time occur at $\mu_0 = 1.17, 1.27, 1.52, 1.96, 3.05$, respectively. These correspond to magnetic field values $B_{\rm ref} = 83.29, 76.56, 64.06, 49.72, 31.91$ mG, respectively. The normalized ambipolar diffusivity $\tilde{\eta}_{\rm AD,0} = \tilde{Z}_0 \mu_0^{-2} \tilde{\tau}_{ni,0} = 0.29, 0.25, 0.17, 0.10, 0.04$, respectively, for the above mentioned values of μ_0. These arise from $\eta_{\rm AD,0} = V_{A,0}^2 \tau_{ni,0} = 3.95, 3.35, 2.34, 1.41, 0.58$, in units of 10^{17} cm^2 s^{-1} for $\mu_0 = 1.17, 1.27, 1.52, 1.96, 3.05$. Meanwhile, $\tilde{\eta}_{\rm OD,0}$ does not explicitly depend on the magnetic field strength. Finally then, from Figure 2.10(c), we obtain the peak preferred fragmentation mass $M_{g,m}$ to be 93.13, 56.78, 28.39, 16.13, 10.37 in units of $M_{\rm Jup}$ for $Q = 0, 0.1, 0.2, 0.3, 0.4$, respectively. Here, $M_{g,m} = M'_{g,m} M_c$ and $M_c = \pi \sigma_{n,0} (L_0/2)^2$ as the perturbation is taken to be circular with radius $L_0/2$. For a typical disk temperature $T = 30$ K and neutral number density $n_{n,0} = 10^{11}$ cm^{-3}, $M_c = 4.18 \times 10^{-5}\, M_\odot$.

Protostellar disks in the early embedded class 0 phase can be prone to GI, especially while they are still accreting matter from their surrounding envelope (Vorobyov & Basu, 2006). Resistive MHD simulations also show that the magnetic field that is dragged in from the core collapse leads to mildly supercritical disks in which magnetic dissipation mechanisms are active (Hirano et al., 2020). Hydrodynamic simulations of global disk evolution have established that the Q parameter, although initially derived through a local analysis, has wide ranging applicability to understanding global nonlinear disk evolution (see, e.g., Vorobyov & Basu, 2006,

2007). For the intermediate regime $1 \lesssim Q \lesssim 2$, small-amplitude fluctuations can persist and lead to meaningful flocculent spiral structure. In the decidedly unstable regime $Q \lesssim 1$, grand design spiral arms are formed and clumps within them can form if the local cooling time is also less than the orbit time (Vorobyov & Basu, 2010b); this is a criterion on the nonlinear evolution that is not present in an isothermal linear analysis. Giant planet (or other companion) formation by GI can then occur. The effect of the magnetic field on this scenario is just beginning to be explored. Magnetic fields and nonideal MHD lead to a more complex instability criterion including affecting the length scales and timescales of the instabilities, as we have shown in this paper. The diffusivities play an important role in setting these quantitatively, and for $\mu_0 > 1$ the preferred modes generally have larger length scales and longer timescales than in the hydrodynamic case.

Future global simulations of the long term evolution of disks including nonideal MHD will be able to explore the effect of nonideal MHD in clump formation and can potentially use the linear results in this paper as a benchmark. The OD will also introduce important nonlinear effects, since the resistive heating (not present in our linear isothermal analysis) can potentially counteract the surface cooling. In fact, as Lizano et al. (2010) point out, a large amount of OD is required in order to reduce the magnetic flux of disk material to the values inferred from the paleomagnetism of meteorites in our solar system.

2.5 Summary

We have studied the effect of ambipolar diffusion (AD) and Ohmic dissipation (OD) on gravitational instability within rotationally-supported protostellar disks, employing a linear analysis. Our model clouds are isothermal, partially ionized, thin planar sheets with a finite local vertical half thickness. Here, we highlight several interesting results that emerge.

We derive generalized criteria of Toomre instability that has a magnetic dependence (see Section 2.2.6). We show that the magnetic field strength influences the critical limit of rotation such that the instability criterion appears as $Q < Q_{\rm crit,m}$. In the hydrodynamic limit ($\mu_0 \to \infty$), $Q_{\rm crit,m}$ reduces to $1/(2\tilde{C}_{\rm eff,0})$, which is equivalent to standard Toomre's instability criterion. With the magnetic diffusion effects, i.e., AD and/or OD, the value of $Q_{\rm crit,m}$ also reverts back to that of the hydrodynamic case (see Figure 2.3).

Subcritical clouds ($\mu_0 < 1$) are stable against gravitational fragmentation in the flux-freezing limit ($\tilde{\eta}_{\rm OD,0} \to 0, \tilde{\tau}_{ni,0} \to 0$). Supercritical clouds ($\mu_0 > 1$) are unable to support themselves against their own gravity and are prone to collapse even in the flux-freezing regime. In that regime, adding rotation helps to stabilize the longer wavelengths to a greater extent (refer to Figure 2.5(b)). However, in the presence of any form of magnetic diffusion (OD or AD), a fastest growing mode of gravitational instability having a minimum growth timescale and an associated preferred length scale can be obtained even for subcritical clouds (Figure 2.8). The two nonideal MHD effects reveal qualitatively similar kinds of features in the gravitationally unstable modes, but there are quantitative differences. For highly subcritical clouds the preferred length scale in the AD only case converges to $2\lambda_{\rm T}$, i.e., twice the thermal critical length scale, as in the highly supercritical (i.e., nonmagnetic) limit. For OD it converges to $\lambda_{\rm T}$, the minimum possible wavelength for instability due to the presence of thermal pressure, since the OD-driven modes have stronger affinity for short wavelengths. In this highly subcritical limit, the timescale of the fastest growing OD mode tends to infinity, since the preferred wavelength is converging to $\lambda_{\rm T}$. However, for AD, the diffusivity is proportional to the square of the field strength, and this compensates for the strong magnetic support, and enforces a finite constant drift speed and growth time that is independent of μ_0 for $\mu_0 \ll 1$. In a realistic situation of a partially ionized protostellar disk, OD and AD are simultaneously active, and in this case AD places an upper bound on the timescale of the diffusive-driven instability.

A peak length scale for collapse occurs at transcritical (but slightly supercritical, $\mu_0 \gtrsim 1$) mass-to-flux ratios, but the peak occurs at different values for OD and AD and also depending on the value of the diffusivities. For very high diffusivities, the peak can disappear. The timescale for growth of the transcritical modes is intermediate between the dynamical (free-fall) time and the ambipolar diffusion time.

The interplay of the effects of two nonideal MHD effects together with rotation in a protostellar disk can be seen in Figure 2.10 (Section 2.3.3). Rotation makes the growth timescale longer and the peak preferred length scale becomes shorter because of an additional support from rotation against gravitational collapse. The peak preferred wavelength of instability gradually moves to a larger μ_0 (~ 2) as rotation increases. Furthermore, we find that the peak preferred mass for collapse exceeds the thermal critical (Jeans) mass by a factor of up to 10 when

including OD and/or AD. The peak preferred fragmentation mass is likely to be $\sim 10-90\ M_{\rm Jup}$ (see Section 2.4, Figure 2.10(c)). This magnetic field dependent mass creates a modified threshold for AD and/or OD driven gravitational fragmentation in the magnetized disks.

The linear analysis we have presented is formally applicable to a local patch within a larger disk-like cloud. The inclusion of rotation, OD, and AD makes the results particularly relevant for protostellar disks. A local analysis of a nonmagnetic rotating cloud yields the usual Toomre criterion, which has proven surprisingly effective in the interpretation of the global evolution of disks that contain significant inhomogeneities. In a similar manner, our results may prove to be useful in the analysis of global nonideal MHD models of disk evolution. Such simulations are in their infancy, and the role of OD and AD in regulating GI and giant planet formation may prove to be crucial. Future simulations have much to explore.

2.6 Appendices

2.6.1 Units of Defined Parameters

The typical values of the units used and other derived quantities are

$$\sigma_{n,0} = \frac{3.63\times10^{-3}}{\left(1+\tilde{P}_{\rm ext}\right)^{1/2}}\left(\frac{n_{n,0}}{10^3\ {\rm cm}^{-3}}\right)^{1/2}\left(\frac{T}{10\ {\rm K}}\right)^{1/2}\ {\rm g\ cm}^{-2}, \tag{2.104}$$

$$L_0 = 1.54\times10^{4}\left(\frac{T}{10\ {\rm K}}\right)^{1/2}\left(\frac{10^3\ {\rm cm}^{-3}}{n_{n,0}}\right)^{1/2}\left(1+\tilde{P}_{\rm ext}\right)^{1/2}\ {\rm AU}, \tag{2.105}$$

$$t_0 = 3.98\ \times10^{5}\left(\frac{10^3\ {\rm cm}^{-3}}{n_{n,0}}\right)^{1/2}\left(1+\tilde{P}_{\rm ext}\right)^{1/2}\ {\rm yr}, \tag{2.106}$$

$$c_s = 0.188\left(\frac{T}{10\ {\rm K}}\right)^{1/2}\ {\rm km\ s}^{-1}, \tag{2.107}$$

$$M_0 = 9.76\times10^{-2}\left(\frac{T}{10\ {\rm K}}\right)^{3/2}\left(\frac{10^3\ {\rm cm}^{-3}}{n_{n,0}}\right)^{1/2}\left(1+\tilde{P}_{\rm ext}\right)^{1/2}\ M_\odot\,, \tag{2.108}$$

$$B_{\rm ref} = \frac{5.89\times10^{-6}}{\mu_0}\left(\frac{n_{n,0}}{10^3\ {\rm cm}^{-3}}\right)^{1/2}\left(\frac{T}{10\ {\rm K}}\right)^{1/2}\left(1+\tilde{P}_{\rm ext}\right)^{-1/2}\ {\rm G}\,, \tag{2.109}$$

$$\eta_{\rm AD,0} = 6.01 \times 10^{21} \frac{\mu_0^{-2}}{(1+\tilde{P}_{\rm ext})} \left(\frac{T}{10\,{\rm K}}\right)\left(\frac{10^{-7}}{\chi_{i,0}}\right)\left(\frac{10^3\,{\rm cm}^{-3}}{n_{n,0}}\right) {\rm cm}^2{\rm s}^{-1}. \tag{2.110}$$

2.6.2 Collision timescales

We use the collision time formula between the different species s and neutrals as computed by Dapp et al. (2012), employing the work by Mouschovias (1996). The following expression is the collision time for a charged species s with the neutrals:

$$\tau_{sn} = k_{s,\rm He} \frac{m_s + m_{\rm H_2}}{\rho_n \langle \sigma w \rangle_{s\rm H_2}}, \tag{2.111}$$

where σ is the elastic scattering cross-section for electron-neutral or ion-neutral encounters, and w equals the relative velocity of the charged particle as seen from the rest frame of the neutrals. The angular bracket denotes an average over the velocity distribution function of the charged species. The quantity $k_{s,\rm He}$ is a correction factor due to the fact the gas also contains helium. Helium contributes only a small correction due to its low polarizability as compared to H_2 (see Spitzer, 1978; Mouschovias, 1996):

$$\begin{aligned} k_{s,\rm He} &= 1.23 \quad \text{if s = i,} \\ &= 1.21 \quad \text{if s = e.} \end{aligned} \tag{2.112}$$

The values of the collision rate $\langle \sigma w \rangle_{s\rm H_2}$ are (Mott & Massey, 1949; McDaniel & Mason, 1973):

$$\begin{aligned} \langle \sigma w \rangle_{s\rm H_2} &= 1.69 \times 10^{-9}\,{\rm cm}^3\ {\rm s}^{-1} \quad \text{if s = i,} \\ &= 1.30 \times 10^{-9}\,{\rm cm}^3\ {\rm s}^{-1} \quad \text{if s = e.} \end{aligned} \tag{2.113}$$

2.6.3 Characteristic diffusion length scales for OD and AD

From Equation 2.45 we see that the characteristic diffusion length scale for Ohmic dissipation (OD) is

$$l_{\rm OD} \sim \frac{1}{k}. \tag{2.114}$$

It corresponds to the typically encountered diffusion rate (Equation 2.45) proportional to k^2, arising from the application of a resistivity $\eta_{\rm OD,0}$ within the assumed finite thickness of our

model cloud. Similarly, from Equation 3.5 we see that the characteristic diffusion length scale for ambipolar diffusion (AD) is

$$l_{\rm AD} \sim \left(\frac{k}{Z_0} + k^2\right)^{-1/2}, \tag{2.115}$$

which contains an additional term $(Z_0/k)^{1/2}$ as compared to $l_{\rm OD}$. The diffusion rate (Equation 3.5) is the sum of two terms, with a term proportional to k that comes from the magnetic tension term in the Lorentz force (see Equation 2.15) while a term proportional to k^2 comes from the magnetic pressure gradient force that acts within the finite thickness region of the cloud. The magnetic tension, arising from a surface stress (see Equation 2.12), would exist even in the limit of an infinitesimally thin sheet, and illustrates the fact that the relevant length scale for a diffusive process in the limit of an infinitesimally thin sheet is $l \sim (Z_0/k)^{1/2}$, which is the geometric mean of Z_0 and $1/k$ (see discussion in Lizano et al., 2010, Appendix). Even though the sheet can be infinitesimally thin, one can still identify an effective length scale $Z_0 \propto c_s^2/(G\sigma_{n,0})$ as a combination of the relevant parameters. The OD term would also attain such a form if the sheet was infinitesimally thin and we only considered the dissipation of surface currents, as shown by Lizano et al. (2010). In this study we consider the OD of the current inside the finite thickness disk to be the most applicable.

2.6.4 Effective Sound Speed

In Figure 2.14, we review properties of the normalized local effective sound speed ($\tilde{C}_{\rm eff}$) and initial vertical half-thickness ($\tilde{Z}_0$) as a function of dimensionless external pressure ($\tilde{P}_{\rm ext}$). In the limit of low external pressure ($P_{\rm ext} \to 0$), the local effective sound speed reduces to the isothermal sound speed (see Equation 2.21) i.e., $\tilde{C}_{\rm eff} = 1$ (see Equation 2.54). We see that in this limit ($P_{\rm ext} \ll (\pi/2)G\sigma_{n,0}^2$), the half-thickness $Z_0 \propto 1/\sigma_{n,0}$ (see Equation 2.40). In this case, the half-thickness increases in the direction of decreasing surface density, and the external pressure acts to contribute a force in the direction opposite that of the surface density increase. Hence, there is an increased restorative effect to density perturbations and therefore an increased effective sound speed. Whereas in the regime of large external pressure ($P_{\rm ext} \gg (\pi/2)G\sigma_{n,0}^2$), Z_0 becomes proportional to $\sigma_{n,0}$, determined by the interplay between internal thermal pressure within the cloud and the external pressure. In this case, the half-thickness decreases in the direction of decreasing surface density, and the external pressure acts to contribute a force in

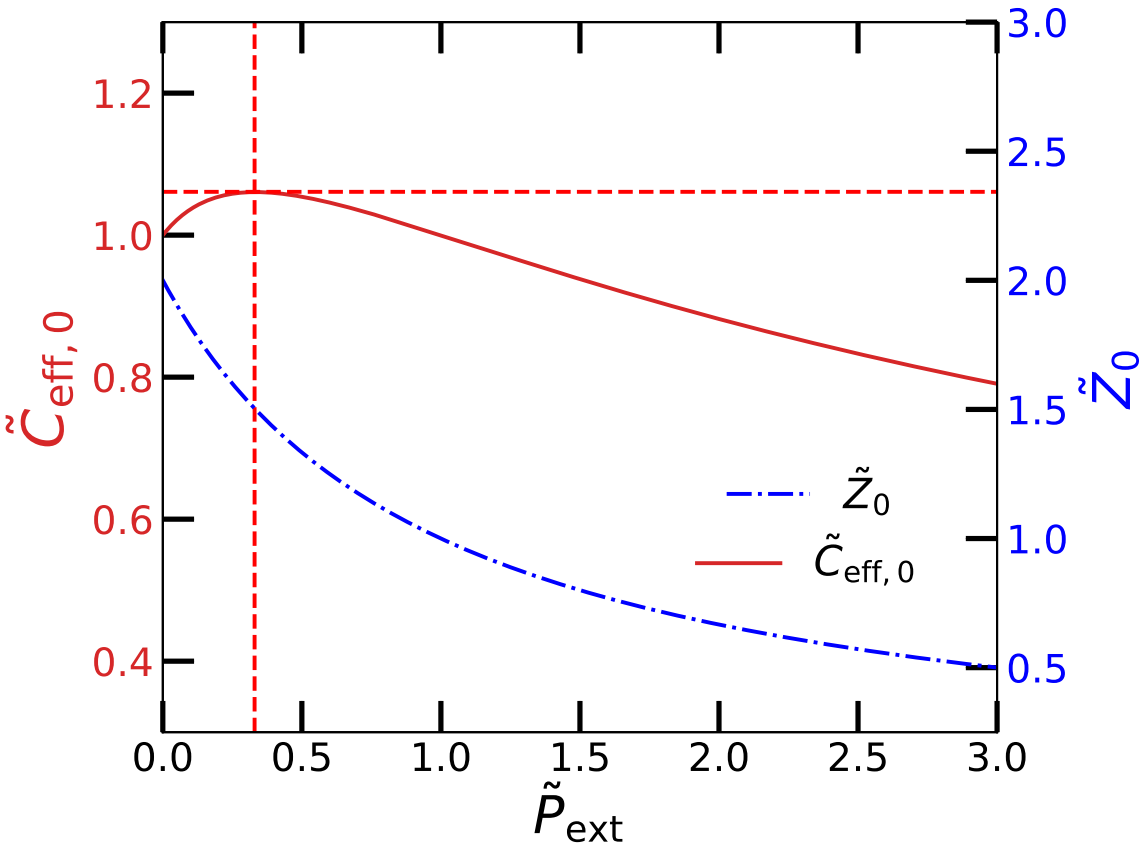

Figure 2.14: Normalized local effective sound speed ($\tilde{C}_{\rm eff}$) and normalized effective local vertical half-thickness ($\tilde{Z}_0$) as functions of the normalized external pressure $\tilde{P}_{\rm ext}$. The value of $\tilde{C}_{\rm eff}$ is maximum (=1.061) at $\tilde{P}_{\rm ext} = 1/3$ (as shown by the dashed horizontal and vertical lines).

the same direction as the surface density increase. Hence, there is a decreased restorative effect to density perturbations and therefore a decreased effective sound speed. As a result, $\tilde{C}_{\rm eff,0}$ attains a maximum (=1.061) at $\tilde{P}_{\rm ext} = 1/3$ and thereafter gradually decreases, while $\tilde{Z}_0$ gradually decreases with increasing $\tilde{P}_{\rm ext}$, as can be seen from Equation 2.57.

2.6.5 Notes on Generalized Toomre Criterion

In the limit of flux-freezing the dispersion relation is

$$\omega^2 = 4\Omega^2 + k^2(C_{\rm eff,0}^2 + V_{A,0}^2) - 2\pi G k \sigma_{n,0}(1 - \mu_0^{-2}). \tag{2.116}$$

To minimize ω^2, the criteria are $d(\omega^2)/dk = 0$ and $d^2(\omega^2)/dk^2 > 0$ at $k = k_{\rm min}$, yielding

$$k_{\rm min} = \frac{\pi G \sigma_{n,0}(1-\mu_0^{-2})}{(C^2_{\rm eff,0} + V^2_{A,0})} \,. \tag{2.117}$$

Now, to obtain the instability criterion, we set $\omega^2 < 0$ at $k = k_{\rm min}$, which gives

$$4\Omega^2 + k^2_{\rm min}(C^2_{\rm eff,0} + V^2_{A,0}) - 2\pi G k_{\rm min}\sigma_{n,0}(1-\mu_0^{-2}) < 0\,, \tag{2.118}$$

yielding

$$\frac{\Omega(C^2_{\rm eff,0} + V^2_{A,0})^{1/2}}{\pi G \sigma_{n,0}(1-\mu_0^{-2})} < \frac{1}{2}. \tag{2.119}$$

In the dimensionless form it becomes

$$\begin{aligned} \frac{c_s\,\Omega}{\pi G\sigma_{n,0}} \frac{(\tilde{C}^2_{\rm eff,0} + \tilde{Z}_0\mu_0^{-2})^{1/2}}{(1-\mu_0^{-2})} &< \frac{1}{2}\,, \\ \text{or,}\;\; Q\frac{(\tilde{C}^2_{\rm eff,0} + \tilde{Z}_0\mu_0^{-2})^{1/2}}{(1-\mu_0^{-2})} &< \frac{1}{2}\,, \\ \text{or,}\;\; Q_{\rm eff} &< \frac{1}{2}\,, \\ \text{or,}\;\; Q < \frac{1}{2}\frac{(1-\mu_0^{-2})}{(\tilde{C}^2_{\rm eff,0} + \tilde{Z}_0\mu_0^{-2})^{1/2}} &= Q_{\rm crit,m}\,, \end{aligned} \tag{2.120}$$

where

$$Q_{\rm eff} = \frac{\Omega(C^2_{\rm eff,0} + V^2_{A,0})^{1/2}}{\pi G\sigma_{n,0}(1-\mu_0^{-2})} = Q\frac{(\tilde{C}^2_{\rm eff,0} + \tilde{Z}_0\mu_0^{-2})^{1/2}}{(1-\mu_0^{-2})}. \tag{2.121}$$

See Section 2.2.6 for further discussion.

2.6.6 Notes on Stationary field limit

In the limit of stationary magnetic fields, $\omega \delta B'_{z,\mathrm{eq}} \to 0$, the resulting dispersion relation can be obtained using Equations (2.42) to (2.45). It follows that

$$\begin{vmatrix} -\omega & k_x c_s & k_y c_s & 0 \\ \frac{k_x}{k} A_1 & -\omega\, c_s & 0 & \frac{k_x}{k} A_2 \\ \frac{k_y}{k} A_1 & 0 & -\omega\, c_s & \frac{k_y}{k} A_2 \\ 0 & \frac{k_x}{\mu_0} c_s & \frac{k_y}{\mu_0} c_s & -i(\theta+\gamma) \end{vmatrix} = 0 \tag{2.122}$$

$$\Rightarrow \omega^2 + \omega \frac{ikA_2}{\mu_0(\theta+\gamma)} - kA_1 = 0\,, \tag{2.123}$$

where A_1, A_2, θ, and γ are explicitly written in Section 2.2.4. Recall that θ and γ represent the case of AD and OD, respectively. Simplifying each individual term of Equation 2.123 yields

$$\omega^2 = \omega'^2 \, \frac{(2\pi G \sigma_{n,0})^2}{c_s^2}, \tag{2.124}$$

$$\begin{aligned} \omega \frac{ikA_2}{\mu_0 \theta} &= \omega \frac{ik}{\mu_0} \frac{\left(2\pi G \sigma_{n,0}\, \mu_0^{-1} + k\, V_{A,0}^2\, \mu_0\right)}{\tau_{ni,0}\left(2\pi G \sigma_{n,0} \mu_0^{-2} k + k^2 V_{A,0}^2\right)} \\ &= i \frac{\omega'}{\tilde{\tau}_{ni,0}} \, \frac{(2\pi G \sigma_{n,0})^2}{c_s^2}, \end{aligned} \tag{2.125}$$

$$\begin{aligned} \omega \frac{ikA_2}{\mu_0 \gamma} &= i\omega \frac{\left(2\pi G \sigma_{n,0}\, \mu_0^{-1} + k\, V_{A,0}^2\, \mu_0\right)}{\mu_0 \eta_{\mathrm{OD},0} k} \\ &= i \frac{\omega'}{\tilde{\eta}_{\mathrm{OD},0} k' \mu_0^2} \, (1 + k' \tilde{Z}_0) \, \frac{(2\pi G \sigma_{n,0})^2}{c_s^2}, \end{aligned} \tag{2.126}$$

$$kA_1 = k(C_{\mathrm{eff},0}^2 k - 2\pi G \sigma_{n,0}) = (\tilde{C}_{\mathrm{eff},0}^2 k'^2 - k') \frac{(2\pi G \sigma_{n,0})^2}{c_s^2}. \tag{2.127}$$

For the case of only OD (set $\theta = 0$), combining 2.124, 2.126, 2.127 we obtain the resulting dispersion relation and corresponding growth timescale as shown in Equation 2.91 and Equation 2.92. For the case of only AD (set $\gamma = 0$), combining 2.124, 2.125, 2.127 we obtain the resulting dispersion relation and corresponding growth timescale as shown in Equation 2.95 and Equation 2.96.

2.6.7 Additional figures of normalized growth timescale vs. length scale

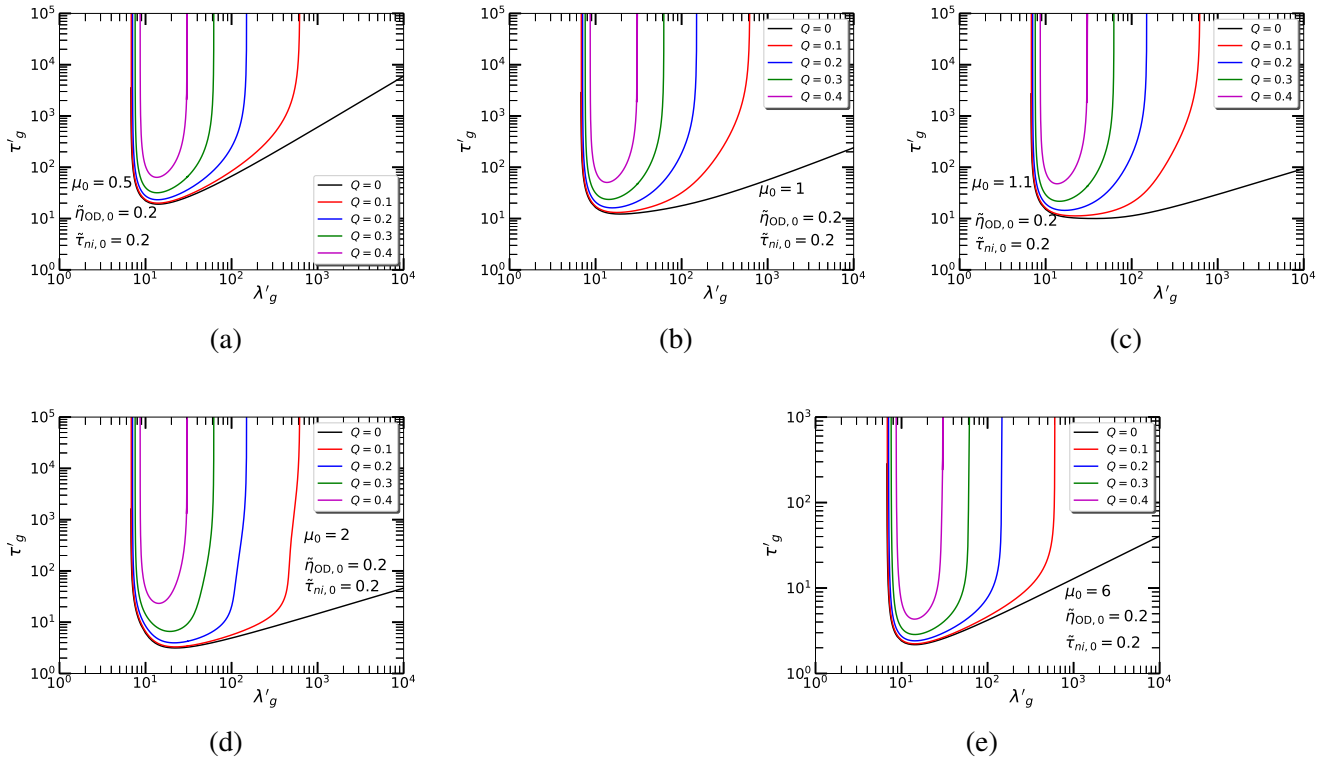

Figure 2.15: Normalized growth time $\tau'_g = \tau_g/t_0$ of gravitationally unstable mode as a function of the normalized wavelength $\lambda'_g = \lambda_g/L_0$ for models with a fixed normalized Ohmic diffusivity $\tilde{\eta}_{\mathrm{OD},0} = 0.2$ and neutral-ion collision time $\tilde{\tau}_{ni,0} = 0.2$, for different normalized mass-to-flux-ratio $\mu_0 = 0.5, 1, 1.1, 2, 6$. Each figure shows timescale curves for models with different normalized rotation $Q = 0$ (black), 0.1 (red), 0.2 (blue), 0.3 (green), and 0.4 (magenta).

Figure 2.15 shows the curves of normalized growth timescale as a function of normalized length scale for different normalized rotation $Q = 0, 0.1, 0.2, 0.3, 0.4$. This figure represents our model of the protostellar disk for distinct normalized mass-to-flux ratios $\mu_0 = 0.5, 1, 1.1, 2, 6$, with $\tilde{\eta}_{\mathrm{OD},0} = 0.2$ and $\tilde{\tau}_{ni,0} = 0.2$, corresponding to $n_{n,0} = 10^{11}$ cm^{-3}. This is one of our fundamental results, which can be obtained by plotting the normalized form of the full dispersion relation as seen in Equation 2.63. Because of the combination of both nonideal MHD effects, the timescale versus length scale curve attains a minimum at a smaller value of τ'_g even for the subcritical case $\mu_0 = 0.5$ as compared to the case when only one nonideal MHD effect is present. With the transition of μ_0 from subcritical to supercritical, these curves gradually approach to that of the hydrodynamic case. See Section 2.3.2, 2.3.3 for a detailed discussion.

2.6.8 Monochromatic Perturbation

Here we focus on the form of the eigenfunctions with a single wavenumber k. The column density perturbation is of the form

$$\delta\sigma'_n(x,y,t) = \delta\sigma'_{n,a}\,\mathrm{Re}\left[e^{i(kx-\omega t)}\right], \tag{2.128}$$

where we take the uniform background state ($\sigma'_{n,0} = 1$) with a perturbed amplitude $\delta\sigma'_{n,a}$. Our dispersion analysis signifies that the linear disturbances are independent of the angle of their propagation (α). Hence, the choice of direction of propagation becomes irrelevant to our context. The reference has been set up by making $\alpha = 0$ (parallel to the x- axis), which means that $k'_y = 0$, such that we can write $k'_x = k'_z \equiv k'$ (see Section 2.2.3). By adding a column density perturbation in this way, we calculate the initial velocity and magnetic field perturbations that are congruent with our system of equations. We explicitly derive the equations for perturbed quantities from the dimensionless set of equations shown in Section 2.2.5. Now, solving for the initial perturbations $\delta v'_{n,x}$, $\delta v'_{n,y}$, $\delta v'_{i,x}$, $\delta v'_{i,y}$, $\delta B'^{\mathrm{FF}}_{z,\mathrm{eq}}$, $\delta B'^{\mathrm{OD}}_{z,\mathrm{eq}}$, and $\delta B'^{\mathrm{AD}}_{z,\mathrm{eq}}$ in terms of the given $\delta\sigma'_{n,0}$, k'_x, and $\tau'_g = i/\omega'$ (as a function of $\lambda' = 2\pi/k'$) yields

$$\delta v'_{n,x}(x,y,t) = \frac{\lambda'}{2\pi\tau'_g}\delta\sigma'_{n,a}\ \mathrm{Re}\left[e^{i\left(\frac{\pi}{2}+kx-\omega t\right)}\right],\quad \delta v'_{n,y}(x,y,t) = 0 \tag{2.129}$$

$$\begin{aligned}\delta v'_{i,x}(x,y,t) = \left[\frac{\lambda'}{2\pi\tau'_g} - K_1\right]\delta\sigma'_{n,a}\ \mathrm{Re}\left[e^{i\left(\frac{\pi}{2}+kx-\omega t\right)}\right],\\ \delta v'_{i,y}(x,y,t) = 0,\end{aligned} \tag{2.130}$$

where

$$K_1 = \frac{\tilde{B}^2_{\mathrm{ref}}\lambda'\tilde{\tau}_{ni,0}}{\lambda' + 2\pi\tau'_g\tilde{\tau}_{ni,0}\tilde{B}^2_{\mathrm{ref}}\left(1+\frac{2\pi\tilde{Z}_0}{\lambda'}\right)}\left(1+\frac{2\pi\tilde{Z}_0}{\lambda'}\right). \tag{2.131}$$

Linearization and normalization of $F_{\mathrm{Mag,x}}$ yields

$$F'_{\mathrm{Mag,x},0} = \frac{F_{\mathrm{Mag,x},0}}{(2\pi G\sigma^2_{n,0})} = -\frac{ik'_x}{k'_z}\,\tilde{B}_{\mathrm{ref}}\,(1+k'_z\,\tilde{Z}_0)\,\delta B'^{\mathrm{AD}}_{z,\mathrm{eq}}\,e^{i(kx-\omega t)}. \tag{2.132}$$

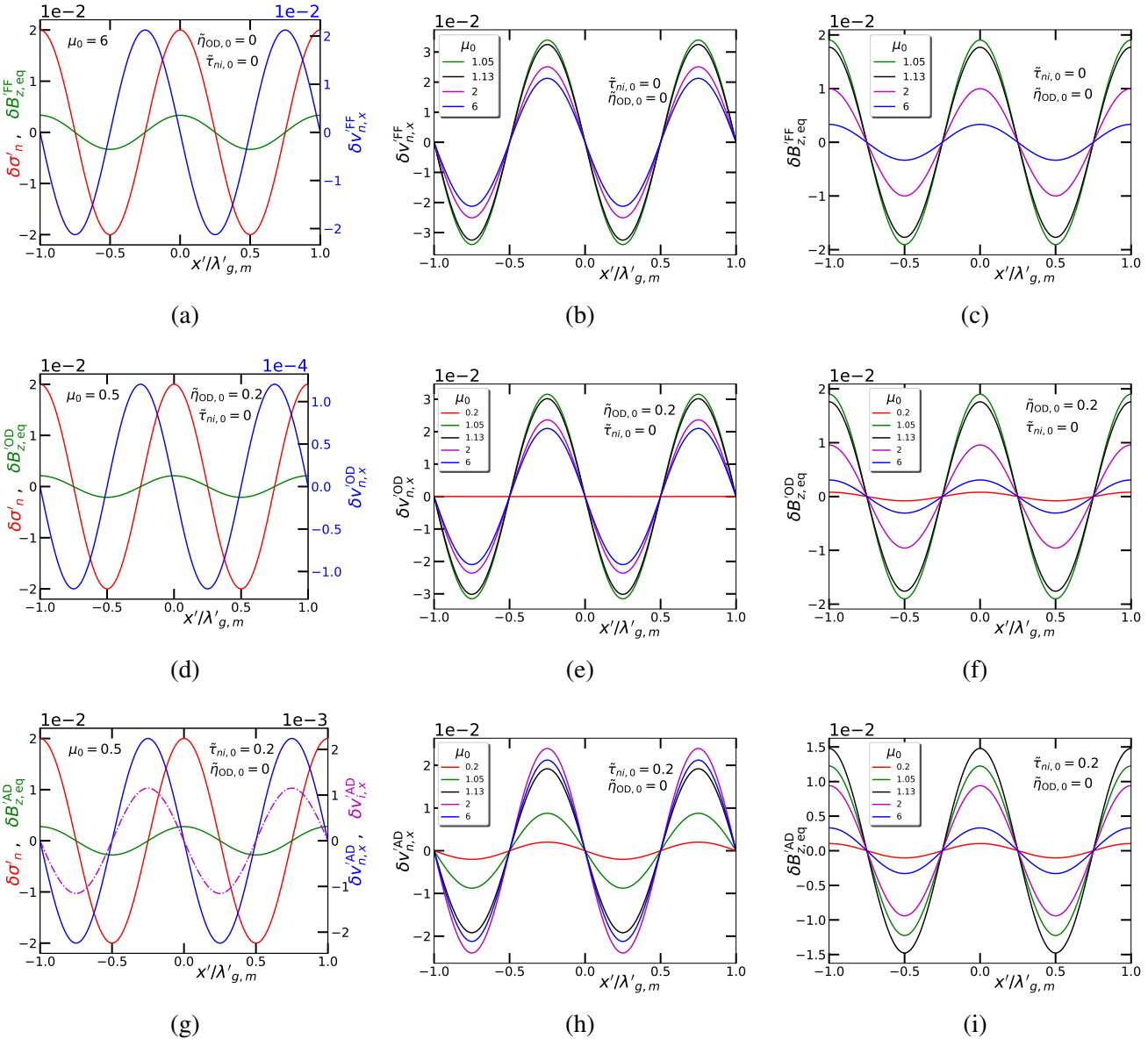

Figure 2.16: Normalized amplitudes of perturbed eigenfunctions as a function of $x'/\lambda'_{g,m}$ ($x' = x/L_0$, $\lambda'_{g,m} = \lambda_{g,m}/L_0$). The upper, middle and lower panels show the cases of flux-freezing (FF), Ohmic dissipation (OD), ambipolar diffusion (AD), respectively. The first column (a, d, g) of each of three panels represents the spatial variation of normalized perturbed column density field ($\delta\sigma'_n$) (red), perturbed velocity field for neutrals ($\delta v'_{n,x}$), perturbed magnetic field ($\delta B'_{z,\rm eq}$) for a fixed μ_0. For the case with AD the perturbed normalized velocity fields of ions ($\delta v'_{i,x}$) (magenta) is also shown in (g). The second (b, e, h) and third (c,f,i) column of these panels show the case of perturbed velocity field of neutrals ($\delta v'^{\rm FF}_{n,x}$, $\delta v'^{\rm OD}_{n,x}$, $\delta v'^{\rm AD}_{n,x}$) and magnetic field ($\delta B'^{\rm FF}_{z,\rm eq}$, $\delta B'^{\rm OD}_{z,\rm eq}$, $\delta B'^{\rm AD}_{z,\rm eq}$), respectively, for different values of μ_0 = 0.2 (red), 1.05 (green), 1.13 (black), 2 (magenta), 6 (blue). Note that for the flux-freezing case (a, b, c), only supercritical normalized mass-to-flux-ratios ($\mu_0 > 1$) are considered.

Applying the condition $k'_x = k'_z \equiv k'$ to the above expression and plugging it back into the linearized and normalized form of Equation 3.22 yields

$$\delta v'_{i,x} = \delta v'_{n,x} + \tilde{\tau}_{ni,0}\left(-i\tilde{B}_{\rm ref}\,(1 + k'\,\tilde{Z}_0)\right)\,\delta B'^{\rm AD}_{z,\rm eq}\,. \tag{2.133}$$

Further simplification of Equation 2.133 by substituting $\delta B'^{\rm AD}_{z,\rm eq}$ (see Equation 2.136) gives Equation 2.130.

Moving to the perturbed eigenfunctions for magnetic field, in the limit of flux-freezing ($\tilde{\eta}_{\rm OD,0} \to 0$, $\tilde{\tau}_{ni,0} \to 0$),

$$\delta B'^{\rm FF}_{z,\rm eq}(x, y, 0) = \tilde{B}_{\rm ref}\;\delta\sigma'_{n,a}\;{\rm Re}\left[e^{i(kx-\omega t)}\right]. \tag{2.134}$$

In the limit of only OD ($\tilde{\tau}_{ni,0} \to 0$),

$$\delta B'^{\rm OD}_{z,\rm eq}(x, y, t) = \left[\frac{\tilde{B}_{\rm ref}\lambda'^2}{\lambda'^2 + 4\pi^2\tau'_g\tilde{\eta}_{\rm OD,0}}\right]\delta\sigma'_{n,a}\;{\rm Re}\left[e^{i(kx-\omega t)}\right]. \tag{2.135}$$

In the limit of only AD ($\tilde{\eta}_{\rm OD,0} \to 0$),

$$\delta B'^{\rm AD}_{z,\rm eq}(x, y, t) = \left[\frac{\tilde{B}_{\rm ref}\lambda'}{\lambda' + 2\pi\tau'_g\tilde{\tau}_{ni,0}\tilde{B}^2_{\rm ref}\left(1 + \frac{2\pi\tilde{Z}_0}{\lambda'}\right)}\right]\delta\sigma'_{n,a}\;{\rm Re}\left[e^{i(kx-\omega t)}\right]. \tag{2.136}$$

At $t = 0$, considering only the initial real amplitude, ${\rm Re}[e^{i(kx-\omega t)}]$ and ${\rm Re}[e^{i(\frac{\pi}{2}+kx-\omega t)}]$ can be written as $\cos(2\pi x/\lambda)$ and $-\sin(2\pi x/\lambda)$, respectively. By defining the correspondence between the perturbed physical variables in this way, we are selecting the eigenvector of the perturbation at a single wavelength (λ'). We call this a monochromatic perturbation that can excite a single eigenmode of our model cloud at $t = 0$, corresponding to a particular λ' for each different μ_0 (recall $\tilde{B}_{\rm ref} = 1/\mu_0$). When one initiates the time evolution of a model cloud in this fashion, the subsequent evolution is the continuous growth of that specific excited eigenmode. At $t = 0$, the perturbed eigenmodes can be written as the following:

$$\delta\sigma'_n(x, y, 0) = \delta\sigma'_{n,a}\;\cos\left(\frac{2\pi x}{\lambda}\right), \tag{2.137}$$

$$\delta v'_{n,x}(x,y,0) = -\frac{\lambda'}{2\pi\tau'_g}\,\delta\sigma'_{n,a}\,\sin\left(\frac{2\pi x}{\lambda}\right), \tag{2.138}$$

$$\delta v'_{i,x}(x,y,0) = -\left[\frac{\lambda'}{2\pi\tau'_g} - K_1\right]\,\delta\sigma'_{n,a}\,\sin\left(\frac{2\pi x}{\lambda}\right), \tag{2.139}$$

$$\delta B'^{\rm FF}_{z,\rm eq}(x,y,0) = \tilde{B}_{\rm ref}\;\delta\sigma'_{n,a}\,\cos\left(\frac{2\pi x}{\lambda}\right), \tag{2.140}$$

$$\delta B'^{\rm OD}_{z,\rm eq}(x,y,0) = \left[\frac{\tilde{B}_{\rm ref}\lambda'^2}{\lambda'^2 + 4\pi^2\tau'_g\tilde{\eta}_{\rm OD,0}}\right]\delta\sigma'_{n,a}\,\cos\left(\frac{2\pi x}{\lambda}\right), \tag{2.141}$$

$$\delta B'^{\rm AD}_{z,\rm eq}(x,y,0) = \left[\frac{\tilde{B}_{\rm ref}\lambda'}{\lambda' + 2\pi\tau'_g\tilde{\tau}_{ni,0}\tilde{B}^2_{\rm ref}\left(1+\frac{2\pi\tilde{Z}_0}{\lambda'}\right)}\right]\delta\sigma'_{n,a}\,\cos\left(\frac{2\pi x}{\lambda}\right). \tag{2.142}$$

Now, we are interested to study the spatial variation of these dimensionless perturbed real amplitudes, e.g., as a function of $x/\lambda\,(= x'/\lambda' = (x/L_0)/(\lambda/L_0))$. In this calculation, we take τ'_g as $\tau'_{g,m}$, the shortest growth time and λ' as $\lambda'_{g,m}$, the preferred length scale corresponding to the shortest timescale.

Figure 2.16 shows the spatial variation of the perturbed column density function ($\delta\sigma'_n$), the perturbed velocity field for neutrals ($\delta v'_{n,x}$) and ions ($\delta v'_{i,x}$), and perturbed equatorial magnetic field ($\delta B'_{z,\rm eq}$) for three different MHD regimes: flux-frozen (FF), OD, and AD. We adopt $\delta\sigma'_{n,a} = 0.02$ to illustrate the regime of linear disturbances. Overall, we notice that adding a small amplitude perturbation to the initial column density ($\delta\sigma'_n$) gives rise to a perturbed magnetic field (as denoted by $\delta B'^{\rm FF}_{z,\rm eq}$, $\delta B'^{\rm OD}_{z,\rm eq}$, $\delta B'^{\rm AD}_{z,\rm eq}$) that follows the similar trend as $\delta\sigma'_n$ but has a relatively smaller amplitude as shown for each individual case (see the green line in Figure 2.16 a, d, g). This implies that the perturbation in the magnetic field will grow in the same way as the column density because the field lines are (at least partially) attached to matter. Whereas, the perturbed velocity field ($\delta v'_{n,x}$ and $\delta v'_{i,x}$) evolves keeping a phase-shift of $\pi/2$ with respect to the perturbed column density field for all three cases, denoting inward motion toward the density peak. For the case of OD, $\delta v'_{n,x} = \delta v'_{i,x}$ and for the case of AD we need to study the velocities separately (see Figure 2.17 for the detailed discussion). For the case of flux-freezing, as

shown by the upper panel of Figure 2.16 (see a, b, c), we study eigenfunctions for supercritical clouds. For the OD and AD cases we study the subcritical as well as supercritical clouds, as shown in the middle panel (see Figure 2.16 d, e, f) and lower panel (see Figure 2.16 g, h, i), respectively. In the flux-frozen case, we find that the amplitude of $\delta v_{n,x}^{\prime \mathrm{FF}}$ gradually decreases as μ_0 increases (see Figure 2.16b). In contrast, for the case with OD and AD (see Figure 2.16e and f, respectively), as μ_0 goes from a subcritical value to a supercritical region, $\delta v_{n,x}^{\prime \mathrm{OD}}$ and $\delta v_{n,x}^{\prime \mathrm{AD}}$ attain a maximum at a nearly transcritical μ_0. Similarly, from Figure 2.16(c) we notice that maximum amplitude of the perturbed magnetic field for the case of flux-frozen goes down rapidly as μ_0 increases implying that the magnetic field contribution becomes less effective as it moves to a more supercritical regime. Whereas, we see that maximum amplitude of the perturbed magnetic field for the case of OD and AD increase up to a certain μ_0 and then drop off for greater μ_0 as seen from Figure 2.16(f) and (i) respectively. The value of μ_0 with the peak perturbed magnetic field amplitude corresponds to the peak preferred length scale for the model with $\tilde{\eta}_{\mathrm{OD},0} = 0.2$ and $\tilde{\tau}_{ni,0} = 0$, as well as for the model with $\tilde{\tau}_{ni,0} = 0.2$ and $\tilde{\eta}_{\mathrm{OD},0} = 0$.

Figure 2.17(a) and (b) show a compact depiction of the maximum amplitude of the perturbed velocity field as a function of μ_0 for the cases with only OD and only AD, respectively. For the case with only OD, neutrals and all the charged particles move collectively as a single fluid. Hence, the perturbed velocity is the same and is identified only by $|\delta v_{n,x}^{\prime \mathrm{OD}}|_{\mathrm{max}}$ which is equal to $|\delta v_{i,x}^{\prime \mathrm{OD}}|_{\mathrm{max}}$, (recall Equation 2.23). However, for the case of only AD, one can obtain the perturbed velocity field separately for ions and neutrals. We find that the maximum amplitude of perturbed velocity for ions ($|\delta v_{i,x}^{\prime \mathrm{AD}}|_{\mathrm{max}}$) is much less than that of neutrals ($|\delta v_{n,x}^{\prime \mathrm{AD}}|_{\mathrm{max}}$) over the entire subcritical region. With increasing $\tilde{\eta}_{\mathrm{OD},0}$ and $\tilde{\tau}_{ni,0}$, the maximum amplitude of perturbed infall velocity gradually increases for $\mu_0 < 1$. Finally, in the highly supercritical regime ($\mu_0 \sim 10$), all the curves for nonideal MHD cases attain the limiting value obtained for the flux-frozen (FF) case. This is because in this limit, the motion is dominated by gravity and all the particles move together.

Figure 2.17(c) and (d) present the maximum amplitude of the perturbed magnetic field as a function of μ_0 for OD and AD, respectively. For $|\delta B_{z,\mathrm{eq}}^{\prime \mathrm{OD}}|_{\mathrm{max}}$ and $|\delta B_{z,\mathrm{eq}}^{\prime \mathrm{AD}}|_{\mathrm{max}}$, the peaks occur at nearly transcritical values that correspond to the peak preferred length scale for each respective case as seen in Figure 2.8(b) and (d). This feature uncovers the fact that magnetic

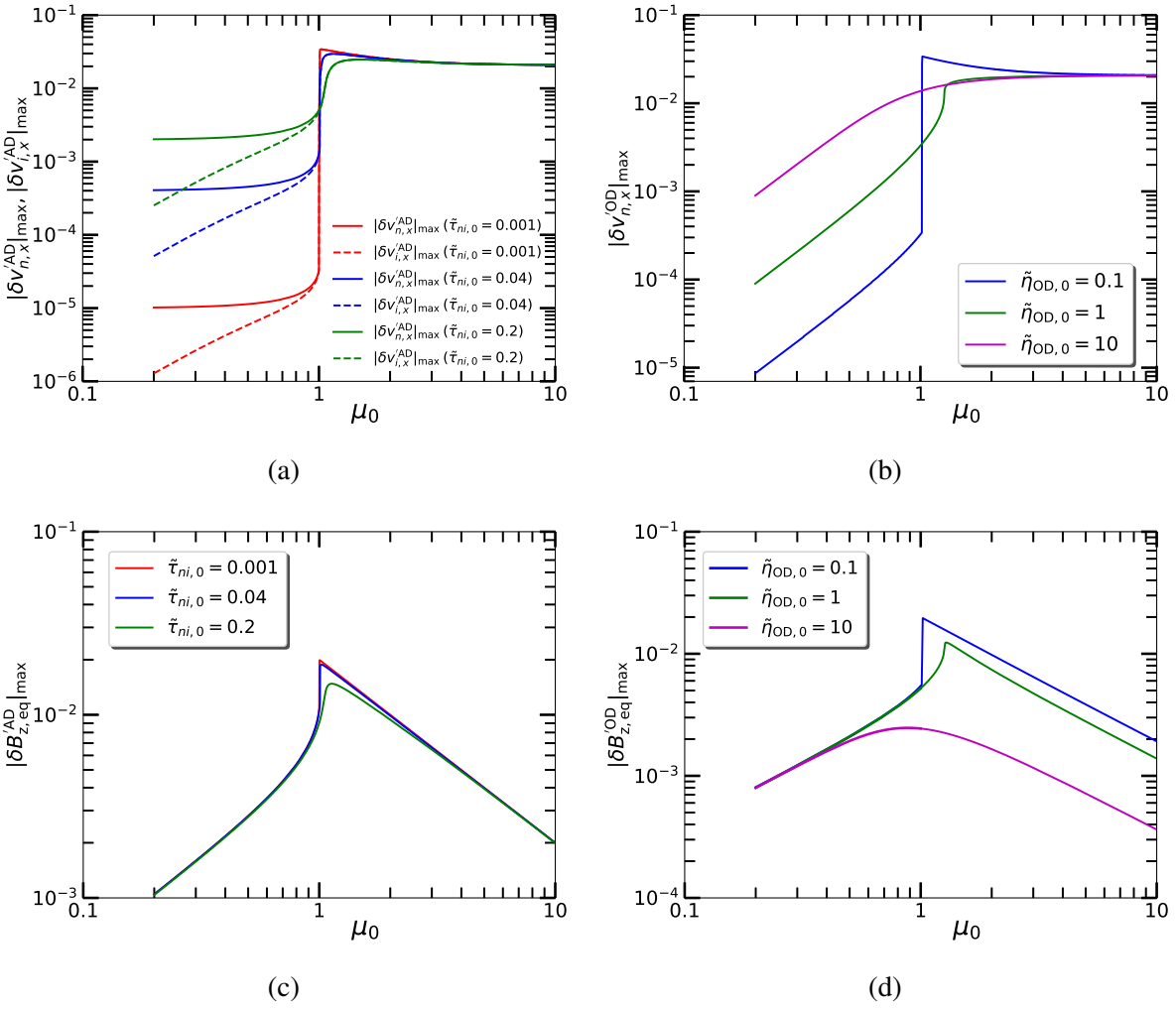

Figure 2.17: Normalized maximum amplitude of perturbed velocity field and perturbed magnetic field as a function of normalized mass-to-flux-ratio (μ_0). Upper left and lower left panel shows the cases for ambipolar diffusion with different normalized neutral-ion collision times $\tilde{\tau}_{ni,0} = 0.001, 0.04, 0.2$. Upper right and lower right panel shows the cases for Ohmic dissipation with different normalized Ohmic diffusivity $\tilde{\eta}_{OD,0} = 0.1, 1, 10$.

field provides the greatest support at a specific μ_0 that corresponds to the peak preferred length scale of gravitational instability. In the hydrodynamic limit ($\mu_0 \to \infty$), all the curves for FF, OD, and AD (see Equations (2.140) to (2.142)) will diminish to zero.

Not surprisingly, the shortest growth timescale as obtained in Figure 2.8(a) and (c) can also be deduced using the maximum amplitude of perturbed velocity field of neutrals for each

respective case (i.e., FF, AD, OD), using

$$\tau'_{g,m} = \frac{\lambda'_{g,m}}{\left|\delta v'_{n,x}\right|_{\max}} \frac{\delta\sigma'_{n,a}}{2\pi}\,, \tag{2.143}$$

which is derived from Equation 2.138. Coming to the case of AD, we know that collisions between neutrals and ions give rise to a drift speed between the two fluids. For ion fluid there is a balance between the Lorentz force and the drag force due to friction with neutrals. While for the neutral fluid, the inward pull of gravity is opposed by collisions with ions and other forces.

In the subcritical regime ($\mu_0 < 1$) the neutrals also come into an effective force-balance, between gravity and the collisions with ions. As a consequence, the infall motion of the neutrals ($|\delta v'^{\rm AD}_{n,x}|_{\max}$) gets plateaued at a terminal velocity and becomes independent of μ_0. Therefore, the timescale of contraction reaches a saturation in the regime $\mu_0 < 1$. But the ions are still tied to the field lines and hence the infall motion of ions as denoted by $|\delta v'^{\rm AD}_{i,x}|_{\max}$ gradually increases toward the supercritical regime. For the case of only OD, all particles move together, but collisions cause a loss of induced current, which dissipates the magnetic flux. When this happens in the subcritical clouds, it is a cause for slow contraction of the perturbed column density field.

2.6.9 Calculation of W_*

Using the thin-disk formalism, we earlier calculated the thermal midplane pressure for the neutrals including the effects of the weight of the gas column, the external pressure, and the magnetic pressure. Now, we investigate the effect of a central star (once present) of mass M_* by including it in our vertical pressure balance equation (Dapp et al., 2012), which becomes

$$\rho_{n,0} c_s^2 = \frac{\pi}{2} G\sigma_{n,0}^2 + P_{\rm ext} + W_*, \tag{2.144}$$

where W_* is the extra vertical squeezing due to the newly formed star's gravitational field, integrated up to the disk's local vertical finite half-thickness Z_0. Therefore, it is

$$W_* = 2GM_*\rho_{n,0} \int_0^{Z_0} \frac{z\,dz}{(r^2+z^2)^{3/2}}\,, \tag{2.145}$$

where z is the vertical coordinate and $r^2 = x^2 + y^2$. Using the one-zone approximation we integrate from $z = 0$ to a fixed Z_0 ($= \sigma_{n,0}/(2\rho_{n,0})$). Then we do a negative binomial expansion of the integrated result $\left[1/r - 1/(r^2 + Z_0^2)^{1/2}\right]$ under the approximation $Z_0/r \ll 1$, keeping leading order terms to yield

$$W_* = \frac{GM_*\rho_{n,0}Z_0^2}{r^3} = \frac{GM_*\sigma_{n,0}^2}{4\rho_{n,0}r^3}\,. \tag{2.146}$$

Next, we calculate a surface density keeping $\rho_{n,0}$ fixed. Substituting W_* into Equation 2.144, and using Equation 2.146, one finds the modified expression

$$\sigma_{n,0} = \left[\frac{\rho_{n,0}\ c_s^2}{\frac{\pi}{2}G(1+\tilde{P}_{\rm ext}) + \frac{GM_*}{4\rho_{n,0}r^3}}\right]^{\frac{1}{2}}\,. \tag{2.147}$$

We choose $M_* = 0.01\ M_\odot$ and $r = 50$ AU, corresponding to a very early stage of star formation, yielding $M_*/(4\rho_{n,0}r^3) = 0.03$ and $\sigma_{n,0} = 59.36$ g cm^{-2} from Equation 2.147, which is roughly the same as the protostellar disk surface density for $T = 30$ K if we take $W_* = 0$ in our model. Therefore, we see that Equation 2.147 can be simplified to the former Equation 2.41 when $M_* = 0$. Whereas, at a later stage of protostar formation, taking $M_* = 0.5\ M_\odot$ and $r = 50$ AU, we find $\sigma_{n,0} = 43.53\,{\rm g\,cm^{-2}}$ since $M_*/(4\rho_{n,0}r^3) = 1.54$. We can also write a generalized expression for Z_0 including the effects of M_* as follows:

$$Z_0 = \frac{1}{2\rho_{n,0}}\left[\frac{\rho_{n,0}\ c_s^2}{\frac{\pi}{2}G(1+\tilde{P}_{\rm ext}) + \frac{GM_*}{4\rho_{n,0}r^3}}\right]^{\frac{1}{2}}\,. \tag{2.148}$$

For the case of $M_* = 0$, the above expression can be reduced to $Z_0 = \sigma_{n,0}/(2\rho_{n,0})$ using Equation 2.41. Using Equation 2.148, the values of Z_0 are calculated to be 5.11 AU and 3.74 AU for $M_* = 0.01\ M_\odot$ and $0.5\ M_\odot$, respectively.

Bibliography

Allen A., Shu F. H., Li Z.-Y., 2003, ApJ, 599, 351

Alves F. O., Girart J. M., Caselli P., Franco G. A. P., Zhao B., Vlemmings W. H. T., Evans M. G., Ricci L., 2017, A&A, 603, L3

Andrews S. M., et al., 2018, ApJ, 869, L41

Aso Y., et al., 2015, Keplerian and Infall Motions Around the Late-Phase Protostar TMC-1A. p. 285

Aso Y., et al., 2017, ApJ, 850, L2

Bailey N. D., Basu S., 2012, ApJ, 761, 67

Basu S., Ciolek G. E., 2004, ApJ, 607, L39

Basu S., Mouschovias T. C., 1994, ApJ, 432, 720

Basu S., Mouschovias T. C., 1995a, ApJ, 452, 386

Basu S., Mouschovias T. C., 1995b, ApJ, 453, 271

Basu S., Vorobyov E. I., 2012, ApJ, 750, 30

Basu S., Ciolek G. E., Wurster J., 2009a, New A, 14, 221

Basu S., Ciolek G. E., Dapp W. B., Wurster J., 2009b, New A, 14, 483

Binney J., Tremaine S., 2008, Galactic Dynamics: Second Edition. Princeton University Press, USA

Bjerkeli P., van der Wiel M. H. D., Harsono D., Ramsey J. P., Jørgensen J. K., 2016, Nature, 540, 406

Bodenheimer P., 1995, ARA&A, 33, 199

Brauer R., Wolf S., Flock M., 2017, A&A, 607, A104

Chandrasekhar S., Fermi E., 1953, ApJ, 118, 116

Ching T.-C., Lai S.-P., Zhang Q., Yang L., Girart J. M., Rao R., 2016, ApJ, 819, 159

Ciolek G. E., Basu S., 2006, ApJ, 652, 442

Ciolek G. E., Mouschovias T. C., 1993, ApJ, 418, 774

Ciolek G. E., Mouschovias T. C., 1994, ApJ, 425, 142

Ciolek G. E., Mouschovias T. C., 1998, ApJ, 504, 280

Dapp W. B., Basu S., 2010, A&A, 521, L56

Dapp W. B., Basu S., Kunz M. W., 2012, A&A, 541, A35

Davis L., 1951, Physical Review, 81, 890

Fiedler R. A., Mouschovias T. C., 1993, ApJ, 415, 680

Galli D., Lizano S., Shu F. H., Allen A., 2006, ApJ, 647, 374

Gonçalves J., Galli D., Girart J. M., 2008, A&A, 490, L39

Hirano S., Machida M. N., 2019, MNRAS, 485, 4667

Hirano S., Tsukamoto Y., Basu S., Machida M. N., 2020, ApJ, 898, 118

Huang J., et al., 2018, ApJ, 869, L43

Indebetouw R., Zweibel E. G., 2000, ApJ, 532, 361

Kataoka A., et al., 2015, ApJ, 809, 78

Kataoka A., et al., 2016, ApJ, 831, L12

Kratter K., Lodato G., 2016, ARA&A, 54, 271

Kudoh T., Basu S., 2011, ApJ, 728, 123

Kudoh T., Basu S., Ogata Y., Yabe T., 2007, MNRAS, 380, 499

Lee C.-F., Ho P. T. P., Li Z.-Y., Hirano N., Zhang Q., Shang H., 2017, Nature Astronomy, 1, 0152

Lee C.-F., Li Z.-Y., Hirano N., Shang H., Ho P. T. P., Zhang Q., 2018, ApJ, 863, 94

Lefloch B., et al., 2015, A&A, 581, A4

Li Z. Y., Banerjee R., Pudritz R. E., Jørgensen J. K., Shang H., Krasnopolsky R., Maury A., 2014, in Beuther H., Klessen R. S., Dullemond C. P., Henning T., eds, Protostars and Planets VI. University of Arizona Press, p. 173 (arXiv:1401.2219), doi:10.2458/azu_uapress_9780816531240-ch008

Lizano S., Galli D., Cai M. J., Adams F. C., 2010, ApJ, 724, 1561

Machida M. N., Inutsuka S.-i., Matsumoto T., 2007, ApJ, 670, 1198

Machida M. N., Matsumoto T., Inutsuka S.-i., 2016, MNRAS, 463, 4246

Masson J., Chabrier G., Hennebelle P., Vaytet N., Commerçon B., 2016, A&A, 587, A32

McDaniel E. W., Mason E. A., 1973, Mobility and diffusion of ions in gases. John Wiley and Sons, USA

Mellon R. R., Li Z.-Y., 2008, ApJ, 681, 1356

Mestel L., Spitzer L. J., 1956, MNRAS, 116, 503

Morton S. A., 1991, PhD thesis, Illinois Univ. at Urbana-Champaign, Savoy.

Mott N. F., Massey H. S. W., 1949, The theory of atomic collisions. 2nd ed.. Oxford University Press, Oxford

Mouschovias T. C., 1978, in Gehrels T., Matthews M. S., eds, IAU Colloq. 52: Protostars and Planets. University of Arizona Press, p. 209

Mouschovias T. C., 1996, in Tsinganos K. C., Ferrari A., eds, Vol. 481, NATO Advanced Science Institutes (ASI) Series C. Kluwer Academic Publishers, pp 505–538

Mouschovias T. C., Ciolek G. E., 1999, in Lada C. J., Kylafis N. D., eds, Vol. 540, NATO Advanced Science Institutes (ASI) Series C. Kluwer Academic Publishers, p. 305

Myers P. C., Stephens I. W., Auddy S., Basu S., Bourke T. L., Hull C. L. H., 2020, ApJ, 896, 163

Nakano T., Nakamura T., 1978, PASJ, 30, 671

Nakano T., Nishi R., Umebayashi T., 2002, ApJ, 573, 199

Ohashi N., et al., 2014, ApJ, 796, 131

Pattle K., et al., 2017, ApJ, 846, 122

Pérez L. M., et al., 2016, Science, 353, 1519

Planck Collaboration et al., 2015, A&A, 576, A106

Planck Collaboration et al., 2016, A&A, 586, A138

Plunkett A. L., Arce H. G., Mardones D., van Dokkum P., Dunham M. M., Fernández-López M., Gallardo J., Corder S. A., 2015, Nature, 527, 70

Saigo K., Tomisaka K., 2006, ApJ, 645, 381

Sakai N., et al., 2014, Nature, 507, 78

Shu F. H., 1992, Physics of Astrophysics II. Gas Dynamics. University Science Books, https://books.google.ca/books?id=QH1uQgAACAAJ

Shu F. H., Adams F. C., Lizano S., 1987, ARA&A, 25, 23

Shu F. H., Allen A., Shang H., Ostriker E. C., Li Z.-Y., 1999, in Lada C. J., Kylafis N. D., eds, Vol. 540, NATO Advanced Science Institutes (ASI) Series C. Kluwer Academic Publishers, p. 193

Spitzer L., 1978, Physical processes in the interstellar medium. John Wiley and Sons, USA, doi:10.1002/9783527617722

Stamatellos D., Whitworth A. P., 2009, MNRAS, 392, 413

Tokuda K., et al., 2016, ApJ, 826, 26

Tomida K., Okuzumi S., Machida M. N., 2015, ApJ, 801, 117

Toomre A., 1964, ApJ, 139, 1217

Tsukamoto Y., 2016, PASA, 33, e010

Tsukamoto Y., Okuzumi S., Iwasaki K., Machida M. N., Inutsuka S., 2018, ApJ, 868, 22

Vlemmings W. H. T., Surcis G., Torstensson K. J. E., van Langevelde H. J., 2010, MNRAS, 404, 134

Vorobyov E. I., 2016, A&A, 590, A115

Vorobyov E. I., Basu S., 2006, ApJ, 650, 956

Vorobyov E. I., Basu S., 2007, MNRAS, 381, 1009

Vorobyov E. I., Basu S., 2010a, ApJ, 714, L133

Vorobyov E. I., Basu S., 2010b, ApJ, 719, 1896

Vorobyov E. I., Basu S., 2015, ApJ, 805, 115

Wurster J., Li Z.-Y., 2018, Frontiers in Astronomy and Space Sciences, 5, 39

Wurster J., Bate M. R., Price D. J., 2018, MNRAS, 476, 2063

Yang H., Li Z.-Y., Looney L., Stephens I., 2016a, MNRAS, 456, 2794

Yang H., Li Z.-Y., Looney L. W., Cox E. G., Tobin J., Stephens I. W., Segura-Cox D. M., Harris R. J., 2016b, MNRAS, 460, 4109

Chapter 3

Variation of the core lifetime and fragmentation scale in molecular clouds as an indication of ambipolar diffusion

A version of this chapter has been published as a Letter in the Astronomy & Astrophysics Journal as Das I., Basu S., & Andre P. 2021 A&A 649, L13.
DOI:10.1051/0004-6361/202140404

3.1 Introduction

There are still many gaps in our understanding of the condensation of dense structures out of the diffuse interstellar medium (ISM). There are reasons to think that the influence of the magnetic field is preponderant. In recent years, remarkable observational data have been obtained by Planck Collaboration et al. (2016) that allow a quantitative analysis of the relative orientation of the magnetic field within a set of nearby ($d < 450$ pc) molecular clouds. These observations have helped to establish the significance of magnetic fields in the formation of dense structures on physical scales ranging from approximately 1 to 10 pc. They show a clear correlation in the direction of elongation of high-density regions (number column density $N_{\rm H} \gtrsim 10^{22}$ cm^{-2}), which appears to be perpendicular to the ambient magnetic field direction.

Molecular clouds are known to contain hierarchical nested density structures with, for example, clumps, filaments, and cores (see André et al., 2014; Dobbs et al., 2014; Heyer & Dame,

2015). Pokhrel et al. (2018) studied hierarchical structure over five different scales (ranging from $\gtrsim$ 10 pc to 10 AU) in the Perseus molecular cloud using new observations from the *Herschel*, the *James Clerk Maxwell Telescope* (JCMT), the *Submillimeter Array* (SMA), the *Very Large Array* (VLA). They compared the number of fragments with the number of Jeans masses at each scale to calculate the Jeans efficiency, which is the ratio of observed to expected number of fragments. Könyves et al. (2015) used the results of the *Herschel* Gould Belt survey (HGBS- André et al., 2010) in the Aquila molecular cloud complex, and compared the numbers of prestellar cores in various density bins to the number of young stellar objects (YSOs). They estimated that the lifetime of prestellar cores is $\sim$ 1 Myr, which is about four times longer than the core free-fall time, and that the lifetime decreases as the average core density increases. While current observations cannot determine whether ambipolar diffusion (neutral-ion slip) is occurring during the initiation of gravitational collapse, nonideal magnetohydrodynamic (MHD) simulations suggest it plays an important role in establishing mildly supercritical mass-to-flux ratios in prestellar cores, whether starting from small-amplitude perturbations (see Kudoh et al., 2007; Basu et al., 2009a) or from large-scale turbulent or converging flows (see Nakamura & Li, 2005; Basu et al., 2009b; Chen & Ostriker, 2014). Furthermore, in mildly supercritical regions, the hybrid modes driven by gravity and neutral-ion slip result in preferred length scales and growth times that can significantly exceed the Jeans scale and free-fall time, respectively (see Basu & Ciolek, 2004; Ciolek & Basu, 2006; Bailey & Basu, 2012).

In this Letter, we probe the variation of lifetime and fragmentation scales of dense structures in molecular clouds as a consequence of ambipolar diffusion. We apply the results of a linear analysis of ambipolar-diffusion-driven fragmentation in planar, isothermal, weakly ionized, self-gravitating sheetlike magnetic clouds. The calculated shortest growth timescale and preferred fragmentation mass for collapse are used to explain the observationally estimated lifetime of prestellar cores and the number of enclosed cores in a parent clump. In Section 3.2 we describe the analytic model, in Section 3.3 we present a comparison with the observational findings, and finally, in Section 5.4 we summarize and draw conclusions from our results.

3.2 Analytic model

We model interstellar molecular clouds as self-gravitating, partially ionized, isothermal, magnetic, planar, thin sheets with infinite extent in the x- and y-directions and a local vertical half-thickness $Z(x, y, t)$. Although sheets are an idealized geometry, a structured background state like a sheet or filament does capture the essential feature of a preferred scale of instability that is related to the local density scale length; this would not appear if assuming a uniform background. We note that the critical length scale and timescale using thin-disk geometry can differ typically by a factor of approximately two as compared to using a spherical (uniform) geometry as the thin sheet exhibits stronger gravitational field for a fixed surface density (and mass). Our static initial state also does not include the effect of any large-scale motion that modifies the evolutionary timescale. The nonaxisymmetric equations and formulations of the model have been described in detail in several papers (Ciolek & Basu, 2006; Bailey & Basu, 2012). The evolution equations include the nonideal MHD effect of ambipolar diffusion, the process by which neutrals are partially coupled to magnetic field through collisions with ions. This effect is quantified by the neutral-ion collision (momentum-exchange) timescale (e.g., Basu & Mouschovias, 1994):

$$\tau_{ni} \equiv 1.4 \frac{m_i + m_n}{m_i} \frac{1}{n_i \langle \sigma w \rangle_{i\mathrm{H}_2}}, \tag{3.1}$$

where $\langle \sigma w \rangle_{i\mathrm{H}_2}$ is the average collision rate between ions of mass m_i (singly ionized Na, Mg, and HCO, adopted to have a mass of 25 amu) and neutrals of mass m_n (= 2.33 amu). We adopt a neutral–ion collision rate between H_2 and HCO^+ of $1.69 \times 10^{-9} \mathrm{cm^3 s^{-1}}$ (McDaniel & Mason, 1973). For the ion number density n_i, there is an assumed constant power-law approximation of the form $n_i \propto n_{n,0}^{1/2}$ (Ciolek & Basu, 2006; Ciolek & Mouschovias, 1998), where $n_{n,0}$ is the initial uniform number density of neutrals. The typical observed ionization fraction in molecular clouds (primarily due to cosmic ray ionization) (Elmegreen, 1979; Tielens, 2005) is

$$\chi_i = 10^{-7} \left(\frac{n_{n,0}}{10^4 \ \mathrm{cm^{-3}}} \right)^{-1/2}. \tag{3.2}$$

Such low ionization means that ambipolar diffusion is unavoidable in molecular clouds, but there is still enough coupling with the charged species for the neutrals to be affected by the magnetic field. This is because of the high polarizability of the neutrals, particularly H_2 molecules (Osterbrock, 1961). The threshold for whether a region of a molecular cloud is magnetically dominated or gravitationally dominated is given by the normalized mass-to-flux ratio,

$$\mu_0 \equiv 2\pi G^{1/2} \frac{\sigma_{n,0}}{B_{\rm ref}}, \tag{3.3}$$

where $\sigma_{n,0}$ is the initial uniform column density of the sheet, $B_{\rm ref}$ is the magnetic field strength of the background reference state, G is the universal gravitational constant, and $(2\pi G^{1/2})^{-1}$ is the critical mass-to-flux ratio for gravitational collapse (Nakano & Nakamura, 1978). Regions with $\mu_0 < 1$ are defined as subcritical, regions with $\mu_0 > 1$ are defined as supercritical, and regions with $\mu_0 \approx 1$ are defined as transcritical. For small amplitude perturbations, the governing equations can be combined to yield the following dispersion relation:

$$\begin{aligned}(\omega + i\,\theta)\left[\omega^2 - C_{\rm eff,0}^2\,k^2 + 2\pi G\sigma_{n,0}k\right] = \\ \omega\left[2\pi G\sigma_{n,0}k\mu_0^{-2} + k^2\,V_{A,0}^2\right],\end{aligned} \tag{3.4}$$

where

$$\theta = \tau_{ni,0}\left(2\pi G\sigma_{n,0}\mu_0^{-2}k + k^2 V_{A,0}^2\right) = \eta_{\rm AD,0}(k\,Z_0^{-1} + k^2), \tag{3.5}$$

ω is an angular frequency, and $k^2 \equiv k_z^2 = k_x^2 + k_y^2$, where k_x, k_y, k_z (or k) are the wavenumbers in the x-, y-, and z- directions, respectively. To obtain the dispersion relation as shown in Equation 3.4, the linearized perturbed MHD equations are used (see Section 3.5.1). Here, $C_{\rm eff,0}$ and $V_{A,0}$ are the local effective sound speed and the Alfvén speed, respectively. The term $C_{\rm eff,0}$ includes the effects of a restoring force due to an external pressure $P_{\rm ext}$. The dimensionless external pressure $\tilde{P}_{\rm ext}$ ($\equiv 2P_{\rm ext}/(\pi G\sigma_{n,0}^2)$) and temperature ($T$) are kept fixed at 0.1 and 10 K, respectively.

Figure 3.1 presents the normalized shortest growth timescale, $\tau_{g,m}/t_{\rm ff}$, and normalized preferred fragmentation mass, $M_{g,m}/M_{T,m}$, corresponding to this minimum timescale as a function of μ_0 for the case of normalized neutral–ion collision time $\tau_{ni,0}/t_0 = \tilde{\tau}_{ni,0} = 0.2$ which itself corresponds to Equation 3.2. Here, $t_{\rm ff}$ is the dynamical, i.e., free-fall time ($= Z_0/c_s$), $M_{T,m}$ is

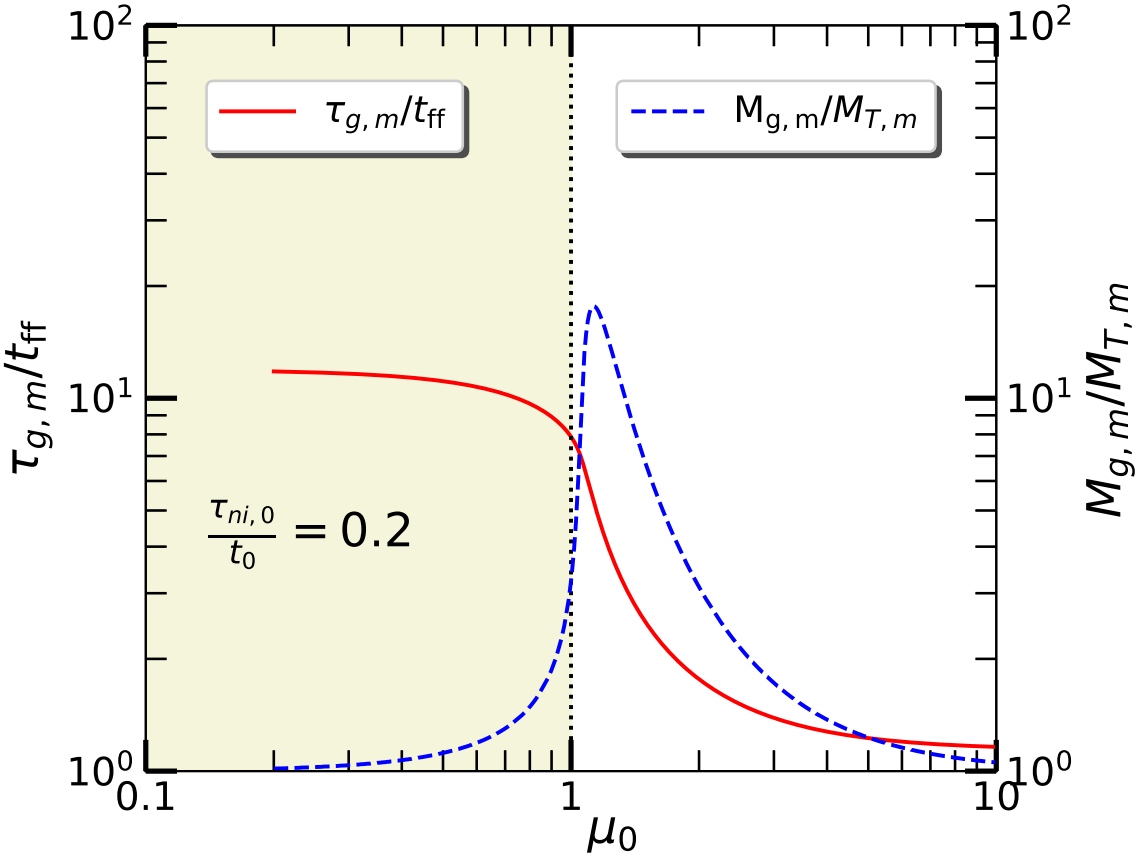

Figure 3.1: Growth timescale $\tau_{g,m}$ (in the units of dynamical or free-fall time $t_{\rm ff}$) and the preferred fragmentation mass $M_{g,m}$ (in the units of preferred thermal fragmentation mass $M_{T,m}$) of the most unstable mode as a function of the normalized mass-to-flux ratio (μ_0). The model utilizes the standard ionization fraction corresponding to a normalized neutral–ion collision time $\tau_{ni,0}/t_0 = \tilde{\tau}_{ni,0} = 0.2$. The shaded and unshaded zones represent the subcritical ($\mu_0 < 1$) and supercritical ($\mu_0 > 1$) regimes, respectively. The present paper focuses on the (mildly) supercritical regime.

the preferred thermal mass based on our model, and $M_{T,m} = (4\pi C_{\rm eff,0}^2/c_s^2)^2 M_0$, where M_0 is effectively the Jeans mass. See Section 3.5.1 for definitions and typical values of the units of time (t_0), length (L_0), and mass (M_0), and other parameters. For all objects shown in Table 3.2, we calculate $M_{g,m}$ in units of $M_c = \pi\sigma_{n,0}(L_0/2)^2 = \pi M_0/4$, as the perturbation is taken to be circular with radius $L_0/2$. As the mass-to-flux ratio goes to the subcritical regime where ambipolar diffusion drives the evolution, the curve of shortest growth timescale approaches a plateau. It is noteworthy that the peak preferred fragmentation mass for collapse exceeds the Jeans mass by a factor of up to ten. Furthermore, for $\tilde{\tau}_{ni,0} = 0.2$, the timescale for collapse of a subcritical region is around $10 - 12$ times longer than that of a supercritical region; this is the origin of the often-quoted result that the ambipolar diffusion time is approximately ten times the free-fall time (Mouschovias, 1991; Ciolek & Basu, 2006; Bailey & Basu, 2012; Das & Basu, 2021). Hereafter, for a better representation, we use n_n, σ_n, and μ instead of $n_{n,0}$, $\sigma_{n,0}$, μ_0, respectively. In this study, we are interested in the regime where the normalized mass-to-flux ratio μ remains in the range $1 \lesssim \mu \lesssim 2$. See Kunz & Mouschovias (2009) for an application of the linear theory in the subcritical regime to model core masses.

3.3 Observational correspondence to prestellar cores

In this section we discuss the relevance of our theoretical results to observational findings, focusing on the mildly supercritical regime.

3.3.1 Lifetime of prestellar cores

The technique for finding the timescale of the core-formation process was introduced by Beichman et al. (1986) in the context of IRAS sources. These authors studied the embedded YSOs within the core sample of Myers & Benson (1983) and Myers et al. (1983), and found that 35 cores had IRAS sources meeting the color-selection criteria of embedded YSOs and 43 had no embedded IRAS sources. Beichman et al. (1986) calculated the percentage of cores with embedded sources to estimate the lifetime of a core without an embedded YSO by comparing it with the lifetime of the embedded YSO phase. Using an estimated lifetime of cores with embedded class II sources of $1 - 2$ Myr (as discussed in Ward-Thompson et al., 1994; Evans et al., 2009), and assuming that the prestellar cores go on to form protostars, the prestellar core

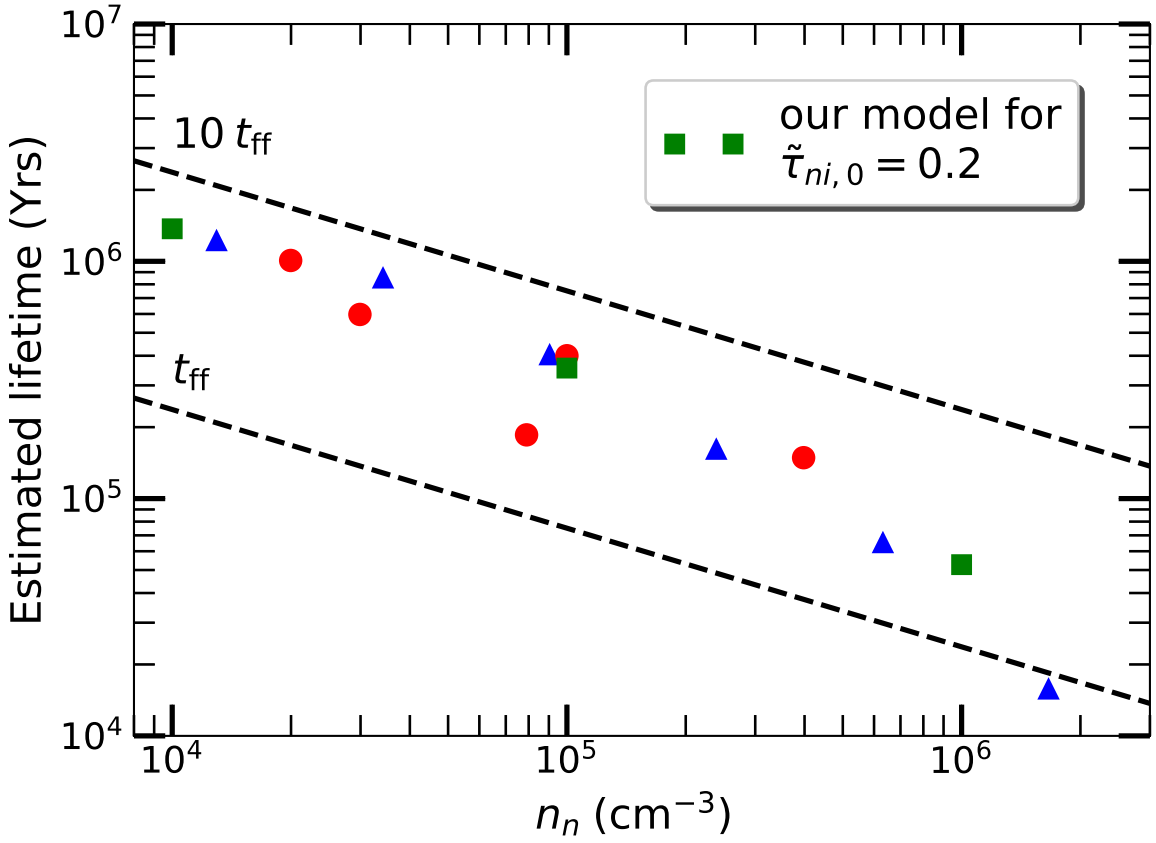

Figure 3.2: Estimated lifetime as a function of number density (n_n). The green filled squares are obtained from our model for a normalized neutral–ion collision time $\tilde{\tau}_{ni,0} = 0.2$. The blue filled triangles show the corresponding data points for the population of 446 candidate prestellar cores identified with *Herschel* in the Aquila cloud (Könyves et al., 2015). Earlier data from Ward-Thompson et al. (2007) are shown by the red circles for better comparison. The black dashed line shows the dynamical time (Z_0/c_s), i.e., the free-fall time, of our model.

lifetime is estimated to be

$$\tau = \frac{\text{\# of cores without embedded sources}}{\text{\# of cores with embedded sources}} \times [1-2]\ \text{Myr}. \tag{3.6}$$

This formula was used by Jessop & Ward-Thompson (2000) on a catalog of molecular cloud cores from the all-sky IRAS Sky Survey Atlas (ISSA), and their Fig. 6 (often called a "JWT" plot) shows the estimated lifetime versus mean density. In a similar way, Könyves et al. (2015) estimated the lifetime of prestellar cores (see their Fig. 9) by comparing the number of prestellar cores found with *Herschel* to the number of Class II YSOs detected by *Spitzer* in the Aquila cloud. This study had the advantage of considering a homogeneous sample of cores from a single cloud (Aquila), measured using a single telescope, tracer (dust), and analysis technique that separated prestellar (gravitationally bound) cores from starless (unbound) cores. Some of the underlying assumptions in these studies are: (1) that prestellar cores will evolve into YSOs in the future; and (2) that star formation proceeds at a roughly constant rate, at least when averaged over an entire cloud.

Figure 3.2 presents the core lifetime (values in green filled squares) estimated from our model as the instability growth time at a particular density n_n, when adopting a specific model for $B_{\rm ref}$ as a function of n_n (see Figure 3.4 and Equation 3.7 below). The corresponding estimated numbers based on the observations of candidate prestellar cores identified with *Herschel* (Könyves et al., 2015) and the literature data (Ward-Thompson et al., 2007) are also shown. We achieve the good correspondence by varying only one relationship, namely that between the normalized mass-to-flux-ratio μ and the number density n_n, with μ ranging from about 1.1 to 1.5 for n_n in the range of $10^4 - 10^6$ cm^{-3}. To calculate μ we evaluate σ_n using Equation 3.13. These values of μ are in the range of mildly supercritical values generally obtained from Zeeman detections and use of the Davis-Chandrasekhar-Fermi (DCF) method (Crutcher, 2012; Pattle & Fissel, 2019). The ionization level is set by the value $\tilde{\tau}_{ni,0} = 0.2$ corresponding to the standard value set by Equation 3.2. Our use of the instability growth time as a proxy for the evolutionary time is similar to the commonly used comparison of the free-fall time at a particular density with the evolutionary time of a core at that density. Figure 3.2 shows that the typical lifetime of prestellar cores decreases from $\sim$ 1.37 Myr for cores with a number density

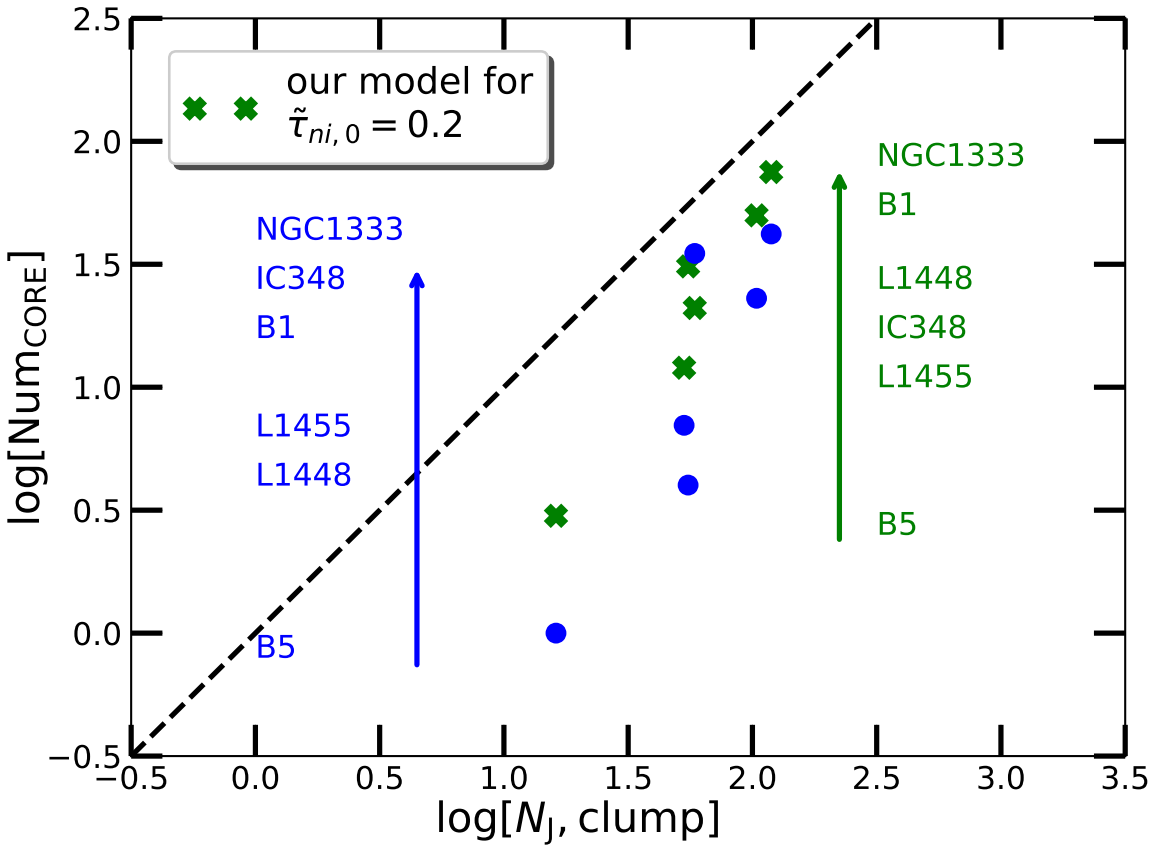

Figure 3.3: Number of enclosed cores (log[Num$_{\rm CORE}$]) as a function of Jeans number (log[$N_{\rm J,\,CLUMP}$]) of clumps. The blue filled circles represent the observed number of enclosed cores as found by Pokhrel et al. (2018). The green filled crosses are obtained from our model for a normalized neutral–ion collision time $\tilde{\tau}_{ni,0} = 0.2$. The black dashed line corresponds to an efficiency of unity.

of $\sim 10^4$ cm^{-3} to ~ 0.35 Myr at $\sim 10^5$ cm^{-3} , and to ~ 0.05 Myr at $\sim 10^6$ cm^{-3} (see Table 3.1). The timescale for collapse of a core with a number density of $\sim 10^4$ cm^{-3} is around $10 - 50$ times longer than that of a highly dense core of $\sim 10^5 - 10^6$ cm^{-3}. The highest density cores are significantly supercritical and evolve essentially on a free-fall timescale ($t_{\rm ff} = Z_0/c_s$) as shown in Figure 3.1. The lower black dashed line presents the dynamical timescale, or free-fall time, as a reference line.

3.3.2 Number of enclosed cores

Sadavoy et al. (2010) used point-source photometry to explore the dense cores in the Perseus star-forming complex as found in surveys with SCUBA (85 μm) and *Spitzer Space Telescope*

(3.6 – 70 μm). Mercimek et al. (2017) characterized the distribution of these cores inside the clumps. Pokhrel et al. (2018) analyzed the submillimeter starless or protostellar cores in the *Herschel* column density maps of Mercimek et al. (2017) and used the estimated mass and areas (see Table 3.2) to determine the average density of each clump for $A_V > 7$ mag. These authors used the dust temperatures from Sadavoy et al. (2014) to estimate the thermal support. To calculate the Jeans number ($N_{\rm J,\,CLUMP} \equiv M/M_{\rm J,th}$, i.e., the number of contained thermal Jeans masses $M_{\rm J,th}$) of the clumps, Pokhrel et al. (2018) used the line-of-sight averaged temperatures and mass derived in Sadavoy et al. (2014).

We fit the observations of the number of enclosed cores ($\rm Num_{CORE}$) in each clump as a function of the corresponding Jeans number of the clumps, as seen in Figure 3.3. We calculate $\rm Num_{CORE}$ in the context of our model by dividing the total clump mass M by the preferred fragmentation mass $M_{g,m}$, adopting $\tilde{\tau}_{ni,0} = 0.2$. We note that $M_{g,m}$ significantly exceeds $M_{\rm J,th}$ for mildly supercritical objects. The Jeans number $N_{\rm J,\,CLUMP}$ is the expected number of cores in the context of thermally regulated fragmentation. See Table 3.2 for detailed specifications of all the clumps. The clumps are arranged in an increasing order of $\rm Num_{CORE}$ (i.e., number of cores). Figure 3.3 shows that the number of cores (blue filled circles) increases with the Jeans number of the clumps, as shown in Figure 6 of Pokhrel et al. (2018). The filled green crosses represent our model values. The black dashed line shows the efficiency of unity ($\epsilon^{\rm th} = 1$, i.e., $\rm Num_{CORE} = N_{J,\,CLUMP}$) corresponding to purely thermally regulated fragmentation. The observations show fewer cores than that predicted with only thermal pressure. This hints at a larger threshold for fragmentation mass that includes effects beyond that set by thermal pressure alone. In our model, $M_{g,m}$ serves such a purpose as a magnetic-field-dependent instability threshold in contrast to a Jeans mass.

It is worth noting that the number of fragmented cores is also dependent on the clump mass. The relatively massive clumps are able to generate more cores and $\rm Num_{CORE}$ comes closer to (but stays below) the value of $N_{\rm J,\,CLUMP}$. Therefore, the number density might not be the only key parameter in this context. The nonthermal motions in these massive clouds could also play a role. However, using the nonthermal dispersion in the calculation of the Jeans mass would not fit the observations for these clouds either, predicting many fewer cores than are observed (see the discussion in Pokhrel et al., 2018).

The inability of the observed nonthermal dispersion to be used as the source of an internal pressure when estimating the number of fragmented cores could possibly be attributed to the following reasons. First, the nonthermal motions may arise at least in part due to large-scale velocity gradients, in which case they cannot act as an effective pressure. Simulations in turbulent boxes that have global stability show that small-scale collapse still occurs unless the driving scale and/or power spectrum is peaked at extremely short scales (e.g., Vazquez-Semadeni et al., 1996; Klessen et al., 2000). Second, the nonthermal dispersion may be dominated by motions in the lowest densities that are traced, while a dense layer that actually undergoes fragmentation may have a lower dispersion that is closer to the thermal value. The latter explanation is supported by simulations (Kudoh & Basu, 2003, 2006; Folini et al., 2004) that show that the velocity dispersion peaks in the low-density regions of a stratified molecular cloud. In observations as well, the velocity dispersion peaks in low-density regions and starless dense cores correspond to minima in velocity dispersion maps (see, e.g., Fig. 13 of Friesen et al., 2017).

3.3.3 Estimation of magnetic field

For gravitationally contracting fragments (particularly cores) in magnetic interstellar clouds, the relation between magnetic-field strength $B_{\rm ref}$ and gas number density n_n is of considerable interest. In Figure 3.4, we present $\log(B_{\rm ref}/\mu G)$ (which is obtained from our model) as a function of $\log(n_n/{\rm cm}^{-3})$ for the two different density regimes shown in Figure 3.2 and Figure 3.3 based on our model for $\tilde{\tau}_{ni,0} = 0.2$. We use the least-squares method to find a best fit to the data:

$$\frac{B_{\rm ref}}{10\,\mu{\rm G}} = A\left(\frac{n_n}{10^4\ {\rm cm}^{-3}}\right)^{\kappa}, \tag{3.7}$$

where $\kappa = 0.427$ and $A = 1.766$, and shown by the black dashed line in Figure 3.4.

Mestel (1965) argued that for a spherically and isotropically collapsing magnetic cloud, the scaling between the magnetic field strength and the density is $B \propto n_n^{2/3}$. This argument is true for a quasi-spherical collapse where both the mass M and the magnetic-flux Φ are being conserved, and the magnetic field energy is insignificant compared to the gravitational energy. Later, Mouschovias (1976a,b) argued that the plasma β ($= 8\pi\rho c_s^2/B^2$) remains constant during self-contraction of a cloud with a dynamically important magnetic field, therefore $B \propto n_n^{1/2}$, although for individual points within the cloud the exponent was in the range $1/3 - 1/2$. These

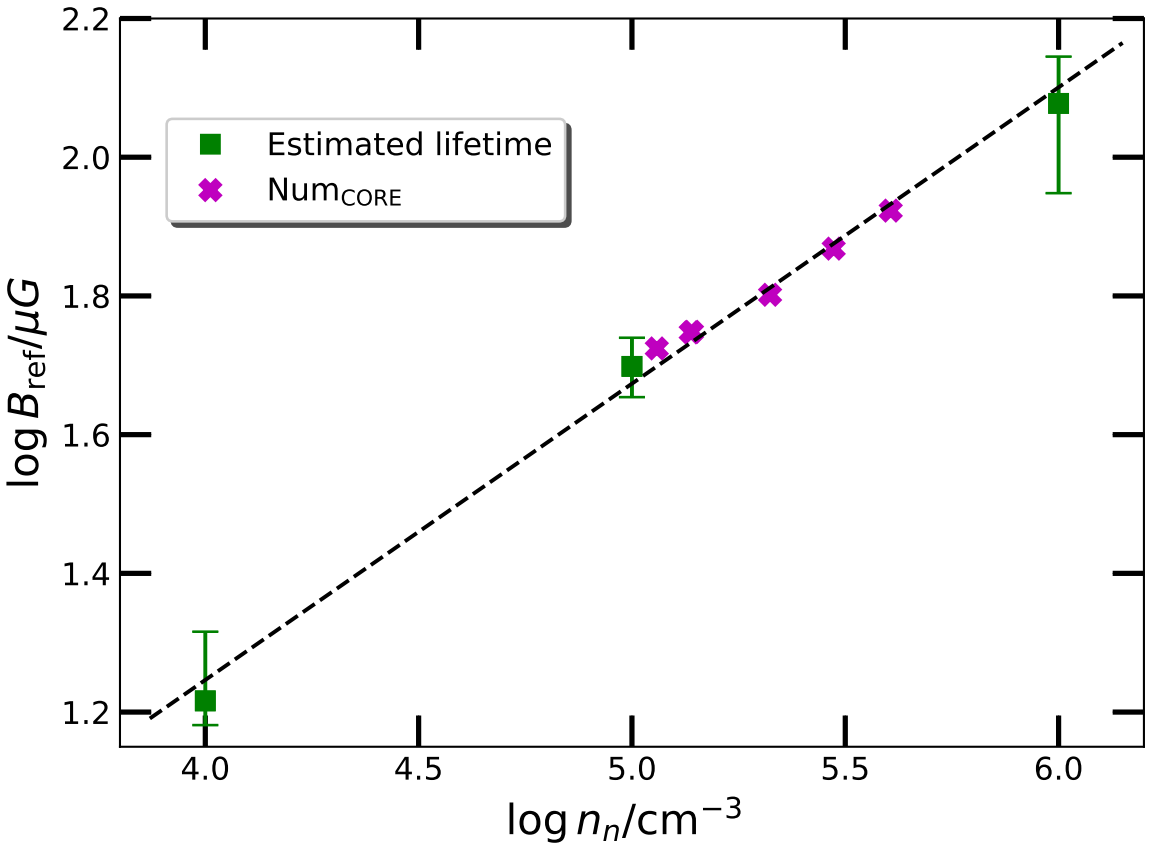

Figure 3.4: Magnetic field $\log(B_{\rm ref}/\mu{\rm G})$ vs. number density $\log(n_n/{\rm cm}^{-3})$. The filled squares and crosses represent the number density region corresponding to the fitting of the lifetime of prestellar cores and $\mathrm{Num_{CORE}}$ as shown in Figure 3.2 and Figure 3.3 (see Table 3.1 & Table 3.2). The dashed line is the least-squares fit. The vertical error bars correspond to magnetic field variations that yield a total factor of two (greater or lesser by a factor $\sqrt{2}$) values of the growth time (lifetime).

theories assume an evolutionary sequence and that the mass-to-flux ratio and internal thermal (or turbulent) velocity dispersion stays fixed. We should keep in mind that the full virial relation is

$$B \propto \sigma\, n_n^{1/2}/\mu\,, \tag{3.8}$$

where σ is the velocity dispersion. With the inclusion of ambipolar diffusion and a systematically increasing value of μ as n_n increases, the slope in the $B_{\rm ref} - n_n$ relation is expected to be less than in the flux-freezing models. On the other hand, a systematic dependence of σ on n_n can also have an effect. Crutcher et al. (2010) fitted a slope of $\approx 2/3$ to Zeeman magnetic field data for an ensemble of dense molecular gas clouds. The $B - n$ relation shown in Figure 3.4 is for prestellar cores while the $B - n$ relation shown by Crutcher et al. (2010) includes a number of massive protostellar cores or clumps. Those objects definitely do not represent an evolutionary sequence, with the higher density objects representing much more massive clouds that also have an increased velocity dispersion σ. A better fit to the ensemble of different clouds measured by the Zeeman effect is $B \propto \sigma n^{1/2}$ (Basu, 2000) and was verified by Li et al. (2015) who used the updated data in Crutcher (2012) and pointed out that the ensemble of objects in the data set also have the correlation $\sigma \propto n^{1/6}$, thereby leading to an apparent $B \propto n^{2/3}$. A similar result was obtained for B determined using the DCF technique (Myers & Basu, 2021).

3.4 Conclusions

We used a semi-analytic model of ambipolar-diffusion-driven gravitational fragmentation in isothermal self-gravitating interstellar molecular clouds. The only requirements in our model are that prestellar cores are transcritical (mildly supercritical), with $1 \lesssim \mu \lesssim 2$, and an evolution toward the higher values of μ as the density increases. With this assumption we show that there is a significant and systematic variation of lifetime and fragmentation scale in molecular clouds. Such systematic variations do not exist in standard thermal-pressure-dominated (Jeans) fragmentation theory and are difficult to reproduce in turbulence-regulated models. Our best-fit model for prestellar cores suggests $B \propto n^{0.43}$ (see Figure 3.4 and Equation 3.7), which attains a shallower slope than the flux-frozen case due to the effects of ambipolar diffusion. The estimated lifetime of prestellar cores and the possible number of cores within a parent clump/cloud based on the model for $\tilde{\tau}_{ni,0} = 0.2$ agree well with that of observations presented

by Könyves et al. (2015) and Pokhrel et al. (2018), respectively. For the lower end ($\sim 10^4\,\mathrm{cm}^{-3}$) of the density regime, the timescale for collapse of prestellar cores is approximately six times longer than the free-fall timescale. On the other hand, for the case of higher number density ($\sim 10^6\ \mathrm{cm}^{-3}$), the timescale is nearly the same as the free-fall timescale. The mass scales of fragment formation are also significantly greater than the Jeans mass in this mildly supercritical regime.

We adopted the dimensionless neutral-ion collision time $\tilde{\tau}_{ni,0} = 0.2$ because of its correspondence to the typical ionization fraction ($\sim 10^{-7}$) at a neutral number density ($\sim 10^4\ \mathrm{cm}^{-3}$). In future studies, the role of varying $\tilde{\tau}_{ni,0}$ could be explored in order to compare with measured ionization fractions in cores (see Caselli et al., 2002), and perhaps constrain the cosmic ray ionization rate (canonical value $\zeta_{\mathrm{CR}} = 10^{-17}\ \mathrm{s}^{-1}$).

Our model provides a means to indirectly infer the effect of ambipolar diffusion on mildly supercritical dense regions (prestellar cores) of molecular clouds. The importance of ambipolar diffusion in dense supercritical molecular cloud gas has not been discussed widely and is independent of its possible effects in low-density molecular cloud envelopes.

3.5 Appendices

3.5.1 System of equations

We formulate model clouds as rotating, self-gravitating, partially ionized, isothermal, magnetic, planar thin sheets with infinite extent in the x- and y- directions and a local vertical half-thickness $Z(x, y, t)$ (see Figure 1 from Das & Basu (2021)). In our model, we adopt a velocity unit of c_s, the isothermal sound speed, and a column density unit of $\sigma_{n,0}$, the initial uniform column density. The length unit is $L_0 = c_s^2/(2\pi G\sigma_{n,0})$, leading to a time unit $t_0 = c_s/(2\pi G\sigma_{n,0})$, where G is the universal gravitational constant. The mass unit is $M_0 = c_s^4/(4\pi^2 G^2\sigma_{n,0})$ and the magnetic field strength unit is $B_0 = 2\pi G^{1/2}\sigma_{n,0}$. The free-fall time is

$$t_{\mathrm{ff}} = Z_0/c_s = (\tilde{Z}_0 L_0)/c_s = \tilde{Z}_0\, t_0\ , \tag{3.9}$$

where

$$Z_0 = \sigma_{n,0}/(2\rho_{n,0}) \tag{3.10}$$

is the initial uniform local vertical half-thickness, with dimensionless form

$$\tilde{Z}_0 = \frac{2}{(1+\tilde{P}_{\rm ext})} \,. \tag{3.11}$$

Here $\tilde{P}_{\rm ext} = 2P_{\rm ext}/(\pi G\sigma_{n,0}^2)$ is the dimensionless external pressure. The initial local effective sound speed, $C_{\rm eff,0}$, comes from

$$C_{\rm eff,0}^2 = \frac{\pi}{2} G\sigma_{n,0}^2 \frac{\left[3P_{\rm ext} + \frac{\pi}{2}G\sigma_{n,0}^2\right]}{\left[P_{\rm ext} + \frac{\pi}{2}G\sigma_{n,0}^2\right]^2} c_s^2, \tag{3.12}$$

and reduces to the isothermal sound speed, c_s, in the limit of very low $P_{\rm ext}$. It can be obtained from the linearized condition of vertical hydrostatic equilibrium:

$$\rho_{n,0}c_s^2 = \frac{\pi}{2}G\sigma_{n,0}^2 + P_{\rm ext} = \frac{\pi}{2}G\sigma_{n,0}^2(1+\tilde{P}_{\rm ext}) \,. \tag{3.13}$$

The initial uniform Alfvén speed $V_{A,0}$ is related to the mass-to-magnetic-flux ratio (μ_0) via

$$V_{A,0}^2 \equiv \frac{B_{\rm ref}^2}{4\pi\rho_{n,0}} = 2\pi G\sigma_{n,0}\mu_0^{-2}Z_0 \ , \tag{3.14}$$

where $\rho_{n,0}$ is the initial uniform volume density. The initial uniform ambipolar diffusivity can be expressed as (see Das & Basu, 2021)

$$\eta_{\rm AD,0} = V_{A,0}^2\tau_{ni,0} = 2\pi G\sigma_{n,0}\mu_0^{-2}Z_0\tau_{ni,0}. \tag{3.15}$$

Now, from the system of governing equations (see Equations (11) to (23) of Das & Basu (2021), which are the fundamental MHD equations obtained by integrating over the z-direction), we obtain a simplified form in x- and y- components:

$$\frac{\partial\sigma_n}{\partial t} + \frac{\partial}{\partial x}(\sigma_n v_{n,x}) + \frac{\partial}{\partial y}(\sigma_n v_{n,y}) = 0, \tag{3.16}$$

$$\frac{\partial}{\partial t}(\sigma_n v_{n,x}) + \frac{\partial}{\partial x}(\sigma_n v_{n,x}^2) + \frac{\partial}{\partial x}(\sigma_n v_{n,x} v_{n,y}) = \sigma_n\, g_x - C_{\rm eff}^2 \frac{\partial \sigma_n}{\partial x} + F_{{\rm Mag},x} + 2\sigma_n \Omega v_{n,y}, \tag{3.17}$$

$$\frac{\partial}{\partial t}(\sigma_n v_{n,y}) + \frac{\partial}{\partial y}(\sigma_n v_{n,x} v_{n,y}) + \frac{\partial}{\partial y}(\sigma_n v_{n,y}^2) = \sigma_n\, g_y - C_{\rm eff}^2 \frac{\partial \sigma_n}{\partial y} + F_{{\rm Mag},y} - 2\sigma_n \Omega v_{n,x}, \tag{3.18}$$

$$F_{{\rm Mag},x} = \frac{B_{z,{\rm eq}}}{2\pi}\left(B_{x,Z} - Z\,\frac{\partial B_{z,{\rm eq}}}{\partial x}\right) + \frac{1}{4\pi}\frac{\partial Z}{\partial x}\left[B_{x,Z}^2 + B_{y,Z}^2 + 2B_{z,{\rm eq}}\left(B_{x,Z}\frac{\partial Z}{\partial x} + B_{y,Z}\frac{\partial Z}{\partial y}\right) + \left(B_{x,Z}\frac{\partial Z}{\partial x} + B_{y,Z}\frac{\partial Z}{\partial y}\right)^2\right], \tag{3.19}$$

$$F_{{\rm Mag},y} = \frac{B_{z,{\rm eq}}}{2\pi}\left(B_{y,Z} - Z\,\frac{\partial B_{z,{\rm eq}}}{\partial y}\right) + \frac{1}{4\pi}\frac{\partial Z}{\partial y}\left[B_{x,Z}^2 + B_{y,Z}^2 + 2B_{z,{\rm eq}}\left(B_{x,Z}\frac{\partial Z}{\partial x} + B_{y,Z}\frac{\partial Z}{\partial y}\right) + \left(B_{x,Z}\frac{\partial Z}{\partial x} + B_{y,Z}\frac{\partial Z}{\partial y}\right)^2\right], \tag{3.20}$$

$$\frac{\partial B_{z,{\rm eq}}}{\partial t} = -\frac{\partial}{\partial x}\left(B_{z,{\rm eq}} v_{i,x}\right) - \frac{\partial}{\partial y}\left(B_{z,{\rm eq}} v_{i,y}\right) + \left[\frac{\partial}{\partial x}\left(\eta_{\rm OD}\frac{\partial B_{z,{\rm eq}}}{\partial x}\right) + \frac{\partial}{\partial y}\left(\eta_{\rm OD}\frac{\partial B_{z,{\rm eq}}}{\partial y}\right)\right]. \tag{3.21}$$

where

$$v_{i,x} = v_{n,x} + \frac{\tau_{ni,0}}{\sigma_n}\left(\frac{\rho_{n,0}}{\rho_n}\right)^{1/2} F_{{\rm Mag},x}, \tag{3.22}$$

$$v_{i,y} = v_{n,y} + \frac{\tau_{ni,0}}{\sigma_n}\left(\frac{\rho_{n,0}}{\rho_n}\right)^{1/2} F_{{\rm Mag},y}. \tag{3.23}$$

Here, $v_{i,x}$, $v_{i,y}$, $v_{n,x}$, and $v_{n,y}$ are the x- and y- components of ion and neutral velocities. The planar sheet is rotating with an angular velocity Ω about the z-axis, so that $\mathbf{\Omega} = \Omega\hat{\mathbf{z}}$. The magnetic field and rotation axis are perpendicular to the sheet. Here, $\eta_{\rm OD,0}$ is the ohmic diffusivity that is considered as a measure of ohmic dissipation. Starting with a static uniform background, any

physical quantity of the thin-sheet equations can be expanded by writing it via

$$f(x, y, t) = f_0 + \delta f_a e^{i\left(k_x x + k_y y - \omega t\right)}, \tag{3.24}$$

where f_0 is the unperturbed background state, δf_a is the amplitude of the perturbation, k_x, k_y, and k are the x-, y-, and z- wavenumbers, respectively, and ω is the complex angular frequency. For assumed small-amplitude perturbations such that $|\delta\, f_a| \ll f_0$, and retaining the linearized form of the perturbed quantities from Eqs. 3.16, 3.17, 3.18 and 3.21, the following equations are obtained:

$$\omega\, \delta\sigma'_n = k_x\, c_s\, \delta v'_{n,x} + k_y\, c_s\, \delta v'_{n,y}\ , \tag{3.25}$$

$$\begin{aligned} \omega\, c_s\, \delta v'_{n,x} = {} & \frac{k_x}{k}\left[C^2_{\rm eff,0}\, k - 2\pi G\sigma_{n,0}\right]\, \delta\sigma'_n + i\, 2\Omega c_s \delta v'_{n,y} \\ & + \frac{k_x}{k}\left[\, 2\pi G\sigma_{n,0}\, \mu_0^{-1} + k\, V^2_{A,0}\, \mu_0\, \right]\, \delta B'_{z,\rm eq}\ , \end{aligned} \tag{3.26}$$

$$\begin{aligned} \omega\, c_s\, \delta v'_{n,y} = {} & \frac{k_y}{k}\left[C^2_{\rm eff,0}\, k - 2\pi G\sigma_{n,0}\right]\, \delta\sigma'_n - i\, 2\Omega c_s \delta v'_{n,x} \\ & + \frac{k_y}{k}\left[\, 2\pi G\sigma_{n,0}\, \mu_0^{-1} + k\, V^2_{A,0}\, \mu_0\, \right]\, \delta B'_{z,\rm eq}\ , \end{aligned} \tag{3.27}$$

$$\begin{aligned} \omega\, \delta B'_{z,\rm eq} = {} & \frac{k_x}{\mu_0}\, c_s\, \delta v'_{n,x} + \frac{k_y}{\mu_0}\, c_s\, \delta v'_{n,y} \\ & - i\left[\eta_{\rm OD,0}\, k^2 + \tau_{ni,0}\, \left(2\pi G\sigma_{n,0}\mu_0^{-2} k + k^2\, V^2_{A,0}\right)\right]\, \delta B'_{z,\rm eq}, \end{aligned} \tag{3.28}$$

where the perturbed eigenfunctions $\delta\sigma_n$, $\delta v_{n,x}$ (and $\delta v_{n,y}$), $\delta B_{z,\rm eq}$ are normalized by $\sigma_{n,0}$, c_s, and B_0 ($= 2\pi G^{1/2}\sigma_{n,0}$), respectively, such that $\delta\sigma'_n = \delta\sigma_n/\sigma_{n,0}$, $\delta v'_{n,x} = \delta v_{n,x}/c_s$, $\delta v'_{n,y} = \delta v_{n,y}/c_s$, and $\delta B'_{z,\rm eq} = \delta B_{z,\rm eq}/B_0$. Now, finding the determinant from the above set of equations one obtains the full dispersion relation

$$\begin{aligned} & \left(\omega + i\,[\theta + \gamma]\right)\left(\omega^2 - C^2_{\rm eff,0}\, k^2 + 2\pi G\sigma_{n,0} k - 4\Omega^2\right) \\ & \qquad = \omega\, \left[2\pi G\sigma_{n,0} k\mu_0^{-2} + k^2\, V^2_{A,0}\right]\ . \end{aligned} \tag{3.29}$$

This is derived in Das & Basu (2021) (see Equation (47)), where

$$\gamma = \eta_{\rm OD,0}\, k^2\ , \tag{3.30}$$

which is same as Equation (45) of Das & Basu (2021), and θ is described earlier (see Equation 3.5 and Equation (46) of Das & Basu (2021)). Finally, the dispersion relation (see Equation 3.4) is the same as the Equation 3.29 when setting $\Omega = 0$ and $\eta_{\rm OD,0} = 0$. In the above, we discuss all the equations in detail for completeness and clarity of our model. See also Equations 32(a)–32(d) of Ciolek & Basu (2006) for the dimensionless representation of the Equations (3.25) to (3.28) for the model with $\Omega = 0$ and $\eta_{\rm OD,0} = 0$; also see Equations (10) to (13) of Bailey & Basu (2012) for the dimensional representation of Equations (3.25) to (3.28) for the same model.

Based on these parameters, typical values of the units used and other derived quantities are

$$\sigma_{n,0} = \frac{3.63\times10^{-3}}{\left(1+\tilde{P}_{\rm ext}\right)^{\frac{1}{2}}}\left(\frac{n_{n,0}}{10^3\,{\rm cm}^{-3}}\right)^{\frac{1}{2}}\left(\frac{T}{10\,{\rm K}}\right)^{\frac{1}{2}}\ {\rm g\ cm}^{-2}, \tag{3.31}$$

$$L_0 = 7.48\times10^{-2}\left(\frac{T}{10\,{\rm K}}\right)^{\frac{1}{2}}\left(\frac{10^3\,{\rm cm}^{-3}}{n_{n,0}}\right)^{\frac{1}{2}}\left(1+\tilde{P}_{\rm ext}\right)^{\frac{1}{2}}\ {\rm pc}, \tag{3.32}$$

$$t_0 = 3.98\ \times10^{5}\left(\frac{10^3\,{\rm cm}^{-3}}{n_{n,0}}\right)^{\frac{1}{2}}\left(1+\tilde{P}_{\rm ext}\right)^{\frac{1}{2}}\ {\rm yr}, \tag{3.33}$$

$$c_s = 0.188\left(\frac{T}{10\,{\rm K}}\right)^{\frac{1}{2}}\ {\rm km\ s}^{-1}, \tag{3.34}$$

$$M_0 = 9.76\times10^{-2}\left(\frac{T}{10\,{\rm K}}\right)^{3/2}\left(\frac{10^3\,{\rm cm}^{-3}}{n_{n,0}}\right)^{1/2}\left(1+\tilde{P}_{\rm ext}\right)^{1/2}\ M_\odot\,, \tag{3.35}$$

$$\tau_{ni,0} = \frac{3.74\times10^{4}}{\left(1+\tilde{P}_{\rm ext}\right)}\left(\frac{T}{10\,{\rm K}}\right)\left(\frac{0.01\ {\rm g\ cm}^{-2}}{\sigma_{n,0}}\right)^{2}\left(\frac{10^{-7}}{\chi_{i,0}}\right)\ {\rm yr}\,, \tag{3.36}$$

$$B_{\rm ref} = \frac{5.89\times10^{-6}}{\mu_0}\left(\frac{n_{n,0}}{10^3\,{\rm cm}^{-3}}\right)^{1/2}\left(\frac{T}{10\,{\rm K}}\right)^{1/2}\left(1+\tilde{P}_{\rm ext}\right)^{-1/2}\ {\rm G}\,. \tag{3.37}$$

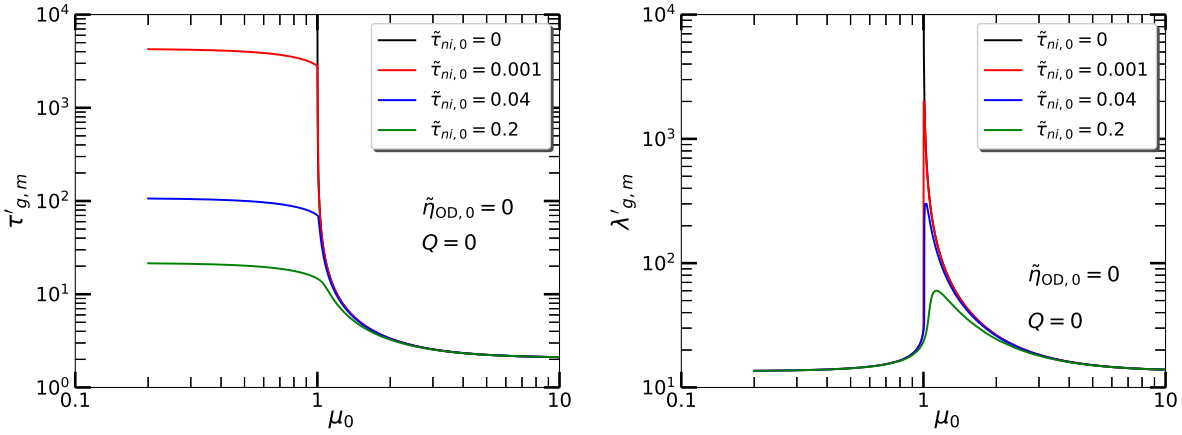

Figure 3.5: Top: Normalized shortest growth time of gravitationally unstable mode ($\tau'_{g,m} = \tau_{g,m}/t_0$) as a function of normalized mass-to-flux ratio (μ_0). Bottom: Normalized preferred length scale of the most unstable mode ($\lambda'_{g,m} = \lambda_{g,m}/L_0$) as a function of the normalized mass-to-flux ratio (μ_0). Each panel shows curves for models (as shown in Equation 3.4) with normalized neutral–ion collision time $\tilde{\tau}_{ni,0} = 0$ (black), 0.001 (red), 0.04 (blue), and 0.2 (green). Here, $\tilde{\tau}_{ni,0} = 0$ represents the flux-frozen case as a reference. The Toomre-Q rotation parameter and the dimensionless ohmic diffusivity $\tilde{\eta}_{OD,0}$ are set to be zero. As the degree of ambipolar diffusion (i.e., $\tilde{\tau}_{ni,0}$) increases, the growth timescale and length scale become shorter (see Ciolek & Basu, 2006; Bailey & Basu, 2012; Das & Basu, 2021) for further details.

3.5.2 Tables

Table 3.1: Fitting data for calculating the lifetime of prestellar cores. Here, μ is a free parameter of our model, σ_n is calculated using Equation 3.13, $B_{\rm ref}$ is obtained from Equation 3.3, and $t_{\rm ff}$ is the free-fall timescale. The estimated lifetime of prestellar cores is obtained based on Figure 3.1, as shown in Figure 3.2.

n_n ($\times 10^5$ cm^{-3})	μ	σ_n ($\times 10^{-2}$ g cm^{-2})	$B_{\rm ref}$ (μG)	Estimated lifetime of prestellar cores (Myr)
0.1	1.080	1.094	16.45	1.371 ($\sim 5.777\ t_{\rm ff}$)
1	1.125	3.461	49.94	0.355 ($\sim 4.728\ t_{\rm ff}$)
10	1.486	10.944	119.57	0.053 ($\sim 2.220\ t_{\rm ff}$)

Clump name	Clump Mass ($M_\odot$)	Area (pc^2)	$\sigma_n \times 10^{-2}$ (g cm^{-2})	$n_n \times 10^5$ (cm^{-3})	μ	$B_{\rm ref}$ (μG)	$M_{g,m}$ ($M_\odot$)	$N_J^{\rm th}$	$N_J^{\rm th,nth}$	Num$_{\rm CORE}$	$\epsilon^{\rm th}$	$\epsilon^{\rm th,nth}$
B5	62	0.32	4.064	1.383	1.178	56.01	20.165	16.2	1.5	3	0.185	2.000
L1455	251	1.3	4.050	1.373	1.176	55.90	20.339	53.1	4.3	12	0.226	2.791
IC348	511	2.9	3.697	1.144	1.132	53.00	23.858	58.6	6.4	21	0.358	3.281
L1448	159	0.48	6.948	4.042	1.470	76.73	5.108	55.1	4.6	31	0.562	6.739
B1	598	2.5	5.018	2.107	1.286	63.34	11.738	103.9	9.5	50	0.481	5.263
NGC1333	568	2.0	5.958	2.971	1.379	70.13	7.508	119	10.5	75	0.630	7.142

Table 3.2: Fitting data for calculating the number of enclosed cores (Num$_{\rm CORE}$).
Clump name, Clump Mass, Area, $N_J^{\rm th}$, $N_J^{\rm th,nth}$ are taken from Table 2 of Pokhrel et al. (2018).
In the above table, n_n, σ_n, μ, $B_{\rm ref}$, $M_{g,m}$, Num$_{\rm CORE}$, $\epsilon^{\rm th}$, $\epsilon^{\rm th,nth}$ are evaluated based on our model. Here, σ_n is the clump mass per unit area, n_n is obtained using Equation 3.13, μ is a free parameter of our model, $B_{\rm ref}$ is calculated using Equation 3.3, and $M_{g,m}$ is obtained based on Figure 3.1, Num$_{\rm CORE}$ = Clump Mass/$M_{g,m}$, $\epsilon^{\rm th}$ = Num$_{\rm CORE}$/$N_J^{\rm th}$, $\epsilon^{\rm th,nth}$ = Num$_{\rm CORE}$/$N_J^{\rm th,nth}$.
Table B.2 is arranged in the ascending order of Num$_{\rm CORE}$.

Bibliography

André P., et al., 2010, A&A, 518, L102

André P., Di Francesco J., Ward-Thompson D., Inutsuka S. I., Pudritz R. E., Pineda J. E., 2014, in Beuther H., Klessen R. S., Dullemond C. P., Henning T., eds, Protostars and Planets VI. p. 27 (arXiv:1312.6232), doi:10.2458/azu_uapress_9780816531240-ch002

Bailey N. D., Basu S., 2012, ApJ, 761, 67

Basu S., 2000, ApJ, 540, L103

Basu S., Ciolek G. E., 2004, ApJ, 607, L39

Basu S., Mouschovias T. C., 1994, ApJ, 432, 720

Basu S., Ciolek G. E., Wurster J., 2009a, New A, 14, 221

Basu S., Ciolek G. E., Dapp W. B., Wurster J., 2009b, New A, 14, 483

Beichman C. A., Myers P. C., Emerson J. P., Harris S., Mathieu R., Benson P. J., Jennings R. E., 1986, ApJ, 307, 337

Caselli P., Walmsley C. M., Zucconi A., Tafalla M., Dore L., Myers P. C., 2002, ApJ, 565, 344

Chen C.-Y., Ostriker E. C., 2014, ApJ, 785, 69

Ciolek G. E., Basu S., 2006, ApJ, 652, 442

Ciolek G. E., Mouschovias T. C., 1998, ApJ, 504, 280

Crutcher R. M., 2012, ARA&A, 50, 29

Crutcher R. M., Wandelt B., Heiles C., Falgarone E., Troland T. H., 2010, ApJ, 725, 466

Das I., Basu S., 2021, ApJ, 910, 163

Dobbs C. L., et al., 2014, in Beuther H., Klessen R. S., Dullemond C. P., Henning T., eds, Protostars and Planets VI. p. 3 (arXiv:1312.3223), doi:10.2458/azu_uapress_9780816531240-ch001

Elmegreen B. G., 1979, ApJ, 232, 729

Evans N. J., et al., 2009, ApJS, 181, 321

Folini D., Heyvaerts J., Walder R., 2004, A&A, 414, 559

Friesen R. K., et al., 2017, ApJ, 843, 63

Heyer M., Dame T., 2015, Annual Review of Astronomy and Astrophysics, 53, 583

Jessop N. E., Ward-Thompson D., 2000, MNRAS, 311, 63

Klessen R. S., Heitsch F., Mac Low M.-M., 2000, ApJ, 535, 887

Könyves V., et al., 2015, A&A, 584, A91

Kudoh T., Basu S., 2003, ApJ, 595, 842

Kudoh T., Basu S., 2006, ApJ, 642, 270

Kudoh T., Basu S., Ogata Y., Yabe T., 2007, MNRAS, 380, 499

Kunz M. W., Mouschovias T. C., 2009, MNRAS, 399, L94

Li P. S., McKee C. F., Klein R. I., 2015, MNRAS, 452, 2500

McDaniel E. W., Mason E. A., 1973, Mobility and diffusion of ions in gases. John Wiley and Sons, USA

Mercimek S., Myers P. C., Lee K. I., Sadavoy S. I., 2017, AJ, 153, 214

Mestel L., 1965, QJRAS, 6, 265

Mouschovias T. C., 1976a, ApJ, 206, 753

Mouschovias T. C., 1976b, ApJ, 207, 141

Mouschovias T. C., 1991, ApJ, 373, 169

Myers P. C., Basu S., 2021, arXiv e-prints, p. arXiv:2104.02597

Myers P. C., Benson P. J., 1983, ApJ, 266, 309

Myers P. C., Linke R. A., Benson P. J., 1983, ApJ, 264, 517

Nakamura F., Li Z.-Y., 2005, ApJ, 631, 411

Nakano T., Nakamura T., 1978, PASJ, 30, 671

Osterbrock D. E., 1961, ApJ, 134, 347

Pattle K., Fissel L., 2019, Frontiers in Astronomy and Space Sciences, 6, 15

Planck Collaboration et al., 2016, A&A, 586, A138

Pokhrel R., et al., 2018, ApJ, 853, 5

Sadavoy S. I., et al., 2010, ApJ, 710, 1247

Sadavoy S. I., et al., 2014, ApJ, 787, L18

Tielens A. G. G. M., 2005, The Physics and Chemistry of the Interstellar Medium

Vazquez-Semadeni E., Passot T., Pouquet A., 1996, ApJ, 473, 881

Ward-Thompson D., Scott P. F., Hills R. E., Andre P., 1994, MNRAS, 268, 276

Ward-Thompson D., André P., Crutcher R., Johnstone D., Onishi T., Wilson C., 2007, in Reipurth B., Jewitt D., Keil K., eds, Protostars and Planets V. p. 33 (arXiv:astro-ph/0603474)

Chapter 4

A semi-analytic model for the temporal evolution of the episodic disc-to-star accretion rate during star formation

A version of this chapter has been published in the Monthly Notices of Royal Astronomical Society as Das I. and Basu S. 2022, MNRAS, 514, 5659–5672, DOI:10.1093/mnras/stac1654.

4.1 Introduction

The luminosities of protostars from sub-millimetre/millimetre and mid-infrared observations of nearby molecular clouds reveal low to intermediate mass star formation occurring within dense protostellar cores. In the early phase (so-called Class 0 and Class I phases), a protostar is surrounded by a protostellar disc, which is in turn deeply embedded within an infalling envelope that has emerged from the collapse of the surrounding cloud core. In order to achieve a typical final stellar mass within a certain timescale, the protostar accumulates mass with episodes of vigorous mass accretion rate ($\geq 10^{-4}$ $M_{\odot}\,yr^{-1}$) as observed in FU Orionis (see Audard et al., 2014, and references therein). It is widely accepted that stellar mass is accumulated in a time-dependent and episodic (not steady) fashion. Several surveys of protostars suggest that the luminosities of young stellar objects (YSOs) are about an order of magnitude lower than that expected from a steady mass accretion rate (Enoch et al., 2009; Dunham et al., 2010).

The sporadic and sudden mass accretion bursts give rise to the luminous bursts as observed in YSOs, which are often known as FUor ($\sim 100\,L_\odot$, ~ 100 yr duration, thought to occur mainly in the embedded Class 0/I phase) and EXor ($\sim 10\,L_\odot$, $\sim$ 1yr duration, appearing in the Class II YSOs) eruptions (see Hartmann & Kenyon, 1996; Herbig, 2008; Audard et al., 2014, references therein). The majority of the accretion outbursts that have been detected belong to the star-forming regions within the immediate solar neighbourhood. Less is known about episodic eruptions at larger distances ($\sim$ few kpc) due to drawbacks in time-domain astronomy at those distances.

An additional observational channel that can imply episodic accretion is the luminosity histogram of young stellar objects (YSOs). Several surveys show that the luminosities of YSOs are typically about an order of magnitude lower than that expected from a steady mass accretion rate (Enoch et al., 2009; Dunham et al., 2010). This has been used by the authors to provide further evidence of episodic accretion, in which the majority of time is spent in a lower accretion rate. However, long-term evolution of the accretion rate and low-amplitude variability can also potentially match the observed luminosities of protostars given favourable assumptions (Offner & McKee, 2011; Fischer et al., 2017). Further studies are required to distinguish these scenarios.

The overall protostellar accretion history can be thought of as a combined effect of two successive phases. In the early phase, when the infall of matter from the surrounding envelope is substantial, mass is transported inward because of envelope-induced gravitational instability in a protostellar disc. However, the accretion from the surrounding protostellar disc on to the central protostar primarily occurs at a much lower rate than the envelope accretion. In this early stage, even though both processes are coexisting, the envelope accretion dominates the disc accretion in driving the overall evolution. Simulations show that during the protostellar accretion phase (Class 0/I phase), intermittent accretion bursts occur due to episodes of dense clump infall on to the central protostar (Vorobyov & Basu, 2005b, 2006). Mass is infalling from the envelope to the disc, and the disc is transporting the matter to the star at a different rate. Because of the mismatch between the infall and transport rate, the central protostar mass does not grow at the same rate as the disc mass. Hence, the disc mass becomes comparable to that of the central protostar, which leads to gravitational instability (GI) within the protostel-

lar/protoplanetary disc (PD/PPD). Generally, the disc gets fragmented into large spiral arms and gravitationally bound clumps. Afterward, these clumps migrate inward through the spiral arms and fall to the centre (Vorobyov & Basu, 2005b, 2006), which triggers the luminosity bursts.

In the later phase, when the gas reservoir of the envelope is depleted, mass is accreted on to the star due to internal torques, which usually result in a power-law decrease of mass accretion rate with time. Specifically, for accretion due to gravitational torques within the disc, analytic theory yields the form $\dot{M} \propto t^{-6/5}$ (Lin & Pringle, 1987, hereafter LP) that has also been found in numerical simulations (Vorobyov & Basu, 2008). At these times, disc accretion occurs independent of any exterior influence and the system moves into the Class II phase.

In this paper, we develop a semi-analytic formalism that successfully produces the evolution of the mass accretion rate for specified density and velocity profiles that emerge from the runaway collapse of prestellar cloud core. We treat the prestellar core as an isothermal finite mass reservoir that is in hydrostatic equilibrium. In our model, we incorporate a prescription for generating the vigorous episodic outbursts that arise due to GI within the disc. The effect of GI can be characterized with the Toomre Q-parameter (Toomre, 1964), which in turn can be expressed as a disc-to-star mass ratio that we use widely in our paper. We determine a self-consistent evolution of the mass accretion rate by joining the spherical envelope accretion and the disc accretion, together with the episodic accretion bursts.

The semi-analytic model elucidates the basic physics of otherwise complex nonlinear simulations (e.g. Vorobyov & Basu, 2005b, 2006). Aside from its simplicity and pedagogical value, it opens up new avenues for future work to model episodic accretion. The simulations are used to calibrate the model, and the computational efficiency of a model that requires mere seconds of wall clock run time opens up the possibility of running large parameter surveys and population synthesis modelling. We demonstrate a preliminary example of this by estimating a synthetic luminosity histogram in this paper. Such work can guide interpretation of whether the episodic accretion or a long timescale evolution of the accretion rate is the primary cause of the breadth of observed luminosity histograms.

Our semi-analytic prescription for the determination of the mass accretion rate from the spherical collapse of an isothermal cloud core is described in Section 4.2, where the two cases

of spherical envelope accretion (Section 4.2.2) and disc accretion (Section 4.2.3) are discussed separately. In Section 4.3.1.1 we also provide a semi-analytic prescription to determine the specific angular momentum profile. We describe the formulation of episodic outbursts due to GI in Section 4.2.4. We present our numerical results in Section 5.3. The logical flow of our calculation is described in Section 4.3.2, the temporal evolution of the mass accretion rate is presented in Section 4.3.3, the modelling of the distribution of mass in the disc, star, and envelope is in Section 4.3.4, and the estimation of the luminosity distribution is described in Section 4.3.5. We discuss the applications and limitations of our results in Section 4.4 and summarize the main features of our work in Section 4.5.

4.2 Methodology

We develop a semi-analytic prescription to determine the evolution of the protostellar mass accretion rate during star formation. This requires the modelling of three key ingredients: a prestellar density profile, the envelope accretion on to the disc, and the disc accretion. We describe these in the following subsections.

4.2.1 Prestellar density profile

We start with the modified isothermal density profile

$$\rho(r) = \frac{\rho_c}{1 + (r/r_c)^2} \, , \tag{4.1}$$

where r_c and ρ_c are the central lengthscale and density, respectively. The parameter r_c represents the size of the central flat region of the density profile. Here, r_c is comparable to the central Jeans length, $r_c = kc_s/\sqrt{\pi G \rho_c}$, such that inner profile remains close to that of a Bonnor-Ebert sphere, where c_s is the isothermal sound speed and G is the gravitational constant, k (= 1.1) is a constant of proportionality, $\rho_c = \mu m_{\rm H} n_c$ is the volume density, in which $\mu = 2.33$ and n_c is the central number density. The asymptotic density profile is 2.2 times the equilibrium singular isothermal sphere value $\rho_{\rm SIS} = c_s^2/(2\pi G r^2)$ (see more in Vorobyov & Basu, 2005a). For the sake of convenience of our calculations, we normalize the physical quantities by the following units: $[L] = r_c$, $[t] = 1/\sqrt{G\rho_c}$, $[M] = \rho_c r_c^3$, $[\rho] = \rho_c$, $[v] = [L]/[t] = r_c\sqrt{G\rho_c}$, $[\dot{M}] = [M]/[t]$. Our normalized variables are defined as $\tilde{r} = r/r_c$, $\tilde{t} = t/[t]$, $\tilde{M} = M/[M]$,

$\tilde{v} = v/[v]$, and $\dot{\tilde{M}} = \dot{M}/[\dot{M}]$.

Next, we present the density profile of a tapered isothermal sphere,

$$\rho(r) = \frac{\rho_c}{1 + (r/r_c)^2}\left[1 - \frac{r^2}{R_{\rm out}^2}\right], \tag{4.2}$$

where $R_{\rm out}$ is the outer radius of the cloud. Note that we later use $R_{\rm out}$ as the key parameter to set the cloud mass. The density model of the tapered isothermal sphere provides a modified isothermal profile for an inner region, as well as a very steep outer density profile beyond some radial length scale. Qualitatively, this kind of transition in the density profile is consistent with the transition from an inner region with supercritical mass-to-flux ratio (gravitationally dominated) to a subcritical outer region (magnetically dominated) as found in numerical magnetohydrodynamic (MHD) simulations of the gravitational collapse of a prestellar core (e.g. Ciolek & Mouschovias, 1993; Basu & Mouschovias, 1994). It can also arise in hydrodynamic calculations due to a finite mass reservoir in the numerical domain (Vorobyov & Basu, 2005a). The tapered isothermal sphere mimics these cases by having an enclosed mass that saturates to a final value as $r \to R_{\rm out}$.

4.2.2 Spherical envelope accretion

We consider the collapse of the isothermal prestellar cloud core for modelling the spherical envelope accretion on to a central protostar and disc system.

4.2.2.1 Mass accretion rate from collapse of the cloud

The equation of motion of a pressure-free, self-gravitating spherically symmetric cloud is

$$\frac{dv}{dt} = -\frac{GM(r)}{r^2}, \tag{4.3}$$

where v is the velocity of a thin spherical shell at a radial distance r from the centre of a cloud, and $M(r)$ is the mass inside a sphere of radius r. Equation (4.3) can be integrated to yield the expression for velocity $v(r, t)$ at a given radial distance r and time t, which follows

$$v = -\sqrt{2GM(r_0)\left(\frac{1}{r} - \frac{1}{r_0}\right)}, \tag{4.4}$$

where r_0 is the initial position of a mass shell at $t = t_0$, and $M(r_0)$ is the mass inside r_0. Here, it is assumed that all shells are initially at rest: $v_0(r_0) = 0$. Equation (4.4) can be integrated by introducing a new dimensionless variable β such that

$$r \equiv r_0 \cos^2 \beta \,, \tag{4.5}$$

(see Hunter, 1962). Then the time it takes for a shell located initially at r_0 to move to a smaller radial distance r due to the gravitational pull of the mass $M(r_0)$ is

$$t = \frac{\arccos\,\sqrt{r/r_0} + 0.5\sin(2\arccos\,\sqrt{r/r_0}\,)}{\sqrt{2GM/r_0^3}} \,. \tag{4.6}$$

The values of r and t are sufficient to determine r_0 (a value $> r$ but $< R_{\rm out}$, the radius of the cloud) from Equation (4.6). The dimensionless form of Equations (4.4) and (4.6) are

$$\tilde{v} = -\sqrt{2\tilde{M}(\tilde{r}_0)\left(\frac{1}{\tilde{r}} - \frac{1}{\tilde{r}_0}\right)} \,, \tag{4.7}$$

$$\tilde{t} = \frac{\arccos\,\sqrt{\tilde{r}/\tilde{r}_0} + 0.5\sin(2\arccos\,\sqrt{\tilde{r}/\tilde{r}_0})}{\sqrt{2\tilde{M}/\tilde{r}_0^3}} \,, \tag{4.8}$$

respectively, where $\tilde{r}_0 = r_0/r_c$. Subsequently, we use the obtained value of r_0 in Equation (4.7) to obtain $v(r,t)$. Provided that the shells do not pass through each other (i.e. the mass of a moving shell is conserved, so $dM(r,t) = dM(r_0,t_0)$, the gas density of a collapsing cloud is

$$\rho(r,t) = \rho_0 \,\frac{r_0^2}{r^2}\,\frac{dr_0}{dr} \,, \tag{4.9}$$

where $\rho_0(r_0)$ is the initial gas density at r_0. The ratio of dr_0/dr determines how the thickness of a given shell evolves with time. The relative thickness dr_0/dr is determined by differentiating Equation (4.5) with respect to r_0, yielding

$$\frac{dr}{dr_0} = \frac{r}{r_0} - r_0 \sin(2\arccos\,\sqrt{r/r_0})\frac{d\beta}{dr_0} \,. \tag{4.10}$$

Next, $d\beta/dr_0$ is determined from an alternative form of Equation (4.6):

$$\beta + \frac{1}{2}\sin 2\beta = t\sqrt{\frac{2GM(r_0)}{r_0^3}}\,, \tag{4.11}$$

and differentiating the above with respect to r_0 yields

$$\frac{d\beta}{dr_0} = \sqrt{\frac{G}{2M(r_0)r_0^3}}\left(t\,\frac{r_0}{2r}\right)\left[\frac{dM(r_0)}{dr_0} - \frac{3M(r_0)}{r_0}\right]. \tag{4.12}$$

Normalizing Equation (4.11) and Equation (4.12) we obtain

$$\beta + \frac{1}{2}\sin 2\beta = \tilde{t}\sqrt{\frac{2\tilde{M}(\tilde{r}_0)}{\tilde{r}_0^3}} \tag{4.13}$$

and

$$\frac{d\beta}{d\tilde{r}_0} = \sqrt{\frac{1}{2\tilde{M}(\tilde{r}_0)\tilde{r}_0^3}}\left(\tilde{t}\,\frac{\tilde{r}_0}{2\tilde{r}}\right)\left[\frac{d\tilde{M}(r_0)}{d\tilde{r}_0} - \frac{3\tilde{M}(\tilde{r}_0)}{\tilde{r}_0}\right], \tag{4.14}$$

respectively, where

$$\frac{d\tilde{M}(\tilde{r}_0)}{d\tilde{r}_0} = 4\pi\tilde{\rho}_0(\tilde{r}_0)\tilde{r}_0^2\,. \tag{4.15}$$

Now that the density $\rho(r,t)$ and velocity $v(r,t)$ distributions of a collapsing pressure-free sphere are explicitly determined, the mass accretion rate at any given radial distance r and time t is

$$\dot{M}(r,t) = 4\pi r^2\rho(r,t)v(r,t)\,. \tag{4.16}$$

The normalized form of Equation (4.16) is

$$\dot{\tilde{M}}(\tilde{r},\tilde{t}) = 4\pi\tilde{r}^2\tilde{\rho}(\tilde{r},\tilde{t})\tilde{v}(\tilde{r},\tilde{t})\,. \tag{4.17}$$

4.2.2.2 Evolution of mass accretion rate for different density models

We study the evolution of mass accretion rate for the spherical envelope accretion based on two different density models, a modified isothermal sphere and tapered isothermal sphere, given by Equations (4.1) and (4.2), respectively. The enclosed mass of the modified isothermal density

model of Equation (4.1) is

$$M(r_0) = 4\pi\rho_c r_c^2 \left(r_0 - r_c \arctan \frac{r_0}{r_c} \right) . \tag{4.18}$$

Normalization of Equation (4.18) yields

$$\tilde{M}(\tilde{r}_0) = 4\pi \left(\tilde{r}_0 - \arctan \tilde{r}_0 \right) . \tag{4.19}$$

Next, we calculate the enclosed mass for the tapered isothermal density model of Equation (4.2), which yields

$$\begin{aligned} M(r_0) = 4\pi\rho_c r_c^3 \int_0^{r_0/r_c} \frac{\tilde{r}^2}{1+\tilde{r}^2} d\tilde{r} \\ - \frac{4\pi\rho_c r_c^5}{R_{\rm out}^2} \int_0^{r_0/r_c} \frac{\tilde{r}^4}{1+\tilde{r}^2} d\tilde{r} , \end{aligned} \tag{4.20}$$

where $\tilde{r}$ is the dimensionless radial lengthscale described in Section 4.2.1. After integrating Equation (4.20) we obtain

$$\begin{aligned} M(r_0) = 4\pi\rho_c r_c^2 \left(r_0 - r_c \arctan \frac{r_0}{r_c} \right) \\ - \frac{4\pi\rho_c r_c^5}{R_{\rm out}^2} \left(\arctan \frac{r_0}{r_c} + \frac{r_0^3}{3r_c^3} - \frac{r_0}{r_c} \right) . \end{aligned} \tag{4.21}$$

Normalizing Equation (4.21) yields

$$\tilde{M}(\tilde{r}_0) = 4\pi \left[(\tilde{r}_0 - \arctan \tilde{r}_0) - \frac{1}{\tilde{R}_{\rm out}^2} \left(\arctan \tilde{r}_0 + \frac{\tilde{r}_0^3}{3} - \tilde{r}_0 \right) \right] . \tag{4.22}$$

4.2.3 Disc accretion

The disc accretion plays an important role in the formation and evolution of disc. During the early stellar evolution the solar nebula was an accretion disc (see discussion in Pringle, 1981). Primarily, the matter falls on to the disc from the envelope and then it is partially transported to the star from the disc. In a simple viscous disc, matter is transported inward in an axisymmetric model and results in an accretion rate on to the central star. At the same time, the disc evolution results in a loss of angular momentum associated with the accreting material (Lynden-Bell

& Pringle, 1974; Pringle, 1981). Hartmann et al. (1998) applied such a model in which the accretion and angular momentum transfer/redistribution occurs due to a well-defined viscosity $\nu \propto R^{\gamma}$, where R is the disc radius. This viscosity profile yields a declining mass accretion rate $\dot{M}_{\rm disc} \propto t^{-\eta}$, where $\eta \gtrsim 1.5$ corresponds to $\gamma \gtrsim 1$. Note that any $\eta > 1$ corresponds to a finite mass reservoir. Hartmann et al. (1998) discussed that the limit $\gamma \sim 1$ essentially corresponds to roughly constant α in the turbulent viscosity parameterization of Shakura & Sunyaev (1973), which is $\nu = \alpha c_s H$, where H is the disc scale height (half thickness).

In a more realistic disc, the gravitational torques produced by the nonaxisymmetric structure including spiral arms can dominate the angular momentum transfer. To model such evolution we use the gravitational torque driven accretion (Lin & Pringle, 1987), which leads to $\dot{M}_{\rm disc} \propto t^{-6/5}$, which was also found in simulations by Vorobyov & Basu (2008, see their fig. 3) for late time evolution when envelope accretion had become negligible. The mass of the disc during its evolution can be written as

$$M_{\rm d}(t) = \frac{4\pi}{3}\Sigma_{0d}R_{0d}^2\left(\frac{t}{t_{0d}}\right)^{-1/5} , \tag{4.23}$$

as described in Lin & Pringle (1987), where $M_{0d}(t = t_{0d}) \equiv (4\pi/3)\Sigma_{0d}R_{0d}^2$. So, taking the time derivative of Equation (4.23) yields the mass accretion rate from the disc to the star as

$$\dot{M}_{\rm ds}(t) = -\frac{1}{5}\left(\frac{4\pi}{3}\Sigma_{0d}\, R_{0d}^2\, t_{0d}^{1/5}\right) t^{-6/5} . \tag{4.24}$$

Normalization of Equation (4.24) yields

$$\dot{\tilde{M}}_{\rm ds}(\tilde{t}) = -\frac{C_1}{5}\tilde{t}^{-6/5} , \tag{4.25}$$

where

$$C_1 = \frac{\frac{4\pi}{3}\Sigma_{0d}R_{0d}^2}{\rho_c r_c^3}\left(\frac{t_{0d}}{[t]}\right)^{1/5} \equiv \frac{M_{0d}}{[M]}\left(\frac{t_{0d}}{[t]}\right)^{1/5} = \tilde{M}_{0d}\tilde{t}_{0d}^{1/5} , \tag{4.26}$$

and $\dot{\tilde{M}}_{\rm ds}(\tilde{t}) = \dot{M}_{\rm ds}(t)/[\dot{M}]$. Here $[\dot{M}]$, $[t]$, and $[M]$ are defined in the previous section. Note that use of C_1 requires us to initialize the disc evolution with an initial mass M_{0d} at time t_{0d}. These values are episodically updated in a manner that depends on the mass accretion bursts and is

described in Section 4.2.4.

We take note of the fact that all accretion on to the star is not occurring purely through the disc. Our simplified spherical envelope accretion model implies that some matter would accrete in a direction along or nearly along the rotation axis. Even in a more realistic geometry, some infall may be funneled along the edge of the outflow cavity and directly reach the innermost region of the stellar magnetosphere. Furthermore, the disc-to-star accretion may itself be enhanced above the values calculated above for an isolated disc when there is forcing from envelope accretion. For all of these reasons, we adopt the total accretion rate of mass reaching the star to be

$$\dot{M}_* = \dot{M}_{\rm ds}(t) + q\,\dot{M}_{\rm infall}(t), \tag{4.27}$$

where q is the fraction of envelope mass accretion that goes directly to the star and $\dot{M}_{\rm infall}$ is the accretion rate calculated according to the prescription in Equation (4.16). We adopt $q = 0.1$, which means in practice that the second term in Equation (4.27) will dominate the first until $\dot{M}_{\rm infall}$ undergoes a rapid drop due to the tapering of the isothermal density profile. Once this has happened, the $\dot{M}_*(t)$ will equal $\dot{M}_{\rm ds}(t)$ for subsequent evolution.

4.2.4 Episodic accretion bursts

We invoke the condition for the occurrence of episodic accretion bursts in terms of the Toomre-Q instability criterion:

$$Q \equiv \frac{c_s \Omega}{\pi G \Sigma} \lesssim 1\,, \tag{4.28}$$

where $\Omega = \sqrt{GM_*/R_{\rm d}^3}$ is the Keplerian angular speed, Σ is the disc surface density, M_* is the stellar mass, $M_{\rm d}$ ($\equiv \pi R_{\rm d}^2 \Sigma$) is the disc mass, $R_{\rm d}$ is the disc radius, and c_s and G are defined earlier. We use $c_s/\Omega = H$ for a non-self-gravitating disc in hydrostatic balance, where H is the vertical half-thickness of the disc. Rearranging the parameters within Equation (4.28) yields

$$Q \simeq \frac{H}{R_{\rm d}} \frac{M_*}{M_{\rm d}}\,. \tag{4.29}$$

Therefore, the Toomre instability criterion can be written as

$$\frac{M_{\rm d}}{M_*} \gtrsim \frac{H}{R_{\rm d}}\,. \tag{4.30}$$

For a typical disc, $H/R_{\rm d}$ is a few times 0.1 (see discussion in Kratter & Lodato, 2016). The factor $H/R_{\rm d}$ also includes the effects of the disc surface density profile. The Equation (4.30) is another way of representing gravitational instability in terms of disc-to-star-mass ratio, which is a constraint that is more related to observations. In our model, this depiction is widely used. The disc becomes gravitationally unstable, and a burst occurs, if the disc-to-star-mass ratio satisfies

$$\frac{M_{\rm d}}{M_*} \gtrsim \mathcal{R}_{\rm b}\,, \tag{4.31}$$

where we consider $\mathcal{R}_{\rm b} = 0.33$ as found in the hydrodynamic simulations (e.g. Vorobyov & Basu, 2006). The value of $\mathcal{R}_{\rm b}$ can vary up to $10\% - 20\%$ depending on the numerical model. The disc becomes gravitationally stable after the burst, which means the updated disc-to-star-mass ratio ($\mathcal{R}_{\rm f}$) becomes fairly lower than the threshold. However, it can still be of the order few times ~ 0.1. A very small $\mathcal{R}_{\rm f}$ ($\lesssim 0.1$) is not a good choice as it produces massive bursts that could exceed typical values ($\sim 0.01 - 0.05\,M_\odot$) by a factor up to $10 - 15$. There is some freedom in choosing $\mathcal{R}_{\rm f}$ and we set it to 0.23 in order to obtain a reasonable number of bursts in comparison to simulations. A higher value will result in more bursts and a lesser value yields fewer bursts. During a burst, the disc loses mass and the star gains mass, both in an amount equal to the mass of the clump. So, the updated disc-to star mass ratio becomes

$$\frac{M_{\rm d}^\dagger}{M_*^\dagger} = \mathcal{R}_{\rm f}\,, \tag{4.32}$$

where $\mathcal{R}_{\rm f} < \mathcal{R}_{\rm b}$, $M_{\rm d}^\dagger = M_{\rm d} - M_{\rm burst}$, and $M_*^\dagger = M_* + M_{\rm burst}$. So, simplifying Equation (4.32) the clump mass (often called as burst mass) can be calculated as

$$M_{\rm burst} = \frac{M_{\rm d} - \mathcal{R}_{\rm f}\,M_*}{(1+\mathcal{R}_{\rm f})}\,. \tag{4.33}$$

After every burst, we modify M_{0d} with the updated disc mass. We further calculate $\dot{M}_{\rm ds}$ and C_1 as shown in Equation (4.25) and (4.26) using the updated disc mass until the next burst. We describe our numerical prescription in detail in Section 4.3.2. In our formalism we set the time duration for each burst as

$$\Delta t_{\rm burst} = 100\,\frac{M_{\rm burst}}{0.01\,M_\odot}\ {\rm yr}\,. \tag{4.34}$$

Table 4.1: Model parameters: temperature T, the central number density n_c, the central flat region of the core r_c, outer radius of the core $R_{\rm out}$, mass of core $M_{\rm core}$, and final stellar mass M_* at the end of the desired evolution.

	T [K]	n_c [$\times 10^4$ cm^{-3}]	r_c [pc]	$R_{\rm out}$ [pc]	$R_{\rm out}/r_c$	$M_{\rm core}$ [$M_\odot$]	M_* [$M_\odot$]
MODEL1	12	4.95	0.037	0.118	3.2	0.50	0.28
MODEL2	12	4.95	0.037	0.148	4.0	1.10	0.57
MODEL3	12	4.95	0.037	0.185	5.0	1.98	1.0
MODEL2A	12	8.5	0.028	0.112	4.0	0.84	0.45
MODEL2B	12	2.0	0.058	0.232	4.0	1.74	0.9
MODEL2C	8	3.25	0.037	0.148	4.0	0.75	0.39
MODEL2D	16	6.70	0.037	0.146	4.0	1.46	0.77

For simplicity, we correlate the time duration of the burst with the mass of the burst in a linear fashion such that time duration of an episodic burst of typical mass 0.01 $M_\odot$ is around 100 yr as found in the simulations and observations (Hartmann & Kenyon, 1996; Herbig, 2008; Audard et al., 2014, references therein). The linear relation between the burst mass and its time duration in Equation (4.34) results in an increasing burst duration with time since the relatively more massive clumps (few times 0.01 $M_\odot$) that form at later times in the more massive discs will be tidally sheared into multiple clumps of $\sim$ 0.01 $M_\odot$ that collectively produce a longer duration burst (Vorobyov & Basu, 2015). A linear relation is the simplest function that can be used to show an increasing duration as the burst masses become larger in the later evolution. The simulations do not provide a large number of data points in this regard, so a linear relation is the simplest fitting function and exhibits a luminosity evolution that is reasonable in comparison to the simulations.

4.3 Results

We implement our formalism for models with three different parent core masses as described in Table 4.1. We study cores of different masses by varying the outer radius. The actual size of the prestellar cloud core is one of the significant constraints from observations. For example, in the dense cores in Taurus, 0.02 pc $\lesssim R_{\rm edge} \lesssim$ 0.1 pc (e.g. Motte & André, 2001). Simulations show that beyond some such distance $R_{\rm edge}$, the column density merges into a near-uniform

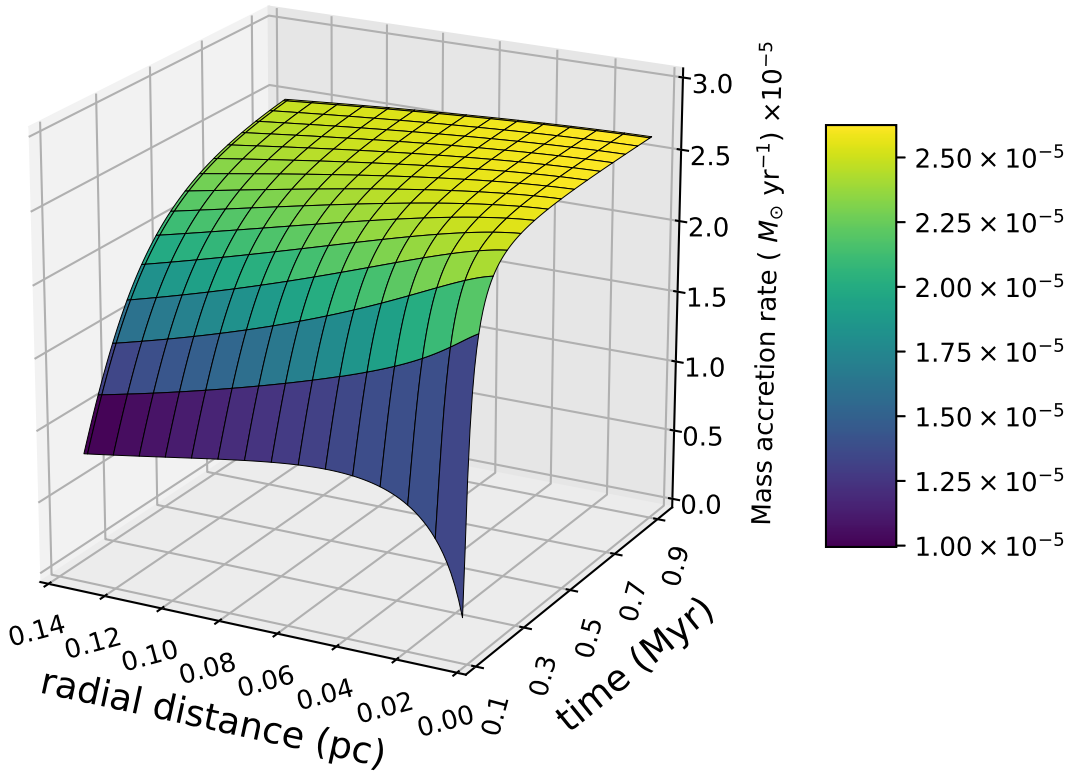

Figure 4.1: 2D representations of mass accretion rate as a function of space and time for the isothermal density profile.

background or fluctuates about a typical mean value resembling the ambient molecular cloud (Basu & Ciolek, 2004).

4.3.1 Envelope accretion

We numerically solve the mass accretion rate using Equation (4.16) for the modified isothermal density profile of Equation (4.1) by combining the Equations (4.3)–(4.16). Figure 4.1 shows the mass accretion rate $\dot{M}(r,t)$ as a function of space and time for a pressure-free cloud with $n_c \sim 5\times10^4$ cm^{-3} and $r_c = 0.037$ pc. The mass accretion rate initially increases with time and appears to approach a constant value at later times $t > 0.7$ Myr. The temporal evolution of the mass accretion rate also has a radial dependence. Hence, we see that at smaller radial distances, $\dot{M}(r,t)$ approaches the constant value at a faster time. In Figure 4.2a, b, c we present the mass accretion rate $\dot{M}(r,t)$ as a function of space and time for the tapered isothermal density profile

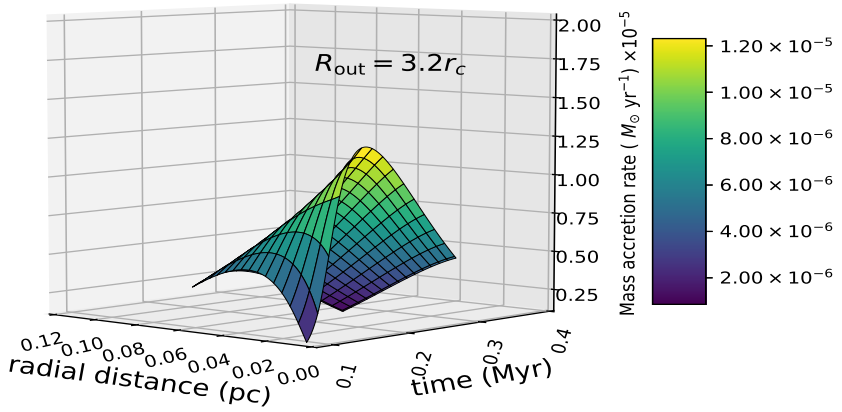

(a)

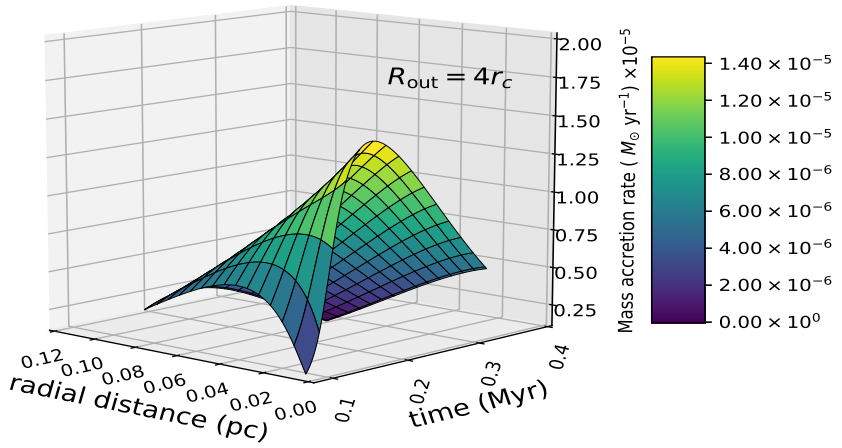

(b)

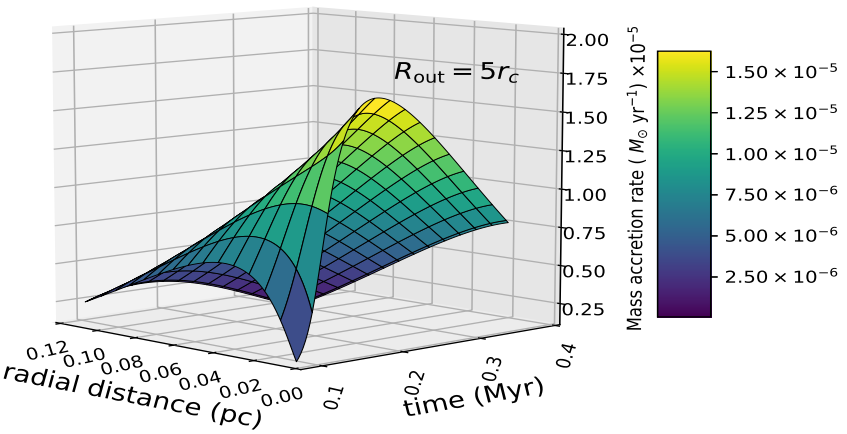

(c)

Figure 4.2: 2D representations of mass accretion rate as a function of space and time for the modified density profile with different outer radius (a) $R_{out} = 3.2r_c$, (b) $R_{out} = 4r_c$, (c) $R_{out} = 5r_c$.

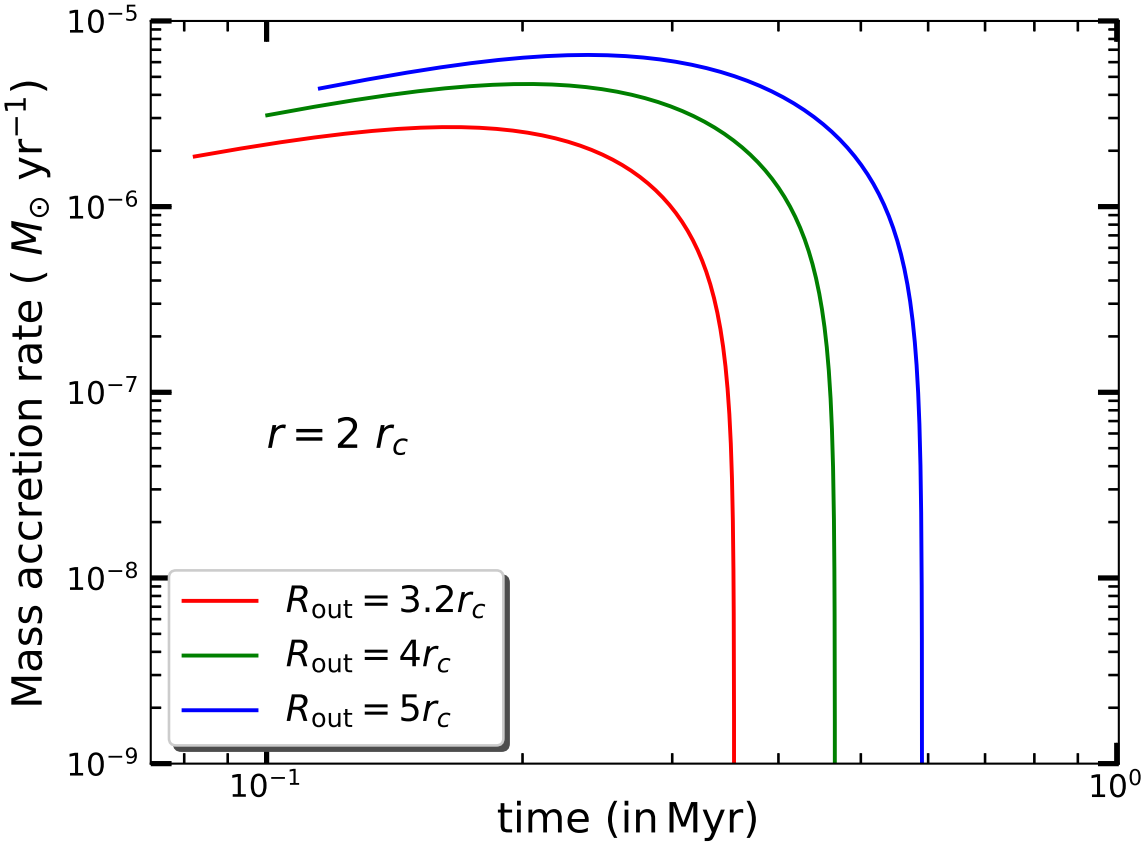

Figure 4.3: 1D representation of the temporal evolution of mass accretion rate for models with $R_{\rm out} = 3.2r_c$ (red line), $R_{\rm out} = 4r_c$ (green line), $R_{\rm out} = 5r_c$ (blue line) calculated at a fixed radial distance $r = 2r_c$.

of Equation (4.2) with three different outer radii $R_{\rm out} = 3.2r_c,\ 4r_c,\ 5r_c$, respectively. Initially $\dot{M}(r,t)$ increases with time. Afterwards, because of the finite mass reservoir when the envelope is depleted, $\dot{M}(r,t)$ gradually decreases over the time as well as over the radial distance. We find the $\dot{M}(r,t)$ rises faster to a peak at a smaller radial lengthscale. With increasing $R_{\rm out}$, $\dot{M}(r,t)$ falls off at a later time. Figure 4.3 shows the temporal evolution of $\dot{M}(r,t)$ at a fixed radial distance $r = 2r_c$ for all three models as shown in Figure 4.2. It is evident from this plot that, with increasing $R_{\rm out}$, $\dot{M}$ starts to evolve at a slightly later time and attains the maximum and then falls after a longer time.

4.3.1.1 Spatial profiles of mass and angular momentum

In our model we deal with the geometry of a spherical cloud with an outer radius $R_{\rm out}$. To obtain the column density and angular momentum as function of an observationally tractable

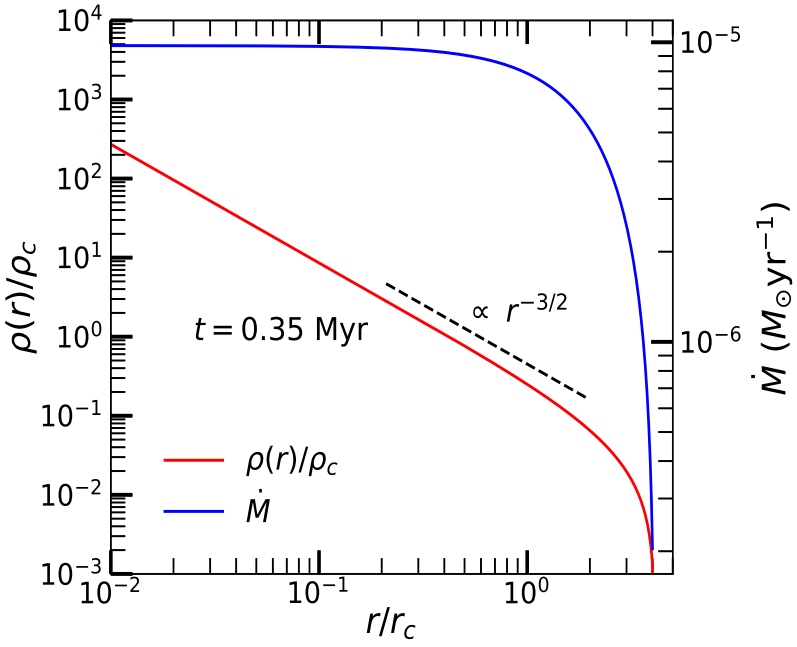

(a)

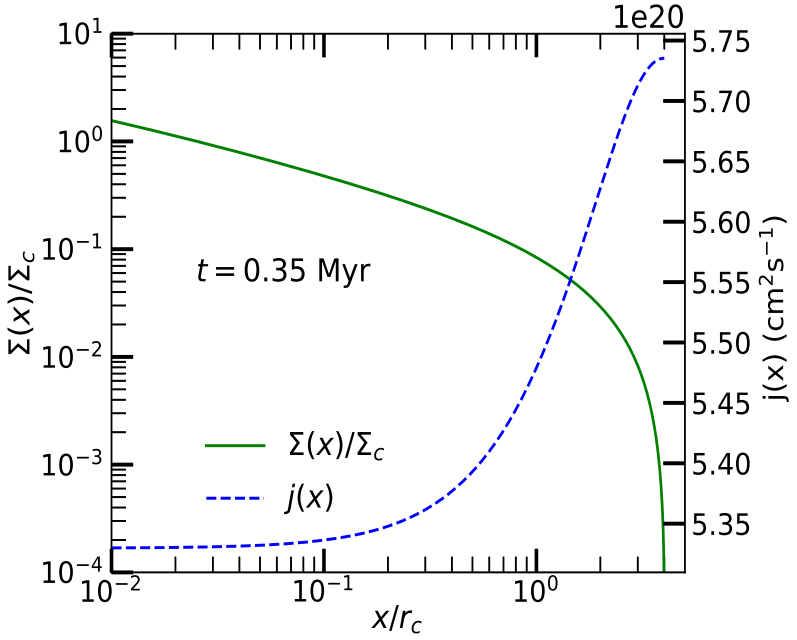

(b)

Figure 4.4: Top: Radial profiles of density $\rho(r)/r_c$ (red) and mass accretion rate $\dot{M}$ (blue) as a function of radial distance x/r_c at a fixed time $t = 0.35$ Myr for model with $R_{\rm out} = 5r_c$. Bottom: Column density $\Sigma(x)/\Sigma_c$ (green) and the specific angular momentum $j(x)$ (blue) as a function of radial offset x/r_c at the same time for the same model.

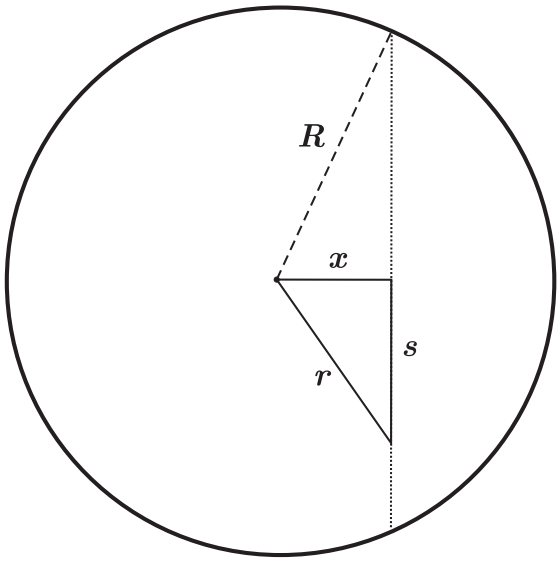

Figure 4.5: Schematic illustration of a cut through a spherical cloud of radius R. The observer is positioned along the direction of the coordinate s, and measures an integrated column density Σ as a function of the offset x (figure taken from Dapp & Basu, 2009).

parameter, we consider a cut through of the spherical cloud. If we are positioned along the direction of line-of-sight coordinate s, then we can measure these quantities as function of radial offset x using the transformation from s coordinate to the radial offset coordinate x, which yields $s = \sqrt{r^2 - x^2}$ and hence $ds = rdr/\sqrt{r^2 - x^2}$. The geometry is portrayed in Figure 4.5. The column density can be calculated by integrating the volume density along a line of sight through the spherical cloud:

$$\begin{aligned} \Sigma(x) &= 2 \int_0^{\sqrt{R_{\rm out}^2 - x^2}} \rho(s) ds \\ &= \int_0^{R_{\rm out}} \frac{\rho(r) r}{\sqrt{r^2 - x^2}} dr \,, \end{aligned} \tag{4.35}$$

as described in § 2.1 of Dapp & Basu (2009). Once $\Sigma(x)$ is obtained, we calculate the enclosed mass by integrating the column density along the radial offset through the sphere, yielding

$$M(x) = \int_0^x \Sigma(x')\, x' dx' \,. \tag{4.36}$$

In Figure 4.4a, we show the evolution of the density $\rho(r)/\rho_c$ (red line) as a function of radial distance r/r_c at a later time $t = 0.35$ Myr. For $r/r_c \lesssim 1$, $\rho(r) \propto r^{-3/2}$, characteristic of an expansion wave (Shu, 1977); and for $r/r_c > 1$, $\rho(r)$ starts to diverge and sharply falls. In our model, $R_{\rm out}$ is not large enough to show a clear power law $\rho(r) \propto r^{-2}$ profile before the steep descent near the edge. In Figure 4.4a, the blue line presents the mass accretion rate $\dot{M}$ (blue line) as a function of r/r_c at $t = 0.35$ Myr. In our work, we exclude the case of large $R_{\rm out}/r_c \sim 10$ or 100 as it will give rise to intermediate to high mass stars.

In Figure 4.4b, the green line shows $\Sigma(x)/\Sigma_c$ as a function radial offset x/r_c at a time $t = 0.35$ Myr for the model with $R_{\rm out} = 5r_c$. Here, $\Sigma_c = \Sigma(x = 0) = 2r_c\rho_c \arctan(R_{\rm out}/r_c)$ for the modified isothermal density profile shown in Equation (4.1) (see more in Dapp & Basu, 2009). The profile of $\Sigma(x)/\Sigma_c$ essentially traces the profile of $\rho(r)/\rho_c$ and falls sharply at the outer edge. Hence, $M(x)$ gets saturated at the outer radius. However, the conservation of the specific angular momentum corresponds to the total enclosed mass $M_{\rm tot}(x)$. It can be calculated as $M_{\rm tot}(x) = M(x) + M_*(t)$, which includes the mass that has reached the star. Here, $M_*(t)$ is the stellar mass at the centre at time t. The relation between specific angular momentum $j(x)$ and the total enclosed mass $M_{\rm tot}(x)$ can be written as

$$j(x) = \frac{\Omega_0 \pi G^{1/2}}{B_{\rm ref}} M_{\rm tot}(x)\,, \tag{4.37}$$

as shown in Basu (1998). Here, Ω_0 is the typical (mean) rotational rate for the dense molecular cloud and is about 10^{-14} rad s^{-1} (see Goodman et al., 1993), and $B_{\rm ref}$ is the canonical magnetic field of 30 μG for a molecular cloud core (see Goodman et al., 1993; Crutcher et al., 1993). We follow a semi-analytic approach to numerically calculate the angular momentum profile at a later phase after the collapse has started. In Appendix 4.6.1, we present the spatial profiles of $\Sigma(x)$ and $j(x)$ at $t = 0$ for the tapered isothermal density profile of Equation (4.2), which are analytically tractable for this special case. In the inner region where $M_*(t) > M(x)$, $M_{\rm tot}(x)$ will be nearly constant and approximately equal to $M_*(t)$. In Figure 4.4b the blue curves shows the specific angular momentum $j(x)$ as a function of x/r_c at a time $t = 0.35$ Myr after the collapse has proceeded and the central star is formed. We notice that within the inner region, $j(x)$ is almost flat up to $x/r_c \approx 0.15$ and then outside this region $j(x)$ increases linearly and comes to

a saturation at the outer edge. This kind of $j(x)$ profile reasonably corresponds to the evolution starting from the prestellar collapse (in the outer region) to a radial expansion wave regime (in the inner region) with $\Omega \propto r^{-2}$ (see Dapp et al., 2012). For a typical $r_c = 0.033$ pc, the break occurs around $x = 1021$ AU. The range of $j(x) \simeq 10^{20} - 10^{21}$ cm^2 s^{-1} and the shape of the profile is generally consistent with observations (e.g. fig. 6 of Ohashi et al. (1997), fig. 13 of Yen et al. (2011), fig. 11 of Kurono et al. (2013), fig. 9 of Yen et al. (2017), and fig. 17(b) of Gaudel et al. (2020)).

4.3.2 Formalism of stellar accretion

In this section we describe (see Figure 4.6) how we obtain the mass accretion rate on to the star, $\dot{M}_*$, with episodic bursts as shown by the black line in Figures 4.7a, 4.8a, 4.9a. Here $\dot{M}_*$ is obtained from the joint result of the infall rate from the envelope and mass transportation rate from the disc to the star. We obtain the temporal evolution of the mass accretion rate at a radial distance $r = 2r_c$ from envelope accretion for the models with different $R_{\rm out}$. We perform the following steps that demonstrate our semi-analytic formalism:

(i) The initial masses of the disc and protostar are set to be 0.001 $M_\odot$ and 0.01 $M_\odot$, respectively. We consider 90% of the total accretion from the envelope goes to the disc and the rest goes directly to the protostar (see Equation (4.27)). At each time, the disc and star mass can be calculated by integrating the respective mass accretion rates from the envelope to the disc and the star, respectively.

(ii) Thereafter the mass transportation is calculated from disc to the star by integrating Equation (4.25). Note that, before the occurrence of the burst, t_{0d} is considered as t_0. We calculate C_1 accordingly as shown in Equation (4.26). The amount of mass that the disc loses is added to the star. We then update the disc and the star masses.

(iii) If the disc-to-star-mass ratio $M_{\rm d}/M_*$ does not go above the threshold, then the disc is gravitationally stable and we calculate the $\dot{M}_*$ using only the contributions of the mass accretion rate from disc to star and from envelope to the star.

(iv) However, if the disc-to-star-mass ratio $M_{\rm d}/M_*$ goes above 0.33 (and the disc mass is at least 0.01 $M_\odot$), the disc becomes gravitationally unstable. The disc transfers the matter to the star (which gives rise to an accretion burst) so that the $M_{\rm d}/M_*$ ratio goes below the threshold

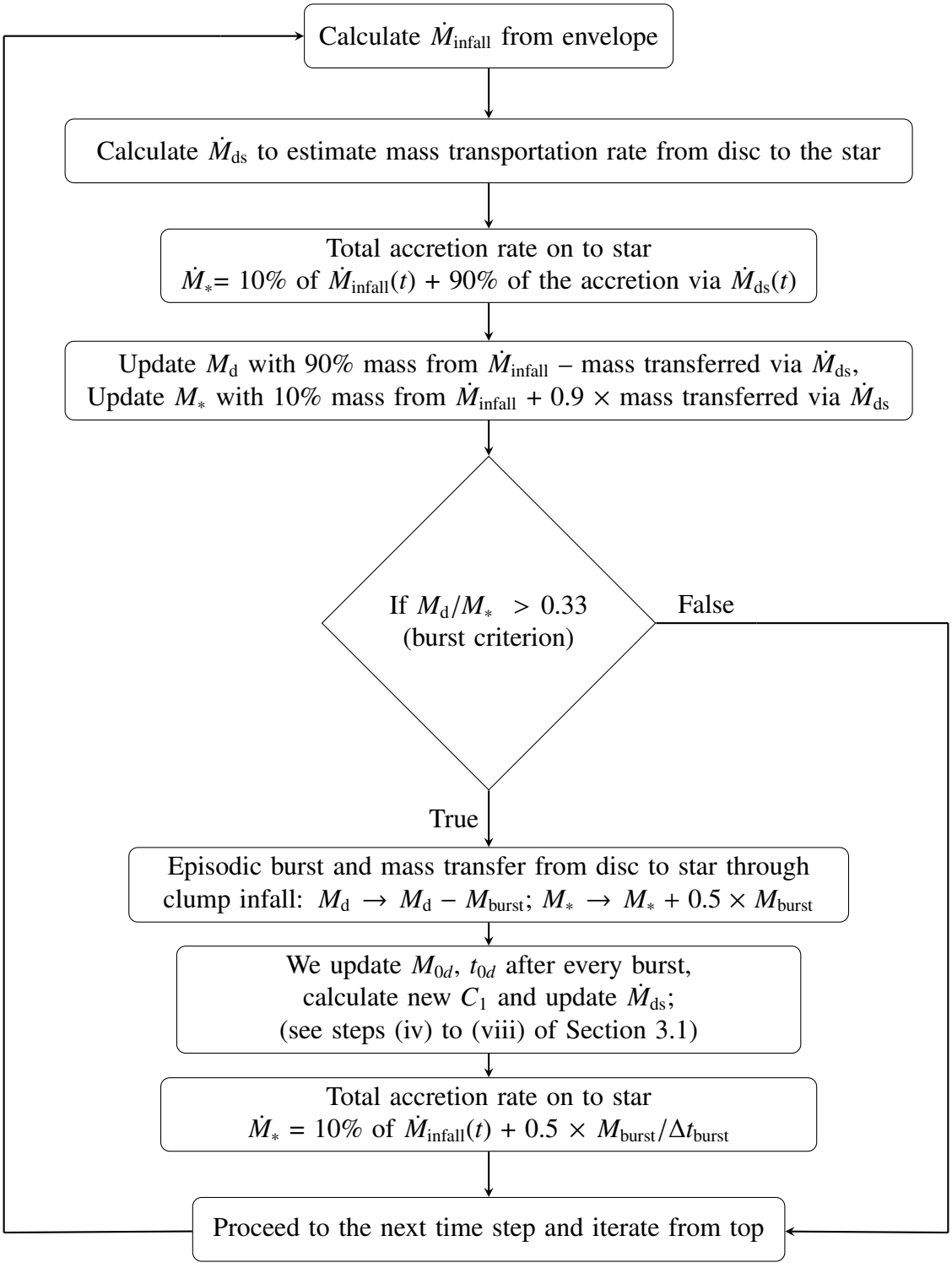

Figure 4.6: Flowchart of our formalism for the episodic accretion model.

and the disc becomes gravitationally stable.

(v) The amount of mass depleted with each burst is called the burst mass and we require that at least 0.01 $M_{\odot}$ should be associated with a burst. During an accretion burst, the burst mass goes from the unstable disc toward the central protostar, adding to its mass. Outflows are taken into account such that during the envelope accretion phase 50% of the mass accreted during a single burst episode goes to the outflows, while 10% of the mass that is accreted via disc-to-star accretion goes to outflows. The molecular outflows are ubiquitous among protostars. The outflow energetics reflects a correlation to the mass infall/accretion rate (Bontemps et al., 1996a). Hence, during the disc accretion phase we update the stellar mass by taking 90% contribution of the disc-to-star mass accretion rate $\dot{M}_{\rm ds}$ as mentioned in the third and fourth step of the flowchart (see Figure 4.6). Whereas, during episodic bursts 50% of the burst mass gets finally accreted onto star as shown in the second last step of the flowchart.

(vi) After the burst, C_1 is calculated using the updated disc mass and t_{0d}. We update t_{0d} to correspond to the most recent burst time and the disc mass is also updated accordingly as mentioned in point (iii).

(vii) Once a burst occurs, we calculate the burst mass as shown in Equation (4.32) and the time duration as shown in Equation (4.34). We calculate the mass accretion rate due to the burst by dividing the burst mass by the time duration of the burst. Then we add this to the pre-calculated mass accretion rate (from the disc and envelope) on to the star to calculate the final $\dot{M}_*$ at that time.

(viii) In between the bursts, the baseline of $\dot{M}_*$ is determined by the net mass accretion rate from the disc to the star and a little portion goes directly from the envelope to the star (see Equation (4.16)).

(ix) We iterate the above steps as described in the points (i)-(viii) and also in Figure 4.6 until the desired end of the evolution.

The envelope accretion and disc accretion continue to coexist until approximately 99% of the envelope has been consumed by the protostar and protostellar disc. After that, the evolution of the mass accretion is set only by the disc accretion, which has a steady form $\dot{M}_{\rm ds} \propto t^{-6/5}$. Hence, when the envelope accretion ends, from then onwards $\dot{M}_*$ (black line) identically overlaps with $\dot{M}_{\rm ds}$ (blue line), as shown in Figures 4.7a, 4.8a, 4.9a. The accretion bursts do not

occur during this phase. Due to the lack of accretion from the envelope, the disc can not become sufficiently massive for the GI that leads to outbursts.

4.3.3 Temporal evolution of the mass accretion rate

Figure 4.7a, 4.8a, 4.9a present the temporal evolution of the mass accretion rate for the models with different core masses as described in the Table 4.1. In each of these figures, the red line shows the mass accretion rate from the spherical envelope accretion, which is similar to the curves shown in Figure 4.3. Moreover, this curve resembles the infall rate from envelope as calculated in the simulations. The black line shows the mass accretion rate on to the central star from the disc and directly from the envelope. The distribution of mass accretion rate from the envelope separately to the disc and to star is mentioned in Section 4.3.2. The spikes represent the episodic accretion bursts. The amplitude of the mass accretion rate at each burst is calculated as the burst mass divided by its time duration (Equation (4.34)). The blue line shows the mass accretion rate from disc to the star via the LP formula (see Equation (4.25)). There is a step-like increment at the occurrence of each burst, which corresponds to an updated intercept C_1 (see Equation (4.26)). The factor C_1 has an implicit time dependence through the updated disc and star mass at the time instance of a burst. The bursts occur due to the onset of gravitational instability within the disc. The disc is transporting material to the star via the LP formula. Simultaneously, the disc is gaining matter from the envelope infall at a different rate. Due to the mismatch between the infall rate and transport rate, the disc becomes sufficiently massive that the disc-to star-mass ratio exceeds the threshold for gravitational Toomre-Q instability. Such a gravitationally unstable disc gets fragmented into spiral arms and clumps. The spiral arms are moving outward (gaining angular momentum) and the clumps are driven inward through the gravitational torques (losing angular momentum) and fall on to the central protostar. This leads to vigorous episodic accretion bursts that produce luminosity outbursts seen in observations.

Because of the finite mass reservoir, the envelope gets depleted at an earlier time for the lower mass cores. At a later time, during the phase with only disc accretion, there is no burst, which delineates the simple power law profile where $\dot{M}_{\rm ds} \propto t^{-6/5}$ with a constant intercept. We notice the total number of bursts is increasing with increasing core mass. We see the least

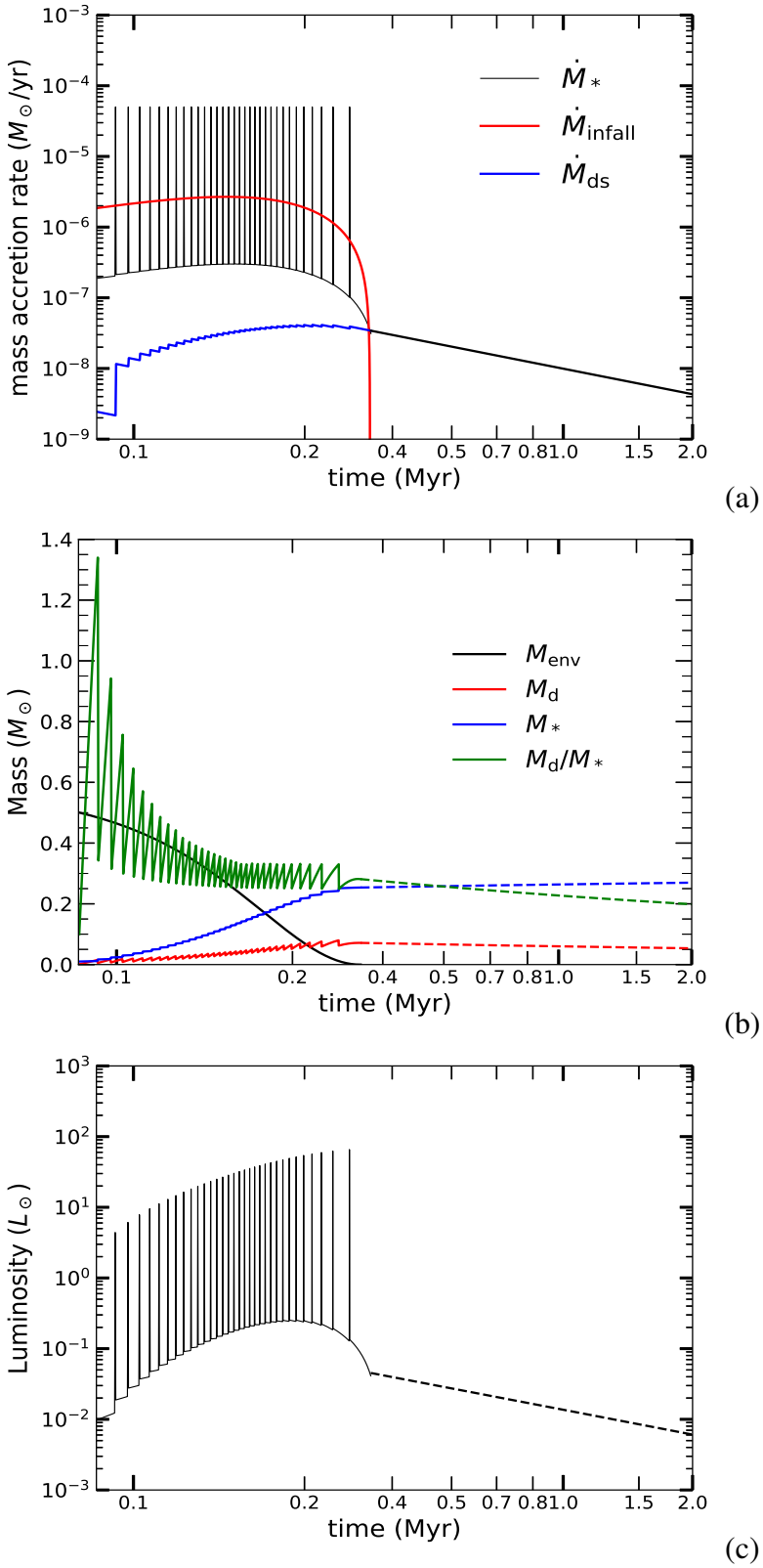

Figure 4.7: MODEL1: (a) temporal evolution of the mass accretion rate (the total number of bursts is 32), (b) distribution of masses in the envelope-disc-star system, (c) temporal evolution of the accretion luminosity distribution. In (b) and (c), the solid line presents the joint evolution from envelope accretion together with disc accretion and the dashed line shows the evolution due to disc accretion only.

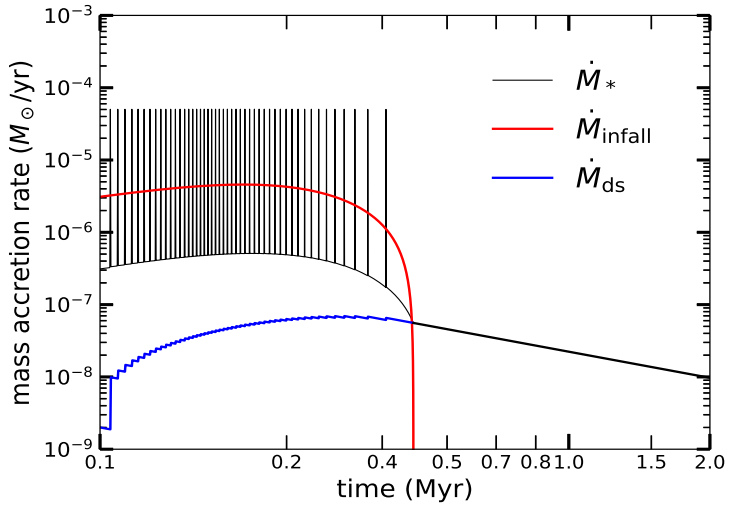

(a)

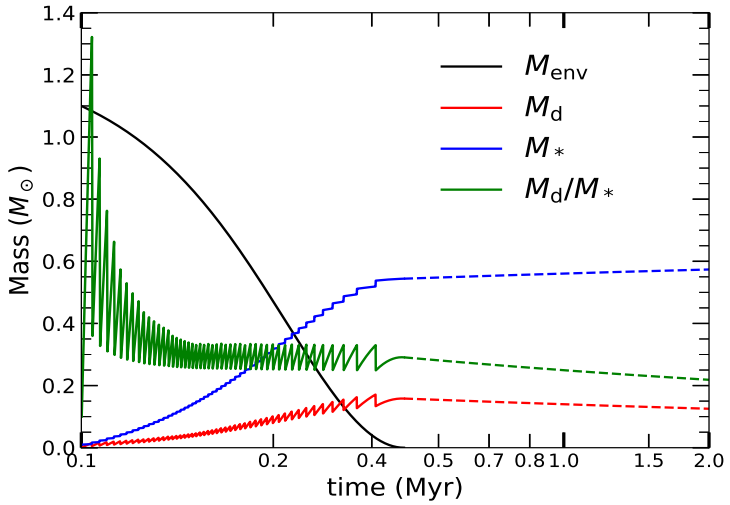

(b)

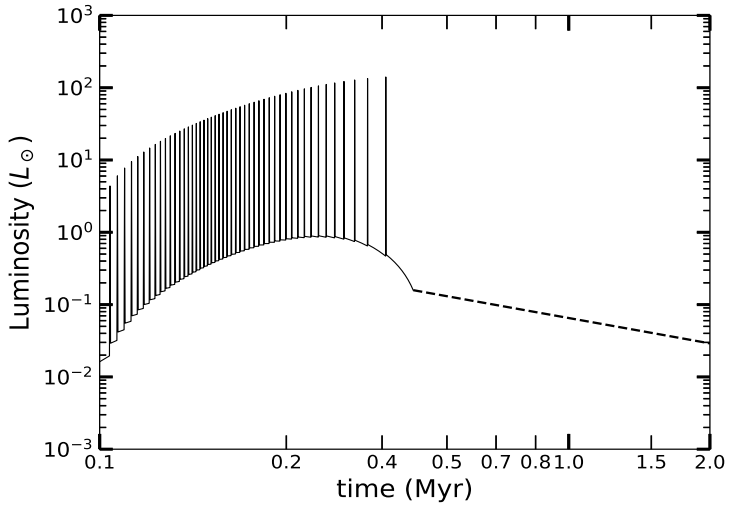

(c)

Figure 4.8: MODEL2: (a) temporal evolution of the mass accretion rate (the total number of bursts is 48), (b) distribution of masses in the envelope-disc-star system, (c) temporal evolution of the accretion luminosity distribution. In (b) and (c), the solid line presents the joint evolution from envelope accretion together with disc accretion and the dashed line shows the evolution due to disc accretion only.

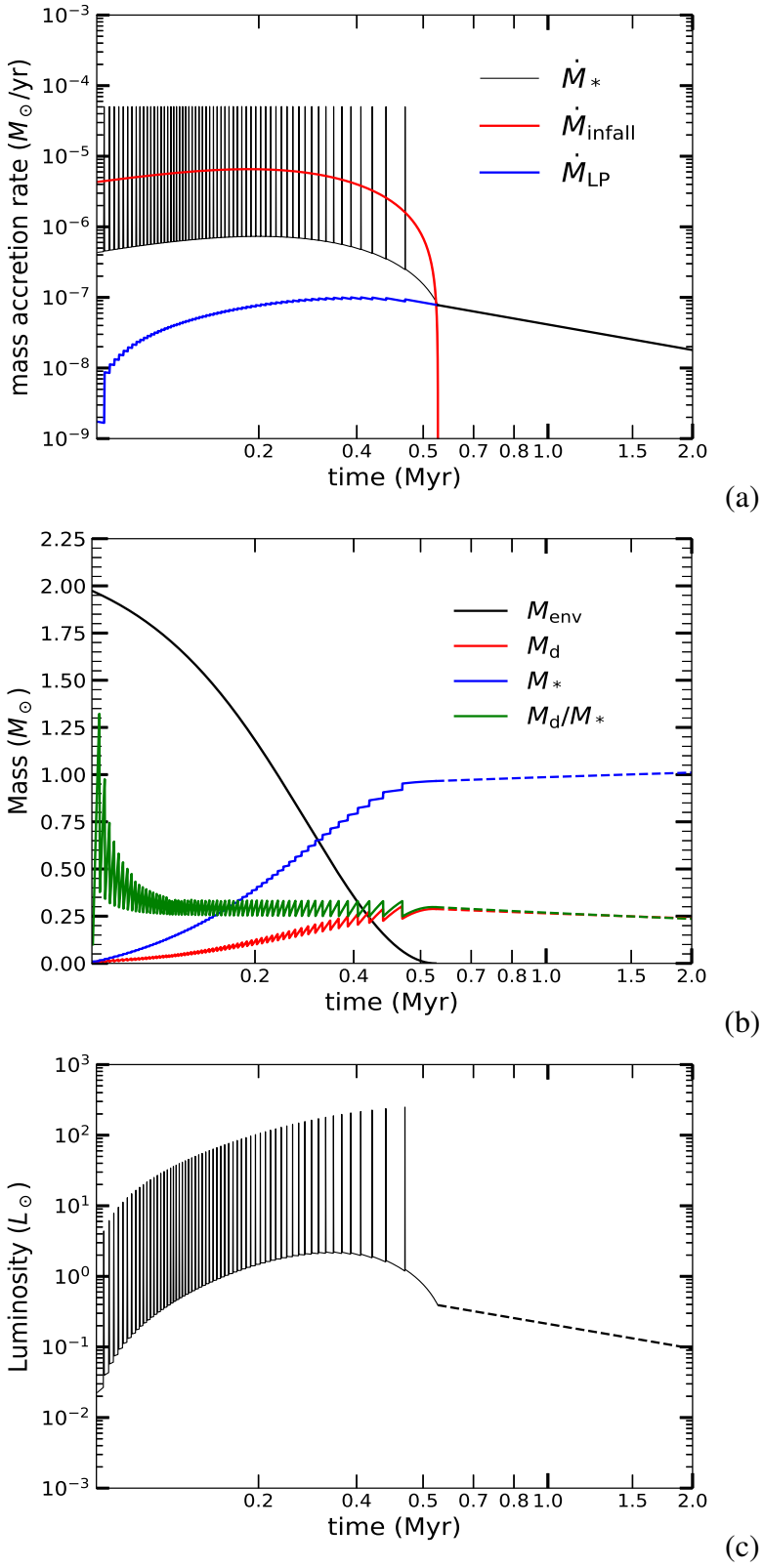

Figure 4.9: MODEL3: (a) temporal evolution of the mass accretion rate (the total number of bursts is 60), (b) distribution of masses in the envelope-disc-star system, (c) temporal evolution of the accretion luminosity distribution. In (b) and (c), the solid line presents the joint evolution from envelope accretion together with disc accretion and the dashed line shows the evolution due to disc accretion only.

number of bursts for MODEL1. Because for the evolution of a small core of 0.5 $M_{\odot}$, the disc does not get much time to continue to grow and spherical envelope accretion ceases early. Additionally, at the very initial time, the baseline of the $\dot{M}$ increases to $\sim 2 \times 10^{-7}\,\mathrm{M_{\odot}\,yr^{-1}}$, $\sim 3\times10^{-7}\,\mathrm{M_{\odot}\,yr^{-1}}$, $\sim 4\times10^{-7}\,\mathrm{M_{\odot}\,yr^{-1}}$ for MODEL1, MODEL2, and MODEL3, respectively. We do not get any burst during the disc accretion phase, which starts typically after $t \approx 0.35$ Myr, 0.45 Myr, and 0.55 Myr for MODEL1, MODEL2, and MODEL3, respectively. Overall, we find that the evolution starts early for a low core mass and it starts at a later time for an increased core mass.

4.3.4 Mass estimation

Figures 4.7b, 4.8b, 4.9b present the masses contained in the envelope (black line), protostellar disc (red line), and the central protostar (blue line), for the models with different core masses as described in Table 4.1. The mass in the envelope gradually falls over the time as it is being continuously absorbed by the protostellar disc and star. In the earlier stage, the spherical envelope accretion (the segments shown by solid lines) takes over the disc accretion (as shown by the corresponding dashed line) until 99% of the envelope mass has been depleted. We find that each sharp increase in the stellar mass is correlated with a corresponding sharp decrease in the disc mass. These sharp step-like increments/decrements happen because of the addition/subtraction of the finite burst mass to/from the star/disc, respectively, during every infall of a clump from the gravitationally unstable disc to the star. The accretion bursts continue to occur until the envelope mass has reduced by 90% – 95% and the mass accretion rate drops to $\sim 10^{-7}\,\mathrm{M_{\odot}\,yr^{-1}}$.

Our study shows that at the end of the evolution the final stellar mass acquired is about 50% of the initial parent envelope mass, which is approximately consistent with some observational estimates (e.g. Alves et al., 2007). Outflows also constrain the final stellar mass as found from the observations and theoretical models. In our model, on average 50 – 60% of the final stellar mass comes from the accretion bursts. However, the observations have been used to estimate that 10% – 35% of the total stellar mass is accumulated during the bursts. This is obtained for low mass star formation (Dunham & Vorobyov, 2012) and also for high mass stars (Caratti o Garatti et al., 2017; Meyer et al., 2017; Magakian et al., 2019). In our study, episodic accretion

plays a dominant role in the stellar mass growth as the disc accretion via the LP formula is not as vigorous as the episodic accretion. A more sophisticated model of mass and angular momentum transfer due to disc viscosity could help to refine the results. We keep this aside for future studies. The green line shows the temporal evolution of the disc-to-star-mass ratio. The spiky behaviour in the temporal evolution of the disc-to-star-mass ratio corresponds to the episodic bursts when the disc loses mass and star gains mass. At the early times, this ratio exceeds unity. Soon after that, the disc-to-star-mass ratio goes below unity, as found in observations. We note that our model is applied to very early times consistent with the Class 0/I phase, when this ratio may be greater than in the later (and more frequently observed) Class II phase when the envelope mass has largely dissipated and bursts are less frequent.

During the episodic bursts, the clumps of $\sim 0.01-0.08\,M_{\odot}$ migrate inward to the centre. As the mass associated with a burst increases so does the time duration of the burst (see Section 4.3.4). It happens because of the choice of a simple linear formula for fitting time duration with the mass for each burst as seen in Equation (4.34); a typical burst of $0.01\,M_{\odot}$ corresponds to a duration of 100 yr. For MODEL1 with core mass $0.5\,M_{\odot}$, the burst masses are ranging from $0.01-0.017\,M_{\odot}$, with a time duration of $110-170$ yr. For MODEL2 with core mass $1.1\,M_{\odot}$, the burst masses range from $0.01-0.037\,M_{\odot}$, with a time duration of $132-377$ yr. For MODEL3 with core mass $\simeq 2\,M_{\odot}$, the burst masses range from $0.01-0.05\,M_{\odot}$, with a time duration of $132-500$ yr up to a time $t = 0.3$ Myr. At a later stage ($0.3\,\mathrm{Myr} < t < 0.46\,\mathrm{Myr}$), for this relatively high-mass model, there are a few bursts (around $4-6$), and the burst mass goes up to $\sim 0.05-0.08\,M_{\odot}$ with a time duration of $500-830$ yr. This amount of mass and time duration for the physical episodic bursts may seem excessive, however it can be thought of as the accumulation of several clumps of $\sim 0.01-0.02\,M_{\odot}$ occurring in rapid succession, each with ~ 100 yr duration. Such clustered (knotty) bursts occur due to the disintegration of large clumps that are tidally disrupted as they approach the star, as described by Vorobyov & Basu (2015) and used by Vorobyov et al. (2018) to explain the multiple knots in the vigorous jets from Herbig-Haro objects. The time resolution of our current scheme is ~ 4 kyr and we note that we do not resolve smaller intervals in order to keep our computation simple. Our aim is to reproduce the big picture of the main characteristics of mass accretion as found from the very time-consuming numerical hydrodynamic simulations. Finally, we notice that sums

of all masses remain constant, which implies that there is a global conservation of mass in our semi-analytic model.

4.3.5 Estimating luminosity and comparing with observations

Figure 4.7c, 4.8c, 4.9c present the temporal evolution of the accretion luminosity for three different core masses, as described in the Table 4.1. In our formalism, we calculate the accretion luminosity as

$$L_{\rm acc} = f_{\rm acc}\,\frac{GM_*\dot{M}_*}{R_*}\,, \tag{4.38}$$

where $\dot{M}_*$ is mass accretion rate on to the central protostar during spherical envelope accretion, M_* and R_* are the stellar mass and radius, respectively. We assume that a factor $f_{\rm acc}$ of the total incoming gravitational potential energy is converted to radiation at a shock front where the infalling material meets the star. Here, we take $R_* = 3\,{\rm R}_\odot$ and $f_{\rm acc} = 0.5$. The luminosity evolution reveals a peaked curve since the product $M_*\dot{M}_*$ reaches a peak at a certain time. At a very early time, $\dot{M}_*$ has a high value and M_* is still low, whereas at a later time, $\dot{M}_*$ decreases and M_* has increased.

Apart from the accretion luminosity, we account for the contribution from the photospheric luminosity. The intrinsic photospheric luminosity can be expressed as

$$L_{\rm phot} = 4\pi R_{\rm eff}^2 \sigma_{\rm SB} T_{\rm eff}^4\,, \tag{4.39}$$

where $\sigma_{\rm SB}$ is the Stefan-Boltzmann constant, and $R_{\rm eff}$ and $T_{\rm eff}$ are the radius and effective temperature of the stellar photosphere, respectively. In general, $L_{\rm phot}$ is much less than $L_{\rm acc}$ during the bursts. In between the bursts it is comparable to $L_{\rm acc}$. For the completeness of our study, we add the contribution from the photospheric luminosity based on the survey of stellar masses (Yorke et al., 1993, 1995) during the evolution, as used in the numerical simulations of Vorobyov et al. (2020).

We present a comparison of different luminosity distributions in Figure 4.10a. The filled histogram shows the luminosity distributions for the Class 0 stellar objects within an evolutionary span of ~ 0.1 Myr based on all the models of different final stellar masses as shown in Table 4.1. This time interval essentially corresponds to the time until the end of the embedded

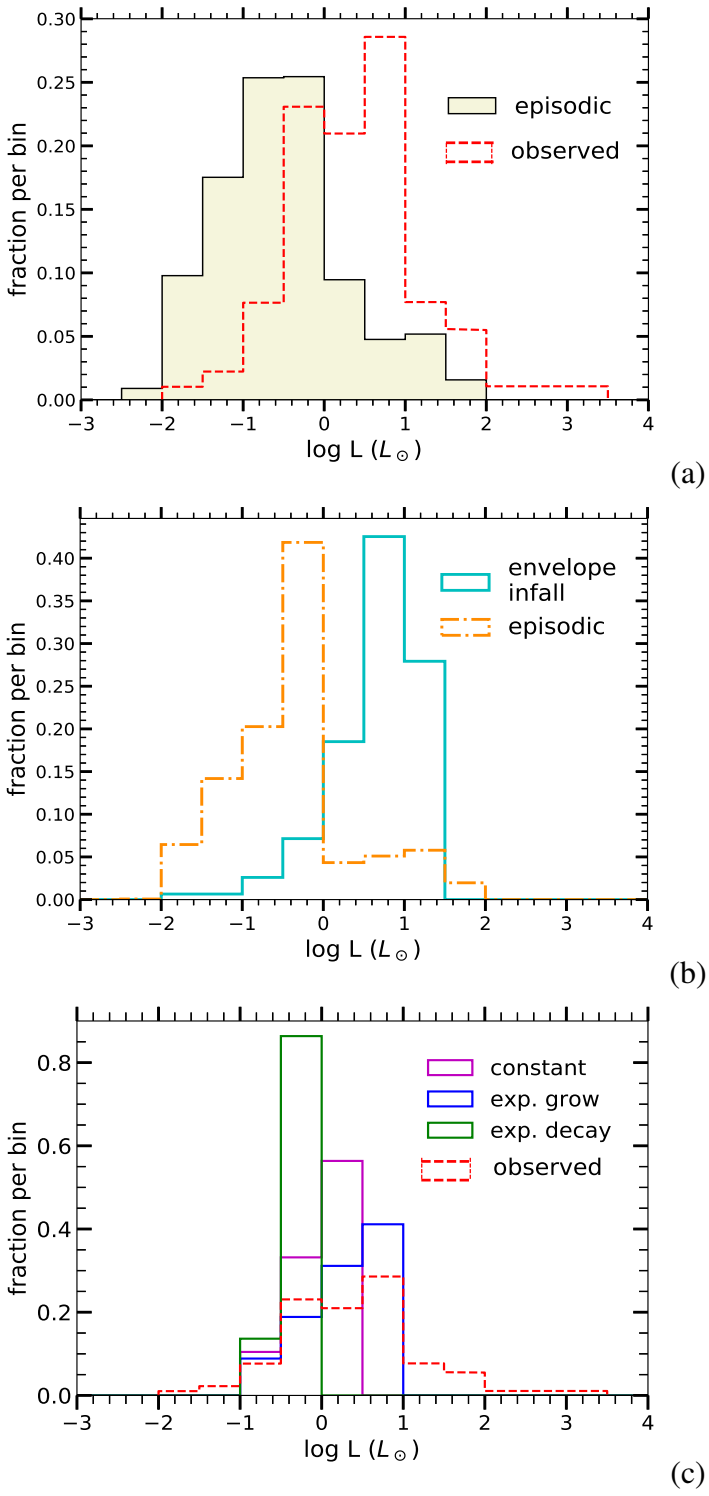

Figure 4.10: Top (a): Histograms of luminosities from our episodic model (the filled histogram), and the observations (red dashed line) as shown in the right panel of figure 2 of Fischer et al. (2017). Middle (b): Histograms of luminosities from a single episodic model (MODEL2) (orange dashed line) and its respective envelope infall model (cyan solid line). Bottom (c): Histogram of luminosity for the analytic models with constant (magenta), exponentially growing (blue), exponentially decaying (green) mass accretion rate. The luminosity histogram from observations is shown in the red dashed line for comparison.

protostellar phase. We consider this time range based on the mass remaining (about 50%) in the envelope for a typical Class 0 object. Once the object goes to the Class I phase, the envelope is diminished. To construct the luminosity histogram (the filled histogram in Figure 4.10a, we consider models with a fairly large range of final stellar masses. We also take into account of the appropriate weights based on the initial mass function (IMF) for the different models categorized by the final stellar mass. These weights for the respective logarithmically spaced mass bins are calculated from the cumulative probability distribution presented in Basu et al. (2015). The red dashed histogram in Figure 4.10a presents the luminosities of YSOs found from the *Herschel* Orion Protostar survey as carried out by Fischer et al. (2017, see their fig. 2). The observed histogram is drawn from 91 Class 0 objects. Figure 4.10b clarifies the difference in luminosity distribution due to episodic accretion in a single model. The histograms in cyan (with solid line) and orange (with dashed line) in Figure 4.10b show the luminosity distributions obtained for MODEL2 calculated from the spherical envelope infall (see the red curve of $\dot{M}_{\rm infall}$ in Figure 4.8a) and the calculated episodic accretion (see the black curve of $\dot{M}_{\rm infall}$ in Figure 4.8a), respectively. The histogram obtained from the spherical envelope infall contains many fewer low luminosity values, corresponding to the 'luminosity problem' when the theoretical mass accretion rate c_s^3/G is compared with the observed rate. In a realistic situation with a rotating core, the nonrotating spherical model value c_s^3/G can be thought of as the envelope accretion on to the disc.

In the filled histogram as obtained from our episodic model and shown in Figure 4.10a, the range of luminosities from $\sim 10\,L_\odot$ to $\sim 100\,L_\odot$ correspond to the episodic bursts. On the other hand, luminosities around $10^{-2}\,L_\odot$ are associated with the early time evolution. However, such faint objects are hard to detect observationally. We compare the observed and theoretically obtained histograms quantitatively by using the histogram intersection method. This method calculates the similarity between two distinct histograms by adding the minimum fraction from each bin, with a maximum possible value of 100% if the histograms are identical. A comparison in this case yields a reasonably good cumulative value of 55%. Sampling over many episodic models of different stellar masses and ages might provide a better match to the peak of the observed histogram and can be pursued in future work.

To investigate the effect of accretion bursts in the luminosity distributions, we also study the

similar diagnostics with a constant mass accretion rate as well as time dependent but smoothly increasing and decreasing mass accretion rates. Figure 4.10b shows the histogram of luminosity distributions for analytic models with constant, exponentially growing, and exponentially decaying mass accretion rate, respectively. The models are described by

$$\dot{M}(t) = \begin{cases} \dot{M}_0 & \text{constant (a)}, \\ \dot{M}_0 e^{(t-t_a)/\tau} & \text{exponentially growing (b)}, \\ \dot{M}_0 e^{-(t-t_a)/\tau} & \text{exponentially decaying (c)}, \end{cases} \tag{4.40}$$

where $\dot{M}_0$ is the initial mass accretion rate 2×10^{-6} $M_\odot$ yr^{-1}, τ is the growth or decay constant for the evolution of mass accretion and is set to 0.1 Myr, t_a is the initial time 0.1 Myr. We evolve these models from 0.1 Myr to 0.2 Myr with the initial $M_* = 0.01\,M_\odot$. We choose this value of τ so that the mass of the YSO at sampled time 0.2 Myr is $0.14\,M_\odot$ for the decaying solution and $0.35\,M_\odot$ for the growing solution. These values contain approximately the expected range of Class 0 object masses in low mass star-forming regions. Substantially different values of τ can lead to a range of protostar masses that are too small or too large. Of course, a more comprehensive study of growing and decaying mass accretion models remains to be done and is beyond the scope of our present work. We find that the range of luminosity distributions for our models are $\sim 0.1 - 1$ $L_\odot$, $\sim 0.1 - 4$ $L_\odot$, $\sim 0.1 - 10$ $L_\odot$ for exponentially decaying, constant, exponentially growing mass accretion rates, respectively. We notice from Figure 4.10c that the entire range (i.e. from the low to high end) of luminosities for the above mentioned analytical models is less than that of the observations. The range of the observational luminosity distribution (the red dashed line in Figure 4.10a) is larger by a few orders of magnitude than that predicted with the constant or smoothly decreasing and increasing mass accretion rates. Note that the luminosity histogram for the model with exponentially decaying mass accretion rate covers the shortest range of luminosities ($0.1\,L_\odot \lesssim L \lesssim 1\,L_\odot$), and is the least viable model. We see that the histogram of total luminosities obtained from our semi-analytic episodic accretion model provides a better fit to the observed histogram. It implies that episodic accretion bursts are required, at least at this initial stage, in order to reach solar-type masses within a decent time interval of ~ 0.1 Myr. Episodic accretion aids in accumulating $\sim 35\%$ of the final

stellar mass within a timeline of ~ 0.1 Myr (as seen in Figure 4.9b).

4.4 Discussion

Our semi-analytic model captures the main physical insights of the evolution of episodic mass accretion rate during star formation. Our prescription captures some basic characteristics such as the evolution of the stellar and disc masses, the episodic accretion bursts, the burst amplitudes and corresponding luminosities. These are obtained in a simple computational scheme that is consistent with the results obtained from detailed hydrodynamic simulations of episodic accretion (Vorobyov & Basu, 2007, see also Vorobyov & Basu (2010, 2015)).

The prestellar core is thought to be threaded by a magnetic field with a supercritical mass-to-flux ratio, so that the magnetic field is weaker than self-gravity and a magnetically-diluted gravitational collapse can happen (e.g. Basu, 1997; Basu & Ciolek, 2004). In this work we ignore the effect of this magnetic field and work in the limit of spherical envelope accretion. We also ignore any modification to the Toomre criterion in the disc due to the magnetic field (Das & Basu, 2021). Our approach in this paper has some conceptual similarity to the work of Terebey et al. (1984), who modeled the quasi-spherical collapse solution of a freely-falling singular isothermal sphere with a perturbational addition of rotation. They also joined the solution at small radii to a disc evolution model. We have studied pure spherical collapse and treated angular momentum as only a passively advected quantity with no dynamical back reaction. Our disc evolution model differs from that of Terebey et al. (1984) in that it features the influence of GI and the occurrence of accretion bursts in the early evolution, and at late times is set by a model of gravitational torques that follows a mass accretion rate time dependence $\propto t^{-6/5}$.

We have derived a profile of specific angular momentum (Figure 4.4b) as found in the observations as measured from $C^{18}O$ ($J = 1 - 0$) in the core and $H^{13}CO^+$ ($J = 1 - 0$) in the envelope (Ohashi et al., 1997; Yen et al., 2011; Kurono et al., 2013). A break point in the profile of specific angular momentum may be related to the transition from an inner density profile $\rho \propto r^{-3/2}$ of dynamical free-fall collapse to an outer profile $\rho \propto r^{-2}$ characteristic of near-equilibrium conditions. This has been investigated by Kurono et al. (2013) and has been seen in theoretical models (e.g. Terebey et al., 1984; Dapp et al., 2012). In our models, we take the cloud radius $R_{\rm out}$ to be $5r_c$, and the transition to a r^{-2} power law in the density profile

is not distinguishable since the density falls sharply near the outer edge. Extending the outer edge of cloud might help to obtain a more distinct power-law break in the density in addition to that in the specific angular momentum along the line-of-sight. Additionally, assigning a rotation profile $\Omega(r)$ to each mass shell during the runaway collapse and studying the evolution self-consistently might be a more realistic way to probing the break in the specific angular momentum during the protostellar collapse.

During the earliest evolution, protostars are embedded and heavily obscured by a dusty envelope. The high extinction inhibits a determination of protostellar evolution, lifetimes, and the accretion process until the envelope mass reduces to $\sim$ 50% of the original. We find that during the very early stage, the ratio $M_{\rm d}/M_*$ goes above 1 during the early evolution of the protostar (see Figures 4.7b, 4.8b, 4.9b), as also found in some numerical simulations (e.g. Machida & Basu, 2019; Xu & Kunz, 2021). We consider 10% of envelope infall goes directly to the star, i.e. it occurs along polar regions and not through a disc. By increasing this fraction, the stellar mass growth will be relatively faster and the disc mass can not grow as substantially. The disc would become less gravitationally unstable and less likely to have episodes of accretion bursts. Our semi-analytic model yields the evolution history even for the early embedded phase, which is important to explain and predict the later phase of star formation.

Work by Armitage et al. (2001) and Bae et al. (2013) has modeled the disc evolution in a semi-analytic manner using a constant or exponentially decreasing external mass infall rate on to the disc. The disc evolves due to viscous terms that model either GI or the magnetorotational instability (MRI) in different regions. These disc models distinguish between a GI-driven outer region and an inner region controlled by MRI. The GI-driven evolution leads to a pileup of matter in the inner region that is then delivered in episodic bursts to the central star through the activation of the MRI. In our work, we have focused on the large-scale picture of episodic accretion by building a model for the envelope accretion and the evolution of the major part of the disc that is driven by GI and gravitational torques. This assumes that the burst properties are set by the physics of the outer disc and we do not include any modulation by the inner disc physics including MRI. Inclusion of a separate model for the inner disc is beyond the scope of our current study but remains a target for the future. Our model is meant to provide a semi-analytic means to model the numerical simulations of e.g. Vorobyov & Basu (2006,

2010, 2015), who modeled disc evolution with envelope infall but had a central sink cell of size several AU that precluded a study of the inner disc physics.

In our work, we have modeled the histogram of luminosity distribution during a limited time range ($\sim$ 0.1 Myr) of the Class 0 and early Class I phase. The choice of such an evolutionary period corresponds to the typical time until the end of the embedded Class 0 phase when about half of the envelope is accreted. Comparing the histogram of luminosity distribution during this time with the observed luminosity histogram for these phases (Fischer et al., 2017), we find that the episodic accretion is needed in order to provide a reasonable match. In our model, we neglect the luminosity contribution from the disc emission as we expect it to be $3-4$ orders of magnitude lesser than either the photospheric or accretion luminosity. As an example many simulations (e.g. Vorobyov & Basu, 2007; Vorobyov et al., 2018, 2020) show an elevated temperature $T \gtrsim 40$ K at radius $r \lesssim 14$ au, and this region would dominate disc emission from larger radii and is also well within the beam size of infrared telescopes used to observe Class 0 objects in the nearest star-forming regions. The estimated contribution to bolometric luminosity $\sim \sigma_{\rm SB} T^4 \pi r^2$ using the above values is only $\sim 10^{-3}\,{\rm L}_\odot$. We also do not include an excess luminosity from external heating of the envelope by the interstellar radiation field. This is more likely to be significant for Class 0 objects since they have more envelope mass to heat, and could dominate at the very early stages with very low mass and luminosity central objects. However, we do not include this effect in our luminosity histograms due to the lack of precise estimates of its value.

In a different study, Offner & McKee (2011) used models of either constant or time-dependent (initially increasing and then tapering off) mass accretion rate and found that the time-dependent models could in some cases provide an adequate fit to the luminosity histogram. Their best fit required an ensemble of objects that had a longer age spread ($\sim$ 0.3 Myr) than generally assumed and an accelerating star formation rate. These effects increase the number of observed young low mass and low luminosity objects. Their model also included a modest degree of episodic accretion. Our mass accretion model contains the initially near constant accretion rate along with bursts and the later tapered accretion rate, due to depletion of envelope accretion as well as the natural decline of disc accretion due to internal torques. A declining accretion rate is a feature of all simulation models that have a finite mass reservoir

(Vorobyov & Basu, 2005a), as well as being inferred from observational analysis of outflow activity (Bontemps et al., 1996b). However, it is also the case that to create high-mass protostars, which are not in the observational samples of Dunham & Vorobyov (2012) and Fischer et al. (2017), a period of exceptionally high mass accretion rate seems required. This is because the total time to form stars of all masses within a stellar cluster seems to be nearly constant (Myers & Fuller, 1993). Using numerical MHD simulations of star cluster formation, Wang et al. (2010) found that massive stars form in the central region of a cluster as a result of global gravitationally-driven flows that are temporally increasing. If this is correct, then one can add a period of temporally increasing accretion rate at later times to account for the relatively small fraction of massive stars. A series of works on the stellar initial mass function have assumed an exponentially increasing accretion rate together with equally likely stopping of accretion in each time interval that allows only a small fraction of protostars to reach the high accretion rate phase and become high mass stars (Myers, 2000; Basu & Jones, 2004; Myers, 2011, 2014; Basu et al., 2015; Hoffmann et al., 2018; Essex et al., 2020). A variety of accretion scenarios, for example, either a long-term lower-amplitude variation or a combination of long-term lower-amplitude variation (i.e. secular variability) and short-term high amplitude accretion (i.e. stochastic variability or episodic accretion) can also be plausible at matching the observed luminosities of protostars (see review by Fischer et al., 2022). Future observations are essential to place tighter constraints on the luminosity evolution, and therefore elucidate the mass assembly history of protostars of all masses.

In future work, we plan to generalize our model to perform a large parameter survey to understand/portray more systemically the physics of mass accretion during star formation. Inclusion of other transport mechanisms such as MRI together with the existing GI approach might give a more complete picture. One can take a random sample of prestellar cores of different masses and study the long-term evolution ($\sim$ 2 Myr) of their protostellar discs and protostars. One can then compare the luminosity distribution for an ensemble of objects of different masses and ages with that of observations.

4.5 Summary

We have presented a semi-analytic model for the temporal evolution of episodic disc-to-star mass accretion rate during star formation. Our formalism can explain the basic features of the hydrodynamic simulations of episodic accretion (Vorobyov & Basu, 2005a, 2006, 2007; Vorobyov et al., 2020) as discussed in Section 5.3. In doing so, it provides an intuitive understanding of the detailed nonlinear physics of the simulations in terms of basic physical principles. The model captures the evolution of the masses of the disc, star, and envelope, as seen in Figure 4.7, 4.8, and 4.9 (as compared to fig 6a of Vorobyov & Basu, 2006). Our formalism combines the spherical envelope accretion with the episodic disc accretion for determining the mass accretion rate on to the star. The former is calculated from the collapse of the prestellar isothermal cloud core for a given density and velocity profile, which controls the infall of the material from the envelope to the disc and a very little portion (about $\sim$ 10% of the infalling matter) directly on to the centre. The latter governs the mass transport from the disc to the star, which follows a power law $\dot{M}_{\rm ds} \propto t^{-6/5}$. We incorporate the episodic accretion bursts due to gravitational instability within the disc by tracking the disc-to-star mass ratio. In our model, both the envelope and disc accretion are co-existing. The envelope accretion dominates the disc accretion in the earlier stages. However, in the later stage, when the envelope mass is depleted, episodic bursts cease to occur and the disc accretion becomes dominant. From then on, the disc accretion solely determines the mass accretion rate on to the central protostar.

Our model includes of the effect of the episodic accretion bursts for determining the mass accretion rate and henceforth the accretion luminosity. We find that a constant or even an exponentially growing or decaying mass accretion rate is not sufficient to produce solar-mass type stars within a typical protostar formation time $\sim$ 0.1 Myr. The episodic bursts work through the migration of clumps of $\sim$ 0.01 $M_\odot$ from the disc to the centre and helps to accumulate enough mass at the centre within a desirable time frame, in contrast to a steady or exponentially increasing or decreasing accretion rate. Our results (e.g. Figure 4.10) indicate that the bursts are required to obtain a good fit to the observed distribution of bolometric luminosities of YSOs, as compared to a smoothly increasing or decreasing evolution of the mass accretion rate. The episodic accretion seems necessary to explain the long-standing 'luminosity problem'.

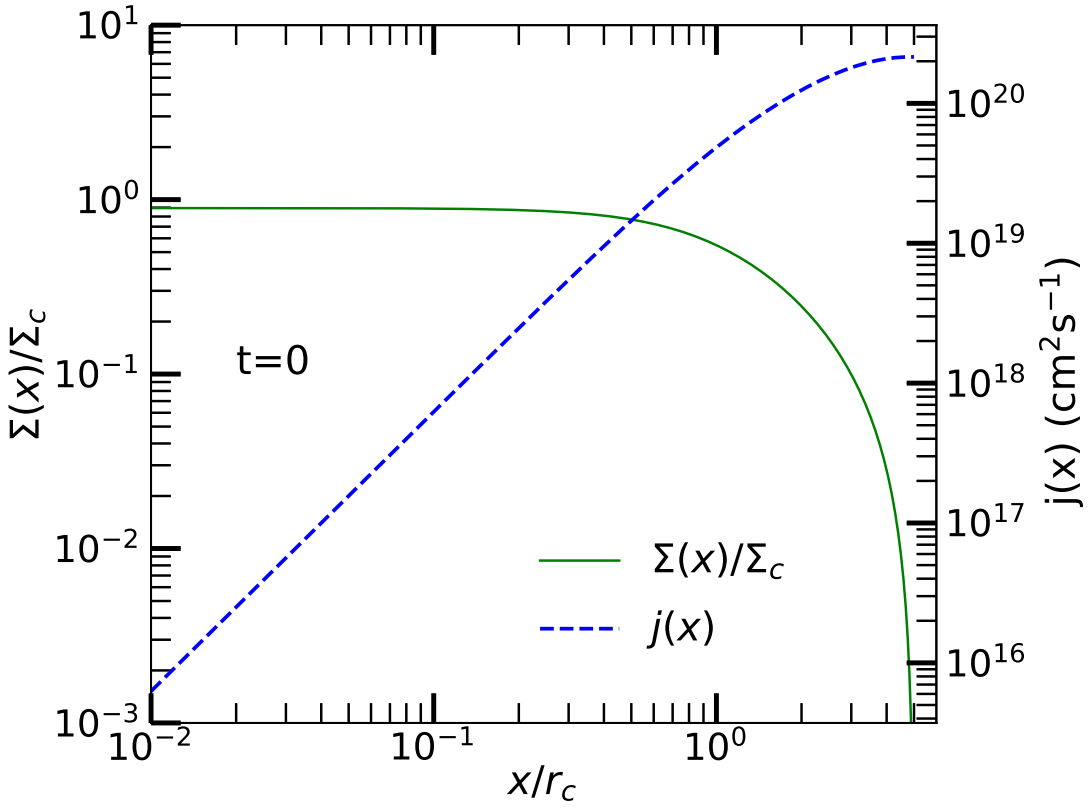

Figure 4.11: Column density $\Sigma(x)/\Sigma_c$ (green), the specific angular momentum $j(x)$ (blue) as a function of radial offset x/r_c at $t = 0$ (analytic solution).

4.6 Appendix

4.6.1 Analytic solutions for mass and specific angular momentum profile

We discuss the semi-analytic approach to evaluate the specific angular momentum $j(x)$ as a function of radial offset x/r_c. We find that the integral is analytically tractable for $t = 0$. Inserting Equation (4.2) into Equation (4.35), the closed-form expression for the column density is

$$\tilde{\Sigma}(\tilde{x}) = \frac{2}{\sqrt{1+\tilde{x}^2}}\left[\arctan\left(\sqrt{\frac{\tilde{R}_{\rm out}^2-\tilde{x}^2}{1+\tilde{x}^2}}\right) - \frac{1}{\tilde{R}_{\rm out}}\left(\sqrt{(\tilde{R}_{\rm out}^2-\tilde{x}^2)(1+\tilde{x}^2)} - \arctan\left(\sqrt{\frac{\tilde{R}_{\rm out}^2-\tilde{x}^2}{1+\tilde{x}^2}}\right)\right)\right], \tag{4.41}$$

where $\tilde{\Sigma} = \Sigma/\Sigma_0$, $\Sigma_0 = \rho_c r_c$, $\tilde{x} = x/r_c$, $\tilde{R}_{\rm out} = R_{\rm out}/r_c$, and the central column density is $\Sigma_c = 2\,\Sigma_0 \arctan(\tilde{R}_{\rm out})$; some of these parameters are defined earlier in Section 4.3.1.1. The

enclosed mass is found by integrating Equation (4.41) according to Equation (4.36), yielding

$$\begin{aligned}\tilde{M}(\tilde{x}) = 2\Bigg[& \sqrt{1+\tilde{x}^2}\arctan\left(\sqrt{\frac{\tilde{R}_{\rm out}^2-\tilde{x}^2}{1+\tilde{x}^2}}\right) - \arctan(\tilde{R}_{\rm out}) + \tilde{R}_{\rm out} \\ & - \sqrt{\tilde{R}_{\rm out}^2-\tilde{x}^2} - \frac{1}{\tilde{R}_{\rm out}^2}\left(\frac{\tilde{R}_{\rm out}^3}{3} - \left(\frac{(\tilde{R}_{\rm out}^2-\tilde{x}^2)^{\frac{3}{2}}}{3}\right) + \sqrt{\tilde{R}_{\rm out}^2-\tilde{x}^2}\right. \\ & \left. -\tilde{R}_{\rm out} + \arctan(\tilde{R}_{\rm out}) - \sqrt{1+\tilde{x}^2}\arctan\left(\sqrt{\frac{\tilde{R}_{\rm out}^2-\tilde{x}^2}{1+\tilde{x}^2}}\right)\right)\Bigg] ,\end{aligned} \tag{4.42}$$

where $\tilde{M} = M/(\rho_c r_c^3)$. We note that the effect of the boundary is exclusively contained in the factor in square brackets. If the quantity $R_{\rm out}$ is large, the power law profile is more pronounced. However, if $R_{\rm out}/r_c$ is of the order of unity (e.g. for our case it is 5), then the cut off dominates close enough to the flat region to prevent the appearance of the power law. In Figure 4.11 the green dashed line shows the analytic Σ/Σ_c curve, which is flat within the inner region $x/r_c \lesssim 1$, and then falls sharply. The integrated $M(x)$ attains a saturation at the outer edge. Keeping in mind at $t = 0$, $M_{\rm tot}(x) = M(x)$. During the pre-collapse phase, $j(x)$ increases linearly with radial offset x/r_c and gets saturated at the very outer radius. This behaviour of $j(x)$ implies the conservation of angular momentum.

Bibliography

Alves J., Lombardi M., Lada C. J., 2007, A&A, 462, L17

Armitage P. J., Livio M., Pringle J. E., 2001, MNRAS, 324, 705

Audard M., et al., 2014, in Beuther H., Klessen R. S., Dullemond C. P., Henning T., eds, Protostars and Planets VI. p. 387 (arXiv:1401.3368), doi:10.2458/azu_uapress_9780816531240-ch017

Bae J., Hartmann L., Zhu Z., Gammie C., 2013, ApJ, 764, 141

Basu S., 1997, ApJ, 485, 240

Basu S., 1998, ApJ, 509, 229

Basu S., Ciolek G. E., 2004, ApJ, 607, L39

Basu S., Jones C. E., 2004, MNRAS, 347, L47

Basu S., Mouschovias T. C., 1994, ApJ, 432, 720

Basu S., Gil M., Auddy S., 2015, MNRAS, 449, 2413

Bontemps S., Andre P., Terebey S., Cabrit S., 1996a, A&A, 311, 858

Bontemps S., Andre P., Terebey S., Cabrit S., 1996b, A&A, 311, 858

Caratti o Garatti A., et al., 2017, Nature Physics, 13, 276

Ciolek G. E., Mouschovias T. C., 1993, ApJ, 418, 774

Crutcher R. M., Troland T. H., Goodman A. A., Heiles C., Kazes I., Myers P. C., 1993, ApJ, 407, 175

Dapp W. B., Basu S., 2009, MNRAS, 395, 1092

Dapp W. B., Basu S., Kunz M. W., 2012, A&A, 541, A35

Das I., Basu S., 2021, ApJ, 910, 163

Dunham M. M., Vorobyov E. I., 2012, ApJ, 747, 52

Dunham M. M., Evans Neal J. I., Terebey S., Dullemond C. P., Young C. H., 2010, ApJ, 710, 470

Enoch M. L., Neal J. I., Sargent A. I., Glenn J., 2009, ApJ, 692, 973

Essex C., Basu S., Prehl J., Hoffmann K. H., 2020, MNRAS, 494, 1579

Fischer W. J., et al., 2017, ApJ, 840, 69

Fischer W. J., Hillenbrand L. A., Herczeg G. J., Johnstone D., Kóspál Á., Dunham M. M., 2022, arXiv e-prints, p. arXiv:2203.11257

Gaudel M., et al., 2020, A&A, 637, A92

Goodman A. A., Benson P. J., Fuller G. A., Myers P. C., 1993, ApJ, 406, 528

Hartmann L., Kenyon S. J., 1996, ARA&A, 34, 207

Hartmann L., Calvet N., Gullbring E., D'Alessio P., 1998, ApJ, 495, 385

Herbig G. H., 2008, AJ, 135, 637

Hoffmann K. H., Essex C., Basu S., Prehl J., 2018, MNRAS, 478, 2113

Hunter C., 1962, ApJ, 136, 594
Kratter K., Lodato G., 2016, ARA&A, 54, 271
Kurono Y., Saito M., Kamazaki T., Morita K.-I., Kawabe R., 2013, ApJ, 765, 85
Lin D. N. C., Pringle J. E., 1987, MNRAS, 225, 607
Lynden-Bell D., Pringle J. E., 1974, MNRAS, 168, 603
Machida M. N., Basu S., 2019, ApJ, 876, 149
Magakian T. Y., Movsessian T. A., Andreasyan H. R., Gevorgyan M. H., 2019, A&A, 625, A13
Meyer D. M. A., Vorobyov E. I., Kuiper R., Kley W., 2017, MNRAS, 464, L90
Motte F., André P., 2001, A&A, 365, 440
Myers P. C., 2000, ApJ, 530, L119
Myers P. C., 2011, ApJ, 743, 98
Myers P. C., 2014, ApJ, 781, 33
Myers P. C., Fuller G. A., 1993, ApJ, 402, 635
Offner S. S. R., McKee C. F., 2011, ApJ, 736, 53
Ohashi N., Hayashi M., Ho P. T. P., Momose M., Tamura M., Hirano N., Sargent A. I., 1997, ApJ, 488, 317
Pringle J. E., 1981, ARA&A, 19, 137
Shakura N. I., Sunyaev R. A., 1973, A&A, 500, 33
Shu F. H., 1977, ApJ, 214, 488
Terebey S., Shu F. H., Cassen P., 1984, ApJ, 286, 529
Toomre A., 1964, ApJ, 139, 1217
Vorobyov E. I., Basu S., 2005a, MNRAS, 360, 675
Vorobyov E. I., Basu S., 2005b, ApJ, 633, L137
Vorobyov E. I., Basu S., 2006, ApJ, 650, 956
Vorobyov E. I., Basu S., 2007, MNRAS, 381, 1009
Vorobyov E. I., Basu S., 2008, ApJ, 676, L139
Vorobyov E. I., Basu S., 2010, ApJ, 719, 1896
Vorobyov E. I., Basu S., 2015, ApJ, 805, 115
Vorobyov E. I., Elbakyan V. G., Plunkett A. L., Dunham M. M., Audard M., Guedel M., Dionatos O., 2018, A&A, 613, A18
Vorobyov E. I., Khaibrakhmanov S., Basu S., Audard M., 2020, A&A, 644, A74
Wang P., Li Z.-Y., Abel T., Nakamura F., 2010, ApJ, 709, 27
Xu W., Kunz M. W., 2021, MNRAS, 508, 2142
Yen H.-W., Takakuwa S., Ohashi N., 2011, ApJ, 742, 57

Yen H.-W., Koch P. M., Takakuwa S., Krasnopolsky R., Ohashi N., Aso Y., 2017, ApJ, 834, 178

Yorke H. W., Bodenheimer P., Laughlin G., 1993, ApJ, 411, 274

Yorke H. W., Bodenheimer P., Laughlin G., 1995, ApJ, 443, 199

Chapter 5

Numerical simulations of mass accretion bursts in magnetized gas-dust protoplanetary disks

A version of this chapter is in preparation for a future publication.

5.1 Introduction

Young stellar objects are generally understood to form because of the gravitational collapse of dense cores and globules containing gas and dust. These are often called as prestellar cores. In the early evolutionary stage (known as embedded phase), the nascent star is still surrounded by the infalling envelope of the natal core. According to the simplest model of low-mass star formation, the typical mass infall rate for an isothermal spherical collapse is $\dot{M}_{\rm infall} \sim c_s^3/G$ (Shu, 1977), given that c_s and G are local sound speed and gravitational constant. This value declines with time due to a depleting mass reservoir in the envelope (Vorobyov & Basu, 2005). However, the instantaneous infall rate is not equal to the mass accretion rate onto the star as most of the matter lands on the disk before it reaches to the star. A wide range of protostellar accretion rates (Enoch et al., 2009) inferred in the embedded phase suggests a strong time variability in accretion. Several physical processes in the disk, for example, gravitational, thermal, and magnetorotational instabilities, can give rise to vigorous luminosity outbursts during which the matter is transported through the disk to the star at the center. The

prototypical sample of bursts are known as FUor eruptions (Herbig, 1966, 1977, named after the first known example of this kind originated from the FU Orionis system) and EXor (EX Lupi-type) eruptions (Herbig, 1989). The physical mechanism of driving these two types of bursts can be different. The peak luminosity during the active phase of the bursts ranges from few tens to several hundreds of solar luminosities ($1\,L_{\odot} \sim 10^{33}\,\mathrm{erg\,s^{-1}}$), in general showing an enhancement in luminosity of three to five magnitudes[1] compared to the pre-burst state (Audard et al., 2014).

In this Chapter, we are only interested to study the FUor outbursts. About half of the known FUors are young embedded objects (Class 0) as found by silicate signatures in their absorption spectra (Quanz et al., 2007). Several dozens of such objects have been discovered (Audard et al., 2014) since 1937, many more candidates are being monitored (Contreras Peña et al., 2017). The burst magnitude can be estimated from multi-wavelength observations. However, the burst duration and frequency is difficult to derive from the observations because of the long timescales of the bursts. Despite several works are made to infer them from the known statistics of the bursts (Scholz et al., 2013; Hillenbrand & Findeisen, 2015; Contreras Peña et al., 2019; Fischer et al., 2019). On the other side, such burst characteristics can be estimated from the well-known hydrodynamic and/or magnetohydrodynamic numerical models (e.g., Vorobyov & Basu, 2010, 2015; Vorobyov et al., 2020). During the vigorous outbursts, the temperature becomes high enough to ionize the chemical species in the inner disk regions. Thus FUors could play as an important tool for studying the chemical composition and dust distribution of the inner disk. Therefore, it is crucial to study the duration, frequency, and mass accretion amplitude (or luminosity) of the bursts that may occur in the early evolution of a young stellar object. These findings further motivates detailed investigations as to the nature of the burst phenomenon. Three-dimensional simulations (e.g., Zhu et al., 2020) are able to provide the subtle details of the burst. However, for studying the burst characteristics over many model realizations, 3D simulations are numerically expensive. In that case, a simplified 2D simulations

[1]Here, magnitude corresponds to the bolometric apparent magnitude scale and it is a unitless measure of the brightness of a celestial object, on an inverse logarithmic astronomical magnitude scale. Any difference of 5 unit corresponds to a factor of 100 in the brightness. In simple words, a magnitude 2 star is exactly 100 times brighter than a magnitude 7 star. Thus each step of one magnitude appears as $\sqrt[5]{100} \approx 2.512$ times brighter than the next faintest. The brighter an object is, the lower the value of its magnitude, with the brightest objects reaching negative values.

can provide a panoramic view of the burst phenomenon over long evolutionary times. We use the two-dimensional magnetohydrodynamical simulations of gas-dust protoplanetary disks in the thin-disk limit which takes into account of the magnetic fields and dynamics of dust growth. These sub-micron sized dust grows to become pebbles, which further grows into planetesimals of size hundreds of kilometers. The planetesimals are considered to be the building blocks of planetary cores, which eventually lead to the formation of exoplanet systems through further processes e.g., gas accretion, pebble accretion.

The Chapter is organized as follows. In Section 5.2, we provide a detailed description of our model. In Section 5.3, we describe the global evolution of the magnetized disk and focus on the magnetorotational instability- (MRI) triggered accretion bursts and comparison with other relevant work. The main discussions are summarized in Section 5.4.

5.2 Methods

In this Chapter, we summarize the numerical magnetohydrodynamics (MHD) model that is used for studying the formation and long-term evolution of protostellar/protoplanetary disks. The simulation is performed using FEOSAD (Formation and Evolution Of a Star And its circumstellar Disk) code which takes into account magnetic fields in the flux-freezing limit as well as the co-evolution of the dust components (small dust and grown dust) as described in detail in (Vorobyov et al., 2020). Our simulation begins from the gravitational collapse of a prestellar core with a uniform mass-to-magnetic-flux ratio. The spatially uniform mass-to-magnetic flux ratio, $\mu = (2\pi\sqrt{G})\Sigma_{\rm g}/B_{\rm z}$, where $\Sigma_{\rm g}$ is the surface density of disk, G is the gravitational constant, and $B_{\rm z}$ is the $z-$component of the magnetic field. In the ideal MHD limit $B_{\rm z}$ stays constant during the entire evolution. The evolution continues into the embedded (Class 0) phase of star formation where the nascent central star is surrounded by a rotationally supported accretion disk along with remaining infalling envelope as shown in Figure 5.1.

5.2.1 Initial Conditions

The initial profile of the gas surface density Σ_g and angular velocity Ω of the prestellar core has the following form:

$$\Sigma_{\rm g} = \frac{r_0\Sigma_0}{\sqrt{r^2 + r_0^2}}\,, \tag{5.1}$$

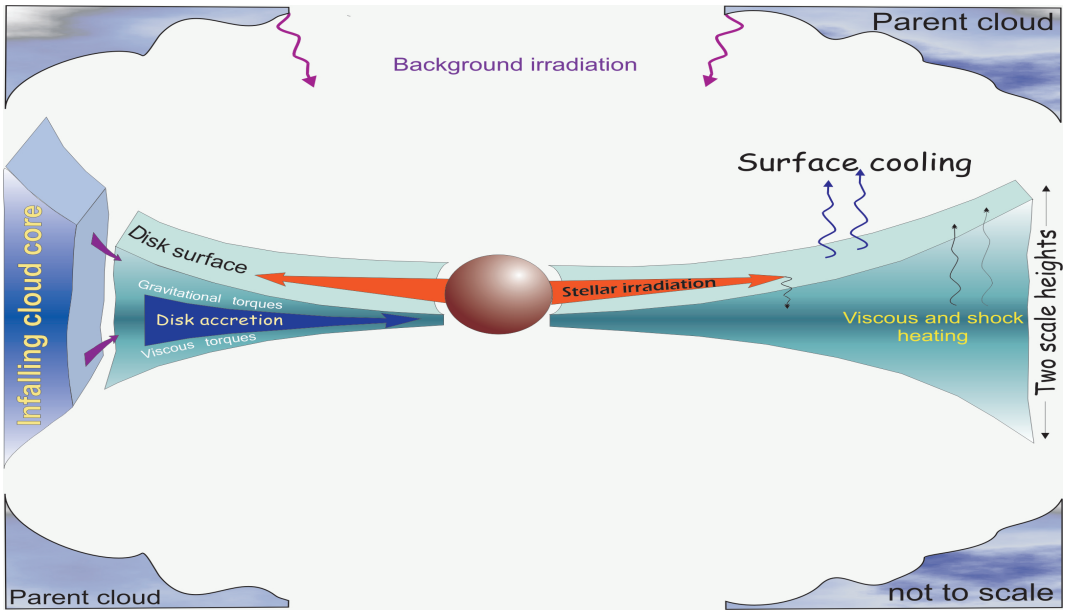

Figure 5.1: Schematic representation of the numerical model. See the text for a detailed explanation (figure taken from Vorobyov & Basu, 2010).

$$\Omega = 2\Omega_0 \left(\frac{r_0}{r}\right)^2 \left[\sqrt{1+\left(\frac{r}{r_0}\right)^2} - 1\right], \tag{5.2}$$

consistent with an axially symmetric core collapse (Basu, 1997). Here, Σ_0 and Ω_0 are the gas surface density and angular speed at the center of the core, $r_0 = \sqrt{A}c_s^2/(\pi G\Sigma_0)$ is the radius of the central plateau (similar to as seen in Figure 1.1), where c_s is the local sound speed in the core, r is the radial distance from the center. The dimensionless parameter A corresponds to the density perturbation and it is set to 2 that makes the core unstable to collapse (see Vorobyov et al., 2020, for more details). The initial prestellar cores with a supercritical mass-to-flux ratio i.e., $\mu > 1$ are understood to form through ambipolar diffusion (neutral-ion drift) driven gravitational collapse. Once collapse begins, the profile of specific angular momentum versus enclosed mass remains conserved. The initial dust-to-gas ratio is set to $1:100$, where all the dust is in the form of small sub-micron dust grains that are fully coupled with the gas component. The gas temperature of the initial prestellar core is set to $T = 20$ K and a uniform background vertical magnetic field of strength is taken as $B_0 = 10^{-5}$ G, in agreement with typical observed values (Crutcher, 2012).

5.2.2 Numerical Equations for gaseous component

The equations of mass continuity, momentum conservation, and energy transport are solved in the thin-disk approximation (Ciolek & Mouschovias, 1993; Basu & Mouschovias, 1994), which can be written as follows

$$\frac{\partial \Sigma_{\rm g}}{\partial t} + \nabla_p \cdot \left(\Sigma_{\rm g} \boldsymbol{v}_p\right) = 0, \tag{5.3}$$

$$\begin{aligned}\frac{\partial}{\partial t}\left(\Sigma_{\rm g}\boldsymbol{v}_p\right) + \left[\nabla \cdot \left(\Sigma_{\rm g}\boldsymbol{v}_p \otimes \boldsymbol{v}_p\right)\right]_p = -\nabla_p \mathcal{P} + \Sigma_{\rm g}\left(\boldsymbol{g}_p + \boldsymbol{g}_*\right) \\ +(\nabla \cdot \boldsymbol{\Pi})_p - \Sigma_{\rm d,gr}\boldsymbol{f}_p + \frac{B_z \boldsymbol{B}_p^+}{2\pi} - H_{\rm g}\,\nabla_p\left(\frac{B_z^2}{4\pi}\right),\end{aligned} \tag{5.4}$$

$$\frac{\partial e}{\partial t} + \nabla_p \cdot \left(e\boldsymbol{v}_p\right) = -\mathcal{P}(\nabla_p \cdot \boldsymbol{v}_p) - \Lambda + \Gamma + (\nabla \boldsymbol{v})_{pp'} : \Pi_{pp'}, \tag{5.5}$$

respectively. Here, the subscripts p and p' refer to the planar components (r, ϕ) in polar coordinates, $\Sigma_{\rm g}$ is the gas surface density, $\mathcal{P}$ is the vertically integrated gas pressure, e is the internal energy per surface area. The viscous stress $\boldsymbol{\Pi}$ tensor is defined as $\boldsymbol{\Pi} = 2\Sigma_{\rm g}\nu\,(\boldsymbol{\nabla} v - (\boldsymbol{\nabla}\cdot\boldsymbol{v})\mathbf{1}/3)$, where ν is the kinematic viscosity, $\mathbf{1}$ is the unit tensor, and $\boldsymbol{\nabla} v$ is the symmetrized velocity gradient tensor (see §2 and Appendix B of Vorobyov & Basu, 2009). Here, $H_{\rm g}$ is the vertical scale height of the gas disk calculated assuming local vertical hydrostatic balance in the gravitational field of disk and star, and $\boldsymbol{v}_p = v_r\hat{\boldsymbol{r}} + v_\phi\hat{\boldsymbol{\phi}}$ is the gas velocity in the disk plane, $\nabla_p = \hat{\boldsymbol{r}}\partial/\partial r + \hat{\boldsymbol{\phi}} r^{-1}\partial/\partial\phi$ is the gradient along the planar coordinates of the disk. The term $\boldsymbol{f}_p$ is the drag force per unit mass between dust and gas, and $\Sigma_{\rm d,gr}$ is the surface density of grown dust (see details in Sec 5.2.3). Here, B_z is the vertically constant but radially and azimuthally varying z-component of the magnetic field within the disk thickness. The planar components of the magnetic field is defined as $\boldsymbol{B}_p^+ = B_r^+\hat{\boldsymbol{r}} + B_\phi^+\hat{\boldsymbol{\phi}}$ where the '+' corresponds to the component at the top of the surface of the disk. The ideal gas equation of state is used to calculate the vertically integrated gas pressure, $\mathcal{P} = (\gamma - 1)e$ with $\gamma = 7/5$. The gravitational acceleration in the disk plane $\boldsymbol{g}_p = g_r\hat{\boldsymbol{r}} + g_\phi\hat{\boldsymbol{\phi}}$, takes into account self-gravity of disk by solving for the disk gravitational potential using the Poisson integral (see details in Vorobyov et al., 2020). The term $\boldsymbol{g}_*$ is the gravitational acceleration due to the central protostar, which only has a ra-

dial component. Once a central protostar is formed, we add stellar gravitational field to the gravitational acceleration $\boldsymbol{g}_p$ in the disk plane. The stellar gravitational field follows:

$$\boldsymbol{g}_* = g_{r,*}\hat{\boldsymbol{r}} = -\frac{GM_*}{r^2}\hat{\boldsymbol{r}}\,, \tag{5.6}$$

where M_* is the accumulated mass in the protostar. Coming to the magnetic field physics, the planar component of the magnetic field at the top surface of the disk is denoted by $\boldsymbol{B}_p^+$ and the midplane symmetry is assumed, such that $\boldsymbol{B}_p^- = -\boldsymbol{B}_p^+$ (Vorobyov et al., 2020). In Equation (5.4) the last two terms on the right-hand side are the Lorentz force (including the magnetic tension term) and the vertically integrated magnetic pressure gradient. The magnetic tension term arises formally due to the Maxwell stress tensor, that can be intuitively understood as the interaction of an electric current at the disk surface (see also Figure 2.1). The discontinuity in tangential field component gives rise to surface current while no current within the disk. The vertical component of magnetic field is calculated by explicitly solving the induction equation in the ideal MHD regime:

$$\frac{\partial B_z}{\partial t} = -\frac{1}{r}\left(\frac{\partial}{\partial r}\left(rv_rB_z\right) + \frac{\partial}{\partial \varphi}\left(v_\varphi B_z\right)\right), \tag{5.7}$$

wherein the advection of B_z is considered. The diffusive effects of Ohmic dissipation and ambipolar diffusion are neglected due to high computational cost. The total magnetic field can be written as the gradient of a scalar magnetic potential $\Phi_{\rm M}$ and the planar component of magnetic field ($\boldsymbol{B}_p^+$) is calculated by solving the Poisson integrals (see details Vorobyov et al., 2020) with the source term of $(B_z - B_0)/(2\pi)$, where B_0 is the constant background field.

The heating and cooling rates Γ and Λ, respectively are based on the analytical calculations of the radiation transfer in the vertical direction (Dong et al., 2016). The equation of cooling rate is as follows:

$$\Lambda = \frac{8\tau_{\rm P}\sigma_{\rm SB}T_{\rm mp}^4}{1 + 2\tau_{\rm P} + 1.5\tau_{\rm R}\tau_{\rm P}}\,, \tag{5.8}$$

where, $T_{\rm mp} = \mathcal{P}\mu/\mathcal{R}\Sigma_{\rm g}$ is the midplane temperature, $\mu = 2.33$ is the mean molecular weight, $\mathcal{R}$ is the universal gas constant, and $\sigma_{\rm SB}$ is the Stefan-Boltzmann constant. Here, $\tau_{\rm P} = 0.5\Sigma_{\rm d,tot}\kappa_{\rm P}$ and $\tau_{\rm R} = 0.5\Sigma_{\rm d,tot}\kappa_{\rm R}$ represent the Planck and Rosseland optical depths to the disk midplane,

where $\kappa_{\rm P}$ and $\kappa_{\rm R}$ are the Planck and Rosseland mean opacities taken from Semenov et al. (2003) and the optical depths in the calculations are proportional to the total dust surface density ($\Sigma_{\rm d,tot}$).

The heating function takes into account the irradiation at the disk surface from the stellar as well as background black-body irradiation. The heating function per unit surface area of the disk is expressed as follows:

$$\Gamma = \frac{8\tau_{\rm P}\sigma_{\rm SB}T_{\rm irr}^4}{1 + 2\tau_{\rm P} + 1.5\tau_{\rm R}\tau_{\rm P}}\,, \tag{5.9}$$

where $T_{\rm irr}$ is the irradiation temperature at the disk surface and is defined as follows:

$$T_{\rm irr}^4 = T_{\rm bg}^4 + \frac{F_{\rm irr}(r)}{\sigma_{\rm SB}}\,, \tag{5.10}$$

where $T_{\rm bg}$ presents the corresponding temperature for the background black-body irradiation, $F_{\rm irr}(r) = L_* \cos\gamma_{\rm irr}/(4\pi r^2)$ is the radiation flux (i.e., energy per unit surface area per unit time) absorbed by the disk surface at radial distance (r) from the central star with a stellar luminosity L_*. Here, the stellar luminosity (L_*) is the sum of the accretion luminosity $L_{*,\rm accr} = 0.5\,GM_*\dot{M}/R_*$ arising from the gravitational energy of accreted gas and the photospheric luminosity $L_{*,\rm ph}$ due to gravitational compression and deuterium burning in the stellar interior, where $\dot{M}$, M_*, and R_* are the mass accretion rate onto the star, stellar mass, and radius of the star, respectively. Here, $\gamma_{\rm irr}$ is the incidence angle of radiation that arrives at the disk surface w.r.t. normal at a radial distance r (see Eq. (10) of §2.1 of Vorobyov et al., 2020). The resulting model has a flared structure, wherein the disk vertical scale height increases with radius. Both the disk and the envelope receive a fraction of the irradiation energy from the central protostar. The adopted opacities in the numerical model of FEOSAD do not take dust growth into account.

5.2.3 Dust Physics

The dust in the numerical model of FEOSAD is based on two components, small dust and grown dust (see Vorobyov et al., 2018b, 2020, for more details). In our numerical model, small dust has a grain size of $a_{\rm min} < a < a_*$, and grown dust corresponds to a size of $a_* \le a < a_{\rm max}$), where $a_{\rm min} = 5 \times 10^{-3}$ μm, $a_* = 1.0$ μm. Here, $a_{\rm max}$ is a dynamically varying maximum

radius of the dust grains, which depends on the efficiency of radial dust drift and the rate of dust growth. Small dust is dynamically coupled with the gas as it is sub-micron dust grains by definition. Whereas, grown dust dynamics is regulated by friction with gas and the total gravitational potential of the star, gas, and dusty components. All dust grains combined are assumed to have a density of $\rho_s = 3.0\,\mathrm{g\,cm^{-3}}$. The equations of continuity and momentum conservation for small and grown dust components are as follows:

$$\frac{\partial \Sigma_{\mathrm{d,sm}}}{\partial t} + \nabla_p \cdot \left(\Sigma_{\mathrm{d,sm}} \boldsymbol{v}_p\right) = -S\left(a_{\mathrm{max}}\right), \tag{5.11}$$

$$\frac{\partial \Sigma_{\mathrm{d,gr}}}{\partial t} + \nabla_p \cdot \left(\Sigma_{\mathrm{d,gr}} \boldsymbol{u}_p\right) = S\left(a_{\mathrm{max}}\right), \tag{5.12}$$

$$\frac{\partial}{\partial t}\left(\Sigma_{\mathrm{d,gr}} \boldsymbol{u}_p\right) + \left[\nabla \cdot \left(\Sigma_{\mathrm{d,gr}} \boldsymbol{u}_p \otimes \boldsymbol{u}_p\right)\right]_p = \Sigma_{\mathrm{d,gr}}\left(\boldsymbol{g}_p + \boldsymbol{g}_*\right) + \Sigma_{\mathrm{d,gr}} \boldsymbol{f}_p + S\left(a_{\mathrm{max}}\right) \boldsymbol{v}_p, \tag{5.13}$$

where $\Sigma_{\mathrm{d,sm}}$ and $\Sigma_{\mathrm{d,gr}}$ are defined as the surface densities of small and grown dust, respectively. The term $\boldsymbol{f}_p$ is the drag force per unit mass due to the back-reaction on the gas due to dust, and $\Sigma_{\mathrm{d,gr}}$ is the surface density of grown dust. The term $\boldsymbol{u}_p$ describes the planar components of the grown dust velocity, and $S\left(a_{\mathrm{max}}\right)$ is the rate of conversion from small to grown dust per unit surface area during one time step (Δt) and $S\left(a_{\mathrm{max}}\right)$ is a function of the fragmentation size of the dust. The rate of conversion from small to grown dust can be described as $S\left(a_{\mathrm{max}}\right) = -\Delta\Sigma_{\mathrm{d,sm}}/\Delta t$ (see §2.2 of Vorobyov et al., 2020). The dust is assumed to mix with the gas along the vertical direction, which is a reasonable approximation for a young disk evolving under both the gravitationally unstable and/or magnetorotationally unstable disks (see Rice et al., 2004; Yang et al., 2018). For a case of a more evolved disks, dust settling becomes significant and accelerates the conversion of small to grown dust (Vorobyov et al., 2018b). The rate of small to grown dust conversion $S\left(a_{\mathrm{max}}\right)$ is derived from the assumption that the size distributions of both the dust populations can be described by a power law with a fixed exponent of -3.5 (see details in Mathis et al., 1977; Vorobyov et al., 2018b, 2020). The evolution of the maximum radius that the grown dust can achieve obeys a continuity equation as following

$$\frac{\partial a_{\mathrm{max}}}{\partial t} + \left(\boldsymbol{u}_{\mathrm{p}} \cdot \nabla_p\right) a_{\mathrm{max}} = \mathcal{D}\,, \tag{5.14}$$

where the growth rate $\mathcal{D}$ represents the coagulation and can be written as

$$\mathcal{D} = \frac{\rho_{\rm d} v_{\rm rel}}{\rho_{\rm s}} \,. \tag{5.15}$$

Here $\rho_{\rm d}$ is the total dust volume density and $v_{\rm rel}$ is the relative dust collision velocity. Furthermore, the maximum size of $a_{\rm max}$ is limited by the fragmentation barrier (Birnstiel et al., 2012), which follows

$$a_{\rm frag} = \frac{2\Sigma_{\rm g} v_{\rm frag}^2}{3\pi\rho_{\rm s}\alpha c_s^2}, \tag{5.16}$$

where $v_{\rm frag}$ is the fragmentation velocity set to $3\,{\rm m\,s^{-1}}$ and c_s is the local sound speed. The growth rate $\mathcal{D}$ is set to zero when $a_{\rm max}$ exceeds $a_{\rm frag}$. In the numerical model of FEOSAD, the dust growth is limited to keep the size of dust particles within the Epstein regime, which means particle size is small enough compared to the mean free path[2]. Under such approximation, the dust can get accumulate on a timescale shorter than that of the orbital timescale at that radius (see more details in Armitage, 2015).

5.2.4 Adaptive viscosity and ionization fraction

In protostellar/protoplanetary disks, viscosity plays a major role for the mass and angular momentum transport. In numerical setup of FEOSAD, the viscosity is taken into account via the viscous stress tensor $\mathbf{\Pi}$ in Eq. (5.4). Note that, gravitational torques, which arises from the non-linear density perturbations in the spiral arms, are another means of transporting mass and angular momentum in disks (see details in Vorobyov & Basu, 2007, 2010). In FEOSAD, viscosity in protoplanetary disks possibly arises primarily due to the turbulence induced by the MRI (Vorobyov et al., 2020). MRI acts in the presence of the magnetic field and causes turbulence in the weakly ionized gas in the shearing Keplerian disk. The magnetic field line linking two fluid elements at different radii is stretched beyond the critical lengthscale, such that it destabilizes the disk by moving the inner fluid element further inward and the outer fluid element further outward (as described in Section 1.4.2.2 of Chapter 1). However, the fluid parcel drifting inward does not necessarily fall onto the star. The phenomena explained above is more of a local outcome. In practice, the collective effect of all these local fluid parcels

[2]The mean free path in the inner protoplanetary disks is $\sim$ 1 cm and larger in the outer disk.

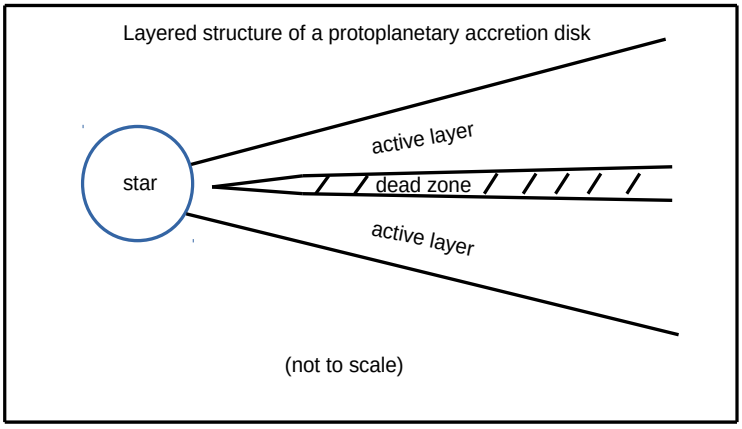

Figure 5.2: Sketch of a layered structure of the protoplanetary accretion disk. The dead zone that forms as the cosmic rays can ionize up to a certain thickness of the layer is sandwiched between the active layers above and below.

moving backward and forward give rise to turbulence eddies in the disk which aid in exchange the angular momentum between the fluid elements and eventually guide some fluid parcels to fall onto the center. Simulations are not yet able to provide any fixed value of effective $\alpha_{\rm eff}$ parameter that requires some self-sustained turbulent state, in which there is a steady inflow to the center. To activate MRI within disks, the temperature of inner disk should have to be sufficient to thermally ionize (ionization temperature is $T \approx 1300\,{\rm K}$) the alkali metals (e.g., potassium). The Galactic cosmic rays are the primary sources of ionization, which is external to the disk and penetrate the disk from both the above and below.

In the inner regions of the disk, the gas surface density is typically large and the midplane is insufficiently ionized for the magnetic field to be well enough coupled to lead to the MRI. The disk in this region is thought to be accreted through a magnetically layered structure (Gammie, 1996; Armitage et al., 2001) as shown in Figure 5.2, wherein most accretion occurs via the MRI-active surface layers and a magnetically dead zone is formed at the midplane. The kinematic viscosity $\nu = \alpha c_s H_{\rm g}$ is parameterized using the Shakura & Sunyaev (1973) prescription. In order to simulate the accretion through a layered disk, we consider an effective and adaptive

parameter $\alpha_{\rm eff}$ as a weighted average which follows:

$$\alpha_{\rm eff} = \frac{\Sigma_{\rm MRI}\,\alpha_{\rm MRI} + \Sigma_{\rm dz}\,\alpha_{\rm dz}}{\Sigma_{\rm MRI} + \Sigma_{\rm dz}}, \tag{5.17}$$

where $\Sigma_{\rm MRI}$ is the gas column density of the MRI-active layer and $\Sigma_{\rm dz}$ is that of the magnetically dead layer at a given radial distance, so that $\Sigma_{\rm g} = \Sigma_{\rm MRI} + \Sigma_{\rm dz}$. Here, $\alpha_{\rm MRI}$ and $\alpha_{\rm dz}$ correspond to the strength of the turbulence in the MRI-active layer and the dead zone, respectively. In the simulations, $\alpha_{\rm MRI}$ is set to the canonical value of 0.1. Due to the nonzero residual viscosity arising from hydrodynamic turbulence driven by the Maxwell stress in the active layer, a very small value of 10^{-5} is considered for $\alpha_{\rm dz}$. Canonically, the column density of the MRI active layer $\Sigma_{\rm MRI}$ is considered to be a constant, at about $100\,{\rm g\,cm^{-2}}$, which is the average penetration/attenuation depth of cosmic rays. Under the regime of low temperatures, $T \lesssim 1000$ K, the ionization fraction (x) is determined from the balance of collisional, radiative recombination, and recombination on dust grains. This is expressed as

$$(1 - x)\xi = \alpha_{\rm r} x^2 n_{\rm n} + \alpha_{\rm d} x n_{\rm n}, \tag{5.18}$$

where x is the ionization fraction, ξ is the ionization rate that is composed of a cosmic-ray ionization rate and the ionization rate by radionuclides (Umebayashi & Umebayashi, 2009), $n_{\rm n}$ is the number density of neutrals, $\alpha_{\rm d}$ is the total rate of recombination onto the dust grains, and $\alpha_{\rm r}$ is the radiative recombination rate having a form $\alpha_r = 2.07 \times 10^{-11}\,T^{-1/2}\,{\rm cm^3 s^{-1}}$ (Spitzer, 1978). In the regions, where the gas temperature exceeds several hundred Kelvin, an additional term is added to the ionization fraction x from Eq. 5.18, which is the thermal ionization calculated by considering the ionization of potassium, the metal with the lowest ionization potential (see details in Vorobyov et al., 2020). The cosmic abundance of potassium set to 10^{-7} for these calculations. The total recombination rate for each dust population (small and grown) is calculated as

$$\langle \alpha_{\rm d} \rangle = \langle X_{\rm d} \cdot \sigma_{\rm d} \cdot v_{\rm i} \rangle, \tag{5.19}$$

where $X_{\rm d}$ is the dust-to-gas volume number density ratio in the disk midplane, and $\sigma_{\rm d} = \pi a^2$ is the grain cross-section, and the bracket $\langle ... \rangle$ denotes averaging over the dust size distribution of

a given dust population (small or grown). The quantity $v_{\rm i}$ represents the approximate thermal speed of ions with mass $30\,m_{\rm H}$, representing the dominant ionic species, e.g., HCO^+, N_2H^+.

The total stellar luminosity $L_{\rm tot}$ is the sum of the accretion luminosity $L_{*,\rm accr}$ and photospheric luminosity $L_{*,\rm ph}$. The accretion luminosity $L_{*,\rm accr} = 0.5\,GM_*\dot{M}/R_*$ arising from the gravitational energy of accreted gas, where M_*, $\dot{M}$, and R_* are the stellar mass, mass accretion rate onto the star, and radius of the star, respectively. The photospheric luminosity $L_{*,\rm ph}$ accounts for the gravitational compression and deuterium burning in the stellar interior. The stellar mass and accretion rate onto the star are determined by taking into account of the amount of matter passing through the sink cell. The photospheric luminosity $L_{*,\rm ph}$ and stellar radius R_* are calculated using the stellar evolution tracks inferred with the STELLAR code of Yorke & Bodenheimer (2008) (see more details in Vorobyov et al., 2020).

In principle, the MRI cannot arise if the wavelength associated with the MRI turbulent eddies exceeds the disk scale height $H_{\rm g}$. So, a disk can become MRI unstable only when the disk vertical scale height $H_{\rm g}$ is greater than the critical wavelength for the MRI to occur under flux-freezing. For such a disk, the MRI wave would be damped if timescale of MRI growth ($\tau_{\rm MRI,g}$) becomes longer than that of damping due to Ohmic dissipation (OD) $\tau_{\rm OD,damping}$. In the numerical model of FEOSAD we neglect the other nonideal MHD effects (ambipolar diffusion and Hall effect) because the Ohmic dissipation is known to prevail in the innermost several au of the disk (Balbus & Terquem, 2001; Kunz & Balbus, 2004). The wavelength of the most unstable MRI mode $H_{\rm g} = 2\pi\eta/v_{\rm A}$ (Sano et al., 2000) is obtained by equating timescale of MRI growth ($\tau_{\rm MRI,g} \equiv H_{\rm g}/v_{\rm A}$) to that of damping due to Ohmic dissipation ($\tau_{\rm OD,damping} \equiv H_{\rm g}^2/\eta$), where η is Ohmic diffusivity and $v_{\rm A} = B/\sqrt{4\pi\rho_{\rm crit}}$ is the Alfvén speed. Note that, Ohmic diffusivity can be written as $\eta = c^2 m_e n_n \langle\sigma v\rangle_{\rm en}/(4\pi e^2 n_e)$, where e is the charge of an electron, $m_{\rm e}$ is mass of the electron and $\langle\sigma v\rangle_{\rm en} = 2\times10^{-9}\,{\rm cm^3\,s^{-1}}$ is the slowing-down coefficient (Spitzer, 1978) for the electron-neutral collisions. Thus the critical gas surface density $\Sigma_{\rm crit}$ ($= \rho_{\rm crit}/(\sqrt{2\pi}H_{\rm g})$) for the MRI development (see details in Vorobyov et al., 2020) is expressed as

$$\Sigma_{\rm crit} = \left[\left(\frac{\pi}{2}\right)^{1/4} \frac{c^2 m_{\rm e}\langle\sigma v\rangle_{\rm en}}{e^2}\right]^{-2} B_z^2 H_{\rm g}^3 x^2\,. \tag{5.20}$$

where $x = n_e/n_n$ is ionization fraction. The criterion stated in Eq. (5.20) formally implies

that there is no MRI if B_z is zero. Note that in this approach, effects of Ohmic diffusivity are considered and other nonideal MHD effects are neglected. The dead zone gas surface density is calculated as following:

$$\text{if } \Sigma_g < \Sigma_{crit} \text{ , then } \Sigma_{MRI} = \Sigma_g \text{ , and } \Sigma_{dz} = 0 \text{ ,} \tag{5.21}$$

$$\text{if } \Sigma_g \geq \Sigma_{crit} \text{ then } \Sigma_{MRI} = \Sigma_{crit} \text{ and } \Sigma_{dz} = \Sigma_g - \Sigma_{MRI} \text{ .} \tag{5.22}$$

The depth of the dead zone in terms of the α_{eff}-parameter can be determined by the balance between Σ_{MRI} and Σ_{dz} using Eq. (5.17). The Eq.(5.21) demonstrates that a sharp increase in Σ_{crit} triggers the burst if the ionization fraction x experiences a sharp rise as well.

5.2.5 Boundary Conditions

The set up of the inner boundary of the computational domain is very crucial. It cannot be placed at a distance from the protostar that is much less than 0.1 au due to strict limitations of the Courant condition. In simple words, Courant condition is the condition that the timestep Δt must be less than the time for information to traverse a cell. Because the reduction in time step imposed by the Courant condition will make the simulations computationally infeasible. On the other hand, placing the inner boundary much farther out (at several au) could eliminate the part of inner disk that may be dynamically important since it is where (at sub-au scales) the GI-induced MRI outbursts take place.

In FEOSAD, a special type of boundary condition is used for the inner boundary for fulfilling the physical realisation. FEOSAD features inflow-outflow boundary condition, wherein the matter is allowed to flow freely from the disk to the sink cell and vice versa. If the matter would be allowed to flow in only one direction at the inner edge, for example, only from the disk to sink cell (inward direction), it causes an artificial drop in the gas density at the inner edge due to lack of compensating back flow. Because, then any wave-like motions at the inner boundary, which are triggered by the spiral density waves in the disk, would result in a disproportionate flow through sink-disk surface. Due to the inflow-outflow boundary condition, the mass exiting the inner boundary is divided between the sink cell and star, with the ratio set to 5% : 95%. It means most of the matter quickly lands on the star after crossing the sink-disk interface. The

material in the sink cell may enter back into the immediate active cell in the disk, based on its radial velocity and surface density gradient. Thus, the behavior of surface densities of gas and dust in the vicinity of the inner boundary can be trusted to be performed accurately without any numerical artefacts. The inflow-outflow boundary condition is explained in detail in Vorobyov et al. (2018b, 2020). The flow of matter from and to the sink cell also carries magnetic flux, hence, the inner boundary condition also modifies the vertical component of magnetic field B_z based on the amount of magnetic flux transported. The inner boundary maintains the initial spatially constant mass-to-magnetic-flux ratio μ across time, which also serves as a test of disk evolution in the ideal MHD limit. The inner boundary conditions also conserve mass and magnetic-flux budget of the star-disk system. The outer boundary of the computational domain is taken as standard free outflow, where the material is only allowed to leave (no inflow) the computational domain.

5.3 Results

We present the results from the simulation model in Table 5.1. In this section, we present

Model	$M_{\rm core}$ [$M_\odot$]	β [%]	Ω_0 [km s^{-1} pc^{-1}]	r_0 [au]	$\Sigma_{g,0}$ [g.cm^{-2}]	$r_{\rm out}$ [pc]	μ	$M_{*,\rm fin}$ [$M_\odot$]
`model-1`	2.04	0.133	1.6	1285	0.249	0.05	2	1.38

Table 5.1: Parameters of the simulation model: initial mass of the core $M_{\rm core}$, ratio of the rotational to gravitational energy β, angular speed Ω_0, gas surface density at the center of the core $\Sigma_{\rm g,0}$, the radius of the central plateau in the initial core r_0, radius of the core $r_{\rm out}$ note that, 1 pc = 206265 au), the mass-to-magnetic flux ratio μ, and the final stellar mass $M_{*,\rm fin}$ at the end of simulation.

numerical results on the long-term evolution of disks. The evolution of the star and disk are interconnected: the star grows according to the mass accretion from the disk and in turn heats the disk according to its photospheric and accretion luminosities. Figure 5.3 shows the long-term evolution (up to 1 Myr) of the star-disk system since the disk formation. Top panel of Figure 5.3 shows the temporal evolution of mass accretion rate $\dot{M}$ (black curve) from disk onto star. The red dashed line shows the infall rate from envelope on the disk versus time that gradually diminishes with time because of the finite mass reservoir. The black curve in

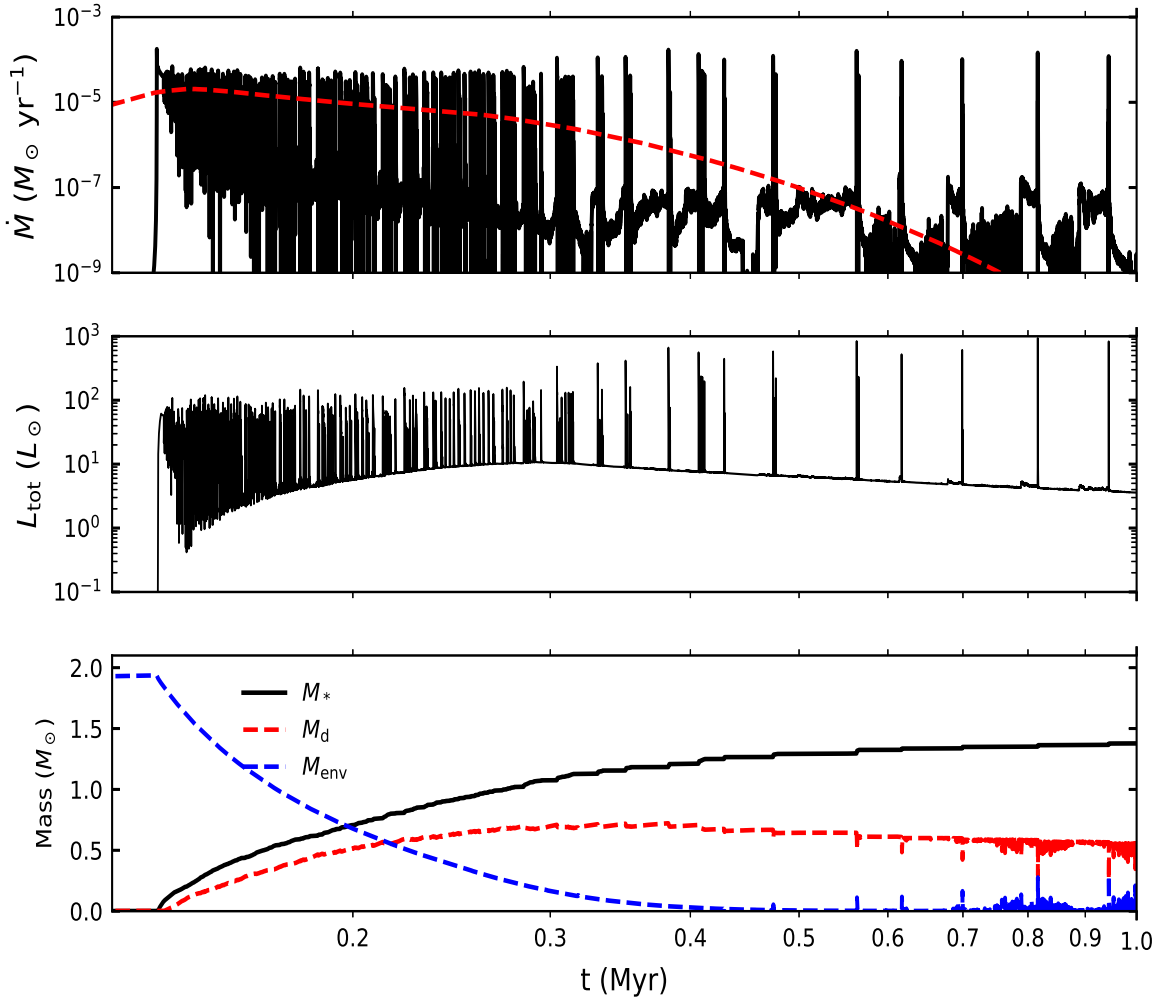

Figure 5.3: Top panel: Long-term evolution of mass accretion rate $\dot{M}$ (black line) along with mass accretion outbursts. Middle panel: Long-term evolution of luminosity $L_{\rm tot}$ along with luminosity outbursts. Bottom panel: evolution of stellar mass M_* (black line), disk mass $M_{\rm d}$ (red line), and envelope mass $M_{\rm env}$ (blue line).

the middle panel presents the temporal evolution of the total luminosity $L_{\rm tot}$ (accretion plus photospheric luminosity), which takes into account of the accretion luminosity along with the photospheric luminosity. The bottom panel shows the mass evolution of envelope $M_{\rm env}$ (blue dashed line), disk $M_{\rm d}$ (red dashed line), star M_* (black line). The temporal evolution of masses obtained from the simulation (solving non-linear terms) is very similar to that obtained from our semi-analytic model (see Figure 4.9b in Chapter 4). The disk forms after the centrifugal barrier (where angular velocity is sufficient to allow the centrifugal force to balance gravity)

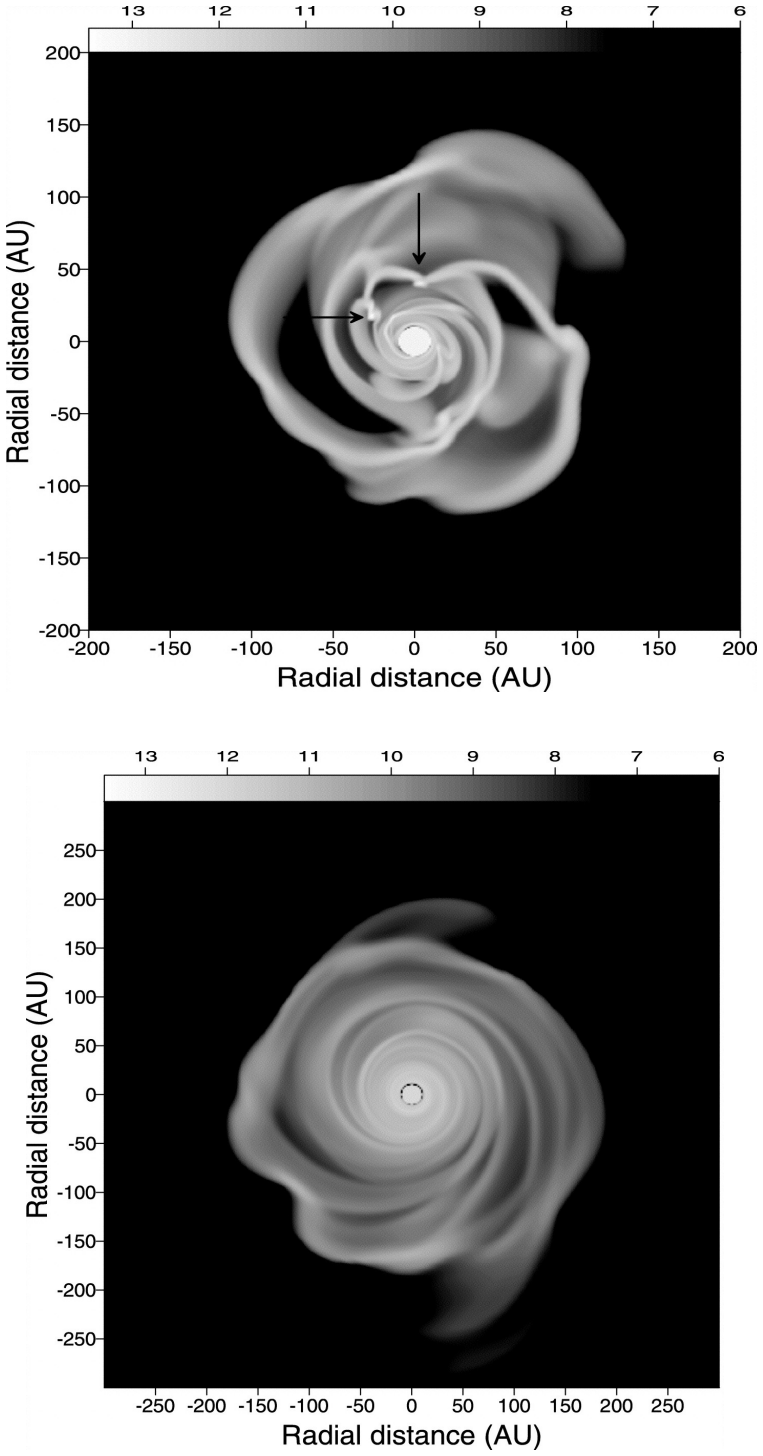

Figure 5.4: Image of the protostellar disk, showing the gas volume density distribution immediately preceding a mass accretion burst (top) and in the quiescent phase between the bursts (bottom). The protostellar /protoplanetary embryos with $n \gtrsim 10^{13}\,\mathrm{cm}^{-3}$ are indicated in the left image (arrows). The scale bar is in cm^{-3}. The bright circle in each image represents the protostar plus some circumstellar matter (Vorobyov & Basu, 2006).

is reached, which prevents further mass infall toward the center. During the initial time, the bursts are more frequent with shorter quiescent periods on the order of a few hundred years. Whereas, in the later time, the quiescent periods between luminosity bursts are much longer, which are on the order of few hundred to a few thousand years.

In our work, the mass accretion bursts are considered to occur as a combined effect of the gravitational instability (GI) in the outer spiral arms and as well as the magnetorotational instability (MRI) in the innermost region of the disk. Though GI and MRI are usually treated in isolation, however, they may coincide at some evolutionary stages of the protoplanetary disks. Observationally, it is hard to distinguish which mechanism solely causes the outburst (Riols & Latter, 2018). During the onset of a GI burst the disk becomes gravitationally unstable giving rise to the local density inhomogeneities. Hence, the spiral arms and dense clumps are formed as a consequence of the elevated mass and angular momentum redistribution within the disk. Thereafter, these clumps are migrated inward and accreted onto the star giving rise to a GI burst. Figure 5.4 shows a two-dimensional image of the gas volume density distribution of a protostellar disk as shown by Vorobyov & Basu (2006). The top panel shows the formation of dense clumps as pointed out by the arrows (Toomre-$Q < 1$) within quite sharp and chaotic spiral arms immediately preceding a mass accretion burst. On the other hand, the bottom panel of Figure 5.4 shows the density distribution during the quiescent phase of accretion ($1 < Q < 2$) when the disk exhibits typically a more diffuse and smoother spiral pattern than in the period before a burst. In contrast, an MRI burst occurs when an inner region reaches a high enough temperature that the ionization threshold of alkaline metals is exceeded. The increased level of ionization leads to effective magnetic coupling and the MRI is activated in the inner region. The nonlinear development of the MRI leads to turbulence, and the interaction of the turbulent eddies leads to an effective viscosity that far exceeds that due to microphysical processes. Here, the effective viscosity reaches a maximum value ($\alpha_{\rm eff} = 0.1$) and the viscous effect leads to rapid redistribution of angular momentum and a burst of mass accretion onto the star.

The top panel of Figure 5.5 shows the temporal evolution of total luminosity from the disk formation instance till 0.3 Myr. The bottom panel shows the zoomed-in version of a single luminosity burst obtained from the numerical simulation (as shown by the black line) for a time interval from $t = [0.2439, 0.2441]$ Myr. This single luminosity burst has sharp rise, slow

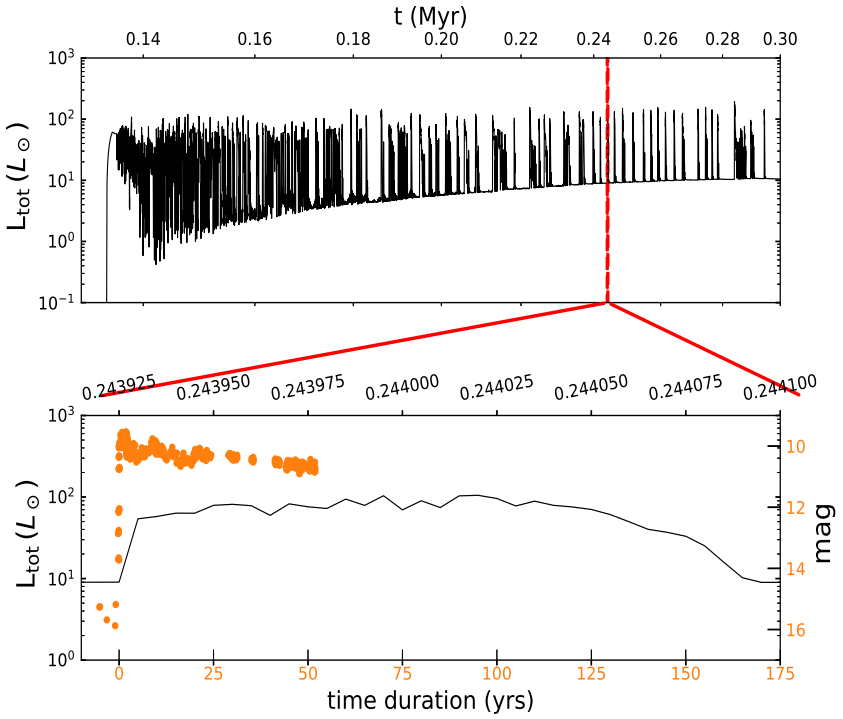

Figure 5.5: Top panel: long-term evolution of luminosity $L_{\rm tot}$ along with luminosity outbursts upto 0.3 Myr. Bottom panel: similar to the top-left panel, but zoomed-in version of a single luminosity burst for a time interval t = [0.2439, 0.2441] Myr (black line). Yellow dotted curve presents the longest ever observed FU Ori burst Herbig (1977).

decline, and a sharp fall. The rise time and duration of the burst are $\sim$ 5 yr and 170 yrs, respectively. The yellow dotted line shows the longest observed FU Orionis outburst (FU Ori itself) (see Herbig, 1977). Such bright patches of eruption (collimated jets of partially ionised gas) from the members of FU Orionis class are often named as "Herbig-Haro (HH) objects". The emission of FU Orionis objects in outburst has been identified as arising from rapidly accreting protoplanetary disks by the observations (Kenyon et al., 1990). Later, in this section, we discussed more about HH objects and present a comparative study between the observed and the numerically simulated burst. This FU Ori burst is in the active state for more than 80 years already. It has a sharp rise time of $\sim$ 1yr and the amplitude declines very slowly (Audard et al., 2014). These key characteristics of the observed FUOri burst are consistent with the findings from our numerical simulations.

To further analyze a single burst, we plot the time evolution of several quantities in Figure 5.6 at the sink-disk interface (0.52 au) as a GI-induced MRI burst developes and decays. The

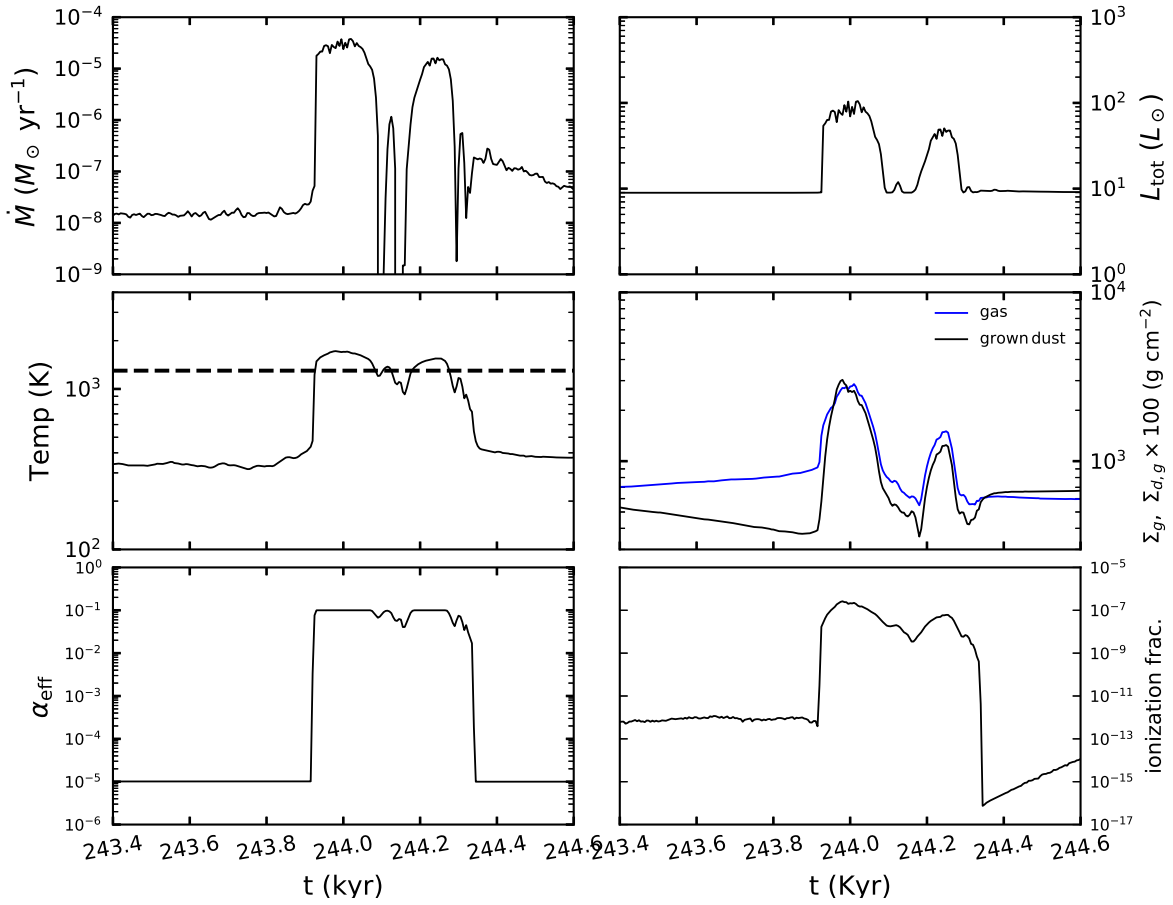

Figure 5.6: Time evolution of several disk and burst characteristics at the sink–disk interface as the burst develops and decays for a FUOr interval $t = [0.2439, 0.2441]$ Myr. Shown are the mass accretion rate (top left), total luminosity (top right), midplane temperature (middle left), gas and grown dust surface densities (middle right), $\alpha_{\rm eff}$ value (bottom left), and ionization fraction (bottom right). The dashed horizontal line in middle left panel denotes the temperature of 1300 K.

top panel of Figure 5.6 shows the mass accretion rate $\dot{M}$ and total luminosity $L_{\rm tot}$; the middle panel shows the midplane temperature $T_{\rm mp}$, surface densities of gas and grown dust ($\Sigma_{\rm g}$ and $\Sigma_{\rm d,g}$ respectively); the bottom panel shows the $\alpha_{\rm eff}-$parameter, and the ionization fraction. The characteristics during the pre-burst phase are similar to that of the post-burst phase. During the active phase, some small-scale variabilities are present. The vertical sharp-drops in the mass accretion rate curve represents that mass accretion has been stopped for that time being. During the active phase of the burst, mass accretion jumps to $\sim 10^{-4}$ $\rm M_\odot\,yr^{-1}$ and it reduces to $\sim 10^{-7}$ $\rm M_\odot\,yr^{-1}$ after the burst. The pre- and post-burst luminosity is about 9 $\rm L_\odot$ and the peak luminosity reaches around 100 $\rm L_\odot$. The midplane temperature before and after burst is around

350 K, and the ionization fraction is around 10^{-12}. Whereas during the burst, the temperature rises up to 1450 K and ionization fraction becomes 10^{-7}. Starting from the onset of the burst, the temperature gradually rises due to heating provided by residual viscosity in the disk and adiabatic compression due to inflow of the matter along spiral arms of the disk (Bae et al., 2014), which further increases thermal collisions and inner disk temperature. Thermal collisions raise the ionization level, the ionization is again accompanied by the viscous heating, and causing the temperature to further increase such that ionization of the alkaline metals (at about 1300 K) can take place and finally the producing burst by raising the $\alpha_{\rm eff}$ (see more discussions in Vorobyov et al., 2020). In the early stage, the inner disk is sufficiently hot to support thermal ionization (ionization temperature $T = 1300$ K) of alkaline metals and the disk is mostly in the MRI-active state. Accumulation of dust and gas in the dead zone induces to trigger the MRI effect. It happens because increased dust and gas density in the dead zone (MRI-inactive) increases the optical depth, which in turn makes the dead zone prone to warm up easily. As the burst decays, gas and grown dust densities decrease, which means loss of disk mass right after the burst.

The upper panel of Figure 5.7 shows the two-dimensional spatial distributions of temperature (first row), ionization fraction (second row), $\alpha_{\rm eff}-$ value (third row) at three different times of burst phases. On the other hand, the lower panel shows the corresponding temporal evolution of the mass accretion burst (left-hand axis) and total luminosity (right-hand axis) where the vertical lines at $t_{\rm A}$, $t_{\rm B}$, and $t_{\rm C}$ resemble the three different time epochs during pre-burst, active-burst, and post-burst phase, respectively. White contours in the two-dimensional panels portrait the dead zone boundary. The dead zone may not be continuous and may be patchy. We see that during pre-burst time, the dead zone forms in the inner disk region and could extend even up to the inner disk boundary (or, in other words, the inner boundary of dead zone coincides with the sink-disk surface). At the outer boundary of dead zone, the ionization fraction is on the order of 10^{-12}, temperature is few hundred Kelvin. As the burst occurs (at $t = t_{\rm B}$), innermost region of the dead zone becomes an MRI-active region and inner dead zone boundary is pushed outwards to about 5 au. During the burst, the sharp rise in the midplane temperature is primarily caused by the adiabatic compression provided by gradually inflowing matter, which makes the inner disk more opaque. The rise in the midplane temperature means that the

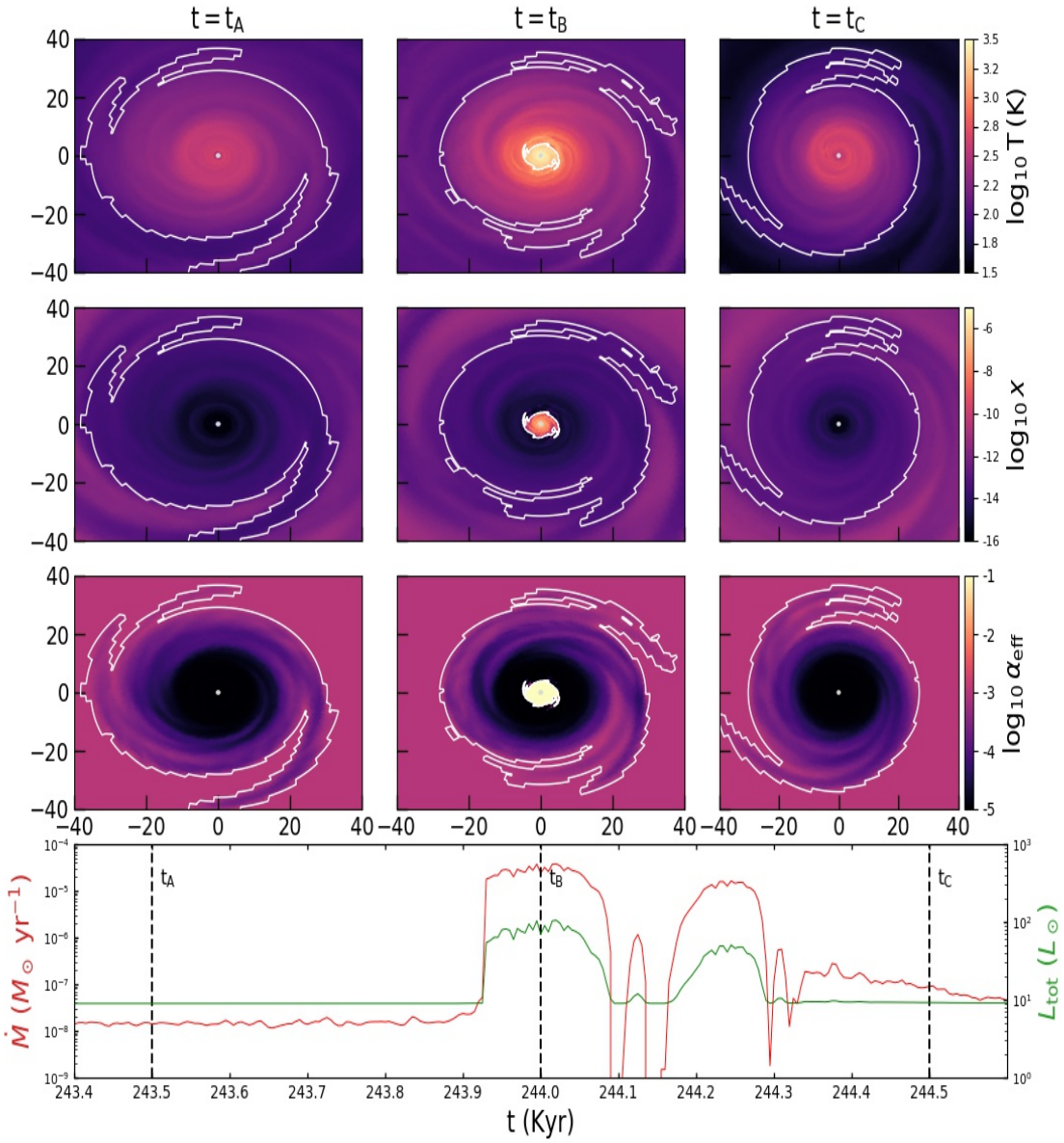

Figure 5.7: Upper rows (top three rows) of panels: two-dimensional distributions (in 80×80 au^2 box) of the gas temperature (first row), ionization fraction (second row), and turbulent parameter $\alpha_{\rm eff}$ (third row) in the region $r \lesssim 40$ au at time instants $t = 243.5,\ 244.0$, and 244.5 Myr marked with three vertical dotted lines in the lower panel, respectively. The white contour delineates the boundary of the dead zone. Lower panel: accretion rate onto the star versus time in the time interval $t = [0.2439, 0.2441]$ Myr after the disk formation.

thermal collisions can ionize the alkaline metals. This rise of ionization increases the magnetic coupling and viscous transport which in turn leads to viscous heating. Finally, the dead zone turns turn into an MRI-active region and an MRI burst occurs. The MRI-activation within the inner disk leads to an enhanced mass accretion rate of about 10^{-4} M$_\odot$ yr^{-1} , ionization fraction

10^{-8} – 10^{-7}, and effective viscosity $\alpha_{\rm eff}$– value of 0.1. After the active burst phase, there is a drop in temperature because of radiative cooling as the inner disk loses mass and becomes relatively less optically thick to its own thermal radiation. The boundary of the dead zone approximately coincides with the isocontours of the ionization fraction, at which the condition for suppressing the MRI is fulfilled.

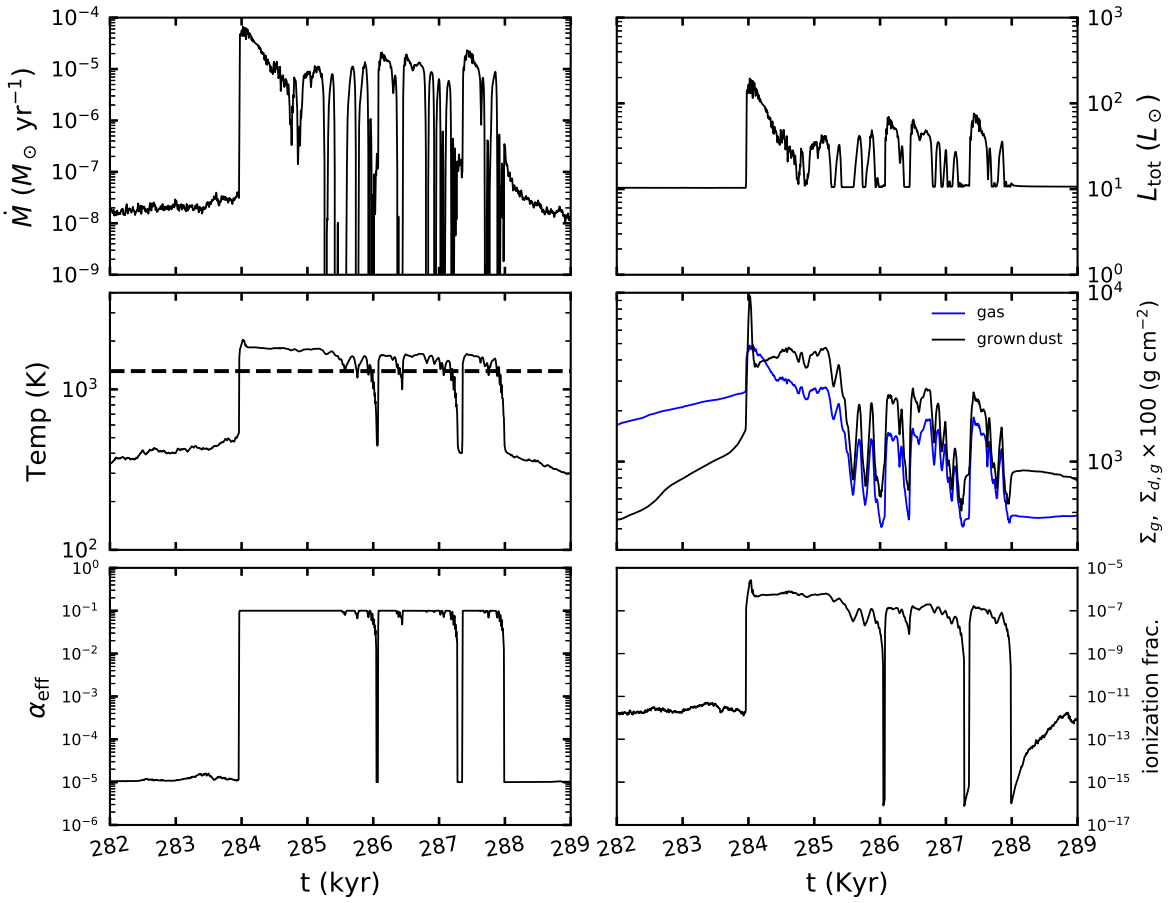

Figure 5.8: Time evolution of several disk and burst characteristics at the sink–disk interface as a burst develops and decays for a time interval t = [0.282, 0.289] Myr. Shown are the mass accretion rate (top left), total luminosity (top right), midplane temperature (middle left), gas and grown dust surface densities (middle right), $\alpha_{\rm eff}$ value (bottom left), and ionization fraction (bottom right). The dashed horizontal line in middle left panel denotes the temperature of 1300 K.

Figure 5.8 shows zoomed-in characteristics of a series of bursts which can be thought as GI-induced successive MRI bursts over a span of ∼ 3940 yr. Since the onset of the initial burst at t = 283.95 Myr until 288.0 Myr, we find there are several small (∼ 34 – 47 $L_\odot$) and medium (∼ 40–75 $L_\odot$) amplitude bursts with the average duration of about 77–134 yrs and 296–396 yrs,

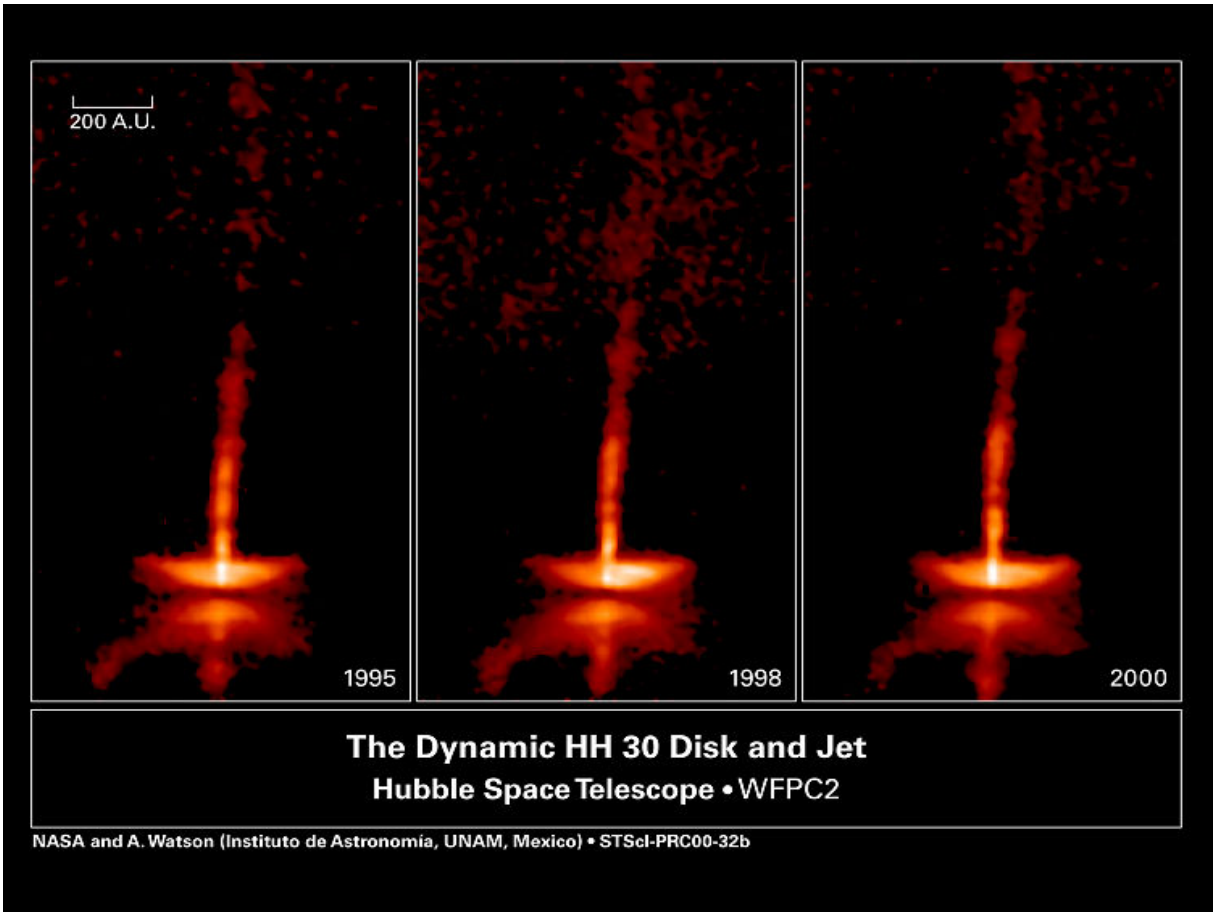

Figure 5.9: The object is known as Herbig-Haro 30 (HH 30), a prototypical young stellar object surrounded by a disk and jet. The Hubble Space Telescope captures the emission in optical wavelength while the young central star is obscured by the dust in the disk and the images show changes over only a five-year period.

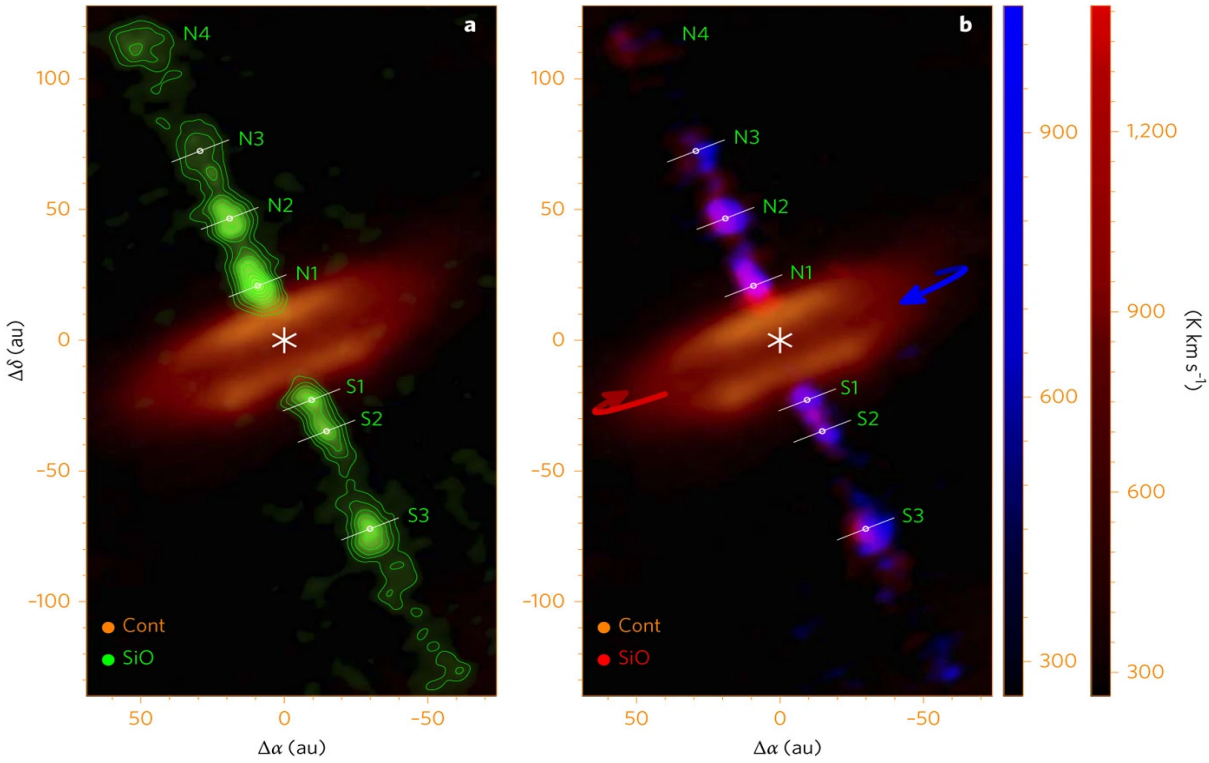

Figure 5.10: Lee et al. (2017) presents ALMA SiO and continuum observations of the rotating outflow from the Class 0 protostar HH 212. While the outflow itself extends to much larger scales, this shows the region within ≈ 120 au of the central source, at a resolution of ≈ 8 au on top of the continuum map of the disk. The maps show the intensity (in unit of $\mathrm{K\,km\,s^{-1}}$) integrated over the outflow velocity range. (a) A chain of SiO knots trace the primary jet emanating from the disk testifying to the episodic nature of the outflow. (b) Blue-shifted and red-shifted SiO emission of the jet plotted with the continuum (disk) emission. The direction of rotation of the disk is shown with blue and red arrows and this is the same as the direction of rotation of the red and blue-shifted jets.

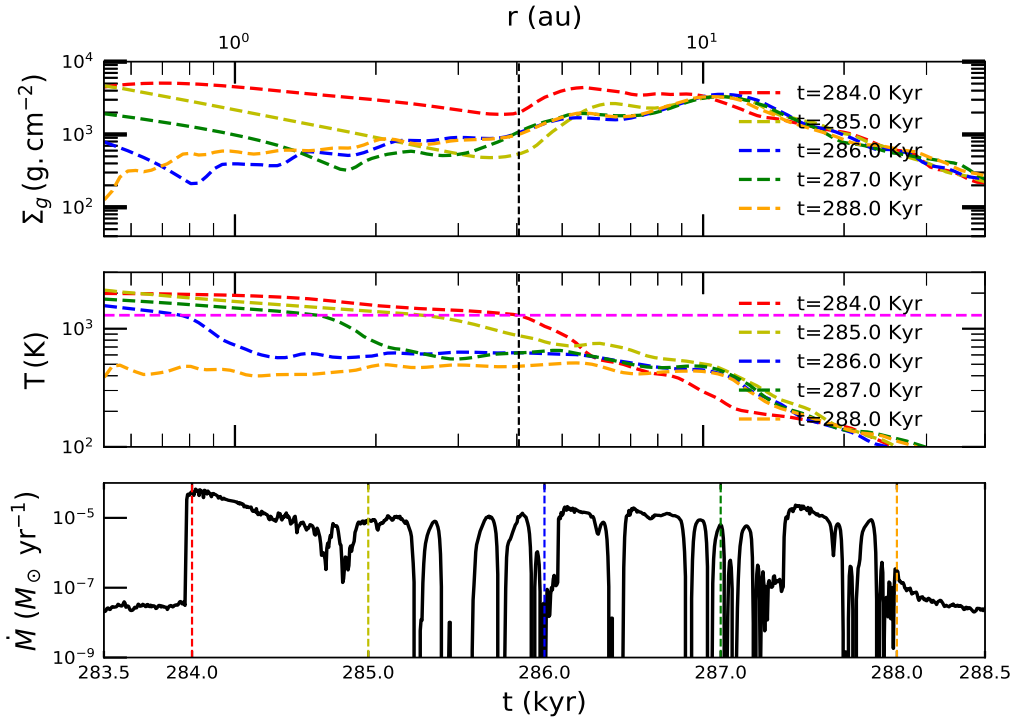

Figure 5.11: Top and middle panel: temporal evolution of the radial distribution of surface density and temperature at different time instances during the burst. Lower panel: Accretion rate history during the burst over a time interval t=[0.2835, 0.2885] Myr. disc radial profiles in the MRI model.

respectively followed by a larger amplitude ($\sim 200\,L_\odot$) burst with duration of about 801 yrs at the initial time. The quiescent phase in between the bursts ranges from $86 - 188$ kyr. The mass associated with the larger-amplitude long-duration, medium amplitude-medium duration, and small amplitude shorter duration bursts are about $17.4, 3.5, 0.8\ M_{\rm Jup}$[3], respectively. This phenomena of a series of episodic accretion bursts might resemble the sequence of knots seen at optical wavelengths in the HH objects as shown in Figure 5.9. Figure 5.9 presents image of object HH30, the emission from a young central star surrounded by a dusty disk seen at optical wavelength. Figure 5.10 shows ALMA SiO and continuum observations of knotty outflow from the Class 0 protostar HH 212, which testifies to the episodic nature of the outflow (Lee et al., 2017). Bontemps et al. (1996) suggest that outflow energetics reflects a correlation to the mass infall/accretion rate such that $\dot{M}_{\rm inflow} \propto \dot{M}_{\rm outflow}$. The knots in the observed molecular jets could correspond to the series of episodic eruptions, i.e., repetitive ejection of clumps

[3] $1\ M_{\rm Jup} \equiv 1047\ M_\odot$

onto the star over a long period of time (~ few hundred to few thousand years) during the star formation process as described by Vorobyov et al. (2018a). Such accretion bursts can be by caused by both the gravitational instability and magnetorotational instability. The chain of knots at different epochs can reveal the variability of outflows in time and episodically ejected accretion bursts. The difference between the dynamic timescales of the ejected knots as found from the observations can be used to estimate the durations of quiescent phases between two consecutive episodic ejections (e.g., Fig. 5 of Vorobyov et al., 2018a).

Figure 5.11 presents the radial profiles of gas surface density (top panel) and temperature (middle panel) at various time instances for the GI induced MRI burst. The lower panel shows the temporal evolution of the mass accretion rate of the burst along with vertical lines representing the five different time instances. The horizontal dashed line (magenta color) in the second panel shows the activation temperature of MRI ($T = 1300$ K). When the temperature drops below this activation threshold, the MRI-active region becomes a dead zone (MRI-inactive). At time $t = 284$ yr (active phase of burst), the MRI-active region extends up to around 4 au. The inner boundary of the dead zone starts where the MRI-active region ends. During the active phase of the burst, the inner boundary of the dead zone gets pushed out to ~ 4 au because of formation of MRI-active region at the center. At this active phase, disk loses mass because of infall of the gaseous clumps onto star, so the surface density of gas also decreases gradually. When the temperature drops below the MRI activation threshold, the surface density of gas also starts to increase as matter starts to pile up in the dead zone, which is reflected as a local minima in the σ_g profile at the inner boundary of dead zone. Enhanced gas surface density also hinders the cosmic rays to penetrate the inner disk and as a result the ionization fraction rapidly drops and the dead zone forms (Elbakyan et al., 2021). However, as time progresses, the extent of the MRI-active region reduces and shrinks toward the inner disk edge. Finally, at $t = 288$ yr when the burst decays significantly, the MRI-active region turns back into a dead zone. The inner boundary of the dead zone eventually approaches toward the inner disk edge (0.52 au).

5.4 Conclusions and Discussions

In this study, we present the results of global long-term numerical magnetohydrodynamic simulations of protostellar disks in the thin-disk limit. The simulation is conducted using coupled dust-gas MHD equations of protoplanetary disks, with a focus on the structure and evolution of GI-induced episodic MRI bursts occurring in the inner disk. The simulations are started with the core collapse phase of a prestellar molecular cloud core, so that the initial conditions could be self-consistent. Our results capture the intricate structure of individual episodic outbursts formed in the inner disk region both in the spatial and temporal domain. Protostellar disks are characterized by time-varying episodic accretion with intermittent bursts. Such FU-Orionis-like eruptions can lead to a sudden deposition of mass at au to sub-au scales within the inner disk either by triggering of magnetorotational instability or gravitational instability. Accretion variability is frequent in the early evolution and reduces with time as the disk instability weakens because of diminishing mass infall from the envelope. The series of GI induced MRI bursts could potentially provide more information on the chain of knots in a molecular jet as found from observations. If the quiescent time between two successive bursts becomes comparable or longer than the planetesimal formation timescale (typically few thousand years), then rapid dust coagulation can likely occur via the streaming instability (Youdin & Goodman, 2005; Youdin & Johansen, 2007). Our results show that during earlier times, the quiescent time between two bursts e.g., at 0.3540 Myr and 0.3823 Myr, is to be $\approx$ 28.3 kyr, and between another two bursts e.g., at 0.4770 Myr and 0.5627 Myr, it is to be 85.7 kyr. Whereas at later times, it is to be $\approx$ 127.2 kyr in between two bursts at 0.8169 Myr and 0.9443 Myr. For the bursts that occurred between $\approx 0.35 - 1$ Myr, the intervening quiescent time for most of the cases is longer than the typical freeze-out time of gas-phase CO (on the order of hundreds to few thousands years) in the envelope (Visser & Bergin, 2012; Vorobyov et al., 2013; Rab et al., 2017). Therefore, studying the quiescent phase i.e., pre- and post-burst phase are dynamically important since planetesimal formation occurs far inwards of the region where CO freezes out.

Although the ideal MHD regime was adopted for the evolution of the magnetic field and the nonideal effects were neglected, this model is far more complex than the gas-only semi-analytic model presented earlier in Chapter 4. In future work, the implementation of nonideal MHD physics, we will able to compare fragmentation lengthscale, timescale and mass scale with the

findings from the linear analysis work by Das & Basu (2021) as presented in Chapter 2. The effect of the inner disk physics on the mass accretion rate history requires high-resolution studies, which are planned for the future. More sophisticated numerical models and observational data are needed to further explore the connections between episodic accretion and the knotted outflows as well as between the time duration of the quiescent phase and the planetesimal formation time.

Bibliography

Armitage P. J., 2015, arXiv e-prints, p. arXiv:1509.06382

Armitage P. J., Livio M., Pringle J. E., 2001, MNRAS, 324, 705

Audard M., et al., 2014, in Beuther H., Klessen R. S., Dullemond C. P., Henning T., eds, Protostars and Planets VI. p. 387 (arXiv:1401.3368), doi:10.2458/azu_uapress_9780816531240-ch017

Bae J., Hartmann L., Zhu Z., Nelson R. P., 2014, ApJ, 795, 61

Balbus S. A., Terquem C., 2001, ApJ, 552, 235

Basu S., 1997, ApJ, 485, 240

Basu S., Mouschovias T. C., 1994, ApJ, 432, 720

Birnstiel T., Klahr H., Ercolano B., 2012, A&A, 539, A148

Bontemps S., Andre P., Terebey S., Cabrit S., 1996, A&A, 311, 858

Ciolek G. E., Mouschovias T. C., 1993, ApJ, 418, 774

Contreras Peña C., et al., 2017, MNRAS, 465, 3011

Contreras Peña C., Naylor T., Morrell S., 2019, MNRAS, 486, 4590

Crutcher R. M., 2012, ARA&A, 50, 29

Das I., Basu S., 2021, ApJ, 910, 163

Dong R., Vorobyov E., Pavlyuchenkov Y., Chiang E., Liu H. B., 2016, ApJ, 823, 141

Elbakyan V. G., Nayakshin S., Vorobyov E. I., Caratti o Garatti A., Eislöffel J., 2021, A&A, 651, L3

Enoch M. L., Neal J. I., Sargent A. I., Glenn J., 2009, ApJ, 692, 973

Fischer W. J., Safron E., Megeath S. T., 2019, ApJ, 872, 183

Gammie C. F., 1996, ApJ, 457, 355

Herbig G. H., 1966, Vistas in Astronomy, 8, 109

Herbig G. H., 1977, ApJ, 217, 693

Herbig G. H., 1989, in European Southern Observatory Conference and Workshop Proceedings. pp 233–246

Hillenbrand L. A., Findeisen K. P., 2015, ApJ, 808, 68

Kenyon S. J., Hartmann L. W., Strom K. M., Strom S. E., 1990, AJ, 99, 869

Kunz M. W., Balbus S. A., 2004, MNRAS, 348, 355

Lee C.-F., Ho P. T. P., Li Z.-Y., Hirano N., Zhang Q., Shang H., 2017, Nature Astronomy, 1, 0152

Mathis J. S., Rumpl W., Nordsieck K. H., 1977, ApJ, 217, 425

Quanz S. P., Henning T., Bouwman J., van Boekel R., Juhász A., Linz H., Pontoppidan K. M., Lahuis F., 2007, ApJ, 668, 359

Rab C., et al., 2017, A&A, 604, A15

Rice W. K. M., Lodato G., Pringle J. E., Armitage P. J., Bonnell I. A., 2004, MNRAS, 355, 543

Riols A., Latter H., 2018, MNRAS, 474, 2212

Sano T., Miyama S. M., Umebayashi T., Nakano T., 2000, ApJ, 543, 486

Scholz A., Froebrich D., Wood K., 2013, MNRAS, 430, 2910

Semenov D., Henning T., Helling C., Ilgner M., Sedlmayr E., 2003, A&A, 410, 611

Shakura N. I., Sunyaev R. A., 1973, A&A, 500, 33

Shu F. H., 1977, ApJ, 214, 488

Spitzer L., 1978, Physical processes in the interstellar medium. John Wiley and Sons, USA, doi:10.1002/9783527617722

Umebayashi T., Umebayashi T., 2009, ApJ, 690, 69

Visser R., Bergin E. A., 2012, ApJ, 754, L18

Vorobyov E. I., Basu S., 2005, MNRAS, 360, 675

Vorobyov E. I., Basu S., 2006, ApJ, 650, 956

Vorobyov E. I., Basu S., 2007, MNRAS, 381, 1009

Vorobyov E. I., Basu S., 2009, MNRAS, 393, 822

Vorobyov E. I., Basu S., 2010, ApJ, 719, 1896

Vorobyov E. I., Basu S., 2015, ApJ, 805, 115

Vorobyov E. I., Baraffe I., Harries T., Chabrier G., 2013, A&A, 557, A35

Vorobyov E. I., Elbakyan V. G., Plunkett A. L., Dunham M. M., Audard M., Guedel M., Dionatos O., 2018a, A&A, 613, A18

Vorobyov E. I., Akimkin V., Stoyanovskaya O., Pavlyuchenkov Y., Liu H. B., 2018b, A&A, 614, A98

Vorobyov E. I., Khaibrakhmanov S., Basu S., Audard M., 2020, A&A, 644, A74

Yang C.-C., Mac Low M.-M., Johansen A., 2018, ApJ, 868, 27

Yorke H. W., Bodenheimer P., 2008, in Beuther H., Linz H., Henning T., eds, Astronomical Society of the Pacific Conference Series Vol. 387, Massive Star Formation: Observations Confront Theory. p. 189

Youdin A. N., Goodman J., 2005, ApJ, 620, 459

Youdin A., Johansen A., 2007, ApJ, 662, 613

Zhu Z., Jiang Y.-F., Stone J. M., 2020, MNRAS, 495, 3494

Chapter 6

Summary

In this Thesis, we highlight the importance of the self-gravity, magnetic field, nonideal MHD, episodic accretion on the star formation process. Starting from the evolution of the prestellar cores to the formation of a star-disk system, these processes all play an important role. Some of the important results from the different chapters are compiled in this chapter.

In Chapter 2, we present a semi-analytic model using linear stability analysis (in the limit of thin-disk approximation) to explore gravitational instability in a rotating protostellar disk in the presence of two nonideal MHD effects: Ohmic dissipation and ambipolar diffusion (Das & Basu, 2021). Ohmic dissipation is important in the innermost regions of a disk, whereas ambipolar diffusion is dominant in the outer parts of disks. Our results may prove to be useful in the analysis of global nonideal MHD models for the evolution of rotationally supported self-gravitating protostellar disks. We derive a generalized Toomre instability criterion for a rotating fluid modified by the magnetic field in the flux-freezing limit. We then study the effect of the nonideal MHD effects on the gravitational instability. Qualitatively, we see that both the nonideal MHD effects behave similarly. However, the timescales and lengthscales of instability also depend on the neutral-ion collision time (the measure of ambipolar diffusion) and Ohmic diffusivity (the measure of Ohmic dissipation), rotation parameter (Toomre-Q). For a supercritical cloud (gravity dominated), when nonideal MHD (i.e., diffusion of magnetic field) effects are included, the results get reduced to that of the hydrodynamic (non-magnetic) case. We found that in the presence of nonideal MHD effects, the peak fragmentation mass occurs at a slightly transcritical mass-to-magnetic flux ratio and exceeds the non-magnetic

(thermal, or Jeans) scale by a factor of up to 10, and the fragmentation mass is likely to be around 10 – 90 times the Jupiter mass ($1 M_{\rm Jup} \approx 10^{-3} M_{\odot}$). We apply our results to protostellar disk properties in the early embedded phase that are probed by astronomical observations. Giant planets in many extrasolar systems are now thought to form by a direct gravitational instability rather than the traditional hypothesis of planetesimal accretion.

In Chapter 3, we apply the linear analysis results of ambipolar diffusion-driven gravitational instability (Ciolek & Basu, 2006) to fit the data of the evolutionary time/lifetime and fragmentation mass of prestellar cores identified with Herschel Space Observatory in the Aquila cloud. We also fit the number of enclosed cores formed in a parent clump measured in Perseus cloud complex with the Submillimeter Array (SMA) (Das et al., 2021). The model discussed in Ciolek & Basu (2006) can be derived from our general semi-analytic model as presented in Das & Basu (2021) in the limit of negligible rotation and Ohmic resistivity, which is applicable for the case of a molecular cloud rather than a disk. By varying a single parameter, the mass-to-magnetic flux ratio, over the range of observationally measured densities, we use our model-derived instability growth time as a proxy for the evolutionary time of prestellar cores (that varies from 0.1 to a few Myr). Linear analyses show that the lifetime and fragmentation scales are significantly greater than the non-magnetic (Jeans) values even for clouds with mildly supercritical mass-to-flux ratio. Such variations do not exist in the standard thermal pressure dominated (Jeans) fragmentation theory. The preferred fragmentation mass of our model serves as a magnetic field dependent instability threshold, in contrast to a Jeans mass (hydrodynamical limit). Our best-fit model for prestellar cores exhibits a relation in which the magnetic field is directly proportional to the neutral number density, however, it has a shallower slope than the flux-frozen (ideal MHD) case due to the effects of ambipolar diffusion (nonideal MHD).

In Chapter 4, we develop a semi-analytic formalism (Das & Basu, 2022) for the determination of the evolution of the stellar mass accretion rate for specified density and velocity profiles that emerge from the runaway collapse of a prestellar cloud core. Our model provides a self-consistent evolution of the mass accretion rate by joining the spherical envelope accretion with the disk accretion and accounts for the presence of episodic accretion bursts at appropriate times. In our model, we emphasize the gravitational torques as a means of transporting

mass from disk to star through the spiral arms. Our episodic accretion model shows that bursts are required to provide a good match to the observed distribution of bolometric luminosities and toward the efficient mass growth of the protostar. In contrast, a smoothly time-dependent mass accretion rate, whether monotonically increasing or decreasing, is unable to do so. Our framework reproduces key elements of detailed hydrodynamical numerical simulations of disk accretion and can aid in developing intuition about basic physics as well as in comparing theory with observations.

In Chapter 5, we study the detailed structure of the individual accretion burst using numerical MHD simulations of the long-term ($\sim 1.0\,\mathrm{Myr}$) evolution of protoplanetary disks in the thin-disk limit (Vorobyov et al., 2020). Mass accretion bursts are the nonlinear outcome of the transport of clumps within the disk. In Chapter 4, we model the nonlinear effect with simple approximations keeping the linear-order terms. In Chapter 5, we carry out MHD simulations where all the nonlinear equations are solved self-consistently to investigate their global effects within the disk as it evolves from a gravitationally unstable state to a viscous-dominated state. We investigate the physical mechanism causing the episodic bursts and their characteristics in terms of burst duration, rise time, burst amplitude, accreted mass associated with the burst, etc., and compare them with the observed knots in the molecular protostellar jets. Observation and modeling of episodic accretion bursts across a wide range of mass models of YSOs seem to be promising probes for investigating inner disk structure and fragmentation of the outer disk due to gravitational instability.

To sum up, we explore the consequences of gravitational instability and (ideal and non-ideal) MHD effects in the fragmentation of the protostellar disk that occurs in the protostellar phase (after the protostar is born) as discussed in Chapter 2. In addition to that, the prestellar counterpart of this study is also discussed in Chapter 3, which captures the fragmentation of a molecular cloud and evolution of prestellar cores. After studying the fragmentation of molecular cloud core and protostellar disk, we focus on the disk evolution. In Chapter 4, we investigate the significance of episodic accretion toward the overall disk evolution and mass growth of a protostar in the hydrodynamic limit using our semi-analytic model of episodic accretion. Over and above, finally, in Chapter 5, we show the numerical results of magnetohydrodynamic simulation of self-consistent disk evolution starting from prestellar core collapse by taking into

account most of the important disk physics. Future work will involve investigating a much wider range of initial conditions, particularly the magnetic field strength, prestellar cores with different masses, the physics of nonideal MHD. All of our studies from various perspectives fill in many gaps of our knowledge of how the pre-main sequence stars formed over time and consolidate the broad picture of star formation.

The theory of star formation has evolved a lot over the last few decades. A a complete understanding of the role of magnetic fields in the star-disk formation still requires more observational constraints and comparison with theoretical models and global simulations. In principle, the magnetic field acts against the gravitational inward pull and hinders the core-collapse. It is very fascinating to find out under what circumstances gravity can win over all the opposing effects. Understanding the connection between the diffusion of magnetic field and the formation mechanism of the star-disk system is the key to explaining the process of star formation. Future works require an intensive study using three-dimensional nonideal MHD codes (like FLASH, Athena) with a much higher resolution accompanied by multi-wavelength observations (e.g., Herschel, SOFIA, SMA, ALMA, and JCMT) to obtain a three-dimensional picture of the magnetic fields in a star-forming region. It is important to determine how the gas is channeled either along the field lines or through them and triggers the collapse. Additionally, further studies on protostellar/protoplanetary disk could also shed some light on the planetesimal formation that can eventually lead to the formation of exoplanet systems through further processes.

Bibliography

Ciolek G. E., Basu S., 2006, ApJ, 652, 442

Das I., Basu S., 2021, ApJ, 910, 163

Das I., Basu S., 2022, Monthly Notices of the Royal Astronomical Society, 514, 5659

Das I., Basu S., André P., 2021, A&A, 649, L13

Vorobyov E. I., Khaibrakhmanov S., Basu S., Audard M., 2020, A&A, 644, A74

Curriculum Vitae

INDRANI DAS

Department of Physics and Astronomy
University of Western Ontario
1151 Richmond Street
London, Ontario N6A 3K7, Canada

ORCID ID: 0000-0002-7424-4193

Research Interests

- Computational Astrophysics and Magnetohydrodynamic (MHD) simulations
- Role of magnetic field in star formation
- Protoplanetary disks and giant planet formation

Education

2018–2022 †	Ph.D., Physics, University of Western Ontario Thesis: *The role of nonideal magnetohydrodynamic effects, gravitational instability, and episodic accretion in star-formation* Supervisor: Prof. Shantanu Basu	London, Canada
2015–2017	M.Sc., Physics, Indian Institute of Technology Kharagpur SGPA: 8.55/10 Thesis: *The effects of massive neutrinos in the spatial distribution of neutral hydrogen (HI)* Supervisor: Prof. Somnath Bharadwaj	Kharagpur, India
2012–2015	B.Sc., Physics (Honours), University of Calcutta (Bethune College) Grades: First Class with High Distinction (securing 75.75% with rank 13 among 1000 candidates) Minors: Mathematics (First Class with 84%), Computer Science (First Class with 74.6%)	Kolkata, India

† *By August, 2022*

Publications

Refereed Articles

First authored publications:

- "A semi-analytic model for the temporal evolution of the mass accretion rate during star formation", **Indrani Das**, Shantanu Basu, 2022, Monthly Notices of Royal Astronomical Society, 514, 5659-5672
- "Variation of the Core Lifetime and Fragmentation Scale in Molecular Clouds as an Indication of Ambipolar Diffusion", **Indrani Das**, Shantanu Basu and Philippe André, 2021, Astronomy & Astrophysics Letters, 649, L13
- "Linear Stability Analysis of a Magnetic Rotating Disk with Ohmic Dissipation and Ambipolar Diffusion", **Indrani Das** and Shantanu Basu, 2021, Astrophysical Journal, 910, 163 (25pp)

Co-authored publications:

- "Synthetic Polarization Maps of an Outflow Zone from Magnetohydrodynamic Simulations", Gianfranco Bino, Shantanu Basu, Masahiro N. Machida, Aris Tritsis, Mahmoud Sharkawi, Kundan Kadam,**Indrani Das**, 2022, to appear in Astrophysical Journal, arXiv: 2207.01743
- "Hourglass Magnetic Field from a Survey of Current Density Profiles", Gianfranco Bino, Shantanu Basu, Mahmoud Sharkawi, **Indrani Das**, 2022, New Astronomy, 90, 101667
- "Radiative Transfer and Generalized Wind", Christopher Essex and **Indrani Das**, 2020, Entropy 22(10), 1153

In preparation (First authored):

- "Numerical simulations of mass accretion bursts in magnetized gas-dust protoplanetary disks", **Indrani Das**, Shantanu Basu, Eduard I. Vorobyov, 2022

Conference Proceedings (Refereed)

- "Gravitational Instability of a Magnetic Rotating Disk with Ohmic Dissipation and Ambipolar Diffusion", **Indrani Das** and Shantanu Basu, 2020, Research Notes of the AAS, Volume 4, Number 12 (236th AAS Meeting)

ADS Library: https://ui.adsabs.harvard.edu/public-libraries/M6XcZNshRQilGuwOAq49uA
Google scholar: Indrani Das Google Scholar

Software/Technical Skills

- Programming Languages : Python, Fortran 90 (Experienced; using for numerical calculations in own research)
  : C, Matlab, Mathematica (Basic knowledge)
- Operating Systems : Linux/Ubuntu, Windows
- Experiences:
  - High Performance Computing : Shared Memory Parallel Computation
    Compute Canada, SHARCNET[1] (Clusters: Cedar, Graham, Narval)
    : utilized ≈ 1 million CPU hours
  - MHD Simulations : FEOSAD code, a high-order finite-difference OpenMP (shared memory) private code

[1] Shared Hierarchical Academic Research Computing Network

Conference/Presented Talks

- Dissertation Talk, 240th AAS Meeting, June 12-16, 2022
- "Semi-analytic modelling of mass accretion during star formation", 238th AAS Meeting, June 7-9, 2021
- "Variation of the Core Lifetime and Fragmentation Scale in Molecular Clouds as an Indication of Ambipolar Diffusion", ISM 2021, Beirut, May 11-14, 2021
- "Variation of the Core Lifetime and Fragmentation Scale in Molecular Clouds as an Indication of Ambipolar Diffusion ", 237th AAS Meeting, Jan 11-15, 2021
- "Linear Stability Analysis of a Magnetic Rotating Disk with Ohmic Dissipation and Ambipolar Diffusion", HL Tau Conference, Dec 7-11 2020
- "Linear Stability Analysis of a Magnetic Rotating Disk with Ohmic Dissipation and Ambipolar Diffusion", 236th AAS Meeting, June 1-5, 2020

Awards

- Awarded Graduate Teaching Assistant Award of Excellence in 2022 by the Physics & Astronomy Department of the University of Western Ontario
- Awarded Mitacs Globalink Research Award of CAD 6000 in 2021
- Awarded "INSPIRE Scholarship for Higher Education" in 2012 (registration number is 2151/2012) of INR 3,00,000 for a total of 5 consecutive years from July, 2012 to July, 2017 (B.Sc. (3 yrs) and M.Sc. (2 yrs)) by the Department of Science and Technology (DST), Government of India, for securing a place among top 1% candidates in India at 10+2 level.

Schools & Workshops

- Summer School in Statistics for Astronomers XVI, June 1-5, 2021
- V Astrochemistry KROME School, Feb 22- Mar 5, 2021
- Astropy Workshop (for Beginners & Advanced), 237th AAS Meeting, Jan 7-8, 2021
- Gravitational Wave Astronomy School, ICTS-TIFR, Bangalore, India, Aug 13-24, 2018
- Gravitational Wave Astronomy School, ICTS-TIFR, Bangalore, India, July 17-28, 2017
- Winter School on Astronomy, Hyderabad, Feb 20-23, 2017
- Summer Internship on "Star orbits in lopsided galaxies", IUCAA, Pune, India, May 15 - June 2, 2016
- 10th Winter school on Astro Particle Physics (WAPP) 2015, Dec 21-29, 2015

Achievements

- Qualified All India Joint Admission Test for M.Sc. in Physics (IIT JAM) in 2015 securing 164th rank among approximately 3000 applicants
- Qualified All India Joint Entrance Screening Test (JEST) in 2015 for M.Sc. and Integrated Ph.D. with 92.29 percentile

Science activities/involvements

Poster Judging :

- Evolutionary Timescales On M Dwarf Planets From Dynamical Stability Arguments, 238th AAS Meeting, May 7, 2021
- The Molecular Content of Planetary Nebulae: The Next Level, 238th AAS Meeting, May 7, 2021
- Modeling Dwarf Galaxies, 238th AAS Meeting, May 9, 2021
- Modeling Dynamics of Massive Black Holes Using Leapfrog Method Simulations, 237th AAS Meeting, 2021
- Resolved Stellar Populations in the Era of JWST and Roman, 237th AAS Meeting, Jan 13, 2021

Languages

- English (Fluent)
- Bengali (Native Language)

Experience in Teaching Science & Programming

Teaching Assistant at University Of Western Ontario since 2018 Fall for the following undergraduate courses:

- Winter 2022 - Gravitational Astrophysics and Cosmology (Astronomy 4602B) for 4th year students of Physics and Astronomy
- Fall 2021 - Numerical and Mathematical Methods (NMM1412A) for 1st year students of Mathematics and Physics
- Winter 2021 - Linear Algebra (AM2811B) for 2nd year students of Mathematics and Physics
- Fall 2020 - Advanced Calculus (Cal 2402A) for 2nd year students of Mathematics and Physics
- Winter 2020 and Fall 2019 - Engineering Calculus (AM1413) for 1st year students of engineering (all disciplines)
- Winter 2019 and Fall 2018 - Calculus (Cal1000) for 1st year students of Mathematics & Physics